



Atmospheric degradation of oxygenated Volatile Organic Compounds

Asma Grira

► To cite this version:

Asma Grira. Atmospheric degradation of oxygenated Volatile Organic Compounds. Other [cond-mat.other]. Université Rennes 1, 2021. English. NNT : 2021REN1S017 . tel-03348008

HAL Id: tel-03348008

<https://theses.hal.science/tel-03348008>

Submitted on 17 Sep 2021

HAL is a multi-disciplinary open access archive for the deposit and dissemination of scientific research documents, whether they are published or not. The documents may come from teaching and research institutions in France or abroad, or from public or private research centers.

L'archive ouverte pluridisciplinaire **HAL**, est destinée au dépôt et à la diffusion de documents scientifiques de niveau recherche, publiés ou non, émanant des établissements d'enseignement et de recherche français ou étrangers, des laboratoires publics ou privés.

THESE DE DOCTORAT

UNIVERSITE DE RENNES 1

ECOLE DOCTORALE N° 596
Matière, Molécules, Matériaux
Spécialité : « Physique »

Par

Asma GRIRA

Atmospheric degradation of Oxygenated Volatile Organic Compounds

Thèse présentée et soutenue à « Rennes », le « 18/02/2021 »
Unité de recherche : Physique Moléculaire

Composition du Jury :

Rapporteur	M. MELLOUKI Wahid	Directeur de Recherche, ICARE
Rapportrice	Mme. PICQUET VARRAULT Bénédicte	Professeur, Université Paris-Est Créteil
Examinatrice	Mme. PERRAUDIN Emilie	Maître de conférences, Université de Bordeaux
Co-Encadrante	Mme. EL DIB Gisèle	Maître de conférences, Université de Rennes1
Co-Directeur de thèse	M. TOMAS Alexandre	Professeur, IMT Lille Douai
Directeur de thèse	M. CANOSA André	Directeur de Recherche, Université de Rennes1

*“What you get by achieving your goals is not as important as
what you become by achieving your goals”.*

- Zig Ziglar -

Acknowledgments

This project could not be fulfilled without a group of people who deserve a sincere "Thank you".

First of all, I would like to thank my committee members: Prof. Abdelwahid Mellouki, Prof. Bénédicte Picquet-Varrault and Dr. Emilie Perraudin, for accepting to examine this work.

I take this opportunity to express my sincere gratitude to the people who played a fundamental role in the success and completion of this project.

I would like to address my thanks to Prof. André Canosa for his support, patience, and wise supervision during this thesis's preparation. I owe him my profound admiration and respect.

My utmost heartfelt gratitude goes to Prof. Alexandre Tomas for his unquestionable and continual support, valuable comments, and patience. Thanks for always having an open door, an open ear for all my questions and suggestions, and thanks for the confidence that he invested in me.

I owe sincere thankfulness to Dr. Gisèle EL Dib for her time, care, and confidence. Without her help and invaluable guidance, this work would not have been completed.

I would like to sincerely acknowledge: Prof. Elena Jiménez and Dr. María Antiñolo from UCLM University (Spain), Prof. Peter Wiesen and Prof. Iulia Patroescu-Klotz from Wuppertal University (Germany), Prof. Iustinian Gabriel Bejan, Prof. Romeo Iulian Olariu, Prof. Cecilia Arsene, and Dr. Cornelia Amarandei from Iasi University (Romania) and Dr. Manolis Romanias, Dr. Sebastian Dusanter and Dr. Marius Duncianu from IMT Lille Douai for their appreciated help, guidance and collaboration at different parts of this thesis.

I take this opportunity to express my gratitude to all my labmates, all the technicians and administrative staff at "IMT Lille Douai" and "Institut de Physique de Rennes", who directly and indirectly contributed to this work.

Throughout these years, I have met so many nice people who have been such a huge and invaluable support for me– so thanks to Mohamed, Safa, Hajer, Farouk, Nourchene, Wejdenne, Fedi and Fethi. For all of them, I would like to say a special "Thank you" for their support and their faithful friendship.

Major support also came from my family, and thus, I want to acknowledge my parents, Messaoud and Zohra, my brother Mohamed, my sisters: Wafa and her husband Marouane, Amel and her husband Mohamed and Safa, my adorable nephews: Mazen, Tamime and Youssef, for their encouragement, support and endless love.

Above all, my greatest thanks go to the omnipresent God for giving me the strength and determination to complete my study successfully.

Asma

Table of Contents

ACKNOWLEDGMENTS.....	I
TABLE OF CONTENTS.....	II
LIST OF FIGURES.....	VII
LIST OF TABLES	XII
LIST OF ACRONYMS	XIV
PREFACE	XVI
I CHAPTER I: BVOCs IN THE TROPOSPHERE	1
I.1 INTRODUCTION.....	2
I.2 CHEMISTRY OF THE TROPOSPHERE.....	2
I.2.1 Atmospheric layers	2
I.2.2 Solar spectrum	3
I.2.3 Tropospheric oxidants	5
I.2.3.1 OH radicals	5
I.2.3.1.1 Sources and levels of OH radicals	5
I.2.3.1.2 Sinks of OH radicals.....	7
I.2.3.2 Tropospheric ozone.....	9
I.2.3.2.1 Sources and levels of O ₃	9
I.2.3.2.2 Sinks of tropospheric O ₃	9
I.2.3.3 NO ₃ radicals.....	10
I.2.3.3.1 Sources and levels of NO ₃ radicals.....	10
I.2.3.3.2 Sinks of NO ₃ radicals	11
I.2.3.4 Cl atoms.....	11
I.2.3.4.1 Sources of Cl atoms.....	11
I.2.3.4.2 Sinks of Cl atoms	13
I.3 AN OVERVIEW OF BVOCs IN THE TROPOSPHERE.....	14
I.3.1 Definition of BVOCs.....	14
I.3.2 Sources and diversity of BVOCs.....	15
I.3.2.1 Terpenoid compounds	15
I.3.2.1.1 Isoprene (n=1).....	15
I.3.2.1.2 Monoterpenes (n=2)	16
I.3.2.1.3 Sesquiterpenes (n=3).....	17
I.3.2.2 Oxygenated compounds (OVOCs)	19
I.3.2.2.1 Aldehydes	19
I.3.2.2.2 Alcohols	20
I.3.2.2.3 Ketones	20
I.3.2.2.4 Organic acids	21
I.3.2.2.5 Ethers and esters.....	21
I.3.2.3 Non-oxygenated compounds (NOVOCs)	21
I.3.2.3.1 Alkanes and alkenes.....	21
I.3.3 Factors affecting BVOCs emissions	22
I.3.3.1 Internal factors	22
I.3.3.1.1 Stomatal regulation	22
I.3.3.1.2 Enzyme activity.....	22

I.3.3.2	External factors	23
I.3.3.2.1	Temperature and light	23
I.3.3.2.2	Relative humidity	23
I.3.3.2.3	Air composition	23
I.3.3.2.4	Mechanical stress, injury and herbivore, and pathogen attacks	24
I.3.4	Ecophysiological functions of BVOC emissions	24
I.4	SINK OF BVOCs IN THE TROPOSPHERE	25
I.4.1	Oxidation processes	26
I.4.1.1	Reaction with OH radicals	26
I.4.1.2	Reaction with NO ₃ radicals	26
I.4.1.3	Reaction with ozone	27
I.4.1.4	Reaction with Cl atoms	28
I.4.2	Photodissociation process	29
I.4.3	BVOCs lifetimes	30
I.5	IMPACTS OF BVOC EMISSIONS	32
I.5.1	Shaping the oxidative capacity of the atmosphere	32
I.5.2	Balancing the global carbon cycle	33
I.5.3	Producing biogenic SOAs	33
I.6	CONCLUSION	34
II	CHAPTER II: EXPERIMENTAL SET-UPS AND METHODS	35
II.1	INTRODUCTION	36
II.2	AN OVERVIEW OF EXPERIMENTAL SET-UPS IN ATMOSPHERIC CHEMISTRY	36
II.2.1	Static techniques	36
II.2.1.1	General description	36
II.2.1.2	Static techniques used in this work	37
II.2.1.2.1	D-ASC – IMT Lille Douai	38
II.2.1.2.2	THALAMOS-ASC – IMT Lille Douai	41
II.2.1.2.3	QUAREC-ASC – Wuppertal University	42
II.2.1.2.4	3m-ASC – Wuppertal University	44
II.2.1.2.5	16L-ASC – UCLM University	45
II.2.1.2.6	CR-ASC – UCLM University	47
II.2.1.3	Comparison of the used ASCs	49
II.2.2	Flow techniques	50
II.2.2.1	General description	50
II.2.2.2	Flow techniques used in this work	50
II.2.2.2.1	LFR – IMT Lille Douai	50
II.2.2.2.2	Cryocell – IPR	53
II.2.2.3	Comparison with other flow techniques	57
II.2.3	Advantages and challenges: static techniques versus flow techniques	59
II.3	AN OVERVIEW OF ANALYTICAL TECHNIQUES IN ATMOSPHERIC CHEMISTRY	60
II.3.1	Gas-phase analysis techniques	60
II.3.1.1	Spectroscopic techniques	60
II.3.1.1.1	Absorption spectroscopy	61
II.3.1.1.2	Laser-Induced Fluorescence	65
II.3.1.2	Mass spectrometry techniques	67
II.3.1.3	Chromatographic techniques	73
II.3.1.3.1	Gas Chromatography (GC)	73
II.3.1.3.2	Liquid chromatography	76
II.3.2	Particle-phase analysis techniques	77
II.3.2.1	SMPS	78

II.3.2.2	FMPS.....	79
II.4	METHODOLOGY.....	81
II.4.1	Determination of rate constants.....	81
II.4.1.1	Photolysis rate constant.....	81
II.4.1.2	Oxidation rate constant.....	82
II.4.1.2.1	Absolute method.....	82
II.4.1.2.2	Relative method.....	84
II.4.1.3	Lifetimes in the atmosphere.....	86
II.4.2	Determination of gas-phase products.....	87
II.4.2.1	Product yields.....	87
II.4.2.2	Addition of an OH scavenger.....	88
II.4.2.3	Determination of carbon balance.....	88
II.4.3	Determination of SOA yields.....	89
II.5	CONCLUSION.....	91
III	CHAPTER III: INFRARED AND UV ABSORPTION CROSS-SECTION MEASUREMENTS OF C₅-C₇ UNSATURATED ALDEHYDES.....	92
III.1	INTRODUCTION.....	93
III.2	INFRARED ABSORPTION-CROSS SECTIONS OF C ₅ -C ₇ UNSATURATED ALDEHYDES.....	94
III.2.1	Experimental conditions and protocols.....	94
III.2.2	Results and discussion.....	95
III.2.2.1	IR absorbance.....	95
III.2.2.2	IR absorption-cross sections.....	97
III.3	UV ABSORPTION-CROSS SECTIONS OF C ₅ -C ₇ UNSATURATED ALDEHYDES.....	99
III.3.1	Experimental conditions and protocols.....	99
III.3.2	Results.....	100
III.3.2.1	UV absorbance.....	100
III.3.2.2	UV absorption-cross sections.....	102
III.3.3	Discussion.....	105
III.3.3.1	Error analysis.....	105
III.3.3.2	Comparison with literature data.....	105
III.3.3.3	Structure effect.....	107
III.3.3.4	Calculation of photolysis rate constants.....	110
III.4	CONCLUSION.....	111
IV	CHAPTER IV: OXIDATION OF UNSATURATED ALDEHYDES AND ALCOHOLS: REACTION WITH OZONE.....	113
IV.1	INTRODUCTION.....	114
IV.2	OXIDATION OF UNSATURATED ALDEHYDES WITH OZONE.....	118
IV.2.1	Determination of rate constants.....	118
IV.2.1.1	Preliminary experiments.....	118
IV.2.1.1.1	Calibration and wall losses of unsaturated aldehydes.....	119
IV.2.1.1.2	Calibration and wall losses of ozone.....	122
IV.2.1.2	Experimental conditions and protocols.....	123
IV.2.1.3	Results.....	125
IV.2.1.3.1	Rate constant of T2P + O ₃	125
IV.2.1.3.2	Rate constant of T2H + O ₃	128
IV.2.1.4	Discussion.....	131
IV.2.1.4.1	Comparison with literature data.....	131
IV.2.1.4.2	Effect of the chain length and the C=C position.....	132
IV.2.1.4.3	Effect of the carbonyl group.....	133

IV.2.1.4.4	Atmospheric implications	134
IV.2.2	Determination of gas-phase products	136
IV.2.2.1	Experimental conditions and protocols	136
IV.2.2.2	Results	137
IV.2.2.2.1	Products of T2P + O ₃	137
IV.2.2.2.2	Products of T2H + O ₃	143
IV.2.2.3	Discussion	150
IV.2.3	Particle-phase study	155
IV.2.3.1	Experimental conditions and protocols	155
IV.2.3.2	Results	156
IV.2.3.2.1	SOAs in T2P + O ₃	156
IV.2.3.2.2	SOAs in T2H + O ₃	159
IV.2.3.3	Discussion	162
IV.3	OXIDATION OF UNSATURATED ALCOHOLS WITH OZONE	163
IV.3.1	Determination of rate constants	164
IV.3.1.1	Experimental conditions and protocols	164
IV.3.1.2	Results	165
IV.3.1.3	Discussion	169
IV.3.1.3.1	Rate constants	169
IV.3.1.3.2	Structure-Activity Relationship (SAR)	173
IV.3.1.3.3	Atmospheric implications	175
IV.4	CONCLUSION	177
V	CHAPTER V: OXIDATION OF UNSATURATED ALDEHYDES AND ALCOHOLS: REACTION WITH CL	
	179	
V.1	INTRODUCTION	180
V.2	OXIDATION OF UNSATURATED ALDEHYDES WITH CHLORINE ATOMS	182
V.2.1	Determination of rate constants	182
V.2.1.1	Experimental conditions and protocols	182
V.2.1.2	Results	185
V.2.1.2.1	Rate constant of T2P + Cl	185
V.2.1.2.2	Rate constant of T2H + Cl	187
V.2.1.2.3	Rate constant of T2Hep + Cl	188
V.2.1.3	Discussion	189
V.2.2	Determination of gas-phase products	192
V.2.2.1	Experimental conditions and protocols	193
V.2.2.2	Results and discussion	194
V.2.2.2.1	Products of T2P + Cl	194
V.2.2.2.2	Products of T2H + Cl	202
V.2.2.2.3	Products of T2Hep + Cl	208
V.2.3	Particle-phase study	213
V.2.3.1	Experimental conditions and protocols	213
V.2.3.2	Results	214
V.2.3.2.1	SOAs in T2P + Cl	214
V.2.3.2.2	SOAs in T2H + Cl	221
V.2.3.2.3	SOAs in T2Hep + Cl	228
V.2.3.3	Discussion	234
V.3	OXIDATION OF UNSATURATED ALCOHOLS WITH CHLORINE ATOMS	234
V.3.1	Determination of rate constants	235
V.3.1.1	Experimental conditions and protocols	235
V.3.1.2	Preliminary experiments: Generation of ion product (P ⁺)	238

Table of Contents

V.3.1.3	Preliminary tests.....	241
V.3.1.3.1	Interference tests between product ions.....	241
V.3.1.3.2	Stability of product ions	246
V.3.1.4	Results	247
V.3.1.4.1	Rate constant of C2P-OI + Cl	248
V.3.1.4.2	Rate constant of T2H-OI + Cl	248
V.3.1.4.3	Rate constant of T3H-OI + Cl	249
V.3.1.4.4	Rate constant of C3H-OI + Cl	250
V.3.1.4.5	Rate constant of 1O-3-OI + Cl	250
V.3.1.5	Discussion.....	251
V.3.1.5.1	Comparison with literature data	251
V.3.1.5.2	Effect of the chain length.....	253
V.3.1.5.3	Effect of the OH group	254
V.4	CONCLUSION	256
VI	CHAPTER VI: OXIDATION OF UNSATURATED ALDEHYDES: REACTION WITH OH.....	258
VI.1	INTRODUCTION	259
VI.2	OXIDATION OF UNSATURATED ALDEHYDES WITH OH	260
VI.2.1	Determination of rate constant	260
VI.2.1.1	Experimental conditions and protocols	260
VI.2.1.2	Results	262
VI.2.1.3	Discussion.....	265
VI.2.2	Determination of gas-phase products and particles formation	267
VI.2.2.1	Experimental conditions and protocols	267
VI.2.2.2	Preliminary results and discussion	268
VI.3	CONCLUSION.....	271
	SUMMARY AND FUTURE WORK.....	272
	REFERENCES	277
	LIST OF PUBLICATIONS.....	299

List of Figures

Figure I.1: Variation of mean temperature (K) with height up to an altitude of 100 km in the atmosphere (Fleming et al., 1990).....	3
Figure I.2: Solar flux outside the atmosphere and at sea level. The absorption bands of atmospheric gases are also shown (Dornelles et al., 2011).	4
Figure I.3: Formation and inter-conversion of OH and HO ₂ radicals in the atmosphere (Holloway and Wayne, 2015).....	8
Figure I.4: Tropospheric ozone formation via interactions between the RO _x and HO _x (blue), NO _x cycles (black), ozone degrading reactions via NMVOC (green), and terminating reactions (red) (Fitzky et al., 2019).....	10
Figure I.5: Overall mechanisms of O ₃ -alkene reactions in the gas and condensed phase (Finlayson-Pitts and Pitts Jr, 1999).	28
Figure I.6: Illustration of the influence of particle size in lung deposition and phagocytosis by the alveolar macrophages (Costa et al., 2016).	34
Figure II.1: (a) Schematic diagram and (b) photo of D-ASC.....	40
Figure II.2: (a) Schematic diagram and (b) photo of THALAMOS-ASC.	42
Figure II.3: Photo of QUAREC-ASC.	43
Figure II.4: Photo of 3m-ASC.....	44
Figure II.5: (a) Schematic diagram of 16L-ASC coupled to FTIR and (b) photo of 16L-ASC.	45
Figure II.6: Photo of the injection system of reactants used at UCLM.....	46
Figure II.7: Photo of CR-ASC.....	48
Figure II.8: Schematic diagram of 16L-ASC and CR-ASC coupled to FTIR and the injection system.....	48
Figure II.9: (a) Schematic diagram and (b) photo of LFR.....	51
Figure II.10: (a) Schematic diagram and (b) photo of Cryocell and PLP-LIF system (El Dib et al., 2013).	55
Figure II.11: Schematic diagram of the bubbler system (El Dib et al., 2013).....	56
Figure II.12: (a) Schematic diagram (adapted from Jiménez et al., 2005 and (b) photo of the set-up employed for UV absorption cross-sections measurements.	62
Figure II.13: Schematic diagram of ozone analyzer.....	63
Figure II.14: Photo of ozone analyzer (a) Environnement SA 42 model and (b) TEI 49C model.	63
Figure II.15: Schematic diagram of Michelson interferometer.	64
Figure II.16: Schematic diagram of the PM system used for the PLP-LIF technique.....	67
Figure II.17: Simplified diagram of Quadrupole Mass Spectrometer (QMS) (Santoiemma, 2018).....	68
Figure II.18: Simplified diagram of PTR-MS (adapted from Amann et al., 2010).	70
Figure II.19: Photo of PTR-ToF-MS (a) 8000 IONICON used at IMT Lille Douai and (b) 4000 IONICON used at UCLM.....	71
Figure II.20: Simplified diagram of SIFT-MS.....	72
Figure II.21: Photo of the Voice200® SIFT-MS used at IMT Lille Douai.	73
Figure II.22: A scheme of sampling set-up on Carbotrap 202 cartridges.	74
Figure II.23: (a) Schematic diagram and (b) photo of the TD-GC-FID/MS device.	76
Figure II.24: (a) Simplified diagram of SMPS (adapted from Lorenzo, 2007 and (b) photo of SMPS (TSI, DMA 3080 and CPC 3788) of IMT Lille Douai.	79
Figure II.25: (a) Simplified diagram of FMPS (adapted from TSI) and (b) photo of FMPS (TSI, 3091) of UCLM University.....	80
Figure II.26: Example of the temporal evolution of M _{SOA,exp} (red) and M _{SOA,corr} (black) formed through the reaction between Trans-2-Pentenal (T2P) and Cl atoms.....	90
Figure III.1: IR absorbance of (a) T2P, (b) T2H, and (c) T2Hep as function of the wavenumber ([Aldehyde] ₀ = 2.5 × 10 ¹⁴ molecule cm ⁻³).....	96

Figure III.2: Beer-Lambert plots (a) T2P, (b) T2H, and (c) T2Hep at four different wavenumbers.	98
Figure III.3: Leak rate constant in UV cell.	100
Figure III.4: UV absorbance of (a) T2P, (b) T2H and (c) T2Hep as function of the wavenumber ($[T2P]_0 = 5.8 \times 10^{16}$ molecule cm^{-3} , $[T2H]_0 = 6.2 \times 10^{16}$ molecule cm^{-3} , $[T2Hep]_0 = 2.8 \times 10^{16}$ molecule cm^{-3}).	102
Figure III.5: Beer-Lambert plots (a) T2P, (b) T2H, and (c) T2Hep at three different wavelengths (300 nm, 330 nm, and 360 nm).	104
Figure III.6: Comparison of the UV spectrum of T2P determined in this work with literature data (Kalalian et al., 2019).	106
Figure III.7: Comparison of the UV spectrum of T2H determined in this work with literature data (O'Connor et al., 2006, Jiménez et al., 2007, Kalalian et al., 2019).	107
Figure III.8: Comparison between the UV spectra of acrolein (JPL 2011) and propanal (JPL 2011).	108
Figure III.9: Comparison between the UV spectra of crotonaldehyde (Magneron et al., 2002) and butanal (Tadić et al., 2001).	108
Figure III.10: Comparison between the UV spectra of T2P (this work) and pentanal (Tadić et al., 2001).	109
Figure III.11: Comparison between the UV spectra of T2H (this work) and hexanal (Jiménez et al., 2007).	109
Figure III.12: Comparison between the UV spectra of T2Hep (this work) and heptanal (Tang and Zhu, 2004).	110
Figure IV.1: Chromatogram of T2H measured in LFR.	119
Figure IV.2: Peak Area measured by GC-MS/FID in LFR versus the calculated concentration of the aldehyde ((a) for T2P and (b) for T2H).	120
Figure IV.3: T2H spectrum measured in D-ASC in the range (650 – 4000 cm^{-1}).	121
Figure IV.4: Peak Area measured by FTIR spectrometer in D-ASC versus the calculated concentration of the aldehyde ((a) for T2P and (b) for T2H).	121
Figure IV.5: The plot of $\ln ([O_3]_0/[O_3])$ versus time for the wall losses of ozone ($[O_3]_0 = 3.9 \times 10^{12}$ molecule cm^{-3}) in D-ASC (the error is 2σ).	123
Figure IV.6: Kinetic measurement of T2P + O_3 reaction in LFR at 298 K: (a) plot of the ozone decay vs. reaction time and (b) plot of pseudo-order rate constant (k') vs. $[T2P]_0$	126
Figure IV.7: Kinetic measurement of T2P + O_3 reaction in D-ASC without an OH scavenger at 298 K: (a) plot of the ozone decay vs. reaction time and (b) plot of pseudo-order rate constant (k') vs. $[T2P]_0$	127
Figure IV.8: Kinetic measurement of T2P + O_3 reaction in D-ASC with an OH scavenger at 298 K: (a) plot of the ozone decay vs. reaction time and (b) plot of pseudo-order rate constant (k') vs. $[T2P]_0$	127
Figure IV.9: Kinetic measurement of T2H + O_3 reaction in LFR at 298 K: (a) plot of the ozone decay vs. reaction time and (b) plot of pseudo order rate constant (k') vs. $[T2H]_0$	129
Figure IV.10: Kinetic measurement of T2H + O_3 reaction in D-ASC without an OH scavenger at 298 K: (a) plot of the ozone decay vs. reaction time and (b) plot of pseudo order rate constant (k') vs. $[T2H]_0$	130
Figure IV.11: Kinetic measurement of T2H + O_3 reaction in D-ASC with an OH scavenger at 298 K: (a) plot of the ozone decay vs. reaction time and (b) plot of pseudo order rate constant (k') vs. $[T2H]_0$	130
Figure IV.12: Temporal evolution of T2P, products identified by FTIR (left axis), and the carbon balance (right axis) are examples of the T2P ozonolysis experiment in QUAREC-ASC.	138
Figure IV.13: Plots of all reaction products (FTIR analysis) as a function of reacted T2P obtained in QUAREC-ASC (without OH scavenger).	138
Figure IV.14: Proposed mechanistic scheme for the ozonolysis of T2P.	142
Figure IV.15: Temporal evolution of T2H, products identified by FTIR (left axis) and the carbon balance (right axis) for an example of T2H ozonolysis experiment in 3m-ASC.	143
Figure IV.16: Plots of all reaction products' concentrations as a function of reacted T2H obtained in the 3m-ASC (without OH scavenger).	144

Figure IV.17: IR spectra obtained in the 3m-ASC in the range 2600 – 3100 cm ⁻¹ . Qualitative reference spectra for propanal (red) and acetaldehyde (blue) together with the residual spectrum after removing T2H, O ₃ , butanal, and glyoxal.	145
Figure IV.18: IR spectra obtained in the 3m-ASC in the range 2500 – 3700 cm ⁻¹ . Qualitative reference spectrum for butanoic acid (green, absorbance * 10 ⁻²) together with the residual spectrum after removing T2H, O ₃ , butanal, and glyoxal.	146
Figure IV.19: Proposed mechanistic scheme for the ozonolysis of T2H.	149
Figure IV.20: Evolution of the SOA number size distribution with reaction time (t) during ozonolysis of T2P (initial reactant mixing ratios [T2P] ₀ = 5.4 × 10 ¹³ molecule cm ⁻³ and [O ₃] ₀ = 9.5 × 10 ¹² molecule cm ⁻³) in D-ASC. No aerosol was present at t = 0 (the corresponding size distribution is flat).	157
Figure IV.21: SOA formation as a function of time for T2P ozonolysis in D-ASC (initial reactant mixing ratios [T2P] ₀ = 5.4 × 10 ¹³ molecule cm ⁻³ and [O ₃] ₀ = 9.5 × 10 ¹² molecule cm ⁻³).	158
Figure IV.22: SOA formation yields vs. aerosol mass concentrations for T2P in D-ASC. The fit is carried out using Odum's one-product model (Odum et al., 1996).	159
Figure IV.23: Evolution of the SOA number size distribution with reaction time (t) during ozonolysis of T2H ([T2H] ₀ = 9.3 × 10 ¹³ molecule cm ⁻³ and [O ₃] ₀ = 9.6 × 10 ¹² molecule cm ⁻³) in D-ASC. No aerosol was present at t = 0 (the corresponding size distribution is flat).	160
Figure IV.24: SOA formation as function of time for T2H ozonolysis in D-ASC ([T2H] ₀ = 9.3 × 10 ¹³ molecule cm ⁻³ and [O ₃] ₀ = 9.6 × 10 ¹² molecule cm ⁻³).	161
Figure IV.25: SOA formation yields YSOA vs. aerosol mass concentrations for T2H in D-ASC. The fit is carried out using Odum's one-product model (Odum et al., 1996).	162
Figure IV.26: The kinetic plot of C2P-OI ozonolysis.	166
Figure IV.27: The kinetic plot of T2H-OI ozonolysis.	167
Figure IV.28: The kinetic plot of T3H-OI ozonolysis.	167
Figure IV.29: The kinetic plot of C3H-OI ozonolysis.	168
Figure IV.30: The kinetic plot of 10-3-OI ozonolysis.	168
Figure IV.31: The kinetic plot of T2O-OI ozonolysis.	169
Figure IV.32: Relationship between O ₃ rate constant ratio and the number of carbon atoms between OH and C=C (for example, C2P-OI has one carbon atom between OH and C=C). Stars (*) represent data for 1-alken-3-ols, circles (●) represent other alkenols.	171
Figure IV.33: Ozonolysis of alkenols: rate constants calculated by SAR vs. those determined experimentally (see Table IV.14). The dashed line is a linear regression on all the data except for 3-methyl-2-buten-1-ol (open circle).	175
Figure V.1: Decays of T2P vs. reference in the presence of Cl atoms.	186
Figure V.2: Decays of T2H vs. reference in the presence of Cl.	187
Figure V.3: Decays of T2Hep vs. reference in the presence of Cl atoms.	188
Figure V.4: IR spectra: Panel A: T2P in the dark. Panel B: after adding Cl ₂ to T2P in the dark. Panel C: under irradiation after 12 min. Panels D, E, and F: spectra of HCl and CO, propanal, and HC(O)OH. Panel G: residual IR spectrum after removing T2P, HCl, CO, HC(O)OH, and propanal.	195
Figure V.5: Concentration-time profile for T2P and the major products using [T2P] ₀ = 5.9 × 10 ¹⁴ molecule cm ⁻³ and [Cl ₂] ₀ = 9.1 × 10 ¹⁴ molecule cm ⁻³	196
Figure V.6: Examples of (a) chromatogram for the gas mixture after 60 min of the reaction of T2P + Cl, (b) determining mass spectra of T2P and the identified products.	197
Figure V.7: Product yields for (a) HCl and CO and (b) HC(O)OH and propanal.	198
Figure V.8: Proposed mechanism for the reaction of T2P with Cl atom: α-addition (a), β-addition (b), and H-abstraction (c).	202
Figure V.9: Concentration-time profile for T2H and the major products using [T2H] ₀ = 4.7 × 10 ¹⁴ molecule cm ⁻³ and [Cl ₂] ₀ = 3.9 × 10 ¹⁴ molecule cm ⁻³	203
Figure V.10: Product yields for (A) HCl and CO and (B) HC(O)OH and propanal.	204
Figure V.11: Proposed mechanism for the reaction of T2H with Cl atom: α-addition (a), β-addition (b), and H-abstraction (c).	208

Figure V.12: Proposed mechanism for the reaction of T2Hep with Cl atom: α -addition (a), β -addition (b), and H-abstraction (c).....	212
Figure V.13: Wall losses of T2P (a) and SOA (b). $[T2P]_0 = 6.5 \times 10^{14}$ molecule cm^{-3} and $[Cl_2]_0 = 11.4 \times 10^{14}$ molecule cm^{-3}	215
Figure V.14: Number-weighted particle size distributions for SOA measured by FMPS at several reaction times of the T2P oxidation initiated by Cl. $[T2P]_0 = 4.7 \times 10^{14}$ molecule cm^{-3} and $[Cl_2]_0 = 10.3 \times 10^{14}$ molecule cm^{-3}	216
Figure V.15: Mass concentration of SOA as function of reaction time between T2P and Cl atoms. $[T2P]_0 = 6.6 \times 10^{14}$ molecule cm^{-3} and $[Cl_2]_0 = 2.0 \times 10^{14}$ molecule cm^{-3}	217
Figure V.16: (a) The plot of $M_{SOA,max}$ versus $[T2P]_0$ and (b) the plot of $M_{SOA,max}$ versus the $[Cl_2]_0$	218
Figure V.17: SOA mass concentration M_{SOA} produced from the T2P+Cl reaction as function of the consumed T2P. $[T2P]_0 = 2.2 \times 10^{14}$ molecule cm^{-3} and $[Cl_2]_0 = 2.4 \times 10^{14}$ molecule cm^{-3} . The SOA yield Y_{SOA} is obtained from the linear least-squares analysis.	220
Figure V.18: The SOA plot yield Y_{SOA} as a function of $M_{SOA,max}$ for the reaction between T2P and Cl considering a particle mass density equal to 1.4 g cm^{-3}	220
Figure V.19: Wall losses of T2H (a) and SOA masses (b). $[T2H]_0 = 2.5 \times 10^{14}$ molecule cm^{-3} and $[Cl_2]_0 = 6.0 \times 10^{14}$ molecule cm^{-3}	222
Figure V.20: Number-weighted particle size distributions for SOA measured by FMPS at several reaction times of the T2H oxidation initiated by Cl. $[T2H]_0 = 2.7 \times 10^{14}$ molecule cm^{-3} and $[Cl_2]_0 = 6.5 \times 10^{14}$ molecule cm^{-3}	223
Figure V.21: SOA formation as function of reaction time between T2H and Cl atoms. $[T2H]_0 = 1.3 \times 10^{14}$ molecule cm^{-3} and $[Cl_2]_0 = 1.4 \times 10^{14}$ molecule cm^{-3}	224
Figure V.22: (a) The plot of $M_{SOA,max}$ versus $[T2H]_0$ and (b) the plot of $M_{SOA,max}$ versus the $[Cl_2]_0$	225
Figure V.23: SOA mass concentration M_{SOA} produced from the T2H + Cl reaction as a function of the consumed T2H. $[T2H]_0 = 3.9 \times 10^{14}$ molecule cm^{-3} and $[Cl_2]_0 = 4.5 \times 10^{14}$ molecule cm^{-3} . The SOA yield Y_{SOA} is obtained from the linear least-squares analysis.	227
Figure V.24: The SOA plot yield Y_{SOA} as a function of $M_{SOA,max}$ for the reaction between T2H and Cl considering a particle mass density equal to 1.4 g cm^{-3}	227
Figure V.25: Wall losses of T2Hep (a) and SOA (b) masses. $[T2Hep]_0 = 1.0 \times 10^{14}$ molecule cm^{-3} and $[Cl_2]_0 = 3.4 \times 10^{14}$ molecule cm^{-3}	229
Figure V.26: Number-weighted particle size distributions for SOA measured by FMPS at several reaction times of the T2Hep oxidation initiated by Cl atoms. $[T2Hep]_0 = 1.0 \times 10^{14}$ molecule cm^{-3} and $[Cl_2]_0 = 3.4 \times 10^{14}$ molecule cm^{-3}	229
Figure V.27: Mass concentration of SOA as function of reaction time between T2Hep and Cl atoms. $[T2Hep]_0 = 1.4 \times 10^{14}$ molecule cm^{-3} and $[Cl_2]_0 = 1.4 \times 10^{14}$ molecule cm^{-3}	230
Figure V.28: (a) The plot of $M_{SOA,max}$ versus $[T2Hep]_0$ and (b) the plot of $M_{SOA,max}$ versus the $[Cl_2]_0$	231
Figure V.29: SOA mass concentration M_{SOA} produced from the T2Hep + Cl reaction as a function of the consumed T2Hep. $[T2Hep]_0 = 4.3 \times 10^{14}$ molecule cm^{-3} and $[Cl_2]_0 = 1.2 \times 10^{14}$ molecule cm^{-3} . The SOA yield Y_{SOA} is obtained from the linear least-squares analysis.	233
Figure V.30: SOA plot yields Y_{SOA} as a function of $M_{SOA,max}$ for the reaction between T2Hep and Cl considering a particle mass density equal to 1.4 g cm^{-3}	233
Figure V.31: Temporal evolution of the C2P-OI and the reference compounds (THF (a), propan-1-ol (b), and octane (c)).	237
Figure V.32: Time evolution of THF product ions with only C2P-OI and Cl_2 injected in THALAMOS-ASC.	241
Figure V.33: Time evolution of propan-1-ol product ions with only C2P-OI and Cl_2 injected in THALAMOS-ASC.	242
Figure V.34: Time evolution of octane product ions with only C2P-OI and Cl_2 injected in THALAMOS-ASC.	243
Figure V.35: Time evolution of C2P-OI product ions with only THF and Cl_2 injected in THALAMOS-ASC.	244
Figure V.36: Time evolution of C2P-OI product ions with only propan-1-ol and Cl_2 injected in THALAMOS-ASC.	245

Figure V.37: Time evolution of C2P-Ol product ions with only octane and Cl ₂ injected in THALAMOS-ASC.	245
Figure V.38: Relative loss of C2P-Ol vs. that of tetrahydrofuran (THF) (a), propan-1-ol (b), and octane (c) in the Cl atom-initiated reaction.	248
Figure V.39: Relative loss of T2H-Ol vs. that of THF (a), propan-1-ol (b), and octane (c) in the Cl atom-initiated reaction.	249
Figure V.40: Relative loss of T3H-Ol vs. that of THF (a), propan-1-ol (b), and octane (c) in the Cl atom-initiated reaction.	249
Figure V.41: Relative loss of C3H-Ol vs. that of THF (a), propan-1-ol (b), and octane (c) in the Cl atom-initiated reaction.	250
Figure V.42: Relative loss of 10-3-Ol vs. that of THF (a), propan-1-ol (b), and octane (c) in the Cl atom-initiated reaction.	250
Figure V.43: Rate constants of the reaction of Cl atoms with 2-alken-1-ols (red) and 3-alken-1-ols (blue) vs. the number of carbon atoms (the open circles represent the values of the current study).	254
Figure V.44: The rate constant of the reaction of Cl atoms with a series of alkenes (red) and alken-1-ols (blue) vs. the number of carbon atoms (the open circles represent the values of the current study).	255
Figure VI.2: Example of OH's temporal LIF signal obtained at 298 K and 7.4 Torr, [OH] ₀ = 5.4 × 10 ¹¹ radical cm ⁻³ , [T2P] ₀ = 6.5 × 10 ¹⁴ molecule cm ⁻³ , carrier gas: Ar. The red curve represents an exponential fit of the decaying LIF signal.	263
Figure VI.3: Pseudo-first-rate constant, k', versus the initial concentration of the unsaturated aldehyde [T2P] ₀ at 298 K and different pressures ranging from 7.4 to 471 Torr. Uncertainty is twice the statistical standard deviation (±2σ).	264
Figure VI.4: Evolution of the SOA number size distribution with reaction time (t) during the reaction between T2P and OH ([T2P] ₀ = 3.7 × 10 ¹³ molecule cm ⁻³ , [CH ₃ ONO] ₀ = 12.3 × 10 ¹³ molecule cm ⁻³ , [NO] ₀ = 12.3 × 10 ¹³ molecule cm ⁻³) in QUAREC-ASC.	269
Figure VI.5: Evolution of the SOA number size distribution with reaction time (t) during the reaction between T2H and OH ([T2H] ₀ = 4.5 × 10 ¹³ molecule cm ⁻³ , [CH ₃ ONO] ₀ = 12.3 × 10 ¹³ molecule cm ⁻³ , [NO] ₀ = 12.3 × 10 ¹³ molecule cm ⁻³) in QUAREC-ASC.	269
Figure VI.6: SOA formation as function of reaction time for T2P in QUAREC-ASC ([T2P] ₀ = 3.7 × 10 ¹³ molecule cm ⁻³ , [CH ₃ ONO] ₀ = 12.3 × 10 ¹³ molecule cm ⁻³ , [NO] ₀ = 12.3 × 10 ¹³ molecule cm ⁻³).	270
Figure VI.7: SOA formation as function of reaction time for T2H in QUAREC-ASC ([T2H] ₀ = 4.5 × 10 ¹³ molecule cm ⁻³ , [CH ₃ ONO] ₀ = 12.3 × 10 ¹³ molecule cm ⁻³ , [NO] ₀ = 12.3 × 10 ¹³ molecule cm ⁻³).	270

List of Tables

Table I.1: The skeletal structure of some selected compounds that belong to the terpenoids.....	18
Table I.2: Calculated tropospheric lifetimes for a selected BVOCs of the reaction with OH, NO ₃ , and O ₃ (Atkinson and Arey, 2003).....	31
Table II.1: Summary of all ASCs used in this work.....	49
Table II.2: Flow techniques used in atmospheric chemistry studies (adapted from Duncianu et al., 2012).	58
Table II.3: Summary of the FTIR spectrometers used in this work.....	65
Table II.4: Characteristics of the used PTR-ToF-MS in this work.....	71
Table II.5: GC oven temperature program.....	75
Table II.6: Composition of the mobile phase during HPLC-UV analysis.....	77
Table III.1: Summary of the saturated vapor pressure of T2P, T2H, and T2Hep.	94
Table III.2: Summary of IR absorption cross-sections of T2P, T2H, and T2Hep determined at four different wavenumbers.....	98
Table III.3: Summary of UV absorption cross-sections of T2P, T2H, and T2Hep determined at three different wavelengths. Uncertainties are one standard deviation.	104
Table III.4: A summary of the experimental conditions and analytical techniques for literature data and the determined UV spectra for T2P and T2H.	105
Table III.5: Variation of the photolysis constant (J) of T2P, T2H, and T2Hep for $\theta = 20^\circ - 70^\circ$	111
Table IV.1: Summary of rate constants, methods, and analytical techniques used in previous works of the reactions between C ₅ -C ₆ unsaturated aldehydes and ozone at 298 K.	115
Table IV.2: Summary of rate constants, methods, and analytical techniques of previous works of C ₅ -C ₈ unsaturated alcohols and ozone reactions.	116
Table IV.3: Summary of experimental conditions used for the kinetic studies of T2P and T2H ozonolysis.	125
Table IV.4: Summary of determined rate constants for T2P ozonolysis.....	127
Table IV.5: Summary of determined rate constants for T2H ozonolysis.	130
Table IV.6: Summary of the rate constants for the reactions of a series of C ₃ -C ₉ alkenals with ozone at room temperature and atmospheric pressure.	132
Table IV.7: Summary of the rate constants for the reactions of a series of C ₄ -C ₆ alkenes with ozone at room temperature and atmospheric pressure.....	133
Table IV.8: Calculated atmospheric lifetimes of C ₅ -C ₇ unsaturated aldehydes towards atmospheric oxidants (Cl, O ₃ , NO ₃ , and OH) and photolysis.....	134
Table IV.9: Summary of experimental conditions used for the gas-phase product studies of T2P and T2H ozonolysis.	137
Table IV.10: Summary of literature data and the present work for the product formation yields of the ozonolysis of a series of C ₃ -C ₉ unsaturated aldehydes.	150
Table IV.11: Summary of experimental conditions and analytical techniques used for the formed SOA through the ozonolysis of T2P or T2H.....	155
Table IV.12: Summary of experimental conditions used for the kinetic studies of C ₅ -C ₈ unsaturated alcohols ozonolysis.	165
Table IV.13: Summary of the rate constants for the reactions of a series of alkenols with ozone at room temperature and atmospheric pressure.	172
Table IV.14: Calculated atmospheric lifetimes of C ₅ -C ₈ unsaturated alcohols towards atmospheric oxidants (OH, O ₃ , Cl, and NO ₃).	176
Table V.1: Summary of rate constants, methods, and analytical techniques used in previous works of C ₅ -C ₇ unsaturated aldehydes and chlorine reactions.....	180
Table V.2: Summary of rate constants, methods, and analytical techniques used in previous works of the reactions between C ₅ -C ₈ unsaturated alcohols and Cl atoms.	181

Table V.3: Experimental conditions, initial reactant concentrations in the kinetic measurements, and measured loss rate constants.	183
Table V.4: Summary of rate constants of the used reference compounds (isoprene, cyclohexane, ethanol, and propene).	184
Table V.5: Rate constants for the reaction of T2P with Cl atoms.	186
Table V.6: Rate constant for the reaction of T2H with Cl atoms.	188
Table V.7: Rate constants for the reaction of T2Hep with Cl atoms.	189
Table V.8: Summary of the rate constants for the reactions of a series of C ₃ -C ₇ alkenals with Cl atoms at room temperature and atmospheric pressure.	190
Table V.9: Summary of the rate constants for two C ₃ -C ₄ alkenes' reactions with Cl atoms at room temperature and atmospheric pressure.	192
Table V.10: Experimental conditions and techniques used during the product study.	193
Table V.11: Summary of experimental conditions and analytical techniques used for the formed SOA through the T2P + Cl, T2H + Cl, and T2Hep + Cl reactions.	214
Table V.12: Experimental conditions and results obtained for the SOA study.	219
Table V.13: Experimental conditions and results obtained for the SOA study.	226
Table V.14: Experimental conditions and results obtained for the SOA study.	232
Table V.15: Product ion distributions of the H ₃ O ⁺ , NO ⁺ , and O ₂ ⁺ reactions with the studied unsaturated alcohols and reference compounds (BR – branching ratios of product ions). (Data come from the SIFT-MS library).	238
Table V.16: Summary of rate constants of the used reference compounds (THF, propan-1-ol, and octane).	247
Table V.17: Summary of all the rate constants for alcohols' reactions with Cl atoms (all rate constants are expressed in 10 ⁻¹⁰ cm ³ molecule ⁻¹ s ⁻¹).	251
Table V.18: Rate constants for Cl atoms' reactions with unsaturated alcohols at 298 K and atmospheric pressure.	252
Table V.19: Rate constants for Cl atoms' reactions with alkenes at 298 K and atmospheric pressure.	254
Table VI.1: Summary of the rate constants, experimental conditions, and analytical techniques used in previous works for studying the kinetic of T2P + OH reaction at 298 K.	259
Table VI.2: Summary of the laser characteristics used in the kinetic measurement of T2P and OH reaction.	260
Table VI.3: Antoine coefficients were used to calculate the saturated vapor pressure of H ₂ O ₂ at 298 K (Yaws, 2015).	261
Table VI.4: Summary of the initial concentrations used for kinetic measurements of T2P and OH radical reaction at room temperature and (7 – 471 Torr) of pressure.	262
Table VI.5: Summary of rate constants for the reaction of a series of C ₃ -C ₇ unsaturated aldehydes with OH radicals at 298 K.	265
Table VI.6: Summary of the experimental conditions used in product and SOA formations studies.	267

List of Acronyms

T2P	Trans-2-Pentenal
T2H	Trans-2-Hexenal
T2Hep	Trans-2-Heptenal
C2P-Ol	Cis-2-Penten-1-Ol
T2H-Ol	Trans-2-Hexen-1-Ol
T3H-Ol	Trans-3-Hexen-1-Ol
C3H-Ol	Cis-3-Hexen-1-Ol
10-3-Ol	1-Octen-3-Ol
T2O-Ol	Trans-2-Octen-1-Ol
BVOC	Biogenic Volatile Organic Compound
OVOC	Oxygenated Volatile Organic Compound
NMVOC	Non-Methane Volatile Organic Compound
SOA	Secondary Organic Aerosol
BSOA	Biogenic Secondary Organic Aerosol
O ₃	Ozone
Cl	Chlorine atom
OH	Hydroxyl radical
NO ₃	Nitrate radical
RO ₂	Peroxyl radical
THF	Tetrahydrofuran
ASC	Atmospheric Simulation Chamber

LFR	Laminar Flow Reactor
THALAMOS	ThermALLY regulated AtMOSpheric
QUAREC	QUArtez REaCtor
FID	Flame Ionization Detector
MS	Mass Spectrometry
GC	Gaz Chromatography
HPLC	High-Pressure Liquid Chromatography
DNPH	2,4-dinitrophénylhydrazine
IR	Infrared
UV	Ultraviolet
FTIR	Fourier Transform InfraRed spectroscopy
MCT	Mercure Cadmium Telluride
SMPS	Scanning mobility particle sizer
CPC	Condensation Particle Counter
TgC	Teragrams of Carbon
hPa	hectoPascal ($1 \text{ hPa} = 10^2 \text{ Pa}$)
ppbv	part per billion by volume
ppmv	part per million by volume
SAR	Structure-Activity Relationship
DMA	Differential Mobility Analyzer

Preface

This thesis presents the work I have done during my PhD as part of a collaboration between “IMT Lille Douai” and “Institut de Physique de Rennes”. The results presented herein include findings from laboratory experiments done in cooperation of four laboratories: “Centre d’Enseignement, de Recherche et d’Innovation (CERI)-Energie et Environnement” at “IMT Lille Douai”, department “Physique Moléculaire” at “Institut de Physique de Rennes”, the laboratory of Wuppertal University (Germany) and the laboratory of UCLM University (Spain).

This work is part of the national program LEFE “Les Enveloppes Fluides et l’Environnement” coordinated by INSU-CNRS, aiming to better understand the atmosphere and ocean’s functioning and their interactions with the other components of the climate system. Our work represents a part of the axis “CHAT-CHimie Atmosphérique” which aims to better understand and predict the emissions of pollutants, transformation, dispersion in the atmosphere, deposition and estimate their impacts on the environment and the air quality.

This thesis work concentrates on a better understanding of the degradation of biogenic OVOCs in the atmosphere. Therefore, we particularly interested in a series of unsaturated aldehydes and alcohols ($\geq C_5$): Trans-2-Pentenal (T2P), Trans-2-Hexenal (T2H), Trans-2-Heptenal (T2Hep), Cis-2-Penten-1-ol (C2P-Ol), Trans-2-Hexen-1-ol (T2H-Ol), Trans-3-Hexen-1-Ol (T3H-Ol), Cis-3-Hexen-1-Ol (C3H-Ol), 1-Octen-3-ol (1O-3-Ol), and Trans-2-Octen-2-Ol (T2O-Ol). Those compounds can be either emitted directly from vegetation, especially in the presence of stress conditions (Konig, 1995) or formed in-situ in the atmosphere from hydrocarbons due to chemical and photochemical reactions. The selection of the studied BVOCs and their oxidation reactions was based on their interest in the chemistry of the atmosphere.

This thesis aims to study the reactivity of the selected BVOCs and the main atmospheric oxidants (O_3 , Cl atoms and OH radicals). The studied reactions were generated into laboratory reactors simulating the atmospheric physical and chemical conditions.

Rate constants of chemical reactions were measured at atmospheric temperature, reaction mechanisms were determined, and their contributions to the total budget of formed SOA were quantified. This manuscript consists of six chapters:

- Chapter I is a general overview of the composition of the atmosphere, atmospheric layers, solar radiation, BVOC sources, and the diverse physical and photochemical processes influencing their emissions and their atmospheric concentrations were presented. Besides their wide chemical diversity, BVOCs show a wide range of reactivity towards hydroxyl radical (OH), tropospheric ozone, and Cl atom during daytime and nitrate radical (NO₃) during nighttime. The impact of these oxidation reactions on health, environment, and air quality was also exhibited.
- Chapter II displays the main systems and methods used during my Ph.D. to investigate the oxidation reaction of the selected BVOCs with O₃, Cl atoms, and OH radicals.
- Chapter III presents the determined IR and UV absorptions cross-sections for C₅-C₇ unsaturated aldehydes and the contribution of the photolysis pathway to their atmospheric degradation.
- Chapter IV shows the reactivity of C₅-C₆ unsaturated aldehydes and C₅-C₈ unsaturated alcohols with ozone. The first section was dedicated to the kinetic measurements, product investigations, and SOA formations for the ozonolysis of unsaturated aldehydes. However, the second part deals with kinetic measurements of the ozonolysis of C₅-C₈ unsaturated alcohols.
- Chapter V presents the reactivity of C₅-C₇ unsaturated aldehydes and C₅-C₈ unsaturated alcohols with Cl atoms. In the first part, I investigated the kinetic measurements, product investigations, and SOA formations for the reaction of C₅-C₇ unsaturated aldehydes with chlorine. Then, I displayed the measured rate constants of the reaction between C₅-C₈ unsaturated alcohols with Cl.
- In chapter VI, I displayed the reactivity of C₅-C₆ unsaturated aldehydes with OH radicals.

This manuscript ends with a summary of conclusions made of this Ph.D. work, including suggestions for future research.

I Chapter I: BVOCs in the troposphere

I.1 Introduction

The Biogenic Volatile Organic Compounds (BVOCs) represent trace gases emitted from two main sources: biosphere and biomass burning. The detection of BVOCs in the atmosphere goes back to Went, 1960, when he investigated the blue haze's appearance in the mountain areas due to the emission of terpenes from vegetation. Over the last decade, several researchers were interested in a better understanding of BVOCs emission processes, quantifying their fluxes, and assessing their impacts on the environment and climate change. The estimated flux of carbon released annually by terrestrial vegetation is about 1000 TgC, representing around 42% of the total flux of carbon (2400 TgC) (Guenther, 2002).

Once these hydrocarbons are present in the atmosphere, they are surrounded by various tropospheric photo-oxidants, which are highly reactive (Atkinson, 2000). Therefore, these biogenic species largely contribute to photochemical smog formation, tropospheric ozone, hydroxyl radicals and secondary pollutants. Furthermore, the oxidation of biogenic compounds yields lower volatility species, which could be a source of biogenic secondary organic aerosols (BSOAs) (Johnson and Marston, 2008, Peñuelas and Staudt, 2010), one of the most uncertain factors in the global radiation budget (Solomon et al., 2007).

I.2 Chemistry of the troposphere

I.2.1 Atmospheric layers

The atmosphere comprises five layers: the troposphere, the stratosphere, the mesosphere, the thermosphere, and the exosphere. The variation of temperature and pressure as a function of the Earth's altitude defines its different layers. Only the troposphere and the stratosphere have special attention for researchers' community in atmospheric chemistry. This work will concentrate on the troposphere, representing the first layer from the sea level up to 10 – 15 km. The adjacent layer is the stratosphere, and the limit between the troposphere and the stratosphere is called the tropopause. The troposphere comprises two regions: (i) a stagnant region called the boundary layer, which extends from the Earth's surface to at least 1 km, and (ii) a turbulent region called the free troposphere, which extends from the boundary layer up to the tropopause.

Figure I.1 displays the different divisions of the atmosphere, except the thermosphere and the exosphere.

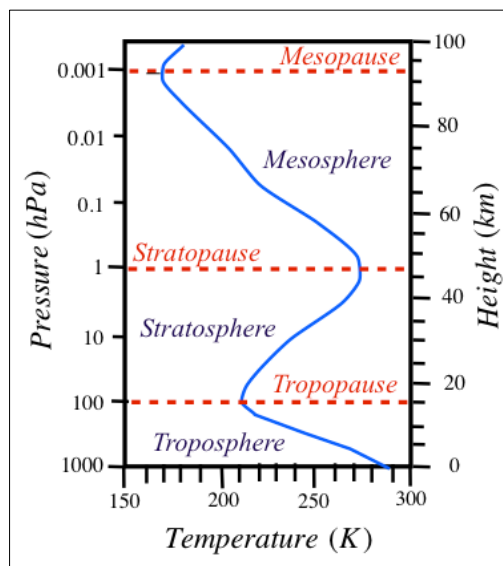


Figure I.1: Variation of mean temperature (K) with height up to an altitude of 100 km in the atmosphere (Fleming et al., 1990).

The troposphere represents a vast pool that contains around 80% of the total atmospheric mass. This layer represents a complex reactor that contains physical and chemical processes occurring under different variable parameters such as temperature, pressure, humidity, and composition.

This layer contains N_2 (78%), O_2 (21%), Ar (< 1%), and a fraction of less than 1% comprises all the remaining trace gases. These trace gases include CO_2 (~ 412 ppmv), CH_4 (~ 1.5 ppmv), NO_2 (~ 500 ppbv), O_3 (~ 20 – 80 ppbv), halogenated compound (3.8 ppbv) and non-methane volatile organic compounds NMVOCs (5 – 20 ppbv) (Wallace and Hobbs, 2006). These trace gases play an essential role in tropospheric chemistry. Indeed, they can ultimately produce tropospheric ozone and secondary organic aerosols (SOAs), which significantly impact air quality and climate change, as discussed below in section I.5.

I.2.2 Solar spectrum

The sunlight represents one of the main engines of atmospheric chemistry.

Figure I.2 displays the sun's spectral irradiance versus wavelength outside the atmosphere (blue) and sea level (red). Technically, there is no absolute limiting line between the Earth's atmosphere and space. However, regions at more than 100 kilometers above the Earth are considered "extraterrestrial" or "top of the atmosphere."

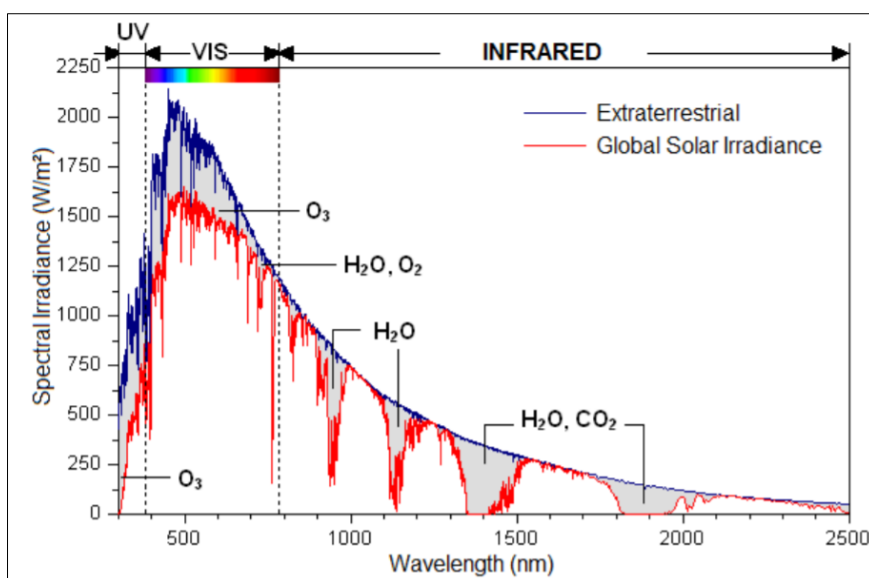


Figure I.2: Solar flux outside the atmosphere and at sea level. The absorption bands of atmospheric gases are also shown (Dornelles et al., 2011).

The solar spectrum contains near UV, visible, and IR regions. Only a fraction of the solar irradiation reaches Earth. The region of wavelengths less than 170 nm is mainly absorbed at about 100 km altitude (mesosphere). The 170 – 290 nm region is absorbed in about 50 to 20 km (stratosphere layer by the stratospheric ozone).

The region from 290 up to 800 nm corresponds to the wavelength reaching the ground level and impacting the troposphere's photochemical processes. The IR region does not have sufficient energy leading to photochemical reactions. However, it corresponds to the maximum absorption region of two greenhouse gases: carbon dioxide (CO₂) and water vapor (H₂O).

I.2.3 Tropospheric oxidants

Oxidation reaction represents a significant sink for organic trace gases in the troposphere. The most recognized tropospheric oxidants are OH radicals, O₃, NO₃ radicals, and Cl atoms.

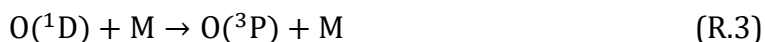
I.2.3.1 OH radicals

I.2.3.1.1 Sources and levels of OH radicals

The hydroxyl radical (OH) plays a crucial role in tropospheric chemistry as it initiates most of the oxidation reactions occurring in the troposphere. The photodissociation of ozone at wavelengths under 310 nm in the presence of water vapor is a significant source of OH radicals in the troposphere (Atkinson and Arey, 2003).



However, most of the produced O(¹D) (90%) will be readily quenched back to ground state O(³P) by air molecules (M), which are N₂ or O₂ as presented in (R.3).



The ground state O(³P) atoms will react with O₂ to recombine O₃ (R.4).



In the absence of NO_x (NO and NO₂), all the photolyzed ozone is reformed according to the mechanism (R.1 – 4). While in the presence of NO_x, ozone reacts with NO to form NO₂ (R.5).



The formed NO₂ will also be photolyzed at a wavelength lower than 400 nm (R.6) and will form O(³P) and then ozone as described in (R.4).



In polluted areas, the photolysis of formaldehyde (HCHO) at a wavelength lower than 356 nm (R.7) generates two radicals of HO₂ as displayed in (R.8) and (R.9) and then two radicals of OH (R.10).



The photolysis nitrous acid (HONO) at a wavelength lower than 400 nm (R.11) and hydrogen peroxide (H₂O₂) at a wavelength lower than 370 nm (R.12) are also considered as sources of OH radicals during daytime (Finlayson-Pitts and Pitts Jr, 1999, Alicke et al., 2002, Delmas et al., 2005).



Other non-photolytic sources can generate OH radicals. For example, the ozonolysis of unsaturated compounds (Jenkin and Clemitshaw, 2000) such as isoprene (Fuchs et al., 2013) and alkenes (Paulson et al., 1999, Atkinson, 2000) represent a source of OH radicals during daytimes. On the other hand, the NO₃-initiated reaction with peroxyacetyl nitrates (RC(O)O₂NO₂) and alkenes (Ren et al., 2006) represent a significant sources of OH radicals during nighttime.

OH radical is highly reactive with various pollutants and trace gases such as VOCs or tropospheric ozone (Atkinson and Arey, 1998, Hofzumahaus et al., 2009). Therefore, OH concentration is shallow compared to other tropospheric oxidants such as O₃ and NO₃.

The OH radical concentrations reach 1×10^6 molecule cm^{-3} (24 h average) and decrease during the night up to 1×10^5 molecule cm^{-3} (Atkinson and Arey, 1998, Atkinson, 2000, Emmerson and Carslaw, 2009).

I.2.3.1.2 Sinks of OH radicals

As we mentioned above, OH is highly reactive with several species, and then it is complicated to detect each sink process separately. The major part of OH is removed with carbon monoxide (CO), producing carbon dioxide (CO_2). The remaining OH reacts with methane (CH_4) and may react with oxidative species as HO_2 (R.13).



In the presence of NO_x , OH reacts with both NO and NO_2 (Finlayson-Pitts and Pitts Jr, 1999) and produces nitrous and nitric acid as displayed in (R.14) and (R.15), respectively.



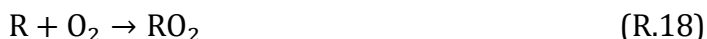
In some areas where NO concentration is lower enough (< 10 pptv), OH also reacts with O_3 (R.16) (Atkinson, 2000).



The OH radical could initiate the degradation of saturated hydrocarbons through the H atom's abstraction from the C-H bond to generate an alkyl radical (R.17).



The alkyl radicals will react with oxygen to generate the corresponding alkyl peroxy radicals (R.18).



In the presence of NO_x , RO_2 radicals will react with NO to form alkoxy radicals RO and NO_2 (R.19).



These NO_2 will be photolyzed (R.6) to regenerate ozone (R.4). The formed RO in (R.19) reacts with oxygen and produces $\text{R}'\text{O}$ and HO_2 radicals (R.20). HO_2 radical reacts with NO to form NO_2 and OH as described in (R.10).



In some areas where NO concentration is lower enough (< 10 pptv), HO_2 also reacts with RO_2 (R.21) and with O_3 (R.22) (Atkinson 2000).



Figure I.3 summarizes all the previous processes for the formation and inter-conversion of OH and HO_2 .

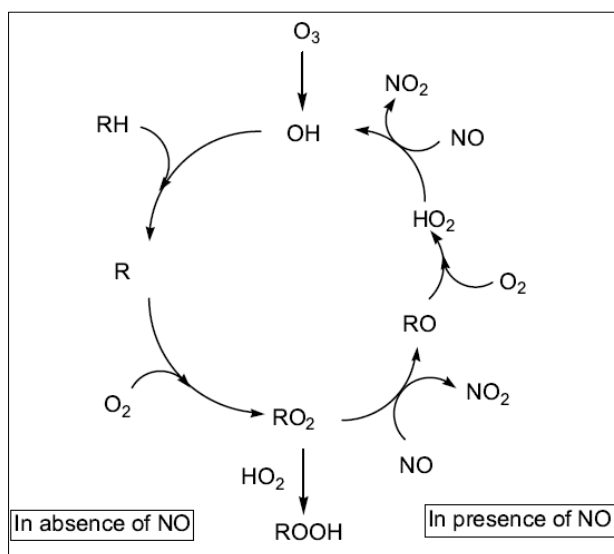


Figure I.3: Formation and inter-conversion of OH and HO_2 radicals in the atmosphere (Holloway and Wayne, 2015).

I.2.3.2 Tropospheric ozone

I.2.3.2.1 Sources and levels of O₃

Tropospheric ozone constitutes roughly 10% of the total atmospheric ozone. Stratosphere to troposphere transport is an important natural source of tropospheric ozone (Guicherit and Roemer, 2000, Akritidis et al., 2016, Akritidis et al., 2018).

However, the dominant source of tropospheric ozone is based on the reaction of atomic oxygen O(³P) and molecule oxygen as described before in (R.4). The atomic oxygen O(³P) is mainly formed through the photolysis of NO₂ (R.6). The formed ozone concentration is dependent not only on NO₂ but also on NO since this later could react with O₃ as mentioned in (R.5) (Atkinson and Arey, 1998, (Jenkin and Clemitshaw, 2000).

The concentrations of HO₂ and RO₂ radicals are dependent upon the solar intensity, which means that ozone will reach its maximum concentrations in the most enlightened hours of the day. The average atmospheric mixing ratio of ozone at the ground level is around 10 to 40 ppbv for clean areas, whereas it reaches 100 ppbv in polluted environments.

I.2.3.2.2 Sinks of tropospheric O₃

During the daytime, ozone is removed mainly by photolysis at wavelengths lower than 310 nm, as described in (R.1). On the other hand, O₃ reacts with unsaturated VOCs during the nighttime and produces OH radicals (Atkinson et al., 2004). In some areas where NO concentration is lower enough (< 10 pptv), O₃ also reacts with OH (R.16) and HO₂ (R.22) (Atkinson, 2000). Tropospheric ozone formation and relevance with NO_x, RO_x, HO_x cycles and NMVOCs are displayed in Figure I.4.

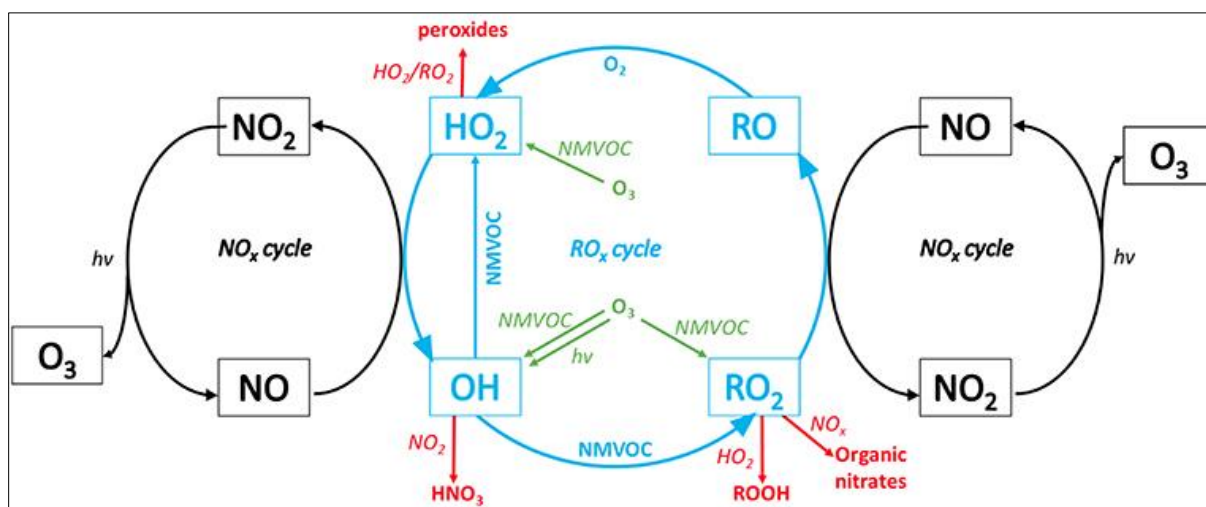


Figure I.4: Tropospheric ozone formation via interactions between the ROx and HOx (blue), NO_x cycles (black), ozone degrading reactions via NMVOC (green), and terminating reactions (red) (Fitzky et al., 2019).

I.2.3.3 NO₃ radicals

I.2.3.3.1 Sources and levels of NO₃ radicals

Nitrate radicals (NO₃) are formed basically at nighttime via the oxidation of NO emitted from soils and all combustion processes or formed in situ through lightening (Jenkin and Clemitshaw, 2000). The oxidation of NO to NO₂ (R.23), followed by the oxidation of NO₂ with O₃ (R.24), which is the major source of NO₃ formation (Atkinson, 2000, Brown and Stutz, 2012).



The reaction between HNO₃ and OH also leads to NO₃ and HO₂ (R.25).



At nighttime and at the ground level near continental areas, NO₃ radical concentrations reach $1 \times 10^{10} \text{ molecule cm}^{-3}$ (430 pptv).

For all the calculated lifetimes of VOCs in this work, we used the average of NO₃ concentrations for 12 h of nighttime, which is equal to 5×10^8 molecule cm⁻³ (20 pptv) (Atkinson and Arey, 1998).

I.2.3.3.2 Sinks of NO₃ radicals

During the daytime, NO₃ is removed through the photolysis process at wavelengths lower than 700 nm (R.26) and 520 nm (R.27). R.26 represents around 90% of the global photolysis process of NO₃.



At nighttime, NO₃ consumption occurs mainly via VOC oxidations, which produce both OH and HO₂ radicals (Jenkin and Clemitshaw, 2000, Monks et al., 2009, Ng et al., 2017). Also, the oxidation reaction of NO₃ with NO (R.28) is an additional removal process of this oxidant during nighttime (Brown and Stutz, 2012).



Finally, NO₃ radicals can react with NO₂ at dark conditions to produce dinitrogen pentoxide (N₂O₅). The latter rapidly dissociates, establishing equilibrium with NO₃ as described in (R.29). Therefore, N₂O₅ is known as a reservoir of NO_x.



I.2.3.4 Cl atoms

I.2.3.4.1 Sources of Cl atoms

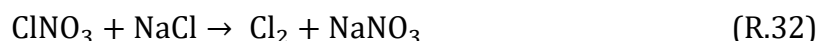
Chlorine atoms (Cl) play a crucial role not only in coastal areas and marine boundary layer but also in continental environments (Atkinson and Arey, 2003, Thornton et al., 2010, Young et al., 2014). Cl atoms are released into the troposphere via multiple mechanisms; the predominant one is sea-salt chloride aerosol (Graedel and Keene, 1996).

Sea-salt chloride aerosol is released by air bubbles bursting at the ocean's surface due to wind stress (Jaeglé et al., 2011). Large droplets readily return to the ocean whereas, smaller droplets may have a long enough lifetime (mins to hours), which allows them to be transported through the boundary layer.

The releasing of this chloride from this sea-salt aerosol can be achieved through several reactions where gas species could be ab/adsorbed onto the sea-salt aerosol and undertake a set of chemical reactions releasing gas-phase inorganic chlorine species. For example, the uptake of N_2O_5 , which could be formed as described in (R.29), onto aerosol to subsequently release nitryl chloride (ClNO_2) (R.30), has been known for some time (Finlayson-Pitts et al., 1989). ClNO_2 photolyzed to Cl atoms and NO_2 (R.31) (Keene et al., 2007, Thornton et al., 2010).



Other mechanisms exist for releasing Cl atoms into the troposphere as the uptake of ClNO_3 on sea-salt aerosol (R.32) following by the photolysis of Cl_2 (R.33) (Keene et al., 2007, Simon et al., 2009, Mielke et al., 2011).



Cl atoms' concentration varies from $1 \times 10^2 \text{ atom cm}^{-3}$ based on VOC ratios analysis (Wingenter et al., 1999) to $1 \times 10^5 \text{ atom cm}^{-3}$ based on Cl family detection (Keene et al., 2007). Atomic chlorine, even if present in the troposphere in small concentrations, can enhance ozone formation in urban atmospheres (Knipping and Dabdub, 2003, Chang and Allen, 2006). This phenomenon starts through the reaction between a hydrocarbon (RH) and a Cl atom (R.34), which produces HCl and alkyl radical (R) (R.34).



This alkyl radical (R) will follow all the reactions from (R.18) to (R.20) to produce then HO₂ and carbonyl (R'O). HO₂ reacts with NO to produce OH and NO₂ (R.10). NO₂ will photolyze and generates atomic oxygen (R.6), which will oxidize with molecular oxygen to form O₃ (R.4).

I.2.3.4.2 Sinks of Cl atoms

Methane is the most prominent compound to remove atomic Cl (R.35) (Atkinson et al., 2001).



Tropospheric ozone can also serve as a Cl sink, as described in the following reaction (R.36).



Chlorine atom is hugely reactive towards VOCs with rate constants, taking into account a few exceptions, which are at least one order of magnitude larger than those with hydroxyl radicals (OH).

Besides, other compounds such as alkanes are rapidly reactive with Cl atoms, whereas they are relatively unreactive to OH radicals (R.37) (Keene et al., 2007).



Alkenes such as ethene and propene could remove atomic Cl by forming chlorinated compounds as described in (R.38) (Keene et al., 2007).



Also, biogenic VOCs such as isoprene, α -pinene, β -pinene, and camphene react with Cl atoms and produce chlorinated BVOCs (Finlayson-Pitts and Pitts Jr, 1999).

I.3 An overview of BVOCs in the troposphere

I.3.1 Definition of BVOCs

Volatile organic compounds, VOCs, are defined by the European directive of the European Community 1999/13/EC of 11 March 1999, based on its chemical composition "any compound containing at least the carbon element and one or more of the following elements: hydrogen, oxygen, sulfur, phosphorus, silicon, nitrogen, or a halogen (chlorine, fluorine or bromine), except carbon oxides and inorganic carbonates and bicarbonates." The concept of volatility is also mentioned in the same article where "any organic compound having at 293.15 K a vapor pressure of 0.01 kPa or more, or having a corresponding volatility under particular conditions of use" is considered as a volatile organic compound.

Although this definition includes many species, the definition given by the United States Environmental Protection Agency (EPA) in 2004 presents some differences. The EPA 2004 considered a second definition for VOCs, which gives more importance to the reactivity of these molecules considering that a VOC is "any compound of carbon, excluding carbon monoxide, carbon dioxide, carbonic acid, metallic carbides or carbonates and ammonium carbonate, which participates in atmospheric photochemical reactions." This definition excluded methane (CH_4), as its low reactivity makes its lifetime very long compared to other VOCs, and induced the appearance of two new common expressions, "Non-Methane Volatile Organic Compounds (NMVOC)" or "Non-Methane Hydrocarbons (NMHCs)". VOCs enter the atmosphere directly through natural and anthropogenic activities. In this way, VOCs are regarded as biogenic VOCs (BVOCs) and anthropogenic VOCs (AVOCs).

On global scales, the emissions of BVOCs contribute with 760 – 1150 TgC year⁻¹ to global VOCs emissions, which exceed AVOCs by a factor of 10 (Guenther et al., 1995, Sindelarova et al., 2014). Regionally the proportions can be different. For example, in Europe BVOCs and AVOCs emissions are comparable in magnitude: biogenic emissions are estimated at around 14 TgC year⁻¹ and anthropogenic around 24 TgC year⁻¹ (Simpson et al., 1999).

Identifying the BVOC sources in the troposphere is one of the main challenges in atmospheric chemistry studies, given their diversity, shallow concentration, and fast reactivity towards tropospheric species.

I.3.2 Sources and diversity of BVOCs

The major sources of BVOCs are woods (822 TgC year⁻¹), shrubs (194 TgC year⁻¹), crops (120 TgC year⁻¹), oceans (5 TgC year⁻¹), and others such as soils, volcanoes, and biomass fires (9 TgC year⁻¹) (Guenther et al., 1995). BVOCs can be separated into three main classes: terpenoids, oxygenated VOCs, and non-oxygenated VOCs.

I.3.2.1 Terpenoid compounds

Terpenoid compounds constitute the most abundant group of BVOCs on the global scale and an important group of aromatic compounds characterizing the odor of many flowers, fruits, seeds, leaves, woods, and roots. The terpenoid group can be divided into two subgroups: a first one whose formula can fit with $(C_5H_8)_n$ and a second one whose formula is different from $(C_5H_8)_n$. Regarding the first subgroup, the value of "n" defines its different classes. In contrast, the second subgroup is classified according to an oxygen atom's presence or absence (oxygenated and non-oxygenated compound).

I.3.2.1.1 Isoprene (n=1)

This compound was discovered in the mid-1950s by Rasmussen and Went 1965, and since then, many other researchers have been interested in it (Kesselmeier and Staudt, 1998, Sharkey et al., 2001, Sanadze, 2004). Isoprene is the most abundant BVOCs in the atmosphere, occupies 44% of the global emitted BVOC, according to Guenther et al., 1995. estimation, whereas, Sindelarova et al., 2014 claimed a higher contribution of about 70%.

Terrestrial plant foliage is responsible for the emission of more than 90% of the total atmospheric isoprene (Guenther et al., 2006). Isoprene release is mainly known from plants such as *Populus*, *Salix*, *Platanus*, *Casuarina*, *Eucalyptus*, *Cocos*, *Elaeis*, as well as from the genus *Picea* (spruces) (Laothawornkitkul et al., 2009) and diverse ferns (Sharkey et al., 2008). The abundance of isoprene in the atmosphere is due to the diversity of plants emitting isoprene. Moreover, its high volatilization does not allow it to be stored in plants.

Isoprene is also emitted by the oceans following phytoplankton and algae (Gantt et al., 2010) and microbes during nutrient cycling of the soil (Guenther et al., 2006). Other studies have shown that animal and human breaths contain isoprene (Sharkey, 1996, Fenske and Paulson, 1999, Hyšpler et al., 2000, Lärstad et al., 2007). There is evidence that isoprene emission from plants helps plants protect themselves from thermal damage (Singsaas et al., 1997, Sharkey et al., 2001). The presence of isoprene in animal and human breaths is still unknown.

1.3.2.1.2 Monoterpenes (n=2)

Monoterpenes represent the second contributor to the total emitted BVOCs in the atmosphere with 11% (Guenther et al., 1995, Sindelarova et al., 2014). They usually have a cyclic structure, with one or more double bond located inside the ring called endocyclic (α -pinene) or outside the ring exocyclic (β -pinene). If the structure has a double bond inside and outside the ring, the structure is called a combined structure, as for limonene. Other acyclic structures exist, such as myrcene.

Monoterpenes are present mainly in essential oils, which are produced by plants. Their production has been found in 46 families of flowering plants and all conifers (Klinger et al., 1994, Fukui and Doskey, 1998, Janson and de Serves, 2001). In the Mediterranean region, monoterpene emissions are dominated by emissions from *Quercus ilex*, *Genista scorpius*, and *Quercus pubescens* (Bertin et al., 1997, Owen et al., 2001). Contrary to isoprene, monoterpenes can be stored by plants (Monson et al., 1995).

Monoterpene emissions have an allelopathic function that allows the plant source to protect itself against abiotic stresses, disruptive agents, or attract pollinating insects. For example, the emission of α -pinene helps the plant adapt to changes in weather conditions such as variation in humidity or the presence of wind (Lamb et al., 1985). Gao et al., 2005 suggested the emission of α -pinene, β -pinene, limonene, α -caryophyllene, borneol acetate, myrcene, tricyclene, and camphene limit bacteriological development and eliminate the presence of fungi in the plant leaves. Conversely, linalool allows the emitting plant to attract pollinators by its citrus scent (Pichersky et al., 1994).

I.3.2.1.3 Sesquiterpenes (n=3)

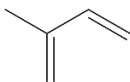
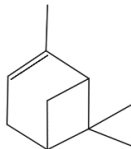
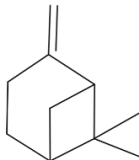
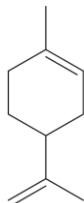
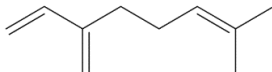
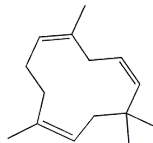
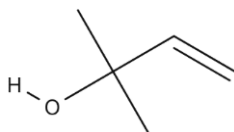
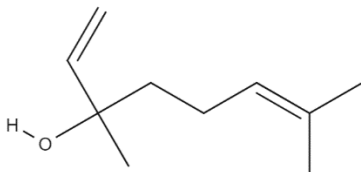
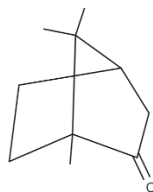
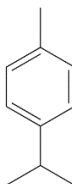
Sesquiterpenes contribute about 2.5% to total BVOC emissions (Sindelarova et al., 2014). Although their low atmospheric concentrations, BVOCs contribute significantly to secondary organic aerosols (SOAs) production (Sakulyanontvittaya et al., 2008, Bouvier-Brown et al., 2009, Guenther, 2013).

Sesquiterpenes are characterized by their low volatility and high reactivity, which results in a typical lifetime of minutes, complicating their detection into the atmosphere. More than 300 species have been classified as sesquiterpenes, but only 30 to 45 have been identified as emitted from vegetation (Graedel, 1979, Helmig et al., 2007, Duhl et al., 2008, Sakulyanontvittaya et al., 2008). Sesquiterpenes include β -caryophyllene, cadinene, humulene, and α -neoclovene.

Sesquiterpenes could be emitted from a variety of trees or agricultural plants such as *Betula pendula*, *Pinus taeda*, *Populus tremula*, *Sambucus nigra*, *Citrus sinensis*, potato plants, sunflower, maize, leaves of tobacco and cotton (Duhl et al., 2008) or by flowers (Chen, 2003). Sesquiterpenes are also released by herbivores damaged leaves (Vuorinen et al., 2004). Sesquiterpenes play critical roles in plant-insect and plant-plant interactions (Duhl et al., 2008). For ($n > 3$), compounds have longer carbon chains and lower volatilities; therefore, they get out automatically from the VOC family.

The second subgroup of terpenoid does not fit with the formula $(C_5H_8)_n$. However, it can be divided into two categories of compounds "oxygenated compounds" such as 2-methyl-3-buten-2-ol, linalool, and camphor and "non-oxygenated compounds" such as p-cymene. Sindelarova et al., 2014 estimated that these compounds contribute less than 2% to total BVOC emissions. Table I.1 displays the names and structures of the cited terpenoid compounds.

Table I.1: The skeletal structure of some selected compounds that belong to the terpenoids.

Terpenoids (C ₅ H ₈) _n			
Hemiterpene (n=1)			
Isoprene			
			
Monoterpenes (n=2)			
Endocyclic	Exocyclic	Combined	Non-cyclic
α-Pinene	β-Pinene	Limonene	Myrcene
			
Sesquiterpenes (n=3)			
β-Caryophyllene			
			
Terpenoids ≠ (C ₅ H ₈) _n			
Oxygenated terpenes			
2-Methyl-3-buten-2-ol (MBO)	Linalool	Camphor	
			
Non-oxygenated terpenes			
p-Cymene			
			

I.3.2.2 Oxygenated compounds (OVOCs)

This group contains compounds that have at least one oxygen atom in their structure. The oxygenated compounds are a large group of hydrocarbons released by various terrestrial ecosystems (Fall, 2003, Peñuelas and Staudt, 2010, Guenther et al., 2012). They play an essential role in the formation of atmospheric constituents as oxidants and aerosols.

I.3.2.2.1 Aldehydes

Among numerous emitted aldehydes, formaldehyde and acetaldehyde represent the two major emitted aldehydes with 0.2% and 1.3% to the total BVOC emissions (Sindelarova et al., 2014). Other studies provided evidence that longer aldehydes such as propanal, butanal, i-butanal, butenal, i-butenal, hexenal, heptenal, octanal, nonanal, and decanal (Isidorov et al., 1985, Konig, 1995, Wildt et al., 2002) have also been detected in the atmosphere. Unsaturated aldehydes such as crotonaldehyde, 2-methyl-2-pentenal, hexenal, Trans-2-hexenal, and Cis-3-hexenal; called "leaf aldehyde" are produced mainly by vegetation (Hatanaka and Harada, 1973, Hatanaka et al., 1987, Hatanaka, 1996) and especially by leafy plants, fruits, cotton, and alfalfa (Buttery et al., 1982, Arey et al., 1991, Tanner and Zielinska, 1994, Davis and Burkholder, 2011).

Non-linear carbon chain aldehydes such as benzaldehyde are one of the most emitted aromatic compounds directly emitted by vegetation or indirectly through carbonyl compounds' oxidation into the atmosphere (Winer et al., 1992, Seco et al., 2007). The oxidation of some biogenic OVOCs with atmospheric oxidants can generate aldehydes, such as the oxidation of methanol, which forms formaldehyde (MacDonald and Fall, 1993, Nemecek-Marshall et al., 1995). The reaction of Cis-3-hexen-1-ol and Cis-3-hexenylacetate, two BVOCs present at high concentrations in the atmosphere, with OH and NO_x, also contribute to the formation of formaldehyde, acetaldehyde, and propanal (Atkinson, 1990, Atkinson, 2007). Alkene oxidations represent a source of aldehydes in the atmosphere (Carlier et al., 1986, Atkinson et al., 1995). Furthermore, heterogeneous ozonolysis reactions at the leaf surfaces generate some aldehydes such as 4-oxopentanal (Fruekilde et al., 1998). Other biogenic sources, such as insects and animals, contribute to aldehyde's total budget in the atmosphere (Morgan and Tyler, 1977).

I.3.2.2.2 Alcohols

Alcohols are among the most abundant VOCs in the global atmosphere. Terrestrial ecosystems are the dominant source of alcohol in the atmosphere (Graedel, 1979). For example, vegetation contributes to 78% of methanol's global annual production, whereas other sources like VOCs oxidations, biomass burning, and biological degradation do not exceed 12% (Jacob, 2005). More recent studies (Millet et al., 2008, Stavrakou et al., 2011) confirmed the importance of leafy vegetation to methanol's total budget, especially for fresh leaves (MacDonald and Fall, 1993, Stavrakou et al., 2011). Methanol is emitted mainly during the plant's growth or its degradation by other organisms (Laothawornkitkul et al., 2009). Methanol contributes 6% to the total BVOC emissions (Sindelarova et al., 2014).

Longer carbon chain alcohols such as ethanol, 1-pentanol, 3-pentanol, 1-hexanol can be formed through an alcoholic fermentation of both leaves and roots (Konig, 1995, Jardine et al., 2009). Unsaturated alcohols such as 2-methyl-1-propanol, 1-penten-3-ol, Cis-2-Penten-1-ol, Trans-2-Hexen-1-ol (Goldan et al., 1993, Davis and Burkholder, 2011) and Cis-3-Hexen-1-ol (Arey et al., 1991, König, 1995) are released by a variety of fruits (grape, orange, apricot, nectarine, peach, plum), dried fruits (pistachio, walnut, almond) and plants (cotton, alfalfa) (Arey et al., 1991, Winer et al., 1992).

I.3.2.2.3 Ketones

Among the ketones group, acetone is one of the most abundant VOCs in the global atmosphere (Khalil and Rasmussen, 1992). Acetone emissions are detected at the headspace of conifer buds (Macdonald and Fall, 1993, Jacob et al., 2002) and generally follow a pathogenic or herbivorous attack (Zagrobelyny and Møller, 2011). Other higher ketones like butanone-2, pentanone-2, octanone-3, methyl-isopropyl-ketone, methyl-vinyl-ketone, 6-methyl-5-hepten-2-one are also released within the atmosphere by plants (Macdonald and Fall, 1993, König, 1995, Singh et al., 1994, Singh et al., 2012). The reaction between foliage and ozone also produces ketones such as acetone, 6-methyl-5-hepten-2-one, and geranyl acetone in the Mediterranean area (Fruekilde et al., 1998).

I.3.2.2.4 Organic acids

Organic acids in the atmosphere have a crucial role in acidifying precipitations in remote areas (Andreae et al., 1988). Formic acid and acetic acid are mainly responsible for influencing these areas' acidity (Lunde et al., 1977, Likens et al., 1983, Andreae et al., 1987, Andreae et al., 1988, Hofmann et al., 1997). Organic acids in the atmosphere represent at 1-3 ppbv (Winiwarter et al., 1988, Talbot et al., 1988). Emissions from both vegetation (Andreae et al., 1988, Graedel et al., 2012) and soil (Sanhueza and Andreae, 1991) are significant sources of organic acids. Indirect sources as the oxidation of isoprene or ethene and propene are discussed in (Andreae et al., 1987) and (Horie and Moortgat, 1991), respectively.

I.3.2.2.5 Ethers and esters

Several previous works have reported the emission of ethers and esters from biogenic sources (Graedel, 1979, Schlitt et al., 1980, Buttery et al., 1982, Butter et al., 1985, Isidorov et al., 1985, Arey et al., 1991, MacDonald and Fall, 1993, König, 1995, Köppmann, 2007). The prominently identified esters are ethylacetate, butylacetate, methylbutyrate, hexylacetate, Cis-3-hexenylacetate, ethylhexylacetate, methylsalicylate, and bornylacetate. The identified ethers are diethyl ether, p-dimethoxy-benzol, 1,8-cineol, estragol, p-methylanisol, furane, 2-methyl-furane, 3-methyl-furane, ethyl, and vinyl-furane.

I.3.2.3 Non-oxygenated compounds (NOVOCs)

I.3.2.3.1 Alkanes and alkenes

C₂-C₄ alkanes are present in the atmosphere at a global concentration of 1 – 3 ppbv. Natural gas and biomass burning are the two primary sources of alkane emissions (Rudolph, 1995, Lindskog, 1997). Contrary to terpenoids and OVOCs, terrestrial vegetation such as trees, crops, and marshland are not significant sources of alkanes (Altshuler, 1983, Guenther et al., 1994). The marine boundary layer is also considered a contributor to C₂-C₄ alkanes formation (Bonsang et al., 1988, Plass-Dülmer et al., 1995). C₂-C₄ alkenes are produced in the absence of any stress factor by all plant tissues. Higher concentrations of alkenes are observed after mechanical stress, arid conditions, high

temperatures, or high pollution episodes (Bucher, 1981, Kimmerer and Kozlowski, 1982, Yang and Hoffman, 1984). C₂-C₄ alkenes can be produced in the marine boundary layer through the photochemical degradation of dissolved organic carbon released by algae (Kesselmeier and Staudt, 1998).

I.3.3 Factors affecting BVOCs emissions

BVOCs are released more or less immediately upon their production, while others are sequestered in specialized cellular compartments. BVOC emissions depend essentially on the volatility of the released compound, the plant (internal factor), and the interaction between the plant and its environment (external factor) (Monson et al., 1995). This section deals with the influence of internal and external factors influencing BVOC emissions.

I.3.3.1 Internal factors

I.3.3.1.1 Stomatal regulation

The emission of BVOCs by leaves occurs through stomata, pores found in the epidermis of leaves, or by their diffusion through the cuticle, the film covering the epidermis, especially when stomata are closed (Harley, 2013). The stomata regulation ensures the exchange of CO₂ and water vapor between the plant and its surrounding. The responsiveness of BVOC emissions to stomatal regulation is complicated and not fully understood by the research community. Some extant models of BVOC emission from leaves, such as Guenther et al., 2006 and Guenther et al., 2012 assume that the stomata do not influence the flux whereas, other studies demonstrate that BVOC emissions are controlled at the scale of stomata (Laothawornkitkul et al., 2009, Harley, 2013). For instance, Tingey et al., 1981 claimed that isoprene is emitted through oak leaves' stomata (*Quercus virginiana*).

I.3.3.1.2 Enzyme activity

The emission of many BVOCs is also correlated with enzyme activities (Kuzma and Fall, 1993, Loreto et al., 2001, Fischbach et al., 2002). Enzyme regulatory mechanisms are based on changing the protein levels, which control BVOC emissions (Yakir et al., 2007).

This phenomenon remains complex to understand since a mixture of different BVOCs may result from different biosynthetic pathways.

I.3.3.2 External factors

I.3.3.2.1 Temperature and light

Temperature plays a positive effect on the emission rates of most BVOCs by enhancing the enzyme activities, raising the compound vapor pressure, and decreasing the resistance of the emission pathway (Penuelas and Llusà, 2001). Indeed, α -pinene releases from *Quercus ilex* increase three times when temperature increase from 293 to 303 K (Loreto et al., 1996).

Moreover, there are differences in response to increasing temperature depending on the compound volatility and biochemistry. For instance, the emission of terpenes with high volatility is more responsive to temperature variation than less volatile ones (Penuelas and Llusà, 2001). Besides, most BVOC emissions are triggered by light. For example, isoprene and monoterpenes emissions are light-dependent (Tingey et al., 1981, Guenther et al., 1991, Wildermuth and Fall, 1996, Kesselmeier et al., 1997). In the case of oxygenated compounds, Kesselmeier et al., 1997 and Staudt et al., 2000 claim the high dependence between the emissions of formic and acetic acids and the presence of irradiance.

I.3.3.2.2 Relative humidity

The relative humidity role is presently not well established since contradictory results can be found in the literature. For instance, some studies suggest that relative humidity has a slight positive effect on BVOC secretions, such as isoprene emissions from eucalyptus and aspen (Guenther et al., 1991, Monson and Fall, 1989) and monoterpene emissions from sage and oak (Dement et al., 1975, Loreto et al., 1996). On the other hand, some studies claim that relative humidity does not influence isoprene and monoterpene release by leaves (Yokouchi and Ambe, 1984, Guenther et al., 1991, Janson, 1993).

I.3.3.2.3 Air composition

Some BVOC emissions are related to the fluctuations of CO₂ and H₂O levels in the atmosphere.

For example, Monson and Fall, 1989 demonstrated that isoprene's emission required the presence of CO₂. This result was then studied by Loreto et al., 1996, who concentrated on assessing the influence of CO₂ on the emission of α -pinene from *Quercus ilex* leaves. In contrast, other BVOC emissions, such as the release of formic and acetic acids from orange foliage, did not present any correlation with CO₂ and H₂O levels.

I.3.3.2.4 Mechanical stress, injury and herbivore, and pathogen attacks

Mechanical stress, injury, herbivore and pathogen attacks can impact the concentration of emitted BVOCs (Kesselmeier and Staudt, 1998). C₆-aldehydes and alcohols are known as stored compounds and are commonly emitted during the damage of leaves (McCall et al., 1994, Sharkey, 1996, Heiden et al., 1999, Engelberth et al., 2004). Monoterpenes can also be emitted after twig frictions (Guenther et al., 1991, Arey et al., 1995). On the contrary, this phenomenon was not observed for non-stored compounds such as isoprene (Monson et al., 1994). Moreover, BVOC emissions increase in response to the plant interactions with animals and other organisms. Several BVOCs are emitted by the attacked plant and act as an "alarm" to neighboring plants. Other BVOCs are released to attract pollinators.

I.3.4 Ecophysiological functions of BVOC emissions

BVOC emissions have essential physiological and ecological roles (Kesselmeier et al., 1997, Jardine et al., 2008, Schuman et al., 2016). The release of BVOCs by plants acts as a means of communication within plants' communities and between plants and their ecosystem. For instance, the emission of BVOCs can protect the plant directly by deter herbivore attacks or indirectly by attracting parasitoids, which will protect the plant (Fineschi and Loreto, 2012). These emissions can also influence the growth and the activity of adjacent plants, insects, and animals (Heil and Bueno, 2007, Holopainen, 2011, Abeles et al., 2012).

The BVOC emissions increase the resistance against biotic stresses inside the leaf tissues (Loreto and Schnitzler, 2010). For example, some leaves produce isoprene to protect themselves against heat stress (Sharkey et al., 2008).

Monoterpenes are also known as defense compounds against pathogen and herbivore attacks (Rosenthal and Berenbaum, 2012). Also, β -pinene plays an internal inhibitor of respiration to limit microbe and fungal growths (Chen et al., 1990).

Terpene emissions are generally related to oxidative stress; this occurs by triggering the excess reactive oxygen species (Loreto and Schnitzler, 2010). For instance, methyl salicylate is released by leaves after the ozone attack of leaves (Heiden et al., 1999). Injured leaves and ripening fruits emit ethene to heal their wounds (Peiser and Yang, 1979, Abeles et al., 2012).

Furthermore, neighboring plants can absorb the damaged plant's emitted volatiles to strengthen their resistance against herbivore attacks (Himanen et al., 2010). For example, the emission of methyl salicylate from tobacco plants affected by the tobacco mosaic virus reacts as an alarm signal to other non-damaged plants (Shulaev et al., 1997).

In the rhizosphere, which is the narrow region of soil directly influenced by root secretions and associated soil microorganisms, both the plant roots and microbial organisms such as bacteria fungi are responsible for the BVOC emissions. Recent studies claimed that the emitted BVOCs from the soil have two essential functions: ensuring the communication between microbial organisms and promoting or inhibiting their growth (Peñuelas et al., 2014, Kai et al., 2016, Van Dam and Bouwmeester, 2016).

I.4 Sink of BVOCs in the troposphere

Once BVOCs are released in the atmosphere, they may undergo either physical processes such as wet and dry deposition (Matsunaga et al., 2007, Spielmann et al., 2017) or photochemical processes such as reaction with hydroxyl radical (OH), nitrate radical (NO_3), ozone (O_3) and chlorine atoms (Cl) (Finlayson-Pitts and Pitts Jr, 1999, Atkinson, 2000). Wet and dry deposition is a potential removal process mainly for long-lived compounds such as methane and methanol (Atkinson and Arey, 2003). On the other hand, photochemical removal processes are expected to be potentially crucial for highly reactive species such as terpenes and carbonyls (see Table I.2) (Ciccioli et al., 2014). The following section represents the degradation mechanism of BVOCs in the atmosphere.

I.4.1 Oxidation processes

I.4.1.1 Reaction with OH radicals

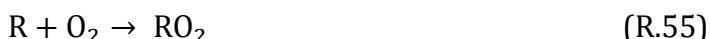
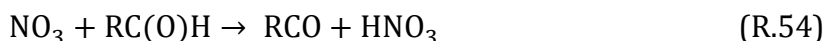
As noted in section I.2.3.1, the hydroxyl radical (OH) is the crucial species in the troposphere, undergoing reactions with hundreds of gases (Thompson, 1992). The oxidation of saturated VOCs such as alkanes, alcohols, carbonyls, ethers, and esters by OH radicals occur only via the H-abstraction from the C-H bonds (R.17). In unsaturated VOCs, the reaction proceeds via the addition to the double bond (R.52) (Atkinson, 2000).



The radicals formed from (R.17) and (R.52) can react with molecular oxygen to generate organic peroxy radicals RO₂ (R.18), which fate depends on the environment. In remote areas where NO_x levels are low, RO₂ reacts with RO₂. In polluted areas where NO_x is high, peroxy radicals (RO₂) convert to alkoxy radicals (RO) through the oxidation of NO to NO₂ (R.19), leading to the formation of ozone.

I.4.1.2 Reaction with NO₃ radicals

The reaction between nitrate radical NO₃ and saturated compounds (R.53) or carbonyl compounds (RCOH) (R.54) proceeds only via H-abstraction. The formed alkyl radicals (R) and (RCO) will oxidize via molecular oxygen to peroxy radicals (RO₂) (R.55) and RCOO₂ (R.56).



The reaction of NO₃ with unsaturated compounds may proceed either via H-abstraction or via addition to the double bond. The H-abstraction occurs, as explained above, for saturated and carbonyl compounds.

The addition of NO_3 to unsaturated compounds in the presence of O_2 produces nitrate alkyl peroxy radicals, which are highly reactive with RO_2 , HO_2 , or NO_2 under dark conditions. These oxidations generate peroxy nitrate, which forms a NO_x reservoir (Jenkin and Clemitshaw, 2000). Furthermore, the oxidation of VOCs with NO_3 can control the $[\text{OH}]/[\text{HO}_2]$ ratio and ozone production rates (Monks et al., 2009, Ng et al., 2017).

I.4.1.3 Reaction with ozone

The ozonolysis of VOCs has been studied both experimentally and theoretically in several studies, including (Atkinson, 1990, Horie and Moortgat, 1998, Witter et al., 2002), considering the crucial interactions between VOCs and ozone in the troposphere. The reaction between ozone and VOCs concerns only unsaturated species. The ozonolysis reaction mechanism has been described in different previous works (Criegee, 1975, Finlayson-Pitts and Pitts Jr, 1986, Johnson and Marston, 2008).

These reactions occur mainly by the addition of ozone to the $\text{C}=\text{C}$ bonds forming a primary unstable ozonide, which rapidly decompose via two pathways producing in each pathway a carbonyl compound (aldehyde or ketone) and a carbonyl oxide intermediate, which is commonly referred to as a Criegee intermediate, (CI). The formed CI is unstable due to its internal energy and then stabilizes by collision or decomposition through three possible pathways: (i) rearranging to an ester or an acid (ester channel), (ii) ejecting $\text{O}(^3\text{P})$ to yield a carbonyl (oxygen-atom channel), or (iii) forming a hydroperoxide via a 1,4-hydrogen shift (hydroperoxide channel) (Hatakeyama and Akimoto, 1994, Jenkin and Clemitshaw, 2000, Winterhalter et al., 1999, Finlayson-Pitts and Pitts Jr, 1999). We have to mention that pathway (ii) is a minor one whereas, both pathways (i) and (ii) are essential and responsible for the formation of free radicals. Figure I.5 displayed all the described channels regarding an alkene's ozonolysis (Finlayson-Pitts and Pitts Jr, 1999).

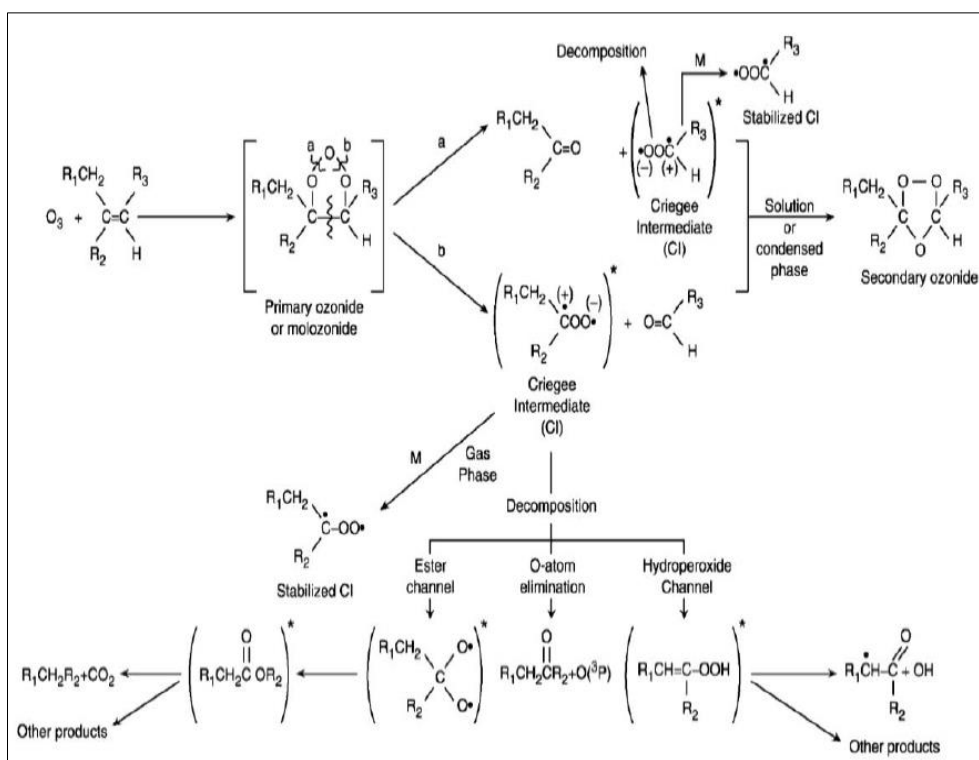


Figure I.5: Overall mechanisms of O_3 -alkene reactions in the gas and condensed phase (Finlayson-Pitts and Pitts Jr, 1999).

I.4.1.4 Reaction with Cl atoms

Cl atoms are very reactive species. Though the rate constants of VOCs reactions with Cl's are generally faster than those with OH radicals, these processes have minor importance given the low tropospheric concentration of Cl. This oxidation has a crucial role not only in the marine boundary layer and coastal regions but also in urban areas (Finlayson-Pitts and Pitts Jr, 1999).

The oxidation of VOCs through Cl atoms occurs via H-abstraction or Cl-addition on the double bond (Atkinson and Arey, 2003). The H-abstraction is the only oxidation pathway for saturated compounds. The addition of a Cl atom on the C=C bond is more favorable for most unsaturated compounds since it produces the most stable substituted radicals. Nevertheless, H-abstraction can also be an important degradation pathway for long-chain alkenes (Nishino et al., 2009).

I.4.2 Photodissociation process

The photodissociation of a generic molecule AB starts by its transformation from the fundamental state AB to an excited state AB* by absorbing the suitable energy (R.39). The latter can dissociate as (R.40) or evolve following different other pathways like emission, energy transfer, isomerization, or non-radiative transition. In the troposphere, BVOCs undergo photodissociation by absorbing incident radiations in the spectral range between 290 and 800 nm (see section I.2.2) (Atkinson, 2000).

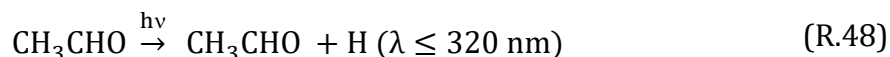
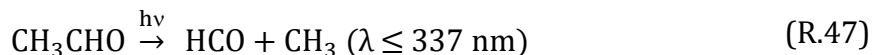
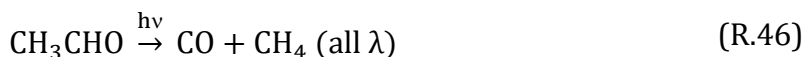


The photodissociation of oxygenated BVOCs occurs via the dissociation of the C-R bond preferentially in the α -position of the carbonyl group (Atkinson and Arey, 2003, Steinbrecher et al., 2004, Blitz et al., 2006). The dissociation mechanisms of the three most photodissociated oxygenated BVOCs: formaldehyde, acetaldehyde, and acetone (Atkinson and Arey, 2003, Mellouki et al., 2015) are presented below.

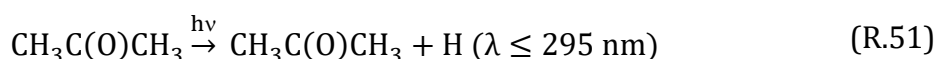
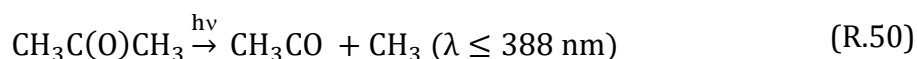
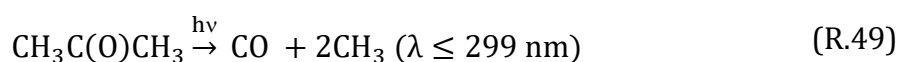
Formaldehyde can be photo dissociated into two stable molecules (R.41) or two radicals (R.42) (Finlayson-Pitts and Pitts Jr, 1999). Both radicals HCO (R.43) and H (R.44) react with molecular oxygen producing HO₂, which can oxidize NO to NO₂ by generating OH radicals (R.45).



In the case of acetaldehyde, three different photolysis pathways (R.46 – 48) are possible (Moortgat et al., 2010).



Regarding acetone, three ways of photodissociation (R.49 – 51) are also possible depending on the incident light's energy (Nádasdi et al., 2007).



I.4.3 BVOCs lifetimes

BVOCs are present in the troposphere, mostly at some pptv to a few tens of ppbv (Fuentes et al., 2000). Their tropospheric levels are continually affected by several physical and chemical processes, as explained above. Each removal process depends on environmental conditions (temperature, pressure, humidity, wind, and speed) and physicochemical characteristics of the compound (volatility, the absorbance of UV-VIS radiations, and molar mass). Generally, photolysis and oxidation reactions of BVOCs dominate their removal and then define their lifetimes in the atmosphere. Other processes like diffusion and deposition remain not well studied, given the complexity of determining the associated loss rates. The knowledge of the oxidant concentrations in the troposphere and the appropriate rate constants for these reactions (BVOC + Oxidant) determine the lifetime of several BVOCs. In the atmosphere, photolysis and oxidation reactions co-occur, so the calculation of BVOC lifetimes is done as explained in section II.4.1.3.

BVOC lifetimes vary from minutes to years (Kesselmeier and Staudt, 1998, Atkinson and Arey, 2003, Williams, 2004). Some of the data present in the literature are reported in this work. Individual lifetimes are displayed in Table I.2 as proposed in the review by Atkinson and Arey, 2003, using the oxidant concentrations indicated in chapter II.

Atkinson and Arey, 2003 did not calculate the BVOC lifetimes due to Cl atom oxidation reactions because, on a global scale, Cl atom reactions are believed to be of minor importance in the BVOC loss process as claimed in previous works (Singh et al., 1996, Rudolph et al., 1996, Rudolph et al., 1997).

Table I.2: Calculated tropospheric lifetimes for a selected BVOCs of the reaction with OH, NO₃, and O₃ (Atkinson and Arey, 2003).

Compound	OH	O ₃	NO ₃
Hemiterpene			
Isoprene	1.4 h	1.3 day	1.6 h
Monoterpenes			
Camphene	2.6 h	18 day	1.7 min
2-Carene	1.7 h	1.7 h	4 min
3-Carene	1.6 h	11 h	7 min
Limonene	49 min	2.0 h	5 min
Myrcene	39 min	50 min	6 min
Cis-/Trans-Ocimene	33 min	44 min	3 min
α-Phellandrene	27 min	8 min	0.9 min
β-Phellandrene	50 min	8.4 h	8 min
α-Pinene	2.6 h	4.6 h	11 min
β-Pinene	1.8 h	1.1 day	27 min
Sabinene	1.2 h	4.8 h	7 min
α-Terpinene	23 min	1 min	0.5 min
γ-Terpinene	47 min	2.8 h	2 min
Terpinolene	37 min	13 min	0.7 min
Sesquiterpenes			
β-Caryophyllene	42 min	2 min	3 min
α-Cedrene	2.1 h	14 h	8 min
α-Copaene	1.5 h	2.5 h	4 min
α-Humulene	28 min	2 min	2 min
Longifolene	2.9 h	> 33 day	1.6 h
Oxygenated			

Acetone	61 day	> 4.5 year	> 8 year
Camphor	2.5 day	> 235 day	> 300 day
1,8-Cineole	1.0 day	> 110 day	1.5 year
Cis-3-Hexen-1-ol	1.3 h	6.2 h	4.1 h
Cis-3-Hexenyl acetate	1.8 h	7.3 h	4.5 h
Linalool	52 min	55 min	6 min
Methanol	12 day	> 4.5 year	2.0 year
2-Methyl-3-buten-2-ol	2.4 h	1.7 day	7.7 day
6-Methyl-5-hepten-2-one	53 min	1.0 h	9 min

These data show that major BVOCs are more reactive with OH and NO₃ than with O₃ although, some exceptions such as β -Caryophyllene and α -Humulene exist. Isoprene is rapidly removed by OH rather than NO₃, whereas most monoterpenes behave inversely to isoprene.

I.5 Impacts of BVOC emissions

I.5.1 Shaping the oxidative capacity of the atmosphere

The presence of BVOCs in the lower troposphere leads to the alteration of the atmosphere's oxidizing capacity given their photolysis and their rapid reactivity with hydroxyl radicals, nitrogen oxides, ozone, and Cl atoms (Atkinson and Arey, 2003, Filella and Peñuelas, 2006). In high NO_x environments, the photolysis of BVOCs contributes to tropospheric ozone formation, which is the third most important greenhouse gas after CO₂ and methane (Solomon et al., 2007, Atkinson, 2000, Koppmann, 2007). Ozone is also the major source of hydroxyl radicals (see section I.2.3.2) and plays a crucial role in photochemical smog (Chameides et al., 1988, Calapietra et al., 2009).

Moreover, tropospheric ozone was reported to have a severe effect on human health and the environment. Due to its oxidative potential, tropospheric O₃ can generate severe respiratory diseases that can contribute to premature death, especially for asthmatic patients. Also, ozone can damage trees and crops by reducing their photosynthesis (Ashmore, 2005, Felzer et al., 2007).

In the unpolluted area, BVOCs contribute to the depletion of hydroxyl radicals, increasing both the concentration and the lifetime of greenhouse gases like methane because OH radicals represent the major sink of methane (Lelieveld et al., 2008).

I.5.2 Balancing the global carbon cycle

The emitted BVOC represents 5 to 10% of the total net carbon exchange in the atmosphere, especially in abiotic or biotic stresses (Peñuelas and Llusà, 2003). In tropical regions, the total average of the emitted BVOCs from vegetation surface are estimated to be at rates from approximately 0.7 g carbon m⁻² per year to 100 g carbon m⁻² per year (Guenther, 2002). This average could reach $(0.75 - 1.2) \times 10^{15}$ g carbon m⁻² per year (Guenther et al., 1995, Lathiere et al., 2006). The release of BVOCs in the atmosphere might impact the total carbon budgets and the level of CO₂, which are susceptible to disturb air quality, and land cover (Kesselmeier, 2002).

I.5.3 Producing biogenic SOAs

BVOCs are the major precursors of biogenic secondary organic aerosols (BSOAs) in the atmosphere. Indeed, the formation of SOAs occurs through the low volatile oxidation products of BVOCs (Hoffmann et al., 1997, Griffin et al., 1999, Arneth et al., 2010).

For instance, sesquiterpenes significantly contribute to BSOA formation compared to isoprene and monoterpenes (Lee et al., 2006). Mentel et al., 2009 claimed that long-chain oxygenated BVOCs are responsible for nucleation and particles' growth. However, the emission of isoprene from the oceans can also be a source of SOAs. Whereas, Arneth et al., 2010 claimed that SOA from marine isoprene is insignificant compared to BVOC from terrestrial vegetations. The SOA formation is highly dependent on the type and the amount of BVOC (Lee et al., 2006) and the meteorological parameters (Athanasopoulou et al., 2013).

SOAs are known to damage the Earth's radiation balance either directly by scattering and absorbing solar radiation or indirectly through their ability to serve as cloud condensation nuclei (CCN), changing the cloud coverage and albedo (Kulmala et al., 2004, Laothawornkitkul et al., 2009, Roberts et al., 2010).

The presence of SOAs in the atmosphere reduces visibility, which is defined as "the farthest distance at which one can see a large, black object against a bright background at the horizon" (Seinfeld and Pandis, 2016). This phenomenon occurs through scattering light and generating what we call a "hazy" appearance, which is the most apparent air pollution characteristic. Moreover, particles can generate several respiratory, cardiovascular, and nervous system diseases (US EPA, 2014). Figure I.6 displays relatively big particles with a diameter ($> 1\mu\text{m}$) trapped in the head region's airways and cause their irritations. On the other side, fine and ultra-fine particles ($< 1\mu\text{m}$) penetrate deeper into the lungs and reach alveoli and lead to harmful infections.

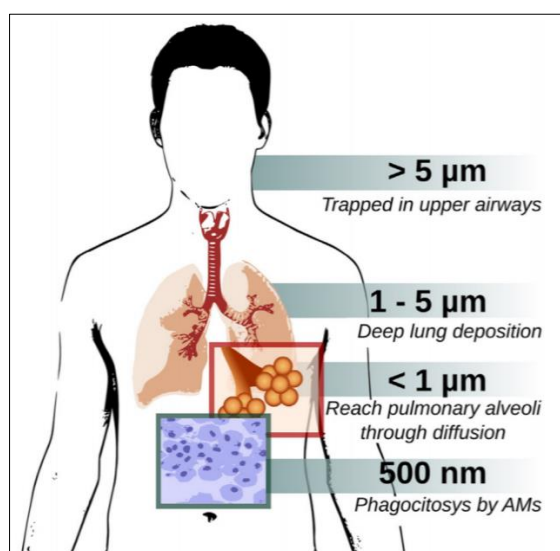


Figure I.6: Illustration of the influence of particle size in lung deposition and phagocytosis by the alveolar macrophages (Costa et al., 2016).

I.6 Conclusion

The present study focuses on improving the level of understanding of unsaturated BVOCs oxidation processes. This chapter displays an overview of the main BVOCs and photo-oxidants sources, their oxidation reactions towards each other, and the impact of these reactions on air quality and climate change.

II Chapter II: Experimental set-ups and methods

II.1 Introduction

During this work, six smog chambers, two flow reactors, and several analytical instruments were used. This chapter provides a detailed description of the experimental techniques and methods used in this work. In the first part, I present the used reactors, and in the second part, I display the used analytical techniques used in atmospheric chemistry. In the third part, I describe the methods and data analysis used in the kinetic studies, the product identification and quantification, and the SOA evaluation.

II.2 An overview of experimental set-ups in atmospheric chemistry

Several parameters, like meteorology and other physio-chemical processes, influence atmospheric chemistry in the ambient. Therefore discontinuous (static or batch) and continuous (flow) systems have been developed since the late 1960s to simplify its understanding (Becker, 2006). Despite that both systems are not artifact-free, they provide a controlled environment to study the formation and the evolution of atmospheric pollutants by isolating the targeted compounds and controlling the reaction environment with the appropriate measuring instruments.

Initially, these techniques were essentially used to produce kinetic data, branching ratios, and product distributions to better understand the gas phase's oxidation mechanism and enrich atmospheric models (Dodge, 2000, Hynes et al., 2005). Moreover, these techniques are also used to evaluate particles' formation (Finlayson-Pitts and Pitts Jr, 1999, Dodge, 2000, Kanakidou et al., 2005, Hallquist et al., 2009). In the next section, both static and flow techniques are displayed, and the used reactors are described in detail.

II.2.1 Static techniques

II.2.1.1 General description

Static systems are closed systems that do not pump the reactants throughout the reactor. In atmospheric chemistry, static techniques consist mainly of Atmospheric Simulation Chamber (ASC) or “smog chambers”. The word “smog” is derived from two terms: smoke and fog, and used to describe any contaminated air.

An ASC's conception needs a deep reflection about several parameters such as the irradiation source, used material, dimension (surface/volume ratio), and pressure and temperature regulation systems.

There are two primary irradiation sources, either natural (solar lights) or artificial (fluorescent tubes). This parameter is one of the most critical since it impacts radical sources, the lifetime of photolyzable products, competitions between processes, and secondary pollutants such as SOAs.

The wall material selection defines two types of chambers: non-rigid chambers working only at atmospheric pressure and rigid chambers working at a specific pressure range. However, they are essentially built to work at a higher or lower pressure range. In rigid chambers, the different atmospheric layers (where the pressure and temperature are significantly lower or higher than atmospheric conditions) can be simulated. The chamber can be profoundly and rapidly cleaned. Whereas in non-rigid chambers, only atmospheric pressure is allowed. The cleaning process is much more complicated because a pressure equilibrium is established between the chamber's pressure and its environment. Therefore, non-rigid chambers are less expensive than rigid ones. The selected material must be transparent to the incident light, inert against chemicals, and resistant to the chemical's adsorption. The most used atmospheric chemistry materials include Teflon (non-rigid chambers), Pyrex, quartz, stainless steel, and aluminum (rigid chambers).

The design of the ASC represents an important step to manage secondary effect. In ASCs, wall losses of compounds introduced in the reactor are a prominent issue. Hence the surface to volume ratio needs to be minimized. Consequently, large chambers should be favored to increase the time compounds need to diffuse from the center to the chamber walls.

II.2.1.2 Static techniques used in this work

In this work, I used two ASCs at IMT Lille Douai, which are D-ASC and THALAMOS-ASC.

Moreover, I had the opportunity to operate QUAREC-ASC as part of a collaboration between IMT Lille Douai and Wuppertal University. Also, I used two other ASCs: 16L-ASC and CR-ASC, as a part of a collaboration between IPR and UCLM University.

To consolidate our results, 3m-ASC has been used by our colleagues at Wuppertal University. In this manuscript, I detailed all the listed ASCs. Each ASC was dedicated to a specific study according to its characteristics such as wall material, size, irradiation source, temperature, and pressure. Analysis techniques will be presented in detail in section II.3.

II.2.1.2.1 D-ASC – IMT Lille Douai

Douai-Atmospheric Simulation Chamber (D-ASC) of IMT Lille Douai laboratory was developed as part of Estelle Turpin's thesis in 2004 (Turpin, 2004). D-ASC has been well described in previous works (Turpin et al., 2006, Bouzidi, 2014, Aslan, 2017, Caravan et al., 2018). D-ASC was generally used to investigate the kinetics and atmospheric degradation mechanisms of several VOCs.

It consists of an FEP (Fluorinated ethylene propylene)-Teflon bag (50 μm of wall thickness) of about 300-L set inside a wooden box, ensuring darkness during experiments. All the box's interior faces are covered with an aluminum coating, allowing better reflection of the radiation emitted by fluorescent tubes (case of photolysis reaction studies). Three types of lamps are available: Philips T-20 M, which emits maximum radiation around 312 nm, Philips TLK & Sylvania Blacklight with a maximum wavelength equal to 365 nm, and monochromatic light lamps at 254 nm. The use of these lamps may increase the temperature inside the wooden box and then inside the D-ASC. Therefore, two fans fixed on the box walls are used to ventilate the interior and keep ambient temperature throughout the wooden box. The box's base contains holes ($d < 1\text{ cm}$) that serve to exchange air with the laboratory.

In this thesis, D-ASC was used for several tasks, such as determining the rate constant for the ozonolysis of unsaturated aldehydes and alcohols (see chapter IV).

The kinetic study of the reaction between unsaturated aldehydes and chlorine atoms was also determined in D-ASC (see chapter V). The investigation of the reaction of methylperoxy and hydroxyl radicals has been carried out also in D-ASC (see chapter VI). This chamber allowed us to investigate the gas-phase reactions and particles' formation throughout the oxidation reaction between unsaturated aldehydes and ozone. Before starting any experiment, the reactor is subject to a cleaning protocol based on its flushing with zero air under lights on.

Switching on the lamps increases the reactor temperature, and as a result, the process of desorption of the adsorbed compounds onto the reactor walls is accelerated. This step was repeated several times. After each cycle, an analysis was carried out using FTIR spectroscopy to ensure the reaction bag and sampling line cleanliness. Then, the analyzed spectrum was compared to previous air spectra inside the chamber. Once the reactor is considered as “clean”, the background spectrum is recorded.

Two ports installed on the reactor walls allow filling and emptying the reactor with purified air, reactants, and gas samples for analysis. For gas reactants such as ozone (O_3) and molecular chlorine (Cl_2), the injection is done directly at the reactor's inlet port using a syringe. Whereas the introduction of liquid reactants starts with the injection of these reactants using a syringe in Pyrex cell kept under vacuum. This set-up allows vaporizing the reactants at temperatures below their boiling point. The vaporized reactant is sent to the D-ASC using a purified flow of air. We also have to mention that all gas flows are controlled by mass flow controllers (MFCs) that are calibrated at IMT Lille Douai.

This chamber is connected to two sampling methods: either by direct sampling via a preheated line (on-line) or by sampling on cartridges (off-line). The online sampling was carried out using an FTIR spectrometer linked to a 2-L White cell with 10 m of the optical path, the ozone analyzer (Environnement SA 42 M), and the Proton-Transfer Reaction Time-of-Flight Mass Spectrometry device (PTR-ToF-MS Inonicon 4000 or PTR-ToF-MS Inonicon 8000). The characterization of particles in D-ASC is carried out with a Scanning Mobility Particle Sizer (SMPS TSI, DMA 3080, and CPC 3788).

The offline mode consists of trapping samples on Carbotrap 202 cartridges and 2,4-DiNitro Phenyl Hydrazine (DNPH) cartridges and then analyzing them with Gas Chromatography-Mass Spectrometry (GC-MS) and High-performance Liquid Chromatography (HPLC), respectively. A schematic diagram and photo of D-ASC are shown in Figure II.1.

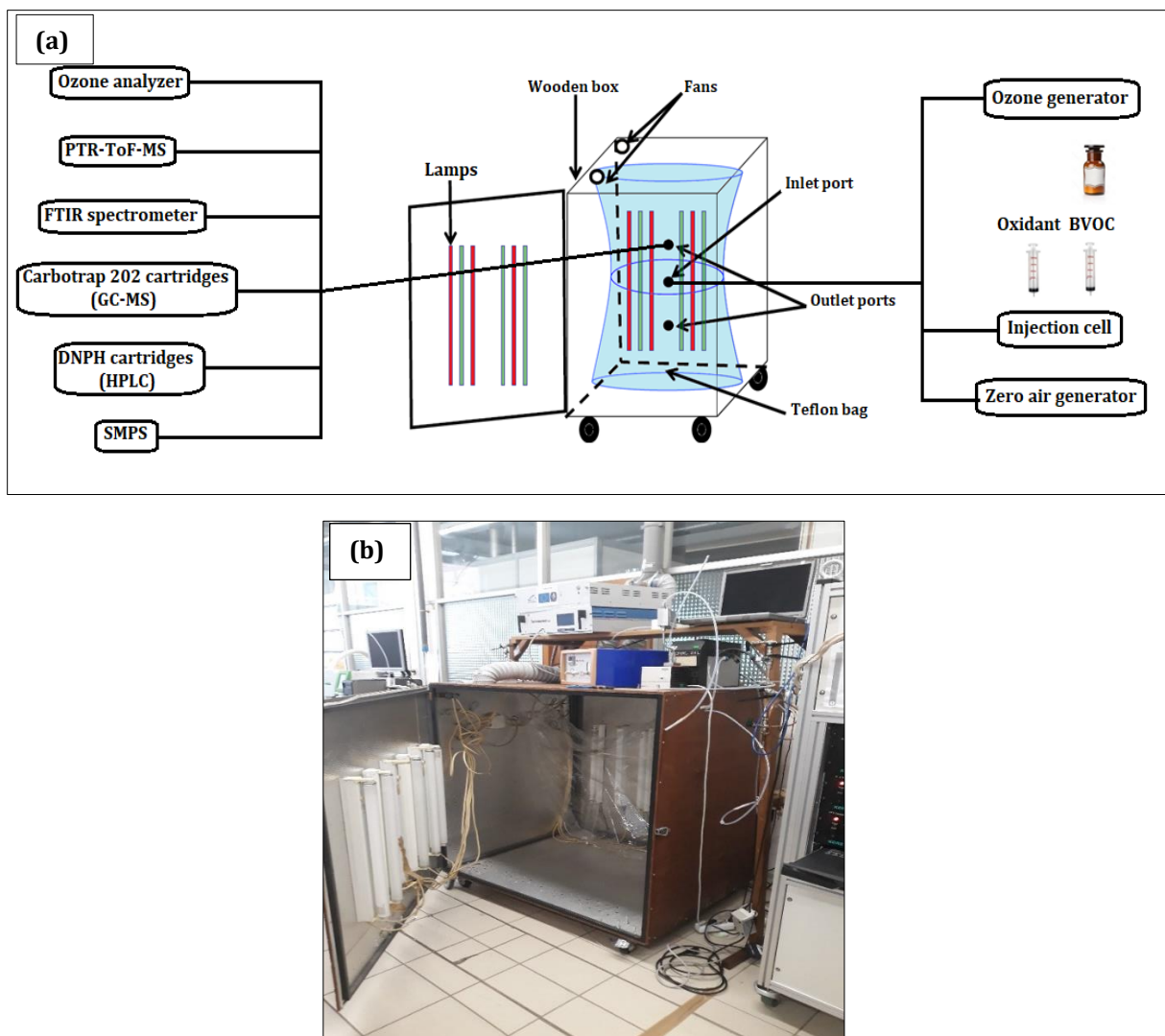


Figure II.1: (a) Schematic diagram and (b) photo of D-ASC.

▪ Calculation of the BVOC concentration

The BVOC concentration in the chamber $[BVOC]_{D-ASC}$ is calculated using the following expression (Eq.1).

$$[\text{BVOC}]_{\text{D-ASC}} = \left(\frac{\rho v}{MV} \right) \times \left(\frac{1}{10^3} \right) \times N_A \text{ (molecule cm}^{-3}\text{)} \quad (\text{Eq.1})$$

where ρ is the density of the BVOC (g cm^{-3}), v is the injected volume of BVOC (μL), M is the molar mass of BVOC (g mol^{-1}), V is the total volume in the D-ASC (cm^3), N_A is Avogadro number ($N_A = 6.02 \times 10^{23} \text{ molecules mol}^{-1}$), the factor $1/10^3$ is related to the conversion of μL to cm^{-3} .

II.2.1.2.2 THALAMOS-ASC – IMT Lille Douai

THALAMOS-ASC (THERmALLY regulated AtMOSpheric Simulation Chamber) is a 600-L cubic Teflon photoreactor. Details of the experimental set-up can be found elsewhere (Osseiran et al., 2020), and only a brief description is given hereafter. The Teflon bag of the chamber is fixed inside a temperature-controlled box which can be regulated between 253 and 333 K. The chamber is surrounded by a set of 20 ultraviolet (UV) lamps which are: (i) 10 UV-A lamps (Philips PL-L 24W/10/4P) with a maximum (λ_{max}) at 365 nm and (ii) 10 mercury lamps (OSRAM HNS-L 24W 2G11) emitting in the UV-C region with a maximum (λ_{max}) at 254 nm.

In the present work, THALAMOS-ASC was used to determine the rate constants of the reaction between a series of C_5 - C_8 unsaturated alcohols and chlorine atoms (see chapter V). The experimental procedure started by cleaning the THALAMOS-ASC by flushing it under heating at 323 K for at least 2 hours using a constant flow of zero air, i.e., 20 L min^{-1} and a similar pumped-out rate. The Teflon bag is equipped with inlet and outlet ports used for reactant injections and reaction mixture sampling. Two fans are mounted inside the reactor to ensure the homogeneity of the gas mixture.

The chamber is connected to a Voice200® SIFT-MS (Selected-Ion Flow-Tube Mass Spectrometry, Syft Technologies) instrument, which samples 10 mL min^{-1} and then allows decay of the reactants to be recorded. The SIFT-MS used in this study is based on the device firstly developed by Adams et al., 1976. Additional descriptions can be found in other papers (Španěl et al., 1998, Diskin et al., 2002, Wang et al., 2003, Smith et al., 2019). Its detection limit is of the order of 1 pptv with a time resolution of one second.

To the best of our knowledge, THALAMOS is among a few smog chambers nationally and internationally that can be operated in such a wide temperature range providing the scientific community with a versatile tool to simulate physicochemical processes. A schematic diagram and a photo of THALAMOS-ASC are shown in Figure II.2.

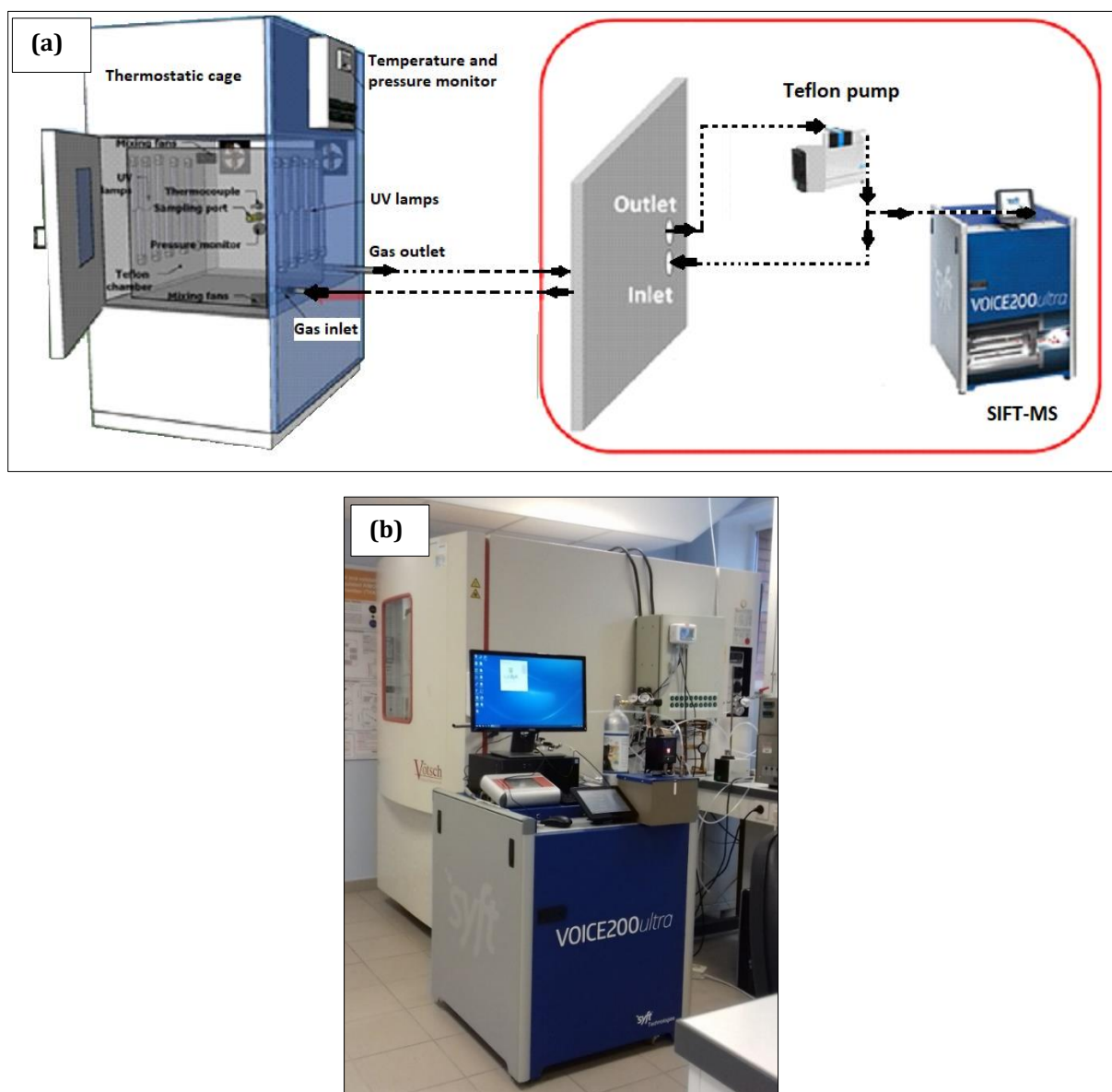


Figure II.2: (a) Schematic diagram and (b) photo of THALAMOS-ASC.

II.2.1.2.3 QUAREC-ASC – Wuppertal University

QUAREC-ASC (QUArtz glass REaction Chamber) consists of two jointed quartz glass cylinders with 0.47 m of inner diameter and 6.2 m of total length representing a volume

of about 1 m³. A detailed description of the reactor was given in Barnes et al., 1993. The reactants' injecting and sampling were carried out through inlet and outlet ports placed on the opposite metal flanges. A turbo-molecular pump backed by a double-stage rotary fore pump was used to empty the reactor.

In this work, QUAREC-ASC was used to identify and quantify products and SOA formations through the reaction between unsaturated aldehydes and two oxidants, namely, ozone and hydroxyl radicals (see chapter IV and VI).

Once the reactants are inside the chamber, three fans can ensure their rapid homogenization and are placed at different chamber positions. The concentrations of reactants and products were obtained by in situ IR absorption spectroscopy using an FTIR spectrometer (Thermo Nicolet Nexus with MCT detector). Particle measurements were made using a Differential Mobility Analyzer (DMA, model 3071A) and a Condensation Particle Counter (CPC, model 3025A). A photo of QUAREC-ASC is shown in Figure II.3.



Figure II.3: Photo of QUAREC-ASC.

II.2.1.2.4 3m-ASC – Wuppertal University

The 3m-ASC is a glass chamber characterized by 480-L of volume and 45 cm of inner diameter. This reactor was detailed previously (Barnes et al., 1993, Gibilisco et al., 2015), and only a brief description is presented here. The chamber is a cylindrical vessel made with borosilicate glass and closed with two aluminum flanges. These flanges contain connection tubes that ensure the injection of both reagent and bath gases.

A pumping system made of a roots pump backed by a double-stage rotary pump was used to evacuate this vessel. The cleaning of this chamber needs several emptying and filling cycles with air. The 3m-ASC was used to investigate the formed products through the oxidation reaction between an unsaturated aldehyde (Trans-2-Pentenal) and ozone.

Liquid reactants are injected directly by a liquid syringe in a flow of synthetic air. The only gas reactant used in this chamber was ozone. A homemade device-generated the latter by corona discharge in a flow of oxygen. A Teflon fan is mounted inside the reactor to ensure the homogeneity of the reaction mixture. The concentrations of reactants and products were obtained by IR absorption spectra using an FTIR spectrometer (Thermo Nicolet 6700 with MCT detector). A photo of 3m-ASC is shown in Figure II.4.



Figure II.4: Photo of 3m-ASC.

II.2.1.2.5 16L-ASC – UCLM University

The 16L-ASC is a Pyrex tube available at UCLM. The inner diameter and the height of the 16L-ASC are 15 cm and 90 cm, respectively. This experimental set-up was described in detail elsewhere (Ballesteros et al., 2009). It consists of a 16L White-type cell equipped with three mirrors (two are placed at the head of and one is fixed at the base of the cell) coated with a silver layer and a reflectance of 99% IR range. Two KBr windows ensure the entrance and exit of the IR beam at the region $650 - 4000 \text{ cm}^{-1}$ in the cell with 2.5 cm of diameter. Once this system is optimized, it offers an optical path length of 96 m. A Nexus 870 Thermo Nicolet FTIR spectrometer is installed below the cell.

Four actinic lamps surround 16L-ASC (Philips Actinic BL TL 40W/10 1SL/25, emitting in the range $340 - 400 \text{ nm}$, $\lambda_{\text{max}} = 365 \text{ nm}$). The whole system is covered with a black cloth to avoid reagent photolysis due to the leaked light. Two fans are mounted at the top of the cell to avoid the cell's heating when lamps are on. A schematic diagram and a photo of 16L-ASC are displayed in Figure II.5.

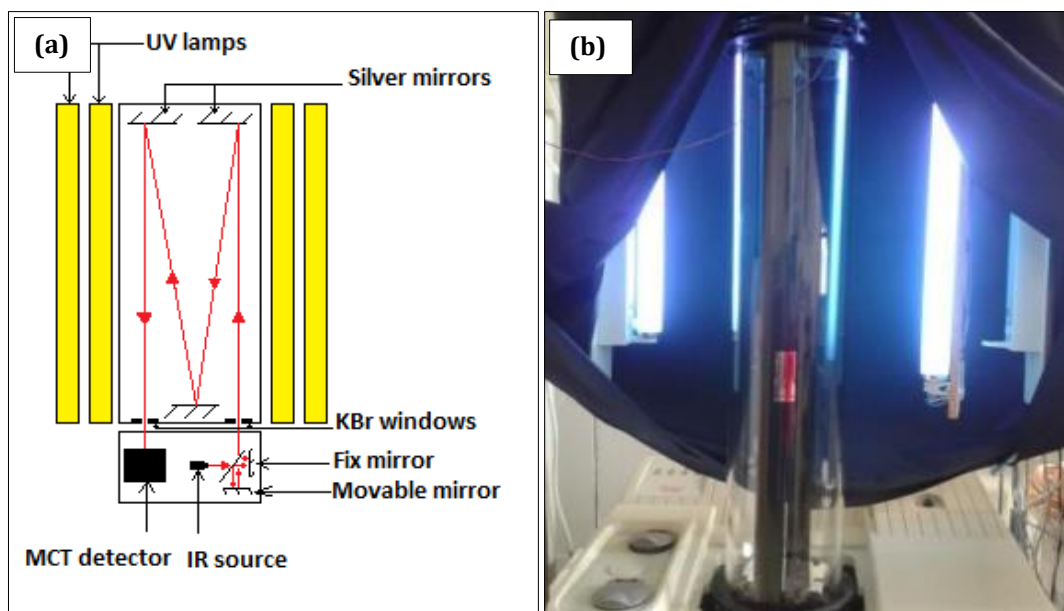


Figure II.5: (a) Schematic diagram of 16L-ASC coupled to FTIR and (b) photo of 16L-ASC.

This set-up was used in this work to investigate the kinetics and mechanism of the reaction between unsaturated aldehydes and chlorine atoms (chapter V). The experimental procedure starts by pumping it down to 10^{-2} mbar several times and flushing it with synthetic air several times. The introduction of reactants in the 16L-ASC is done via a Pyrex manifold system. The inlet (1) and (2) allows the introduction of synthetic air and gaseous reactant (Cl_2), respectively. The inlets (3) and (4) allow the introduction of liquid reagents (unsaturated aldehydes and reference compounds) using a Pyrex tube or Pyrex balloon flask, respectively. The two ports (5) and (6) are connected to MKS pressure gauges (7) of 100 Torr and 1000 Torr, which allow the measurement of the pressure and displayed the value via a pressure monitor (8). The compounds are introduced into the CR-ASC (see the next section) (9) or into the 16L-ASC (10). The outlet (11) ensures the vacuum of the injection line and the 16L-ASC using a trap (12) connected to a vacuum pump (flow rate of $20 \text{ m}^3 \text{ h}^{-1}$) (Figure II.6).



Figure II.6: Photo of the injection system of reactants used at UCLM.

The procedure starts by putting a sufficient quantity of liquid in the tube or the balloon containers for liquid reactants. Then, I make a cooling cycle using liquid nitrogen and pumping the air in equilibrium with the reactant to purify the compound and avoid any other impurities in the air. Finally, I inject the compound's vapor pressure that I need in the horizontal tube to measure the pressure. Once the reactant's pressure is stable, the reactant is sent to the chamber by a synthetic airflow via the manifold system.

II.2.1.2.6 CR-ASC – UCLM University

The CR (Ciudad Real)-ASC is a static reactor developed at the UCLM. This chamber is presented in detail elsewhere (Ballesteros et al., 2009). It consists of a 264-L Pyrex cylindrical reactor with four quartz windows placed inside a box. The chamber is surrounded by a set of 8 actinic lamps (Philips Actinic BL TL 40W/10 1SL/25, emitting in the range 340 – 400 nm, $\lambda_{\text{max}} = 365$ nm). Two fans are mounted inside the box covering the CR-ASC to cool the chamber's air when the lights are on. This set-up was used in this work to investigate the reaction between unsaturated aldehydes and chlorine atoms in terms of product identification and SOA formation.

The CR-ASC is coupled to a Nexus Thermo Nicolet FTIR spectrometer (the same as 16L-ASC) and GC-MS apparatus to measure both reactants and products. Also, particle formations were measured using an FMPS (Fast Mobility Particle Sizer Spectrometer) system. All characteristics of these instruments are detailed in section II.3. Besides, this chamber is connected to a Proton Transfer - Time of Flight – Mass Spectrometer (PTR-ToF-MS 4000 IONICON), which was used to identify the product formed through the reaction of Trans-2-Heptenal with chlorine atoms. The cleaning of CR-ASC is done by several emptying and filling with air. Reactants are introduced to the chamber via the same glass manifold as described in the section above. A photo of CR-ASC is shown in Figure II.7.



Figure II.7: Photo of CR-ASC.

These two ASCs of UCLM University (16L-ASC and CR-ASC) can be used separately or connected in a closed configuration, as showed in Figure II.8.

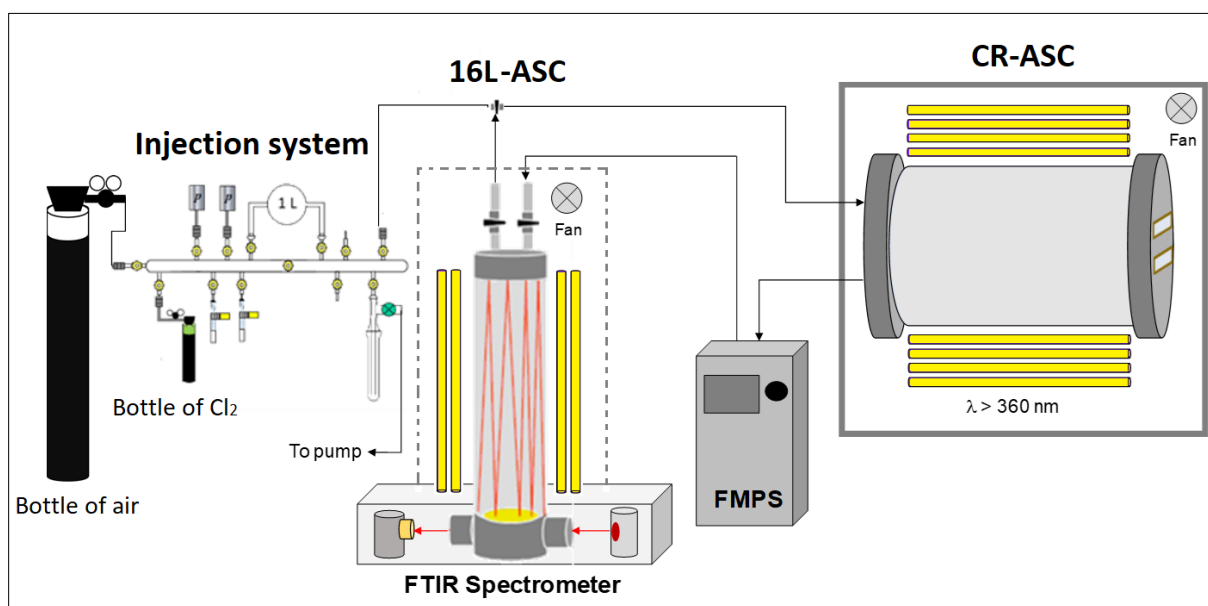


Figure II.8: Schematic diagram of 16L-ASC and CR-ASC coupled to FTIR and the injection system.

II.2.1.3 Comparison of the used ASCs

Table II.1 displays a summary of all the used ASCs. Each one of these chambers has advantages and limitations regarding other ASCs as function of its configuration, including several characteristics such as material, shape, surface/volume ratio, irradiation source, and operating temperature and pressure ranges.

Table II.1: Summary of all ASCs used in this work.

Reference	Name	Localization	Material	Shape	Volume	Irradiation	Temperature/ Pressure
This work & Turpin 2004	D-ASC	Douai, France	Teflon	Bag	300-L	UV lights between 254 and 365 nm	T = 296 k P = 760 Torr
This work & Osseiran et al. 2020	THALAMOS-ASC	Douai, France	Teflon	Cube	600-L	UV lights between 254 and 365 nm	T = 253 - 333 K P = 760 Torr
This work & Olariu et al. 2013	QUAREC-ASC	Wuppertal, Germany	Quartz	Cylinder	1080-L	UV lights between 254 and 365 nm	T = 283-313 K P = 1-760 Torr
This work & Antiñolo et al. 2019	16L-ASC	Ciudad Real, Spain	Pyrex	Cylinder	16-L	UV lights between 340 and 400 nm	T = 296 k P = 760 Torr
This work & Antiñolo et al. 2019	CR-ASC	Ciudad Real, Spain	Pyrex	Cylinder	264-L	UV lights between 340 and 400 nm	T = 296 k P = 760 Torr

D-ASC was used to measure the rate constants of the oxidation reactions between C₅-C₆ unsaturated aldehydes and C₅-C₈ unsaturated alcohols with ozone. However, complementary experiments were done in QUAREC-ASC to identify and quantify the C₅-C₆ unsaturated aldehydes + O₃ reaction products. I want to mention that the product study was done in QUAREC-ASC. This chamber is equipped with an in-situ FTIR spectrometer with an optical path length of 484.7 m and allowed more sensitivity to identify products. On the other hand, the kinetic study of the oxidation reaction between C₅-C₈ unsaturated alcohols and Cl atoms was done in THALAMOS-ASC. This chamber is connected to the SIFT-MS, which allows the detection of both reactants (alcohols and reference compounds) fragments.

The study of the reaction between C₅-C₇ unsaturated aldehydes + Cl atoms was done in the UCLM laboratory where a 16L-ASC was used to measure rate constants CR-ASC was used to identify and quantify the formed products.

II.2.2 Flow techniques

II.2.2.1 General description

Contrary to static techniques, flow techniques work with a continuous flow of reactants in a controlled condition such as temperature, pressure, humidity, flow rates, and regime. In atmospheric chemistry, these reactors study the chemical kinetics of fast reactions since they offer a rapid mixing of components. The flow technique also allows the study of the first steps of SOA formations in terms of nucleation threshold and SOA yield. The conception of these techniques, as described for ASC, needs a deep reflection about the dimension of the set-up, its material, the used lights for photolysis reaction, and which analysis technique can be connected to analyze both reactants and products.

II.2.2.2 Flow techniques used in this work

II.2.2.2.1 LFR – IMT Lille Douai

The LFR (Laminar Flow Reactor) was developed at IMT Lille Douai to better understand the formation processes of SOAs, nucleation thresholds and yields following the reactive species' oxidation. This reactor has been well described in previous studies (Duncianu et al., 2012, Braure et al., 2015, Ahmad et al., 2017). It consists of a vertical Pyrex tube of 1 m length and 10 cm inner diameter working with a total real flow of about 1.5 to 5 L min⁻¹. The total volume is equal to the sum of the zero air and reactants flows. Its volume (and thus reaction time) can be adjusted by vertical sliding of the injection head from which the reaction time is minimal, about 30 seconds to 1 minute. The flow passes from the top to the bottom of the tube. The injection of reactants is ensured by two concentric tubes installed at the top of the main tube. Reactants will be mixed only at the sliding injection head.

This part of the reactor was designed to ensure a fast homogenization of the reactants following their injection. The laminar flow regime is established by a sintered glass wall welded to the injection head.

This set-up was used to determine the rate constant of ozonolysis reaction of unsaturated aldehydes (see chapter IV). Accurate concentrations of unsaturated aldehydes were prepared in canisters by vaporizing small aldehyde aliquots and filling them with air up to about 3 bars. A small flow (typically 10 mL min^{-1}) from the canister was then sent to the mixing chamber before reaching the reactor injection head. Gas chromatography, coupled to a thermal desorption system, was used in online mode to sample and analyze the organic reactants. A double detection by flame ionization (FID) and mass spectrometry (MS) was operated on the GC. The initial concentration of aldehyde was calculated from the FID signal using the calibration curve determined in preliminary works. Ozone was produced by flowing oxygen through an ozone generator (TEI 146) and was analyzed by a UV-absorption-based analyzer (Environnement SA 42 M). Figure II.9 displays a schematic diagram and a photo of LFR.

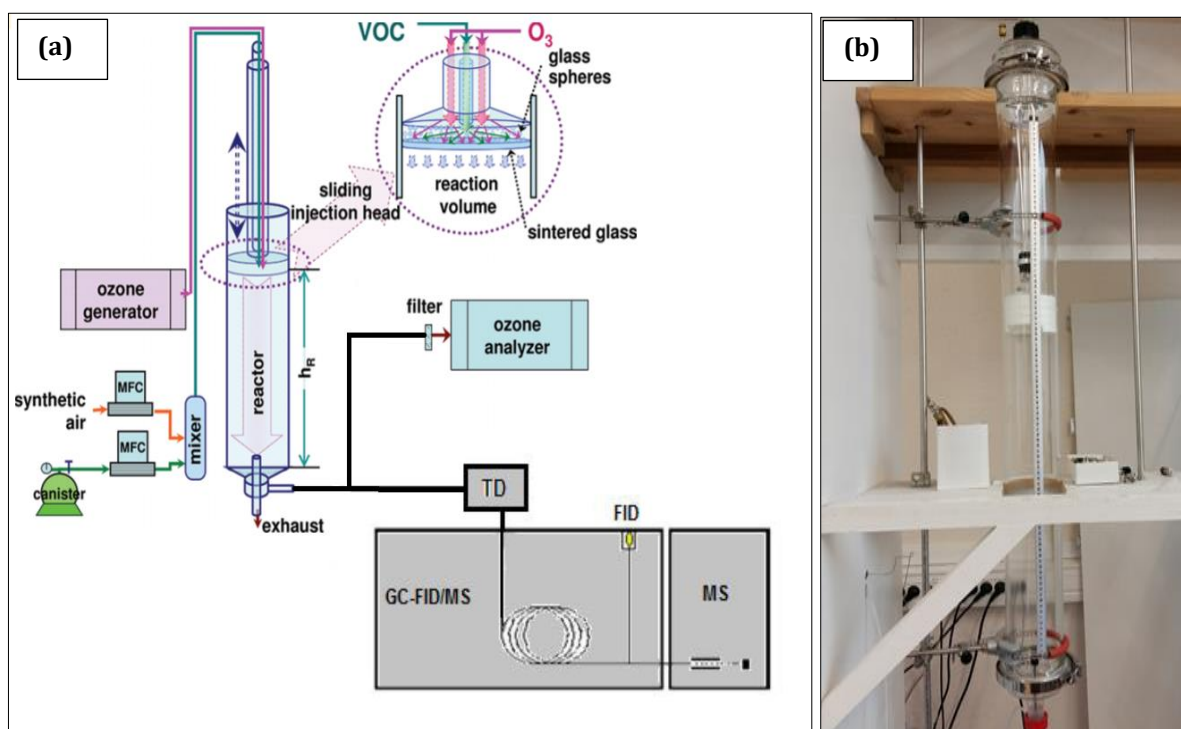


Figure II.9: (a) Schematic diagram and (b) photo of LFR.

▪ Calculation of the BVOC concentration in the canister

For LFR experiments, a 6 L stainless steel canister (SilcoCan, Restek) was used to prepare a stable source of BVOC. The canister's preparation proceeded as follows: the canister was first cleaned by a cycle of filling-emptying using zero air and a pumping system enabling 10^{-2} mbar to be reached. A heater ribbon (333 – 353 K) was attached around the canister to facilitate the remaining reactants' desorption. Then, the canister will be filled with zero air, and the GC-MS device took three samples to ensure the cleanliness of this container. Once the canister was clean, a known volume of the studied BVOC was injected in the canister at low pressure using a microsyringe through a septum fixed at the canister's head. The canister was further filled with purified air at a few bars' pressure (2 – 3 bar). The canister was left to stabilize for at least 30 min and then connected to the LFR. A flow of around 0.1 L min^{-1} was taken and diluted in a total flow of 1.5 to 5 L min^{-1} . This set-up enabled a stable BVOC concentration from a few ppbv to a few ppmv to be obtained in the LFR. The concentration of the BVOC in the canister $[\text{BVOC}]_{\text{canister}}$ (mol L^{-1}) is calculated as follows.

$$[\text{BVOC}]_{\text{canister}} = \frac{\rho v}{MV} (\text{mol L}^{-1}) \quad (\text{Eq.2})$$

where ρ is the density of the BVOC ($\text{g } \mu\text{L}^{-1}$), M is the molar mass of the compound (g mol^{-1}), v is the volume of the injected BVOC in the canister (μL), and V is the total volume of air in the canister (L).

▪ Calculation of the BVOC concentration in LFR

To calculate the concentration of BVOC in the LFR $[\text{BVOC}]_{\text{LFR}}$ (mol L^{-1}), the dilution factor between the flow injected via the canister (q_{BVOC}) and the total flow added to the reactor (q_{tot}) has to be considered (Eq.3).

$$[\text{BVOC}]_{\text{LFR}} = [\text{BVOC}]_{\text{canister}} \times \left(\frac{q_{\text{BVOC}}}{q_{\text{tot}}} \right) (\text{mol L}^{-1}) \quad (\text{Eq.3})$$

To calculate the concentration of the BVOC in the LFR $[\text{BVOC}]_{\text{LFR}}$ in molecule cm^{-3} , we have to multiply the concentration of the aldehyde in (mol L^{-1}) (Eq.3) by the Avogadro constant

($N_A = 6.02 \times 10^{23}$ molecules mol⁻¹) (Eq.4). The factor ($1/10^3$) is related to the conversion from L to cm³.

$$[\text{BVOC}]_{\text{LFR}} = [\text{BVOC}]_{\text{LFR}} \times \left(\frac{1}{10^3} \right) \times N_A \text{ (molecule cm}^{-3}\text{)} \quad (\text{Eq.4})$$

▪ Calculation of the reaction time

To calculate the rate constant, we plotted the $\ln([O_3]_0/[O_3])$ versus the real residence time ($t_{\text{real},i}$) (see section II.4.1.2.1). The flow regime is not entirely a piston; therefore, a correction on the real residence time ($t_{\text{real},i}$) has to be made using a calculated residence time ($t_{\text{calc},i}$).

$$t_{\text{real},i} = \frac{t_{\text{calc},i}}{b_i} \quad (\text{Eq.5})$$

$$t_{\text{calc},i} = \frac{H_i \times S}{Q_{\text{tot}}} \quad (\text{Eq.6})$$

$$b_i = 0.97 + 0.18 \times \exp \left[-\frac{(a_i - 0.38)}{0.21} \right] \quad (\text{Eq.7})$$

$$a_i = \frac{\text{Re}}{H_i} \quad (\text{Eq.8})$$

where H_i are the different position of the reactor ($H_1 = 10$ cm, $H_2 = 30$ cm, $H_3 = 50$ cm, $H_4 = 70$ cm, $H_5 = 90$ cm). Re is Reynolds number ($\text{Re} = (\rho \times d_{\text{int}} \times V)/\mu$) with ρ is the density of the fluid, μ is the dynamic viscosity of the fluid, d_{in} is the internal diameter of the LFR (m), and V is the velocity of the fluid (m s⁻¹). Q_{tot} is the total flow rate, and S is the section area of the LFR ($S = \pi \times (d_{\text{int}}/2)^2$).

II.2.2.2.2 Cryocell – IPR

The Cryocell was built in the Molecular Physics Department of IPR (Institut de Physique de Rennes) at the University of Rennes. The apparatus's description can be found elsewhere; (El Dib et al., 2013, Priya et al., 2015, Sleiman et al., 2016); hence, I only highlight the main points here. The Cryocell is a stainless-steel tube with an internal volume of about 320 cm³ (65 cm length and 2.5 cm inner diameter).

The cell is jacketed with a copper tube, heated with water up to 473 K, and cooled with ethanol down to 183 K. These fluids circulate through the copper tube employing a thermocryostat type Lauda RP 890 (C), which regulates the fluid temperature. Two thermocouples are installed at the gas inlet and slightly upstream of the detection zone, allowing temperature control inside the cell. The pressure of the reaction mixture ranges typically from 5 to 745 Torr. It is adjusted through a diaphragm valve (OerlikonTrivac) and measured with various pressure MKS gauges (10 mbar, 100 mbar, 1000 Torr and 2000 Torr). A schematic diagram and a photo of the Cryocell system are displayed in Figure II.10.

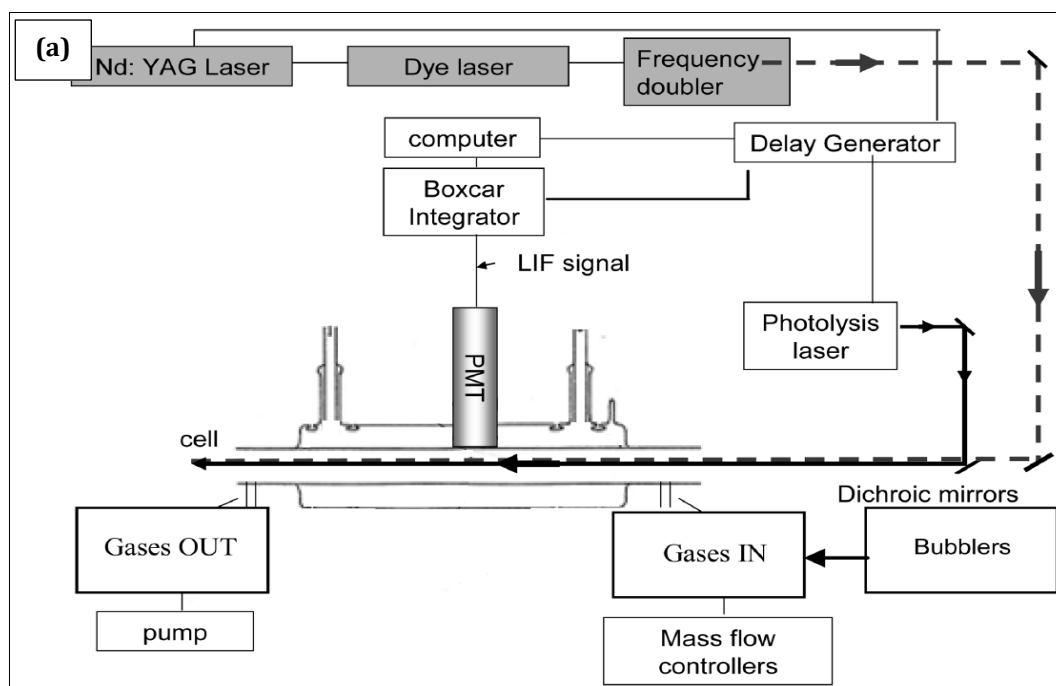


Figure II.10: (a) Schematic diagram and (b) photo of Cryocell and PLP-LIF system (El Dib et al., 2013).

This set-up was used in this work to investigate the kinetics of reactions between unsaturated aldehydes with hydroxyl radicals (OH) (see chapter VI). Hydroxyl radicals are generated from the photolysis of H_2O_2 at 266 nm using the Pulsed-Laser Photolysis (PLP) and measured in-situ using the Laser-Induced Fluorescence (LIF). The PLP-LIF technique will be detailed in section II.3.1.2. The introduction of reactant in the Cryocell is ensured by a system composed of different flowmeters (MKS) ranging from 10 to 10000 mL min^{-1} .

In this thesis, all used reactants are liquid; therefore, the passage of all components through a bubbling system is an essential step to generate their vapor. In the bubbling system, the carrier gas flow is introduced into a Pyrex tube containing the liquid. The pressures of the vapors are controlled by pressure gauges (626B-MKS 10 to 100 Torr). A schematic diagram of the bubbler system is presented in Figure II.11.

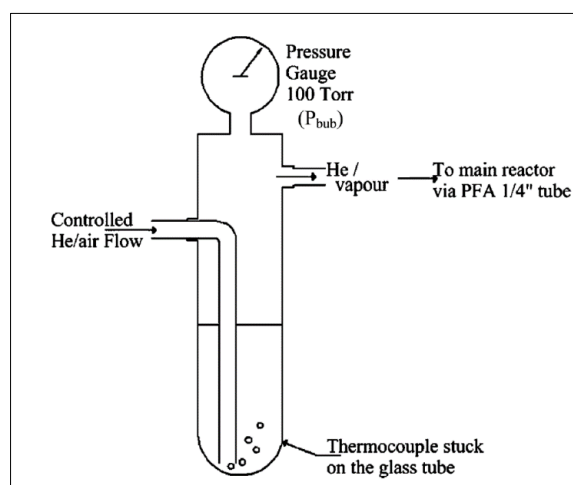


Figure II.11: Schematic diagram of the bubbler system (El Dib et al., 2013).

▪ Calculation of the BVOC concentration in the cell

The concentration of the injected reactant “BVOC” in the cell at the temperature and the cell's pressure is calculated using Eq.9.

$$[\text{BVOC}] = \frac{n_{\text{tot}}}{Q_{\text{tot}}} \times Q_{\text{BVOC}} \quad (\text{Eq.9})$$

Q_{BVOC} is the flow of the pure compound “BVOC,” Q_{tot} is the total flow in the cell, and n_{tot} is the cell's total concentration.

All these parameters have to be calculated at the temperature and the pressure of the Cryocell. Q_{BVOC} can be expressed as function of the carrier gas parameters (Eq.10).

$$\frac{Q_{\text{BVOC}}}{P_{\text{BVOC}}^v} = \frac{Q_{\text{car}}}{P_{\text{car}}^v} \quad (\text{Eq.10})$$

where P_{BVOC}^v is the vapor pressure of the BVOC at the temperature of the bubbler, P_{car}^v and Q_{car} are the pressure and flow of the carrier gas passing through the bubbler at its temperature, respectively. Then, the concentration [BVOC] can be expressed as follows.

$$[\text{BVOC}] = \frac{n_{\text{tot}}}{Q_{\text{tot}}} \times \frac{Q_{\text{car}}}{P_{\text{car}}^v} \times P_{\text{BVOC}}^v = \frac{n_{\text{tot}}}{Q_{\text{tot}}} \times \frac{Q_{\text{car}}}{(P_{\text{Bub}} - P_{\text{BVOC}}^v)} \times P_{\text{BVOC}}^v \quad (\text{Eq.11})$$

where P_{Bub} is the pressure of the bubbler.

II.2.2.3 Comparison with other flow techniques

In the literature, we found several flow techniques used either to study the kinetics of fast reactions between VOCs and atmospheric oxidants or to investigate the formation, the evolution of and the aging of SOAs (Bonn et al., 2002, Lee and Kamens, 2005, Ezell et al., 2010, Bernard et al., 2012, Bilde and Pandis, 2001, Morris et al., 2002, Czoschke et al., 2003, Hearn and Smith, 2004). Table II.2 displays numerous flow reactors used to study oxidation reactions and highlights their differences with LFR and Cryocell.

Table II.2: Flow techniques used in atmospheric chemistry studies (adapted from Duncianu et al., 2012).

Reference	Localization	Material	Length/Diameter (cm)	Total flow (L min ⁻¹)	Analysis instruments	Source of VOC or particles
This work	Douai, France	Pyrex	100/10	1 – 5	TD-GC-FID/MS, O ₃ analyzer	Canister
This work	IPR, France	Stainless steel	65/2.5	10	PLP-LIF	Bubbler
Bernard et al., 2012	Orléans, France	Pyrex	110/1.2	4.6	O ₃ analyzer, NO _x analyzer, CPC	Flask
Ezell et al., 2010	California, USA	Stainless steel	610/45.7	16 – 20	O ₃ analyzer, NO _x analyzer, GC-MS, FTIR, SMPS, nephelometer	No data
Lee and Kamens, 2005	N. Carolina, USA	Glass	100/2.5	5	GC-MS, SMPS	Diffusion into an air flow
Morris et al., 2002	Massachusetts, USA	Glass	60/1.1 - 2.2	1	SMPS, AMS	Nebulizer
Bilde and Pandis, 2001	Pennsylvania, USA	Stainless steel	400/2.2	1.8 – 8.9	TDMA	Nebulizer
Jang et al., 2003	N. Carolina, USA	Glass	200/2.5	3.5 – 4.5	FTIR, SMPS	Bubbler

The previous table shows that the biggest flow reactor is the one of Ezell et al., 2010; therefore, it represents the same advantage and limits as smog chambers. This set-up's total reaction time is longer than other flow reactors, allowing investigation of slow kinetics. Its geometry also allows minimizing side reaction's effect since its surface/volume ratio is lower than all other flow reactors.

The conception of Bernard et al., 2012 reactor was too similar to the LFR reactor and was validated by the ozonolysis of α -pinene. This reaction model was also used to validate other flow reactors (Bonn et al., 2002, Lee and Kamens, 2005). However, the group of Orleans validates their reactor in the absence of OH scavenger and pre-existing particles. On the other hand, other groups used flow reactors to characterize heterogeneous processes between oxidants and pre-existing particles (Morris et al., 2002, Jang et al., 2003, Hearn and Smith, 2004).

II.2.3 Advantages and challenges: static techniques versus flow techniques

Both static and flow techniques, along with field campaigns, provide data to atmospheric models to better understand atmospheric chemistry (Seakins, 2010). Large ASCs (volume $\geq 1 \text{ m}^3$) allow carrying out experiments with low concentrations (few ppb) and slow kinetics with long reaction time (few hours). These set-ups can minimize wall effects. Furthermore, large ASCs furnish an internal space to install in-situ analytical techniques such as long pathways UV, VIS, or IR spectroscopy and Laser-Induced Fluorescence (LIF). Whereas the use of ASC presents three main limitations because of their large volume: (i) they occupy large surfaces in laboratories, (ii) they have expensive running costs, and (iii) they require long times to be cleaned.

Moreover, chamber walls can present a reservoir of radicals and a source of uncertainty in chemical studies into closed systems. For instance, the adsorption of NO_2 and water vapor on the wall surface forms nitrous acid (HNO_2) (R.1), which can photolyze into two radicals, OH and NO (R.2). This reaction presents an additional path for OH radicals' formation in ASC (Finlayson-Pitts and Pitts Jr, 1999).



It is hard to evaluate the chamber walls' impact on the reaction because it depends on the experimental conditions and the chamber's characteristics (Dodge, 2000). The cleaning process of ASC must be followed by an evaluation of the background level of remaining impurities. The evaluation of unavoidable artifacts could minimize their impact on the understanding of the reaction mechanism. Contrary to static techniques, flow techniques usually have smaller dimensions that allow for fast kinetics with a short reaction time (a few minutes). Their small volume and continuous flow make them able to be rapidly homogenized compared to static techniques.

Furthermore, reaction parameters such as temperature, pressure, concentrations, humidity can be rapidly changed and stabilized. Finally, flow reactors can be easily cleaned as compared to ASCs. The use of artificial lights represents a limitation for both static and flow techniques. Artificial sources of lights in indoor ASCs and flow reactors can generate a different spectrum than the solar and then influence the photodissociation of compounds differently.

II.3 An overview of analytical techniques in atmospheric chemistry

II.3.1 Gas-phase analysis techniques

II.3.1.1 Spectroscopic techniques

The majority of analysis techniques are based on spectroscopic methods, which consist of light-molecule interaction. Spectroscopic methods can be distinguished as function of the used spectral regions. Infrared (IR) and ultraviolet-visible (UV-Vis) regions are the most used regions in the electromagnetic spectrum, especially after the invention of the laser technique by Theodore Maiman in 1960 at the Hughes Research Laboratory in California (Maiman, 1960).

II.3.1.1.1 Absorption spectroscopy

Absorption spectroscopy is the most used analysis spectroscopic technique for gas-phase analysis in atmospheric chemistry. This method consists of measuring light after its passage through a sample as a frequency or wavelength function. Quantitative measurements are based on the Lambert-Beer law (Eq.12).

$$A_{\lambda} = \ln\left(\frac{I_0}{I}\right) = \sigma_{\lambda} \times [\text{BVOC}] \times \ell \quad (\text{Eq.12})$$

where A_{λ} is the logarithmic absorbance (no units). I_0 and I are the intensity of incident light and light after passage through the gas cell, respectively. σ_{λ} is the spectral absorption cross-section at the wavelength λ ($\text{cm}^2 \text{ molecule}^{-1}$), $[\text{BVOC}]$ is the concentration of the analyzed molecule (molecule cm^{-3}), and ℓ is the length of the cell (cm). This method allows determining the absorption cross-section at the given absorbed wavelength (λ) provided that the molecule concentration $[\text{BVOC}]$ is entirely known. Conversely, the method allows obtaining the molecule concentration $[\text{BVOC}]$ provided that the absorption cross-section is known (σ_{λ}). We will focus only on UV and IR absorption spectroscopies and their applications in the next two sections.

II.3.1.1.1.1 UV absorption spectroscopy

a) UV absorption cross-sections measurements

UV spectroscopy is based on the absorption of a part of the ultraviolet spectral region. In this region of the electromagnetic spectrum, atoms and molecules undergo electronic transitions of at least one electron from the ground state to an excited state. As part of the collaboration with UCLM, I used a set-up dedicated to measuring the UV spectra of C₅-C₇ unsaturated aldehydes at 298 K in the wavelength range of 270 – 410 nm. Technical details of this set-up are presented in the next section.

▪ Set-up used in this work

The set-up is composed of a jacketed Pyrex cell where a measured vapor pressure of aldehyde is injected and irradiated by a 30-W deuterium lamp (Oriel 63165). This lamp provides a continuous spectrum in the wavelength range of 185 – 400 nm.

The transmitted light was focused onto the entrance slit of the 0.5-m spectrograph (Chromex 500 IS/MS) via a fiber optic cable. The radiation was then dispersed by a 300 grooves/mm grating centered at 330 nm with a spectral resolution of 0.18 nm and detected by a Charge-Coupled Device (CCD) detector (Andor DB401-UV, 1024×256 pixel²). The CCD detector was cooled down to 253 K using a Peltier cooling system to reduce the dark current during the measurement. A Hg/Ar pen-ray lamp allowed wavelength calibration in the detected spectral window. UV absorption cross-sections (σ_λ) were determined using the Beer-Lambert law (Eq.12), seeing that the aldehyde concentration was calculated from the compound's injected vapor pressure in the cell the absorbance A_λ (in base e) was measured. The cell's optical path length ($\pm 2\sigma$) is ($\ell = 107.0 \pm 0.2$ cm). Figure II.12 shows a schematic diagram and a photo of the experimental system employed to measure the UV absorption cross-sections of aldehydes.

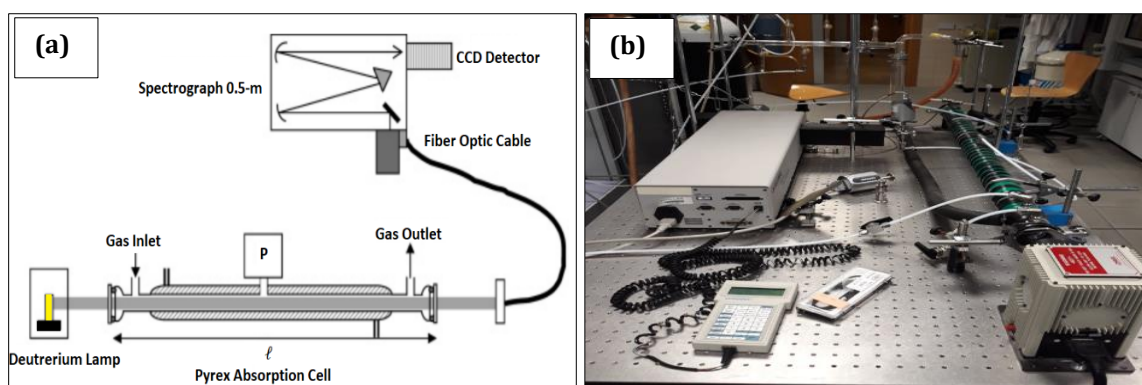


Figure II.12: (a) Schematic diagram (adapted from Jiménez et al., 2005 and (b) photo of the set-up employed for UV absorption cross-sections measurements.

b) Ozone analyzer

In the ozone analyzer, the sample is introduced into two identical measuring cells using a pumping system. These measuring cells are irradiated by UV radiation using a mercury vapor lamp, for which the emitted wavelength is 253.7 nm. In the measurement cell (A), the sample is pumped through an ozone-purifying filter (ozone scrubber), which filters ozone from the sample and the UV detector measures the incident intensity (I_0). Whereas in the measurement cell (B), the UV detector measures the intensity (I).

Ozone concentration is calculated automatically by the instrument, which refers to Beer-Lamber law (Eq.12). A schematic diagram of the ozone analyzer is displayed in Figure II.13.

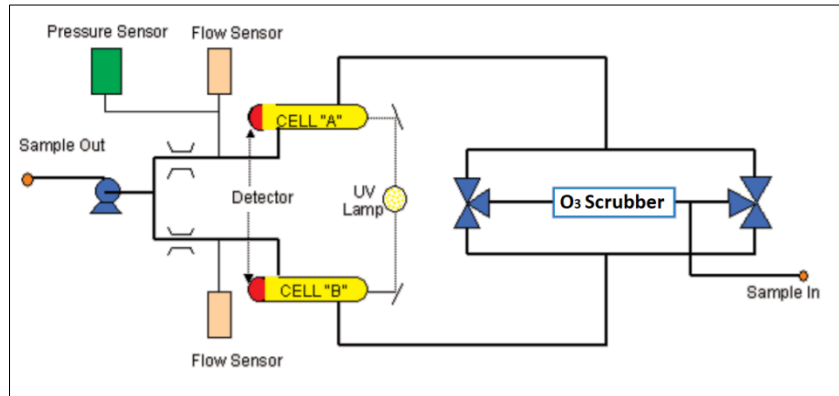


Figure II.13: Schematic diagram of ozone analyzer.

▪ O₃ analyzer used in this work

In IMT Lille Douai, ozone concentration measurements were done using two models of the ozone analyzer. The Environnement SA 42 model can measure high concentrations (up to 40 ppm). On the contrary, the TEI 49C model was used mainly to measure low concentrations (less than 2 ppm). Figure II.14 displayed a photo for each model.

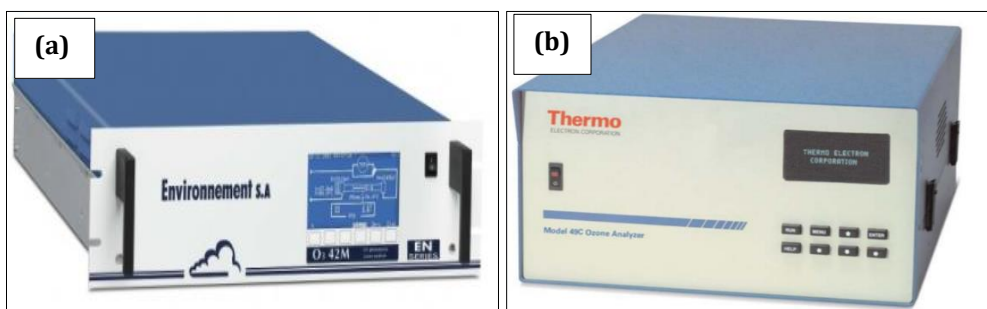


Figure II.14: Photo of ozone analyzer (a) Environnement SA 42 model and (b) TEI 49C model.

II.3.1.1.1.2 IR absorption spectroscopy

a) IR absorption cross-sections measurements

Fourier Transform-Infrared Spectroscopy (FTIR) represents one of the most used IR spectroscopy applications for organic compounds analysis. This instrument provides fast measurement for mixtures without any preliminary preparation. This instrument possesses an IR source that illuminates a Michelson interferometer. The latter produces interference fringes by splitting a beam of incident light so that one beam strikes a fixed mirror and the other a movable mirror. When the reflected beams are brought back together, an interference pattern results; these interferences are collected by a detector, which produces a signal called “interferogram”. The software calculations convert the interferogram to an infrared spectrum using Fourier transforms (Figure II.15).

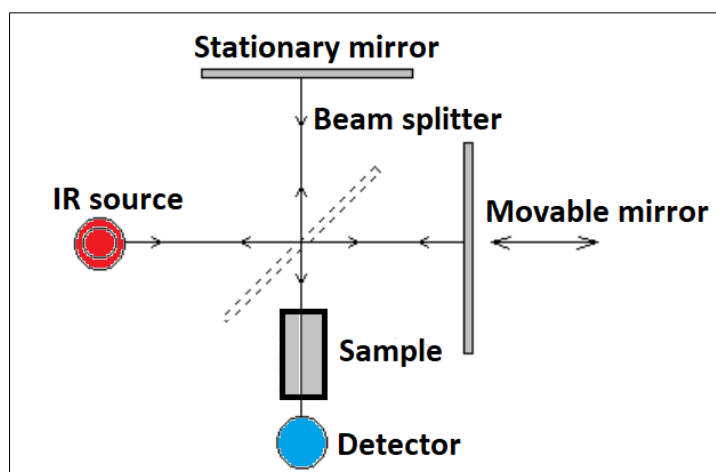


Figure II.15: Schematic diagram of Michelson interferometer.

- **FTIR spectrometers used in this work**

As mentioned before in section II.2.1, D-ASC, QUAREC-ASC, 3m-ASC, 16L-ASC, and CR-ASC are coupled to FTIR spectrometers to analyze both studied BVOCs and their oxidation products. In Table II.3, I summarize all the used FTIR spectrometers used in this work.

Table II.3: Summary of the FTIR spectrometers used in this work.

Laboratory	Reactor	Model	Detector	Pathlength / m	Range / cm^{-1}	Resolution / cm^{-1}	Number of scans	Time of analysis / min
IMT Lille Douai	D-ASC	Nicolet 6700 Thermo Fisher	DTGS (Deuterated Tri-Glycine Sulfate)	10	400 – 4000	2	100	4
Wuppertal University	QUAREC- ASC	Nicolet Nexus	MCT (mercury- cadmium tellurium detector)	484.7	700 – 4000	1	100	5
Wuppertal University	3m-ASC	Nicolet Magna 520	N ₂ -cooled MCT (mercury- cadmium tellurium detector)	48.11	700 – 4000	1	100	5
UCLM University	16L-ASC & CR-ASC	Thermo Nicolet Nexus 870	N ₂ -cooled MCT (mercury- cadmium tellurium detector)	96	650 – 4000	2	100	2

II.3.1.1.2 Laser-Induced Fluorescence

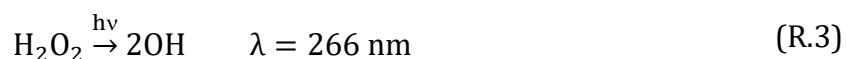
Laser-Induced Fluorescence (LIF) technique consists of exciting a molecule (A) by monochromatic light as a first step. Then, a fraction of the molecule (A) undergoes an electronic transition. It forms an excited state (A*) depending on the concentration of irradiated species (A), the photon cross-section, and the light intensity.

The excited species (A^*) then return to the ground state (A) either by fluorescence emission or non-radiative energy transfer during the collision with another molecule (M) (also called quenching).

LIF technique is generally used in combination with the Pulsed Laser Photolysis (PLP) technique, which provides both OH generation and detection. In this thesis, I used a PLP-LIF system placed in the IPR laboratory and coupled with Cryocell (see section II.2.2.2.2). This instrument was used during the measurement of the reaction kinetics between unsaturated aldehydes and OH radicals. The technical characteristics and the operating procedure of the PLP-LIF will be detailed in the paragraph below.

▪ PLP-LIF at IPR laboratory

The PLP-LIF technique was used in the present work coupled to the Cryocell-IPR to produce and detect OH radicals. OH radicals were produced by photolysis of H_2O_2 using an Nd: YAG laser (Neodymium-doped Yttrium Aluminium Garnet) model Spectra-Physics GCR 190 pulsed at 10 Hz with a quadrupled frequency at 266 nm and working at 10 ns of pulse duration (R.3).



The excitation beam comes from a frequency-doubled dye laser (Spectron SL 4000G) using the rhodamine 590 dissolved in methanol. This laser is pumped by the frequency-doubled output of an Nd: YAG laser (Spectron SL 803) working at a pulse duration of 10 ns. The dye laser is set to generate a 282 nm beam capable of exciting the OH radicals.

The light emitted by the excited OH radicals is collected perpendicular to the laser beams using two lenses and an interference filter ($\lambda = 310 \text{ nm}$) by a Photo-Multiplier (PM) model (Electron Tubes 9128QB), which converts these photons to an electrical signal. The scattered light from the probe laser's reflections and the photolysis laser on the cell walls represent this technique's main limitation. Therefore, all windows are placed at the Brewster angle. The fluorescence detection system is mounted at 90° regarding the two lasers' plane, and only non-directional light (such as fluorescence and scattering) comes in contact with the PM.

The interference filter makes it possible to select only the desired fluorescence light that avoids the PM's blinding. Figure II.16 displays a simplified diagram of this system.

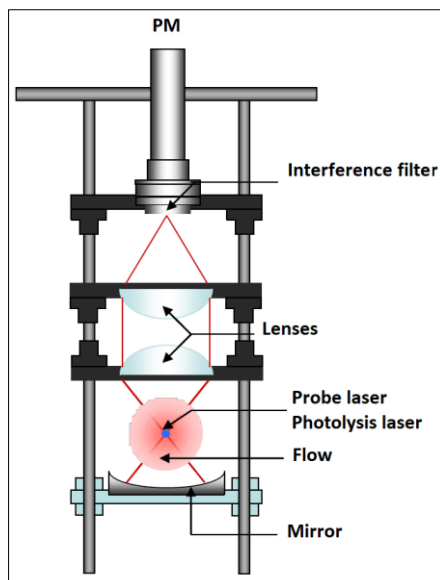


Figure II.16: Schematic diagram of the PM system used for the PLP-LIF technique.

The electrical signal collected by the PM is then integrated by a temporal door function using a Boxcar integrator model (Stanford Research Systems). The integration door function is placed just after the laser probe's pulse, and its width is chosen according to the lifetime of the fluorescence signal to maximize the signal/noise ratio. The integrated signal is averaged, displayed at the oscilloscope screen, and transmitted to the computer through an IEEE interfaced acquisition card (Stanford Research Systems, SR 245). The delay between the two lasers' pulses is ensured by a Delay Generator model (BNC-575), connected to the acquisition card IEEE. A LabVIEW program (National Instruments) was designed in the IPR laboratory to manage the acquired data and its analysis.

II.3.1.2 Mass spectrometry techniques

The mass spectrometry (MS) technique is widely used in atmospheric chemistry since it allows identifying molecule structures. This technique is based on two main parts: an ionization source and a mass analyzer. In MS, molecules are ionized either by Chemical Ionization (CI) or Electronic Ionization (EI).

CI technique is based on forming ions of the compound of interest (A) by ion/molecule reactions. The most common ion/molecule reaction is proton transfer (R.4).



In the EI technique, the compound of interest (A) is bombarded by a low-pressure electron beam ($10^{-5} - 10^{-6}$ mbar). In this collision process, one electron of the molecule (A) will be forced out, and the molecule will be converted to a positive ion ($A^{+\bullet}$) (R.5).



The ionized molecule's acquired energy, which is greater than its ionization energy, can generate consecutive dissociations into ion fragments with smaller masses. These ions are then separated using a Quadrupole Mass Spectrometer (QMS) consisting of four parallel rods with an AC/DC current applied to them. Ions are focused and passed along the middle of the quadrupole rods. Their motion will depend on the electric fields so that only ions of a particular m/z will be in resonance and thus pass through and reach the detector. Figure II.17 shows a simplified diagram of the quadrupole.

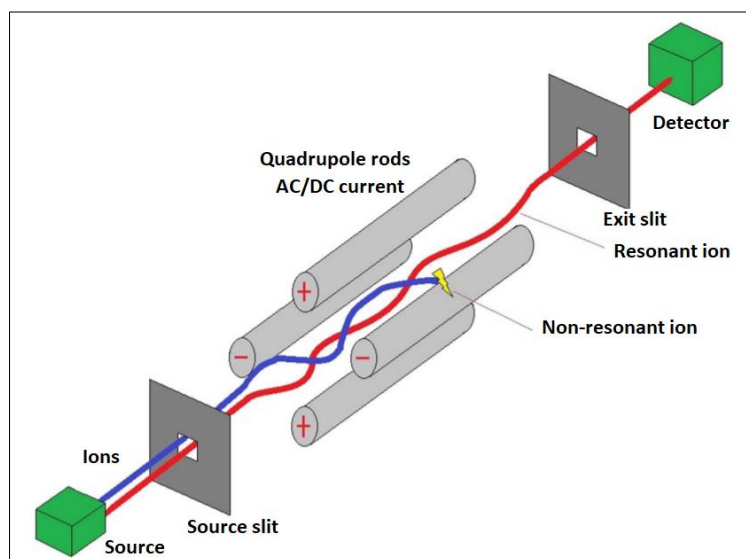


Figure II.17: Simplified diagram of Quadrupole Mass Spectrometer (QMS) (Santoiemma, 2018).

The obtained spectrum is expressed as the signal intensity of an ionized molecule versus its mass/charge ratio.

QMS is characterized by a high scanning speed of the masses (scan) associated with stability and precision and sensitivity of the order of the nanogram of analyte per one gram of sample (ppbv). MS technique can be used in combination with GC (see section II.3.1.3.1), connected to a flow tube reactor such as Proton Transfer Reaction-Mass Spectrometry (PTR-MS), or connected to Selected Ion Flow Tube-Mass Spectrometry (SIFT-MS). These two instruments have been used in this work and are detailed in the next paragraphs.

a) Proton Transfer Reaction-Mass Spectrometer (PTR-MS)

Proton-Transfer Reaction Mass Spectrometer (PTR-MS) is an analytical technique based on chemical ionization through proton transfer. PTR-MS was developed in the mid-1990 by Professor Werner Lindinger and co-workers at the University of Innsbruck in Austria to analyze VOCs in the atmosphere (Lindinger et al., 1998). This device has been adopted as a detector of choice to analyze volatiles in several fields: environmental research, air quality, food, and medical. PTR-MS is composed of three main parts: the ion source, the drift tube, and the ion detection system (Figure II.18).

The ion source consists of a hollow-cathode discharge source where water vapor produces H_2^+ , H^+ , and O^+ ions, further reacting with water molecules to form H_3O^+ . A proton transfer reaction occurs between H_3O^+ ions and the studied VOC (A), as shown in (R.4).

This ionization occurs only if the proton affinity (PA) of the compound R is higher than that of water (166.5 Kcal/mol). Therefore, air compounds (N_2 , O_2 , Ar, and CO_2) do not react with H_3O^+ . On the contrary, they act as thermalizing buffer agents in the drift tube. The ion exiting the drift tube is extracted through an orifice while the buffer is pumped away.

The ion detection system can be either a Quadrupole Mass Spectrometer (QMS) (see section II.3.1.2) or a Time of Flight-Mass Spectrometer (ToF-MS). In a ToF-MS, ions with the same charge are accelerated to the same kinetic energy through an electric field and then separated according to their masses (heaviest ion reach the lowest speed).

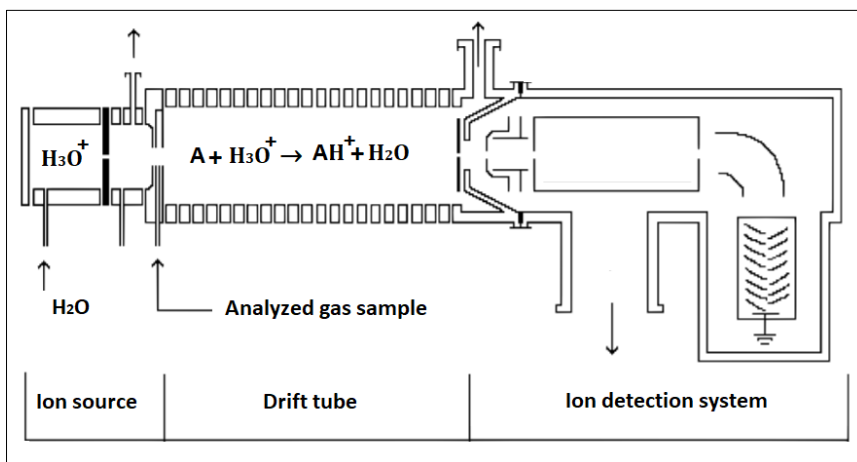


Figure II.18: Simplified diagram of PTR-MS (adapted from Amann et al., 2010).

The advantage of using a ToF-MS instead of a QMS is the higher resolution. Compounds are separated according to their exact mass for the former, while compounds are separated according to their nominal mass for the latter. Thus, more accurate identification of the compounds is then possible by ToF-MS. To conclude, PTR-MS offers a real-time measurement for numerous VOCs without any preliminary preparation of the analyzed sample. Besides, a PTR-MS instrument displays a high sensitivity (10 – 100 pptv) and rapid response time (time required for the instrument to analyze a sample) (1 – 10 sec). However, this device cannot give any additional information about the analyzed compound's identity except its mass. Thus, isomeric compounds cannot be distinguished.

▪ PTR-MS used in this work

Two PTR-MS were used in this work: (a) the PTR-ToF-MS 8000 IONICON was used to quantify the concentration of the studied VOC in D-ASC (IMT Lille Douai), and (b) the PTR-ToF-MS 4000 IONICON was used to identify the products of the reaction between Trans-2-heptenal and Cl atoms using CR-ASC (UCLM). A photo of each PTR-ToF-MS is displayed in Figure II.19.



Figure II.19: Photo of PTR-ToF-MS (a) 8000 IONICON used at IMT Lille Douai and (b) 4000 IONICON used at UCLM.

The main characteristics of IONICON PTR-ToF-MS 8000 and 4000 are summarized in Table II.4.

Table II.4: Characteristics of the used PTR-ToF-MS in this work.

Characteristics	IONICON PTR-ToF-MS 8000	IONICON PTR-ToF-MS 4000
Mass range (atomic mass units amu)	1 – 50000	1 – 10000
Response time (ms)	100	< 100
Sensitivity (@ m/z 181) (cps/ppbv)	> 240	> 8000
Mass resolution (m/dm)	> 4000	> 4500
Limit detection (@ m/z 181) over 1 minute (ppbv)	< 5	< 1
Pulse frequency (kHz)	Up to 80	Up to 150
Adjustable flow (sccm)	50 – 1000	50 – 800

The IONICON PTR-ToF-MS 4000 is the smallest and newest high-resolution PTR-ToF-MS.

b) Selected Ion Flow Tube-Mass Spectrometer (SIFT-MS)

Selected Ion Flow Tube-Mass Spectrometer (SIFT-MS) is a soft chemical ionization technique based on chemical ionization (CI) of the analyte (A) with reagent ions (R^+ : H_3O^+ , NO^+ , and O_2^+). Reagent ions (R^+ : H_3O^+ , NO^+ , and O_2^+) are produced via water vapor and zero air in a microwave resonator. The first quadrupole mass filter allows selecting the desired reagent ion (R^+) based on its m/z ratio.

The selected ion passes to the flow tube reactor, which consists of a metal cylinder, in a carrier gas stream (He at 1 Torr). The gas sample enters into this flow tube through a heated sampling capillary with a constant flow (usually 30 mL). It undergoes a soft ionization reaction depending on its chemical properties, such as proton affinity (PA) and ionization energy. The reaction between the reagent ions (R^+) and the components (A) generates ion products (P^+) and neutral products (N). All these chemical species (R^+ , A, P^+ , and N) are injected into a second quadrupole mass filter to select ions based on their m/z ratio. An electron multiplier detector placed at the exit of the second quadrupole is used to measure the ions' count rates in the selected m/z range. Figure II.20 displays a simplified diagram of this instrument.

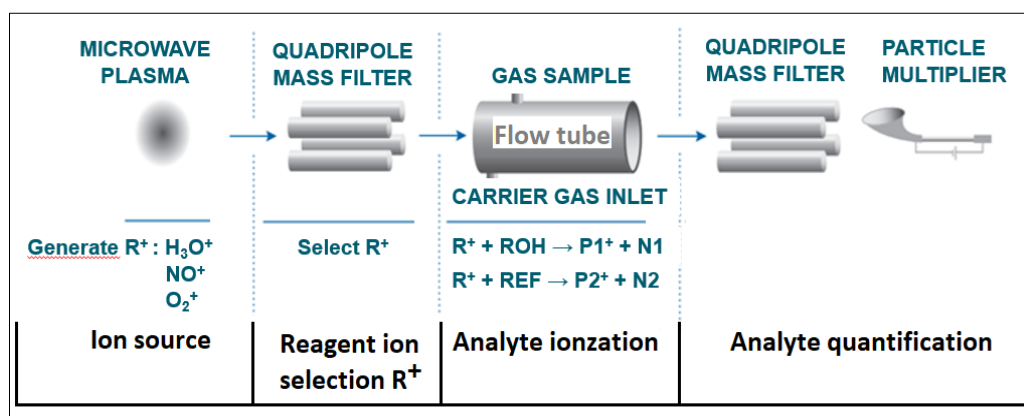


Figure II.20: Simplified diagram of SIFT-MS.

SIFT-MS provides real-time measurements, down to ppbv, with three different reagent ions, increasing the selectivity and identifying gases better. However, SIFT-MS cannot differentiate isomers as well as the PTR-MS instrument.

- **SIFT-MS used in this work**

A Voice200® SIFT-MS model (Syft Technologies, New Zealand) instrument (Figure II.21) connected to Thalamos-ASC of IMT Lille Douai, allowing to measure the rate constant of the reaction between unsaturated alcohols and chlorine atoms.



Figure II.21: Photo of the Voice200® SIFT-MS used at IMT Lille Douai.

PTR-MS and SIFT-MS are both flow-tube-based mass spectrometric techniques that are used to detect VOCs in real-time. The fundamental difference is that SIFT-MS applies three reagent ions (H_3O^+ , NO^+ , and O_2^+) as standard, which gives it a significant advantage.

II.3.1.3 Chromatographic techniques

Chromatography is a qualitative and quantitative analysis technique that separates and then identifies compounds present in a mixture. Two main types of chromatographic techniques are known based on the analyzed sample phase: Gas Chromatography (GC) and High-Performance Liquid Chromatography (HPLC).

II.3.1.3.1 Gas Chromatography (GC)

Gas Chromatography (GC) device is used in analytical chemistry to separate and analyze compounds vaporized without thermal decomposition. In GC, the mobile phase is a carrier gas (usually helium).

The stationary phase is a microscopic layer of liquid or polymer on inert solid support inside a glass or metal tubing piece called a “column”. The analyzed compounds interact with the stationary phase coated inside the column and cause differences between their retention times. GC is usually used in combination with MS techniques such as TD-GC-FID/MS or SPME/GC-MS. Both techniques have been used in this thesis and described in the following paragraphs.

▪ **TD-GC-FID/MS used in this work**

Online analysis of unsaturated aldehydes in LFR is performed with a system composed of a thermal desorption TD system (TD Turbo Matrix 350 Perkin-Elmer) connected to a gas chromatograph GC (Agilent 6890N-G1540N) and coupled to a double detection system: a flame ionization detector (FID) and a mass spectrometer (MS 5975B Inert MSD). TD-GC-FID/MS technique was used offline to identify the ozonolysis products of unsaturated aldehydes in QUAREC-ASC. These analyses are done by analyzing cartridges (Carbotrap 202, Sigma-Aldrich), consisting of stainless-steel tubes containing a few tens of mg of Carbopack B and C adapted to analyze organic compounds (C_5 up to C_{20}). The gas mixture sampling on Carbotrap 202 cartridges was done using the system presented in Figure II.22.

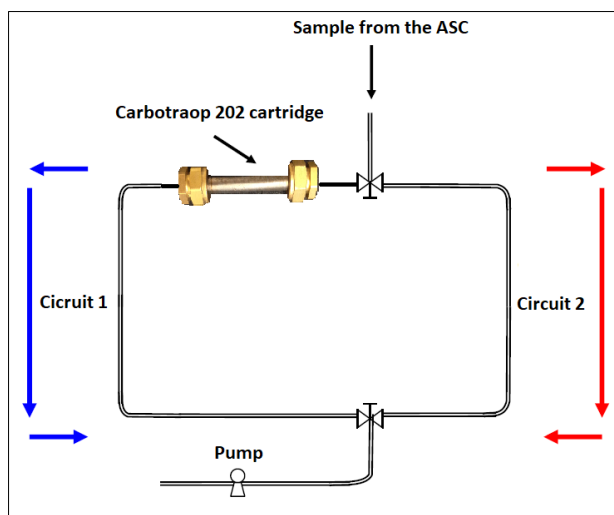


Figure II.22: A scheme of sampling set-up on Carbotrap 202 cartridges.

The gas sample passes from the LFR (online) or Carbotrap 202 cartridge (offline) to the TD using a suction pump with a standard flow rate of 50 mL min^{-1} for 5 min. The sample is collected on a cooled trap (263 K). The latter is then heated to 523 K at a rate of 40 K s^{-1} in splitless mode, allowing the entire sample to pass from the TD to the GC via a heated line (483 K). The capillary column used for the separation of compounds was an apolar type DB-5MS (phenyl polymer (5%) dimethylarylenesiloxane (95%); $(60 \text{ m} \times 320 \text{ } \mu\text{m} \times 1 \text{ } \mu\text{m})$). The GC temperature program is indicated in Table II.5.

Table II.5: GC oven temperature program.

	Ramp rate / K min^{-1}	Temperature / K	Duration / min
Initial state	-	313	2
Ramp 1	3	365	4
Ramp 2	5	433	4
Ramp 3	10	553	2

About one-third of the sample passes to the FID detector, and the rest goes to the MS detector. The FID operation is based on the detection of ions formed during the combustion of carbon-containing compounds in a hydrogen flame. The generation of these ions is proportional to the concentration of organic species in the sample gas stream. The FID detector is generally used to quantify the compounds, whereas the MS detector is used to identify them, using the library of MS spectra provided by the NIST. The analysis by TD-GC-FID/MS results in two chromatograms representing FID and MS signals as function of the retention time (t_R). Figure II.23 presents a simplified diagram and photo of the TD-GC-FID/MS system at IMT Lille Douai.

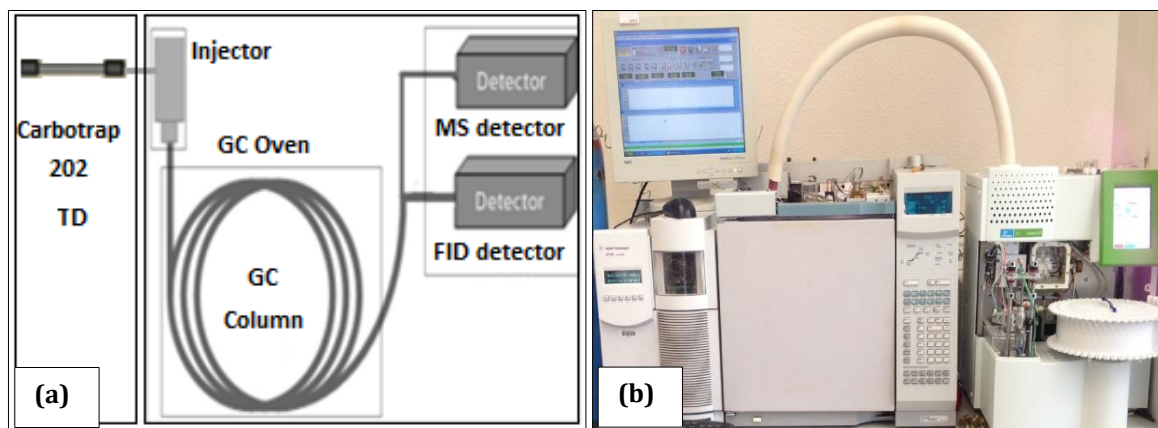


Figure II.23: (a) Schematic diagram and (b) photo of the TD-GC-FID/MS device.

▪ SPME/GC-MS used in this work

The Solid-Phase Micro-Extraction (SPME) technique was used in this work at UCLM University to analyze the reaction mixture in CR-ASC using an absorber fiber type 50/30 μm divinylbenzene/carboxen/polydimethylsiloxane. The coated fiber was exposed to the gas mixture inside the CR-ASC during a specific time. The fiber was thermally desorbed at the GC's heated injection port (at 523 K), entrained by the carrier gas, and then analyzed by a mass spectrometer (MS). The concentration of analysis compounds was examined by monitoring the corresponding chromatographic peak observed at a certain retention time.

II.3.1.3.2 Liquid chromatography

▪ DNPH-HPLC-UV used in this work

DNPH-HPLC-UV technique allows separation, identification, and quantification of a complex mixture. In the present work, this technique was used to identify carbonyl products of the reaction between unsaturated aldehydes and ozone during QUAREC-ASC experiments. A part of the experiments investigating the formed products for the reaction between methylperoxy and hydroxyl radicals in D-ASC was done based on the DNPH-HPLC-UV technique.

This technique consists of taking samples with a flow of about 50 mL min^{-1} for 5 min on a cartridge (Sep-Pack, Waters) containing 2,4-dinitrophenylhydrazine (DNPH).

This substance reacts with carbonyls and forms hydrazone compounds (containing the $>C=NN<$ group), which are then analyzed by “High-Performance Liquid Chromatography” (HPLC) coupled to a UV detector working at 365 nm.

The analysis starts with the desorption of the adsorbed carbonyls via the passage of 5 mL of acetonitrile through the cartridge for 2 – 4 min. The obtained solution is then introduced in the HPLC (Waters 2695, Dual λ 2487 detector) through the mobile liquid phase, which is composed of acetonitrile (ACN), tetrahydrofuran (THF), and water. The composition of the mobile liquid phase is composed as detailed in Table II.6.

Table II.6: Composition of the mobile phase during HPLC-UV analysis.

Analysis step	Time (min)	ACN (%)	THF (%)	Water (%)
Initial condition	$t = 0$ minutes	30	20	50
Progressive elution	$0 < t \leq 15$ minutes	65	5	30
Stabilization	$15 < t \leq 27$ minutes	65	5	30

The separation of compounds is done by entraining a mobile phase flow of about 1.5 mL min^{-1} through a C_{18} reversed-phase column (25 cm \times 4.6 mm \times 5 μm). The concentrations of carbonyl compounds are calculated from the response coefficients determined according to the external calibration method. The standards used are commercial solutions of the hydrazones corresponding to each carbonyl compound.

II.3.2 Particle-phase analysis techniques

The investigation of particle formation in ASCs is based on counting the number of particles for a given diameter range using a laser granulometer such as SMPS and FMPS devices. Other analysis techniques based on Aerosol Mass Spectrometer (AMS), such as High-Resolution Time-Of-Flight Aerosol Mass Spectrometer (HR-TOF-AMS), which can determine the chemical composition of aerosols. In this work, only the particle size distribution of aerosols was investigated using SMPS and FMPS instruments. The operational procedure of both devices is explained in the two next paragraphs.

II.3.2.1 SMPS

Two Scanning Mobility Particle Sizer (SMPS) were used in this work to analyze the particles formed through the ozonolysis of unsaturated aldehydes in D-ASC and QUAREC-ASC. The SMPS combines a differential mobility analyzer (DMA), which realizes a size separation of particles based on electrical mobility, followed by a condensation particle counter (CPC), which counts the fractionated particles (Figure II.24). The produced particles are sampled from the ASC (either D-ASC or QUAREC-ASC) using a silicon/carbon sampling line to reduce electrostatic losses. This sample passes through an impactor, which retains particles with a bigger diameter than its diameter. The sample passes to the neutralizer (85Kr), which brings the charge level on particles to a minimum.

An additional sheath air flow drives the sample from the top to the DMA's bottom, consisting of two coaxial metallic electrodes with a central rod being negatively charged. At the same time, the outer one is electrically grounded. An electric field is then created inside the DMA, which ensures the separation of particles according to their electrical mobility. The latter is defined as the speed at which a charged particle moves into an electric field. Thus, only particles having mobility within a narrow range are extracted through the slot at the electrode base for a given voltage. Particles with higher mobility impact the electrode before reaching the slot, and particles with lower mobility are discarded with the excess air.

Particles pass through the slot at the base of the inner electrode and then to the CPC, where they are counted. The CPC consists of two stages, a saturator stage and a condenser stage. In the heated saturator stage, the particles pass through a saturated vapor of water or butanol. In the cooled condenser, the vapor condenses on the particle surface, increasing the particle size to be easily determined using laser light scattering techniques (Lorenzo, 2007).

- **SMPS of IMT Lille Douai**

For the measurement of particles in D-ASC, an SMPS TSI (DMA 3080 and CPC 3788) was used (Figure II.24). The sampling rate was at the normal mode 0.6 L min^{-1} with a scan time of 150 s for a particle size of 5 to 1000 nm.

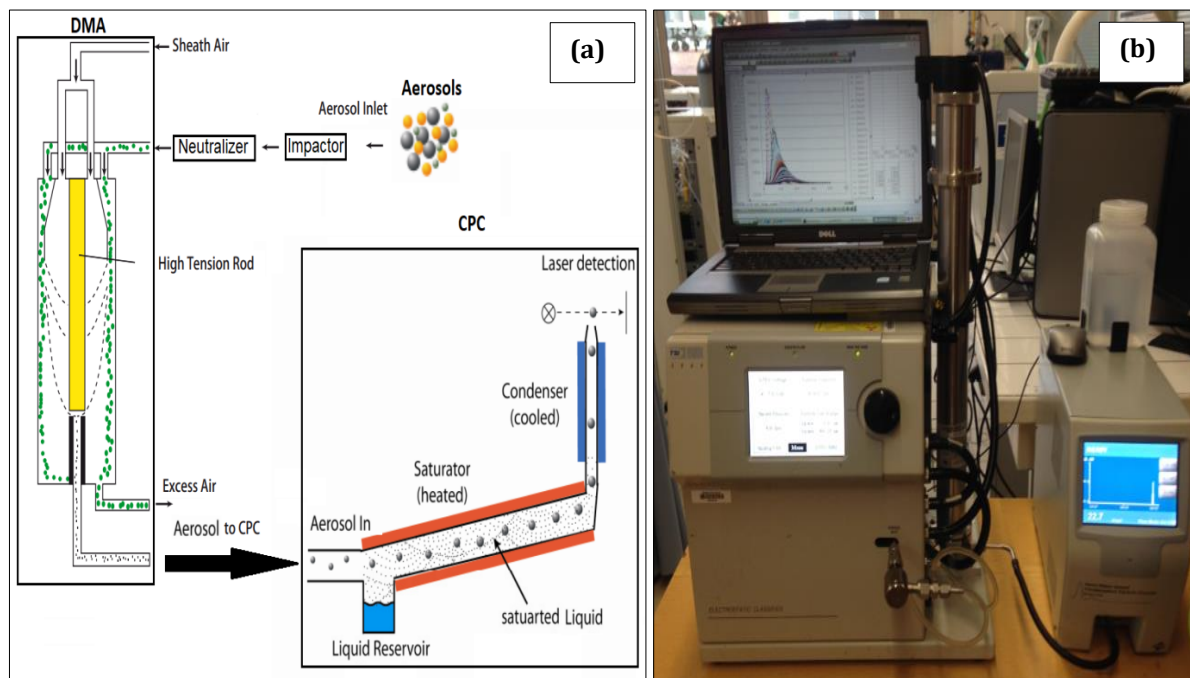


Figure II.24: (a) Simplified diagram of SMPS (adapted from Lorenzo, 2007 and (b) photo of SMPS (TSI, DMA 3080 and CPC 3788) of IMT Lille Douai.

▪ SMPS of Wuppertal University

QUAREC-ASC was coupled to an SMPS TSI (DMA 3071A and UCPC 3025A), which allows the quantification of SOAs. The used flow rate was 0.3 L min^{-1} for a size range from 13.8 to 700 nm.

II.3.2.2 FMPS

The Fast Mobility Particle Sizer (FMPS) was used to analyze the particles generated from the reaction between unsaturated aldehydes and Cl atoms in CR-ASC (Figure II.25). FMPS can determine particles in diameter around 6 to 500 nm with a minimum time resolution of about 1 second. At the entrance of the FMPS, the particles are positively charged in a corona charger. The particle enters the measurement zone near the center of a high-

tension electrode column (similar to a DMA but with inversed polarity). A flow of sheath air separates the aerosol from the electrometers. Indeed, the positively charged particles are repelled by the positive voltage applied to the high-tension electrode and migrate outward to the electrometer. A particle with high electric mobility hits an electrometer near the top of the column. In contrast, a particle with low electric mobility hits an electrometer at the bottom of the column. Instead of varying the voltage and extracting the charged particles at a constant position in the column as an SMPS instrument, the FMPS instrument is based on keeping the voltage constant and measuring the deposited particles with a stack of electrometers along the column

▪ FMPS of UCLM

A FMPS (TSI, Model 3091) was connected in a close circuit to the 16L-ASC and CR-ASC. This instrument is equipped with a stack of 32 electrometers, which correspond to particle diameters from 5.6 nm to 560 nm. The FMPS operates at a high sampling rate of 10 L min^{-1} , which considerably reduces particles' loss due to diffusion.

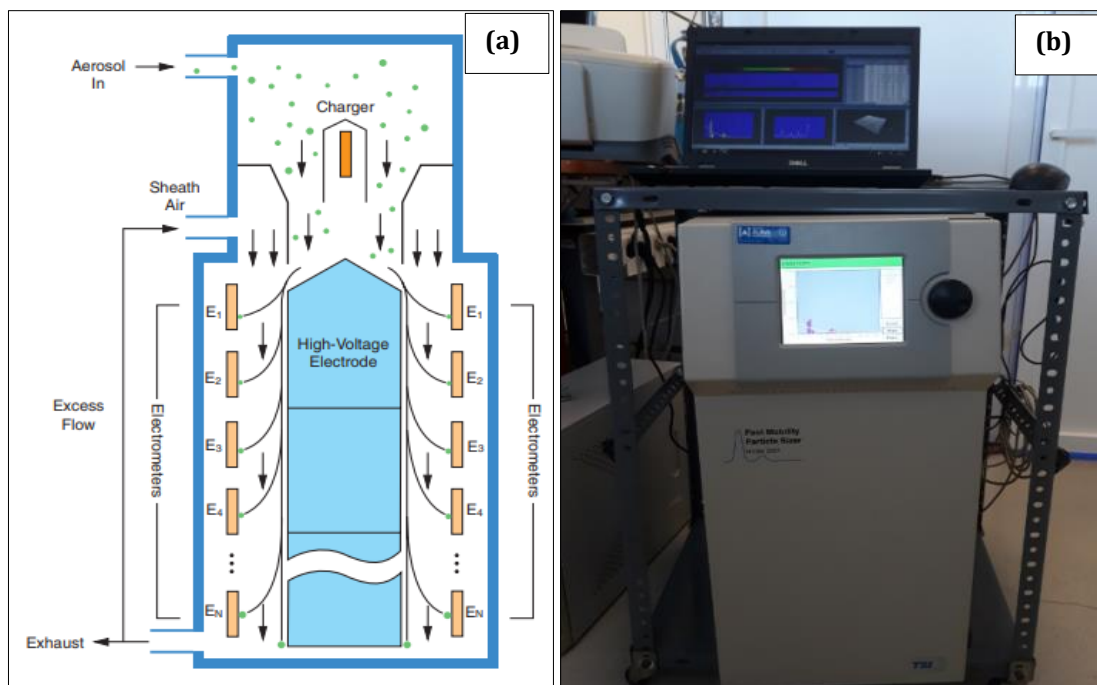


Figure II.25: (a) Simplified diagram of FMPS (adapted from TSI) and (b) photo of FMPS (TSI, 3091) of UCLM University.

The SMPS minimum time resolution reaches 120 seconds for a size range between 5 and 1000 nm. A better time resolution can be achieved using FMPS for a size range between 5.6 and 560 nm. Other fast techniques such as Electrical Diffusion Battery (EDB) and the Diffusion Size Classifier (DISC) cover particle distribution in a size range between 10 and 300 nm with a time resolution of 1 second (Lorenzo, 2007).

Smaller particle fractions lower than 40 nm can be measured by the so-called Neutral cluster and Air Ion Spectrometer (NAIS). NAIS measures the mobility and size distributions of both atmospheric ions and neutral particles (Asmi et al., 2008). Other instruments, such as HR-ToF-AMS, can analyze atmospheric particles' chemical transformation (Duncianu, 2012). All those techniques can be used in combination with a simulation chamber to characterize aerosols (Zhang et al., 2018).

II.4 Methodology

II.4.1 Determination of rate constants

II.4.1.1 Photolysis rate constant

Let us assume that a BVOC (AB) undergoes a photodissociation by absorbing incident radiations (R.6).



The rate expression of this reaction can be described as a first-order process (Eq.13).

$$r = -\frac{d[AB]}{dt} = \frac{d[A]}{dt} = \frac{d[B]}{dt} = J[AB] \quad (Eq.13)$$

where [AB], [A], and [B] are the reactant concentrations of the reactant “AB” and its photolysis products “A” and “B”. $J(\theta, z, T, P)$ is the photolysis rate (or frequency) (s^{-1}) for a given compound in the actinic region at a certain zenith angle (θ) and an altitude (z) and can be calculated as described in (Eq.14).

$$J(z, \theta, T, P) = \int_{\lambda_1 \geq 290 \text{ nm}}^{\lambda_2} \sigma(\lambda, T, P) \Phi(\lambda, T, P) F(\lambda, z, \theta) d\lambda \quad (\text{Eq.14})$$

where $\sigma(\lambda, T, P)$ is the absorption cross-section ($\text{cm}^2 \text{ molecule}^{-1}$). This parameter is the capacity of one molecule to absorb a photon at a specific wavelength λ and specific conditions (T, P) . $\Phi(\lambda, T, P)$ is the quantum yield, which is the probability of the molecule dissociating after absorption of a photon at a specific wavelength λ and specific conditions (T, P) (in $\text{molecule photon}^{-1}$). $F(\lambda, \theta, z)$ is the intensity of the photon flux received by the molecule at the position (θ, z) expressed in ($\text{photon cm}^{-2} \text{ s}^{-1} \text{ nm}^{-1}$). $F(\lambda, \theta, z)$ is usually taken from tabulated data reported for a given wavelength range ($\Delta\lambda$). For that reason, the photolysis rate can be expressed as follows (Eq.15).

$$J(z, \theta, T, P) \simeq \sum_{\lambda_1 \geq 290 \text{ nm}}^{\lambda_2} \sigma(\lambda, T, P) \Phi(\lambda, T, P) F(\lambda, z, \theta) \Delta\lambda \quad (\text{Eq.15})$$

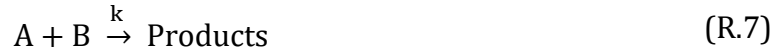
$F(\lambda, \theta, z)$ is usually calculated based on the radiative transfer model developed by Madronich and Flocke, 1999 for cloudless and aerosol-free sky conditions. In this work, the photolysis rates of the studied unsaturated aldehydes were calculated in chapter III.

II.4.1.2 Oxidation rate constant

Understanding the kinetics of reactions between different trace gases and atmospheric oxidants is critical for assessing their atmospheric fates. One of this work's main objectives is to determine the rate constants of oxidation reactions between several BVOCs (A) and oxidants of the atmosphere (B) in static and flow systems. Two methods were used in this work: the absolute and the relative methods. The absolute method is based on measuring the evolution of a key compound's concentration as function of the reaction time. In contrast, the relative method is based on comparing the rate of one reaction to another. These two methods are explained below.

II.4.1.2.1 Absolute method

Let us assume that a BVOC (A) and an atmospheric oxidant (B) are introduced into a reactor and can react with each other (R.7).



where k ($\text{cm}^3 \text{ molecule}^{-1} \text{ s}^{-1}$) is the second-order rate constant for the reaction between (A) and (B). The loss rate of their concentrations $[A]$, $[B]$ as function of time is proportional to these concentrations and expressed in Eq.16.

$$\begin{aligned} -\frac{d[A]}{dt} &= -\frac{d[B]}{dt} = k[A][B] + \sum_i (k_i [S_i] + k_{\text{diff}})[B] \\ &= \left[k[A] + \sum_i (k_i [S_i] + k_{\text{diff}}) \right] [B] = (k[A] + k_0)[B] \\ \text{with } k_0 &= \sum_i (k_i [S_i] + k_{\text{diff}}) \end{aligned} \quad (\text{Eq.16})$$

where $[A]$, $[B]$, and $[S_i]$ are the concentration of A, B, and impurities S_i (in ppm), respectively. k_i and k_{diff} are the rate constants of (B) losses through its reaction with impurities and diffusion, respectively. To simplify the determination of k , one of the most used methods consists of keeping $[A]$ constant and very largely in excess comparing to $[B]$ (pseudo-first-order $[A] \simeq [A]_0$ where $[A]_0$ is the initial concentration of A. The pseudo-first-order rate constant k' (s^{-1}) is then defined in (Eq.17).

$$k' = k[A]_0 + k_0 \quad (\text{Eq.17})$$

The temporal evolution of (Eq.16) transforms to (Eq.18).

$$-\frac{d[B]}{dt} = k'[B] \quad (\text{Eq.18})$$

The integration of (Eq.18) between (t_0 and t) gives (Eq.19).

$$\ln \left(\frac{[B]_0}{[B]_t} \right) = k't \quad (\text{Eq.19})$$

where $[B]_0$ and $[B]_t$ are “B” concentrations at the initial time t_0 and a time t , respectively. The slope of $\ln([B]_0/[B]_t)$ versus t gives the pseudo-first-order rate constant k' .

The determination of k' for different initial concentrations of $[A]_0$ allows extracting the constant rate k of the second-order reaction from Eq.17.

▪ Error analysis

The overall error on the rate constant Δk comes from statistical errors Δk (stat) and systematic errors Δk (syst) and is calculated as follows (Eq.20).

$$\Delta k = \sqrt{\Delta k \text{ (stat)}^2 + \Delta k \text{ (syst)}^2} \quad (\text{Eq.20})$$

Statistical errors Δk (stat) result from a least-squares analysis of the pseudo-first-order rate constant vs. the reagent's initial concentration (A in this case). Systematic errors Δk (syst) due mainly to the difficulties in handling and measuring the concentrations of the studied compound $[A]_0$ with good accuracy (measurements of the areas of the spectroscopic peaks, the possible overlap between spectra, temperature instability, measurements of the vapor pressure or presence of impurities).

II.4.1.2.2 Relative method

The relative method is particularly useful when the absolute concentration of one reactant is difficult to measure, especially in atmospheric chemistry. Therefore, we calculated k_1 from the value of the slope and the constant rate k_2 . This method is based on measuring the BVOC (A) decays compared to that of a reference compound (R), both mixed in the same reaction vessel in the oxidant presence (B). k_1 and k_2 are the rate constants for reaction (R.8) and (R.9), respectively.



$$-\frac{d[A]}{dt} = k_1[A][B] \quad (\text{Eq.21})$$

$$-\frac{d[R]}{dt} = k_2[R][B] \quad (\text{Eq.22})$$

The ratio between (Eq.21) and (Eq.22) eliminates the concentration term of B and allows to get only one expression (Eq.23).

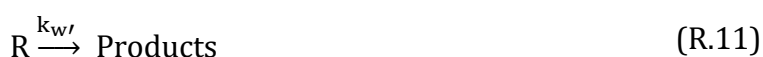
$$\frac{1}{k_1} \frac{d[A]}{[A]} = \frac{1}{k_2} \frac{d[R]}{[R]} \quad (\text{Eq.23})$$

The integration of (Eq.23) gives (Eq.24).

$$\ln \left(\frac{[A]_0}{[A]_t} \right) = \frac{k_1}{k_2} \ln \left(\frac{[R]_0}{[R]_t} \right) \quad (\text{Eq.24})$$

where $[A]_0$ and $[R]_0$ are the initial concentrations for the studied compound A and the reference compound R. $[A]_t$ and $[R]_t$ are the concentration of A and R at time t, respectively.

Other secondary loss processes ((R.10) and (R.11)) may happen simultaneously with reactions (R.8) and (R.9). For instance, in the presence of radiation, both compounds A and R may be able to photo-dissociate/ionize. Further, diffusion and deposition onto the reactor walls can be non-negligible sources of the compounds' disappearance. We note k_w and k_w' the total loss rate constants for A and R, respectively.



The correction of equation (Eq.24) will be done as described in (Eq.25).

$$\ln \left(\frac{[A]_0}{[A]_t} - k_w t \right) = \frac{k_1}{k_2} \ln \left(\frac{[R]_0}{[R]_t} - k_w' t \right) \quad (\text{Eq.25})$$

Since the rate constant, k_2 , for the reaction between the reference compound (R) and (B) is known, the rate constant of the reaction between compounds (A) and (B), k_1 , can be interpreted. In the case that we used n reference compounds, the final value of k_1 is the average of the different $k_{1,i}$ measured with different $k_{2,i}$ (Eq.26).

$$k_1 = \frac{\sum_{i=1}^n k_{1,i}}{n} \quad (\text{Eq.26})$$

▪ Error analysis

The overall error on the rate constant Δk_1 comes from statistical errors $\Delta k_1(\text{stat})$ and systematic errors $\Delta k_1(\text{syst})$ and calculated as follows (Eq.27).

$$\Delta k_1 = \sqrt{\Delta k_1(\text{stat})^2 + \Delta k_1(\text{syst})^2} \quad (\text{Eq.27})$$

Statistical errors $\Delta k_1(\text{stat})$ are calculated according to the following equation:

$$\frac{\Delta k_1(\text{stat})}{k_1} = \frac{\Delta\left(\frac{k_1}{k_2}\right)}{\left(\frac{k_1}{k_2}\right)} + \frac{\Delta k_2}{k_2} \quad (\text{Eq.28})$$

$\Delta(k_1/k_2)$ comes from the slope's determination in (Eq.25) and results from the plot's least-squares analysis. $\Delta(k_2)$ is the uncertainty on the rate constant of the reaction (R.9). Systematic errors $\Delta k_1(\text{syst})$ are estimated based on the errors done during the determination of the reagent concentrations (as explained above for the absolute method).

In the case that we used n reference compounds, the final value of Δk_1 is the average of the different $\Delta k_{1,i}$ measured (Eq.29).

$$\Delta k_1 = \sqrt{\frac{\sum_{i=1}^n (\Delta k_{1,i})^2}{n}} \quad (\text{Eq.29})$$

II.4.1.3 Lifetimes in the atmosphere

The environmental implications of the BVOC chemistries vary from the local to the global scale. Their impacts on the atmosphere are related to their residence time or so-called lifetime (τ). The compound's reactivity with atmospheric oxidants is the major parameter that controls their lifetimes and their effect on air quality. Lifetime due to reaction with a particular oxidant (τ_{Oxi}) or due to UV photolysis (τ_{UV}) is defined as follows:

$$\tau_{\text{Oxi}} = \frac{1}{\sum_i (k_{\text{Oxi}} \times [\text{Oxi}])_i} \quad (\text{Eq.30})$$

$$\tau_{\text{UV}} = \frac{1}{J(z, \theta)} \quad (\text{Eq.31})$$

where k_{Oxi} is the rate constant for the BVOC reaction with the oxidant (i), J is the rate constant of the BVOC photolysis, and $[\text{Oxi}]$ is the averaged atmospheric concentration of the oxidant. The lifetime due to oxidation reaction (τ_{Oxi}) has been estimated, in chapter IV, for a series of unsaturated aldehydes and alcohols, which has been studied in this work. At the same time, the lifetime due to photolysis reaction (τ_{UV}) concerns only carbonyl compounds (aldehydes) since they absorb at a wavelength above 300 nm (see chapter III).

The lifetime (τ_{Oxi}) have been calculated using a 24 h average oxidant concentration in the troposphere of 1×10^6 radical cm^{-3} for OH (Krol et al., 1998), 1×10^3 atom cm^{-3} for Cl as low concentration (Singh et al., 1996), 1×10^5 atom cm^{-3} for Cl as high concentration present in the marine boundary layer and polluted urban regions (Spicer et al., 1998), 1×10^{12} molecule cm^{-3} for ozone (Finlayson-Pitts and Pitts Jr, 1999) and 5×10^8 radical cm^{-3} for NO_3 (Calvert et al., 2011).

II.4.2 Determination of gas-phase products

II.4.2.1 Product yields

Two types of products can be easily distinguished: primary products formed through the oxidation reaction of the reactant and secondary products generated by primary product degradation. The plot of the formed product $[\text{Prod}]$ versus the reactant consumption's $\Delta[\text{React}]$ gives the product yield formation (Y_{Prod}) (Eq.32).

$$Y_{\text{Prod}}(\%) = \frac{[\text{Prod}]}{\Delta[\text{React}]} \times 100 \quad (\text{Eq.32})$$

For primary products, the plot ($[\text{Prod}]$ vs. $\Delta[\text{React}]$) is linear, and the slope represents the yield formation of the product.

For other primary products that are consumed to form secondary products or formed via secondary way, their yield formation is determined via the slope of the plot ([Prod] vs. $\Delta[\text{React}]$) applied only for the first few points where the plot is still linear.

II.4.2.2 Addition of an OH scavenger

Hydroxyl radicals could be generated through Criegee intermediates formed during BVOCs' oxidation (aldehydes and alcohols in this work). Therefore, some experiments were carried out by adding an excess quantity of an OH scavenger. Usually, we used cyclohexane to trap the OH radicals (Aschmann et al., 1997, Alam et al., 2011). The scavenger concentration $[\text{Scavenger}]_0$ was injected at sufficient concentration so that the reaction rate of OH radicals with the scavenger (R.13) exceeded that of the OH with the studied BVOC (R.12) by at least a factor of 10 (Eq.33).



$$\frac{k_{\text{Scav}} \times [\text{Scavenger}]_0}{k_{\text{BVOC}} \times [\text{BVOC}]_0} > 10 \quad (\text{Eq.33})$$

The percentage of trapped OH radicals was calculated using the following equation (Eq.34).

$$\%(\text{OH})_{\text{trap}} = \left(\frac{k_{\text{Scav}} \times [\text{Scavenger}]_0}{(k_{\text{BVOC}} \times [\text{BVOC}]_0 + k_{\text{Scav}} \times [\text{Scavenger}]_0)} \right) \times 100 \quad (\text{Eq.34})$$

II.4.2.3 Determination of carbon balance

To check whether all the degradation products are identified and quantified, it is important to calculate the carbon balance. If all the reaction products are detected and quantified, the reaction's carbon balance must be equal to 100%, calculated as displayed in (Eq.35).

$$\text{Carbon balance (\%)} = \sum_{i=1}^n \frac{[\text{Prod}]_i \times (n_c)_i + [\text{BVOC}]_t \times (n_c)_{\text{BVOC}}}{[\text{BVOC}]_0 \times (n_c)_{\text{BVOC}}} \times 100 \quad (\text{Eq.35})$$

where n is the total number of the quantified products, $[\text{Prod}]_i$ is the concentration of the quantified product (i) at a time (t), $(n_c)_i$ is the number of the carbon atoms of the product (i), $[\text{BVOC}]_0$ is the initial concentration of the reactant BVOC and $(n_c)_{\text{BVOC}}$ is the number of the carbon atoms of the BVOC.

II.4.3 Determination of SOA yields

The SOA yield (Y_{SOA}) determination is an essential parameter for this comparison since it allows to know each compound's potential to generate particles. The SOA yield (Y_{SOA}) is defined in (Eq.36).

$$Y_{\text{SOA}}(\%) = \frac{M_{\text{SOA}}}{\Delta[\text{React}]} \times 100 \quad (\text{Eq.36})$$

where M_{SOA} is the SOA production's mass, and $\Delta[\text{React}]$ is the consumed reactant's mass. The slope of ($M_{\text{SOA}} = f(\Delta[\text{React}])$) represents the yield formation of SOA (Y_{SOA}).

M_{SOA} was determined employing the particle counter (SMPS or FMPS) by converting the measured number concentration of particles to mass concentration, assuming that the particles are perfect spheres and that their density is known. A correction had to be done to consider the particle loss on the walls or the filters in the used particle counter. At the end of the reaction, we turned off the light to avoid any photolysis reaction (for Cl oxidation reaction), and we measured the loss of particles onto the chamber walls. The particle's masses' loss followed the first-order decay with a rate constant, $k_{\text{L,MSOA}}$. $M_{\text{SOA,exp}}$ was corrected using the following equation:

$$M_{\text{SOA,corr}} = M_{\text{SOA,exp}}(1 + k_{\text{L,MSOA}}t) \quad (\text{Eq.37})$$

where t is the reaction time, an example of how M_{SOA} changes with this correction is shown in Figure II.26.

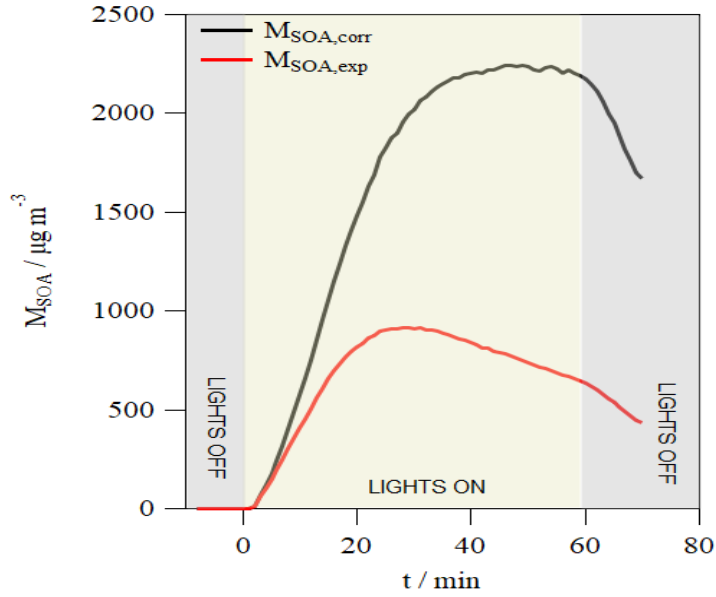


Figure II.26: Example of the temporal evolution of $M_{\text{SOA,exp}}$ (red) and $M_{\text{SOA,corr}}$ (black) formed through the reaction between Trans-2-Pental (T2P) and Cl atoms.

The reactant [React] concentration was monitored using the FTIR spectrometer following one of its characteristics bands by subtracting a calibrated spectrum of this reactant. To correctly determine the variation in concentration, it is important to quantify this reactant's loss onto the system's walls at the beginning of every experiment. The observed decay of reactant generally followed first-order kinetics with a rate constant named $k_{\text{L,React}}$. Taking into account $k_{\text{L,React}}$, it is possible to estimate the theoretical concentration of the reactant, $[\text{React}]_{0,\text{corr}}$, employing the following equation:

$$[\text{React}]_{0,\text{corr}} = [\text{React}]_{0,\text{exp}} \exp(-k_{\text{L,React}}t) \quad (\text{Eq.38})$$

where t is the reaction time and $[\text{React}]_{0,\text{exp}}$ is the initial concentration of reactant measured immediately before starting the reaction. Then, the variation of the reactant $\Delta[\text{React}]$ due to the reaction with an oxidant at every reaction time t can be defined as:

$$\Delta[\text{React}] = [\text{React}]_{0,\text{corr}} - [\text{React}]_{\text{exp}} \quad (\text{Eq.39})$$

where $[\text{React}]_{\text{exp}}$ is the concentration measured experimentally by FTIR at each time after starting the reaction.

In each experiment, M_{SOA} reaches a maximum value $M_{\text{SOA,max}}$, which directly correlates to the SOA yield Y_{SOA} . Indeed, SOA formation can be described by the one-product model proposed by (Pankow, 1994) for which the following equation was recommended by (Odum et al., 1996):

$$Y_{\text{SOA}} = M_{\text{SOA,max}} \left(\frac{\alpha K_p}{1 + M_{\text{SOA,max}} K_p} \right) \quad (\text{Eq.40})$$

where α is the mass-based gas-phase stoichiometric coefficient of a model product, and K_p represents its gas-particle partitioning equilibrium constant.

II.5 Conclusion

This chapter provides an overview of the reactors, the analytical techniques, and the experimental methods used in this thesis. In the present work, we concentrated on determining the rate constants, identifying the products, and quantifying the formed SOAs of the oxidation of a series of biogenic compounds belonging to unsaturated aldehydes and alcohols towards O_3 , Cl , and OH .

III Chapter III: Infrared and UV absorption cross-section measurements of C₅-C₇ unsaturated aldehydes

III.1 Introduction

For carbonyl compounds, photochemical processes are important in the troposphere. The wavelengths, which are shorter than 290 nm, are absorbed mainly by stratospheric ozone. Therefore, in the troposphere, solar radiation with wavelengths longer than 290 nm is the only responsible radiation photochemical process (the so-called actinic radiation). Unsaturated aldehydes are among those carbonyls which exhibit strong absorptions in the IR and UV spectral regions.

In this chapter, we measured the IR and the UV spectra of three unsaturated aldehydes: Trans-2-Pentenal (T2P), Trans-2-Hexenal (T2H), and Trans-2-Heptenal (T2Hep). Experiments were done at the UCLM University together with a postdoctoral researcher (Dr. María Antiñolo). The IR and UV absorption cross-section measurements had to be recorded very carefully because the studied compounds are very sticky.

Absorption of IR radiation brings about molecular vibration changes (see section II.3.1.1). Therefore, the determination of the IR spectra of T2P, T2H and, T2Hep was mainly used to quantify these compounds during their oxidation reactions with chlorine (see chapter V). As far as we know, the IR absorption cross-sections of these three aldehydes have never been determined before.

On the other hand, the C₅-C₇ unsaturated aldehydes photolysis processes due to UV absorptions may contribute to their atmospheric removals. Indeed, little is known about the behavior of their radiation absorption and their possible photolysis. To the best of our knowledge, only one study exists in the literature regarding the measurement of the UV absorption cross-section of T2P (Kalalian et al., 2019) and three determinations of the UV absorption cross-section of T2H (O'Connor et al., 2006, Jiménez et al., 2007, Kalalian et al., 2019). Besides, the UV absorption cross-section of T2Hep has never been determined before.

The photolysis of unsaturated aldehydes is of particular importance not only because it is a source of free radicals in the troposphere but also because it may significantly influence the lower troposphere's oxidizing capacity (Finlayson-Pitts and Pitts Jr, 1999).

III.2 Infrared absorption-cross sections of C₅-C₇ unsaturated aldehydes

III.2.1 Experimental conditions and protocols

The IR absorption cross-sections (σ) of T2P, T2H, and T2Hep were determined for the first time at 296 ± 2 K and 740 ± 20 Torr at $650 - 4000$ cm⁻¹ with a resolution of 2 cm⁻¹. Measurements were carried out in a 96-m Pyrex cell coupled to an FTIR spectrometer (see section II.2.1.2.5).

The experimental procedure started by heating the cell to 323 K and flushing it with synthetic air. Once the cleaning procedure was performed, a background IR spectrum of the cell's synthetic air was acquired. Then, a volume of the studied compound mixed with synthetic air was injected into the cell, and the IR spectrum was recorded. Concentrations of T2P, T2H, and T2Hep, were in the ranges $(0.98 - 7.4) \times 10^{14}$ molecule cm⁻³, $(0.49 - 8.1) \times 10^{14}$ molecule cm⁻³, and $(0.25 - 3.7) \times 10^{14}$ molecule cm⁻³, respectively. The used vapor pressure of the studied aldehydes does not exceed 1.3 Torr.

As I mentioned before, C₅-C₇ unsaturated aldehydes are sticky compounds. To avoid their possible losses onto the walls, I worked with vapor pressures 30 – 90% lower than their saturated vapor pressures. The saturated vapor pressure of T2P and T2H were calculated using Antoine coefficients presented in the book “The Yaws handbook of vapor pressure” (Yaws, 2015). On the other hand, the Antoine coefficients were not available for T2Hep. Table III.1 displayed Antoine coefficients used to calculate saturated vapor pressures for T2P and T2H at 25°C calculated using Antoine coefficients (Yaws, 2015) and values taken from the website (The Good Scents Company Information System, 2018) for T2P, T2H, and T2Hep.

Table III.1: Summary of the saturated vapor pressure of T2P, T2H, and T2Hep.

Compound	T / °C	$\log_{10} P(\text{Torr}) = A - B/[C+T(^{\circ}\text{C})]$			Range of T / °C	P_v^{sat} / Torr ^(b)	P_v^{sat} / Torr ^(c)
		A	B	C			
T2P	25	8.40014	1799.4353	221.592	[21.57 - 123.24]	12.67	11.451
T2H	25	7.36233	1621.8055	215.337	[39.57 - 172.61]	4.11	4.624
T2Hep							1.823 ^(a)

^(a) Not measured; ^(b) Calculated from Antoine coefficients; ^(c) Taken from the website (The Good Scents Company Information System).

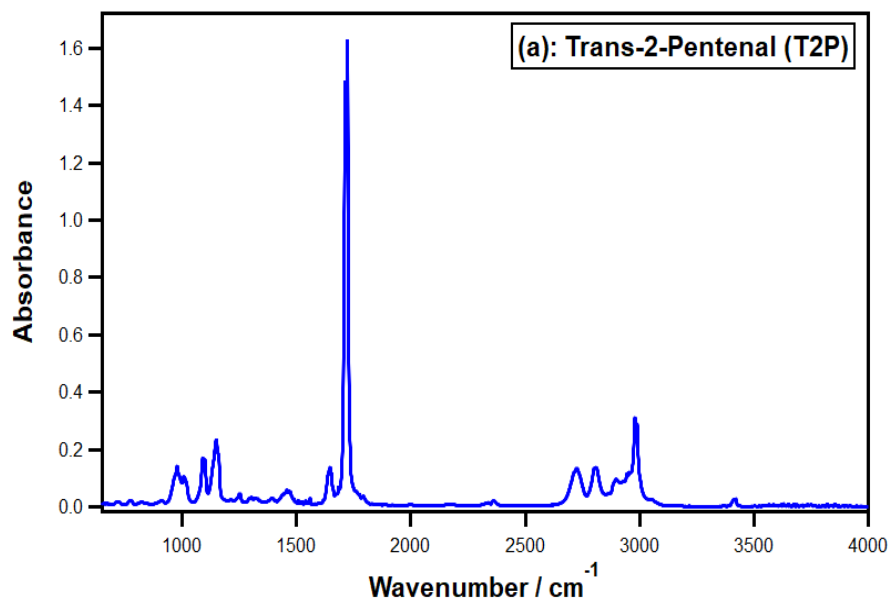
In this chapter and chapter VI, I used the calculated saturated vapor pressure for T2P ($P_{v,T2P}^{\text{sat}} = 12.67$ Torr). Regarding T2H and T2Hep saturated vapor pressures, I selected the data taken from the website (The Good Scents Company Information System) ($P_{v,T2H}^{\text{sat}} = 4.624$ Torr and $P_{v,T2Hep}^{\text{sat}} = 1.823$ Torr) since the temperature range of T2H Antoine Law was higher than 25°C and no data was available for T2Hep.

The reagents employed in this chapter were obtained from the following sources: T2P ($\geq 95\%$, Sigma-Aldrich), T2H (98%, Sigma-Aldrich), T2Hep (97%, Sigma-Aldrich). As can be seen, the purity of compounds was almost higher than 95%. However, further purifications were done to reduce the influence of impurities on the precision of the measurements.

III.2.2 Results and discussion

III.2.2.1 IR absorbance

In Figure III.1, I presented the absorbance A (base e) in peak height versus wavenumber in the range 650 – 4000 cm^{-1} for T2P, T2H, and T2Hep.



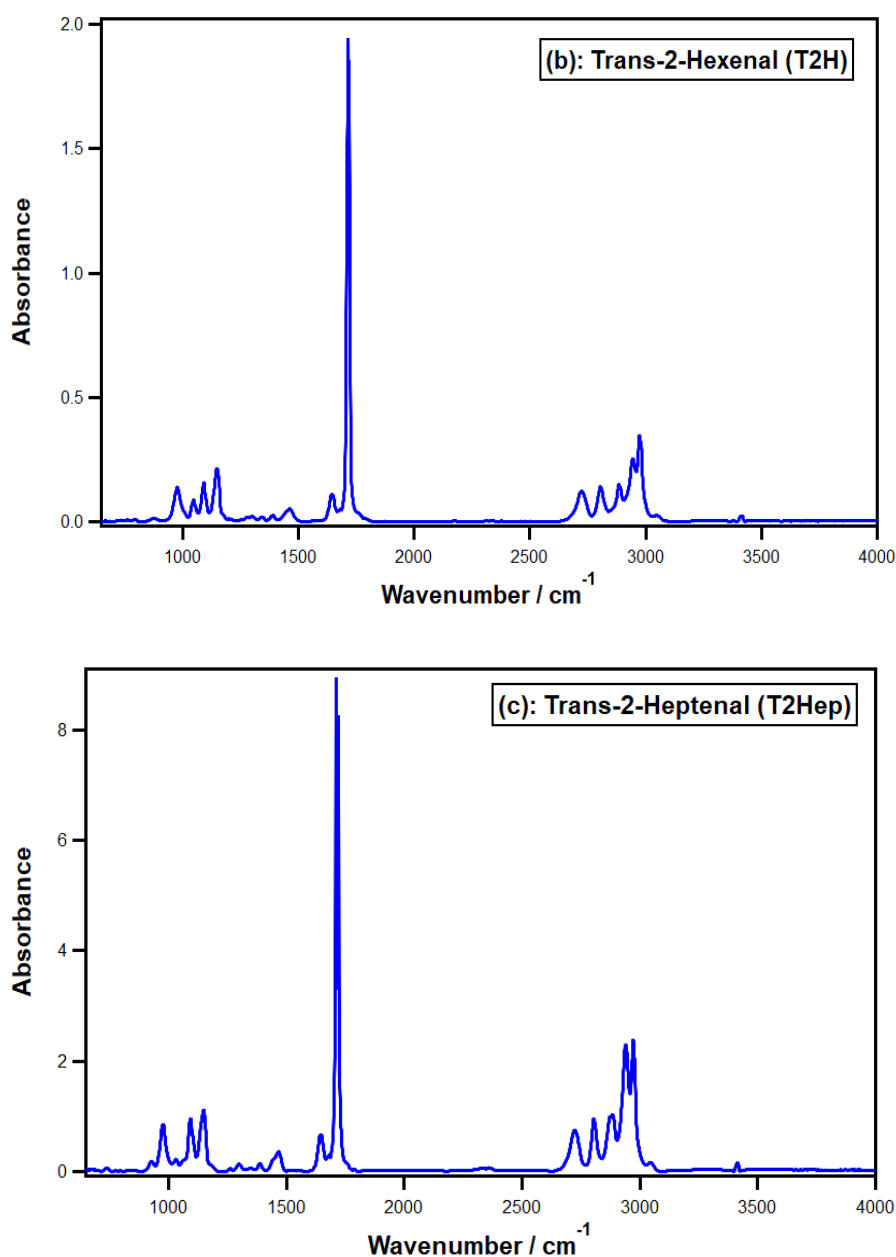
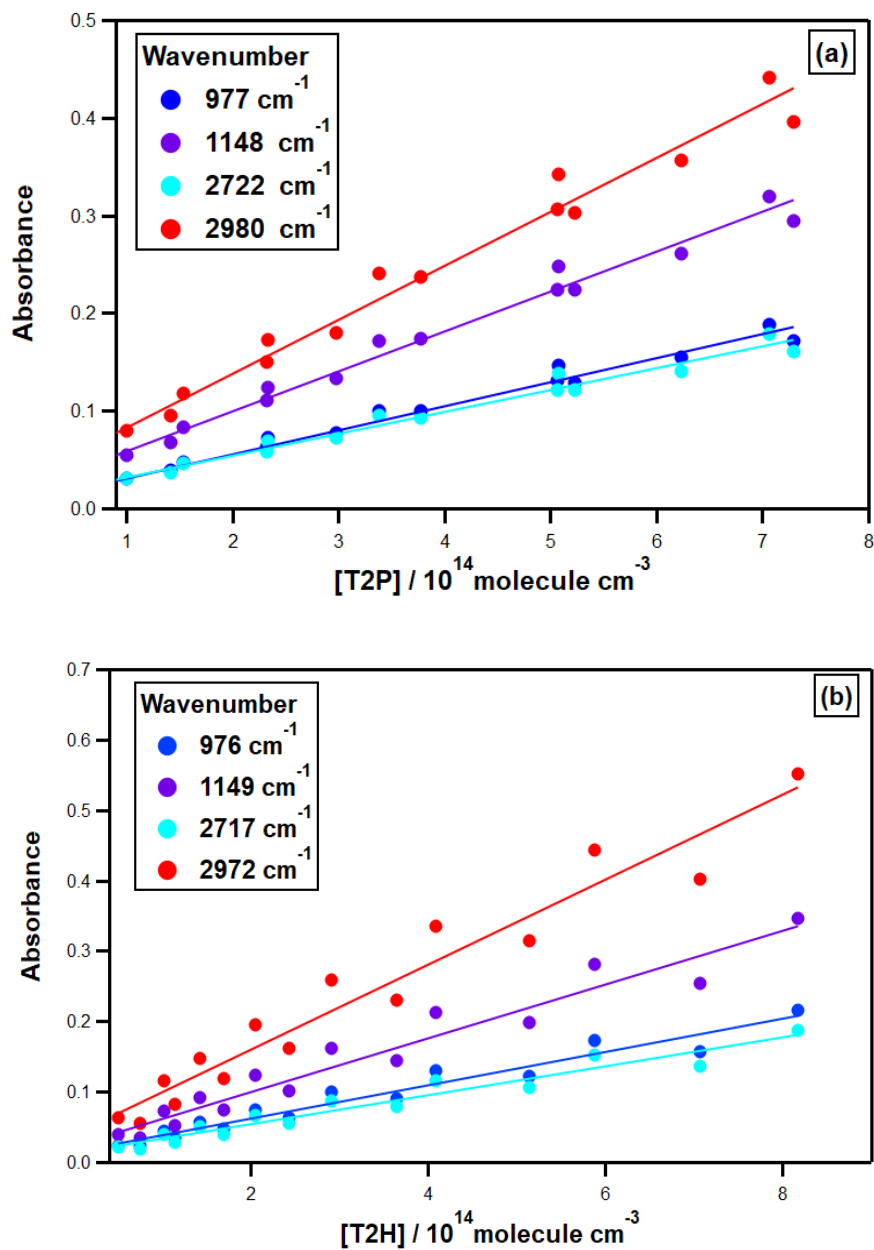


Figure III.1: IR absorbance of (a) T2P, (b) T2H, and (c) T2Hep as function of the wavenumber ($[\text{Aldehyde}]_0 = 2.5 \times 10^{14} \text{ molecule cm}^{-3}$).

The peaks in the 2500 – 3500 cm⁻¹ range belong to the C-H stretching. The highest band located in the 1500 – 2500 cm⁻¹ range is attributed to the C=O stretch. The rest of the bands in the 500 – 1500 cm⁻¹ range belong to the fingerprint region, which contains many peaks, making it difficult to identify individual peaks.

III.2.2.2 IR absorption-cross sections

Figure III.2 displays the Beer-Lambert plots for the three studied aldehydes at four different wavenumbers.



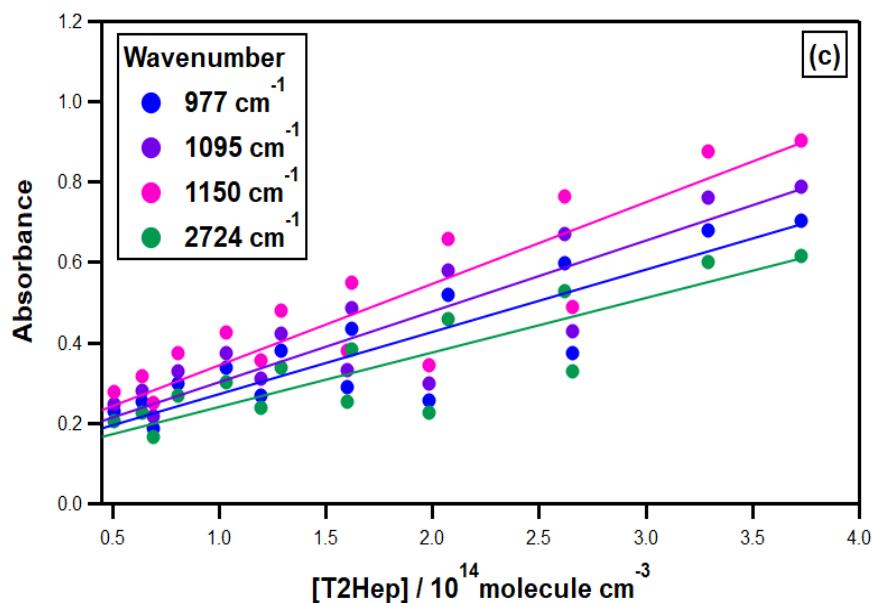


Figure III.2: Beer-Lambert plots (a) T2P, (b) T2H, and (c) T2Hep at four different wavenumbers.

The absorbance values plot versus the aldehyde concentrations at selected wavenumbers shows good linearity in the studied concentration range. The latter shows that the Beer-Lambert Law is accomplished at the studied concentration ranges of T2P, T2H, and T2Hep (see section II.3.1.1.1.1). The absorption cross-section is calculated from these plots' slope, which represents $(\sigma \times \ell)$. Table III.2 summarizes the IR absorption cross-section values (σ) at a specific wavenumber for each compound. Uncertainties are one standard deviation on the slope value divided by the path-length value (ℓ).

Table III.2: Summary of IR absorption cross-sections of T2P, T2H, and T2Hep determined at four different wavenumbers.

Wavenumber / cm ⁻¹	977	1148	2722	2980
σ (T2P) / $\times 10^{-20}$ cm ² molecule ⁻¹	2.5 ± 0.1	4.3 ± 0.2	2.3 ± 0.1	5.8 ± 0.3
Wavenumber / cm ⁻¹	976	1149	2717	2972
σ (T2H) / $\times 10^{-20}$ cm ² molecule ⁻¹	2.5 ± 0.2	4.0 ± 0.3	2.1 ± 0.2	6.3 ± 0.4
Wavenumber / cm ⁻¹	977	1150	1095	2924
σ (T2Hep) / $\times 10^{-19}$ cm ² molecule ⁻¹	1.6 ± 0.2	2.1 ± 0.2	1.8 ± 0.2	1.4 ± 1.6

▪ Error analysis

The overall error on the IR absorption cross-sections, $\Delta\sigma$, was estimated using the following equation:

$$\Delta\sigma = \sqrt{\Delta\sigma(\text{stat})^2 + \Delta\sigma(\text{syst})^2} \quad (\text{Eq.1})$$

where $\Delta\sigma(\text{stat})$ are statistical errors resulting from the absorbance's linear fit versus the aldehyde concentration and were considered one standard deviation in these analyses (Table III.2). The highest uncertainty represents 11.4% (corresponds to T2Hep at 2924 cm⁻¹). $\Delta\sigma(\text{syst})$ are systematic errors resulting from the difficulties in handling aldehydes (sticky compound) and measuring their concentrations. [Aldehyde]₀ is determined with an uncertainty of about 10%. Therefore, a total uncertainty on UV absorption cross-sections was about 15.2%.

III.3 UV absorption-cross sections of C₅-C₇ unsaturated aldehydes

III.3.1 Experimental conditions and protocols

The UV absorption cross-sections (σ) of T2P, T2H, and T2Hep were measured at 296 ± 2 K and in the range 270 – 410 nm with a resolution of 0.18 nm. Experiments were done in 107-cm absorption Pyrex. All technical details about the used technique in the UV spectra measurements were explained in section II.3.1.1.1.1. The experimental procedure started by heating the cell to 323 K and flushing it with synthetic air. Once the cleaning procedure was finished, a background UV spectrum was acquired. Then, the studied compound's volume was introduced to the cell, and the UV spectrum of the studied compound was recorded. Indeed, several spectra (4 for T2P, 7 for T2H, and 8 for T2Hep) were recorded to minimize the systematic errors.

The aldehyde concentrations ranges were: $(0.5 - 9.7) \times 10^{16}$ molecule cm⁻³, $(2.3 - 8.2) \times 10^{16}$ molecule cm⁻³, and $(0.5 - 3.5) \times 10^{16}$ molecule cm⁻³ for T2P, T2H, and T2Hep, respectively (no bath gas added). Those concentrations correspond to a pressure of (0.2 – 3.0) Torr, (0.7 – 2.5) Torr, and (0.2 – 1.1) Torr for T2P, T2H, and T2Hep, respectively. As discussed before, the used vapor pressure was at least 76%, 46%, and 40% lower than the saturated vapor pressure of T2P, T2H, and T2Hep, respectively (Table III.1).

▪ Leak test

Given that UV absorption cross-sections were measured at low pressure, it was necessary to check the cell's leak rate. The latter was performed by measuring the pressure inside the cell as function of time. The cell was first evacuated down to the minimum pressure that could be reached (0.09 Torr). After insulation of the cell, the pressure increase was monitored as function of time. Figure III.3 shows the evolution of cell pressure as function of time.

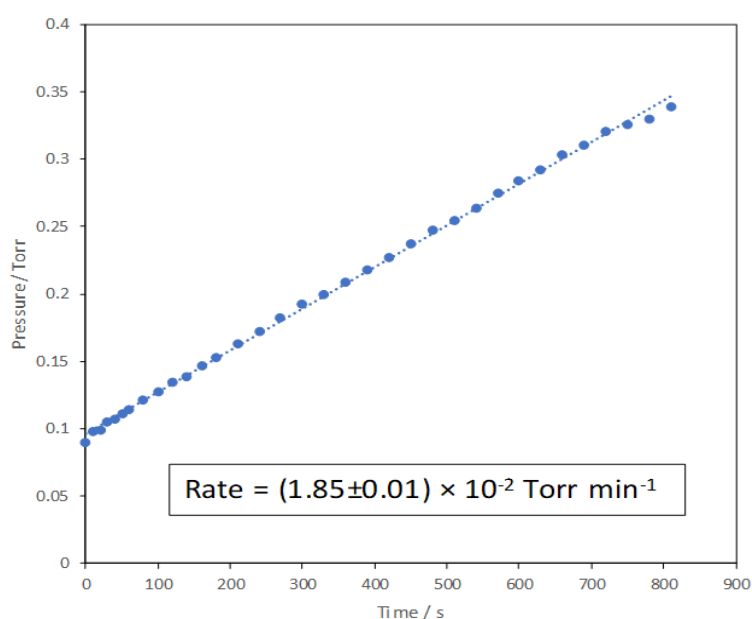


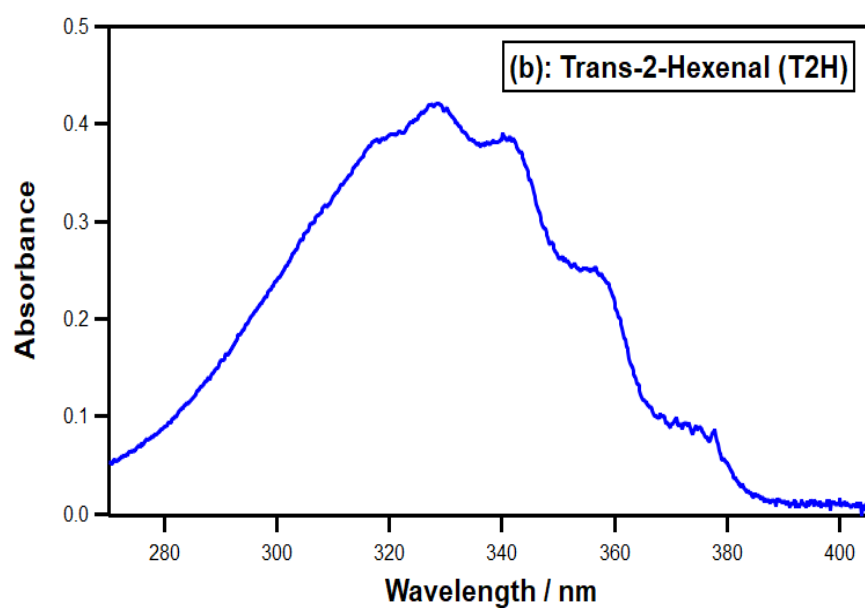
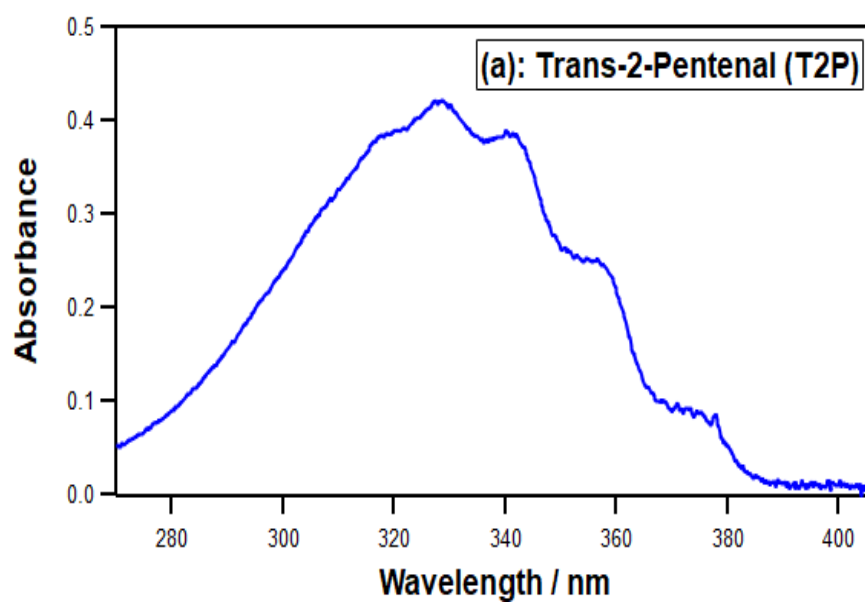
Figure III.3: Leak rate constant in UV cell.

The measurement time needed for taking a UV spectrum is 1.5 min. According to these results, up to 0.03 Torr of air penetrates to the UV cell in this time interval. Considering that the aldehyde pressure introduced in the cell is not usually lower than 1 Torr, the pressure error is less than 3%.

III.3.2 Results

III.3.2.1 UV absorbance

In Figure III.4, I plotted the absorbance A (base e) in terms of peak height versus wavelength in the range 270 – 410 nm for T2P, T2H, and T2Hep.



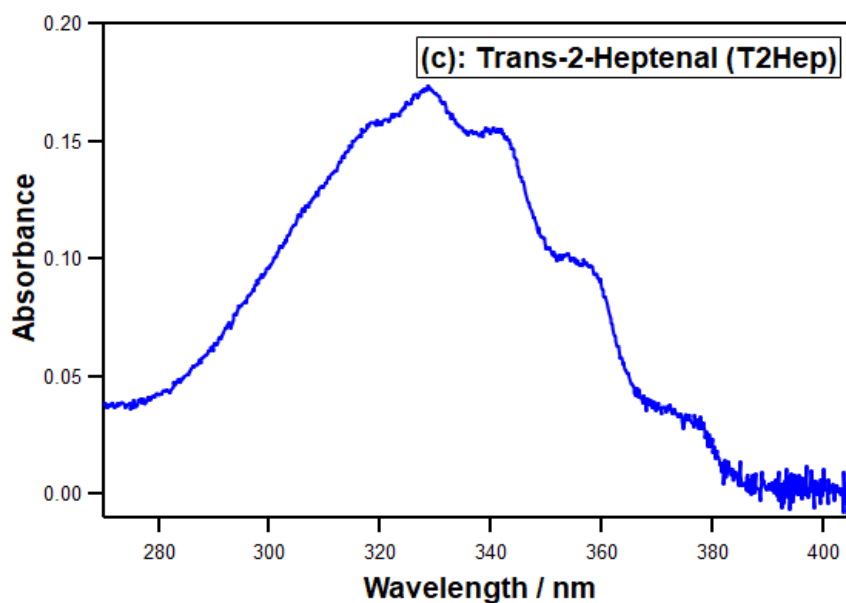
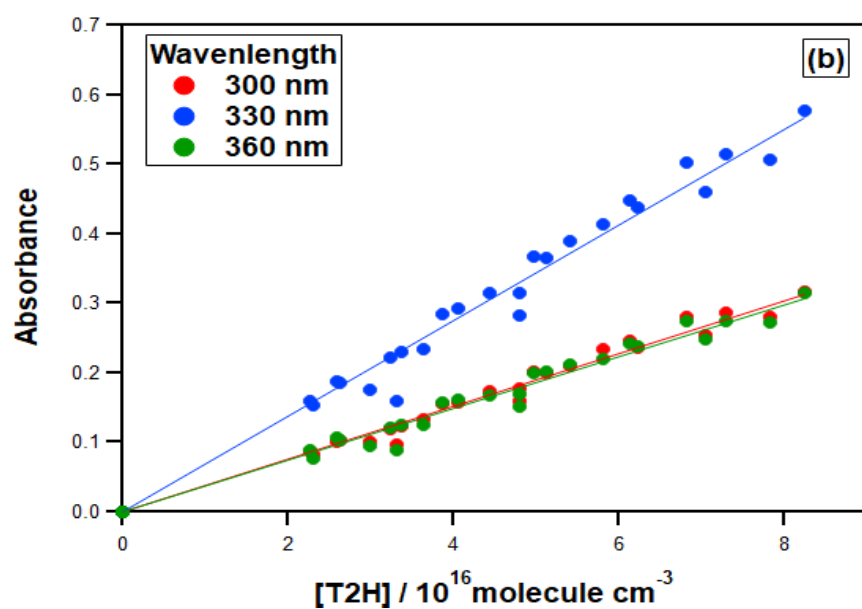
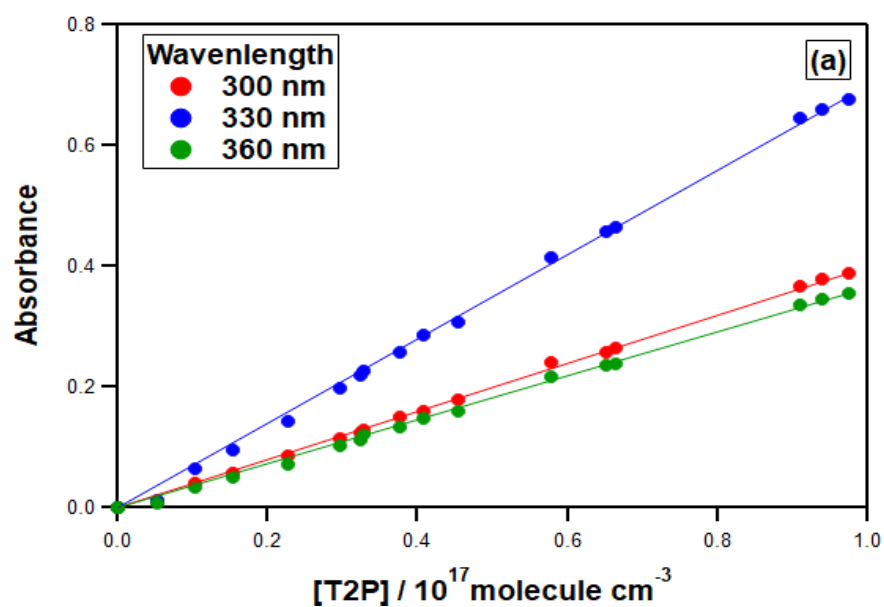


Figure III.4: UV absorbance of (a) T2P, (b) T2H and (c) T2Hep as function of the wavenumber ($[T2P]_0 = 5.8 \times 10^{16}$ molecule cm^{-3} , $[T2H]_0 = 6.2 \times 10^{16}$ molecule cm^{-3} , $[T2Hep]_0 = 2.8 \times 10^{16}$ molecule cm^{-3}).

The UV spectra of the studied compounds show a broad absorption band with a maximum located at the range 320 and 340 nm corresponding to the $n\text{-}\pi^*$ transition of the carbonyl group ($\text{C}=\text{O}$), linked to the possible photodissociation of C₅-C₇ unsaturated aldehydes beyond 290 nm.

III.3.2.2 UV absorption-cross sections

Figure III.5 shows the Beer-Lambert plots for the 3 studied aldehydes at 3 different wavelengths (300 nm, 330 nm, and 360 nm).



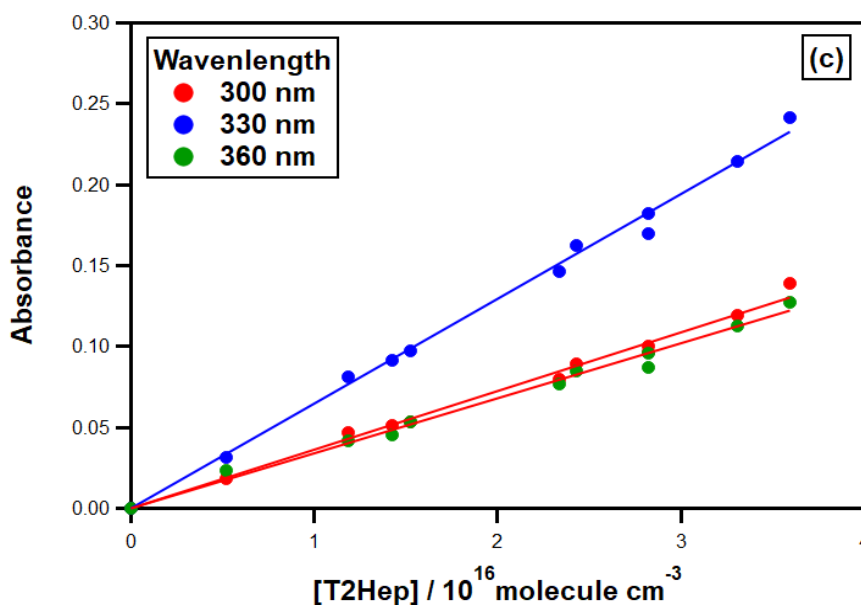


Figure III.5: Beer-Lambert plots (a) T2P, (b) T2H, and (c) T2Hep at three different wavelengths (300 nm, 330 nm, and 360 nm).

The absorbance values plot versus the aldehyde concentrations at selected wavelengths shows good linearity in the studied concentration range. The latter shows that the Beer-Lambert Law is accomplished at the studied concentration ranges of T2P, T2H, and T2Hep. The absorption cross-section is calculated from these plots' slope, which represents ($\sigma \times \ell$). Table III.3 summarizes the UV absorption cross-section values (σ) at a specific wavenumber for each compound. Uncertainties are one standard deviation on the slope value divided by the path-length value (ℓ).

Table III.3: Summary of UV absorption cross-sections of T2P, T2H, and T2Hep determined at three different wavelengths. Uncertainties are one standard deviation.

Wavelength / nm	300	330	360
σ (T2P) / $\times 10^{-20}$ cm ² molecule ⁻¹	3.7 ± 0.1	6.5 ± 0.1	3.4 ± 0.1
σ (T2H) / $\times 10^{-20}$ cm ² molecule ⁻¹	3.6 ± 0.1	6.4 ± 0.1	3.5 ± 0.1
σ (T2Hep) / $\times 10^{-20}$ cm ² molecule ⁻¹	3.4 ± 0.1	6.0 ± 0.1	3.2 ± 0.1

III.3.3 Discussion

III.3.3.1 Error analysis

The total error on the UV absorption cross-sections, $\Delta\sigma$, was estimated using Eq.1. Statistical errors $\Delta\sigma(\text{stat})$ and systematic errors $\Delta\sigma(\text{syst})$ result from the same sources as explained for IR absorption cross-sections errors. $\Delta\sigma(\text{stat})$ was calculated from Table III.3) where the highest uncertainty represents 3.1% (corresponds to T2Hep at 360 nm). $\Delta\sigma(\text{syst})$ was estimated as 10% coming mainly from the aldehyde quantification. An overall uncertainty on UV absorption cross-sections was about 10.5%

III.3.3.2 Comparison with literature data

A summary of the experimental conditions and analytical techniques for literature data and the determined UV spectra for T2H is displayed in Table III.4.

Table III.4: A summary of the experimental conditions and analytical techniques for literature data and the determined UV spectra for T2P and T2H.

Reference	Compound	P / Torr	T / K	λ / nm	Measurement of [Aldehyde]	Cell Path-length
O'Connor et al., 2006	T2H	1 – 5.8	297	290 – 400	FTIR	Pyrex cells with quartz windows.
Jiménez et al., 2007	T2H	0.6 – 3.55	298	210 – 370	Calculated from vapor pressure	Pyrex cells with quartz windows. 107 cm
Kalalian et al., 2019	T2P T2H	1 – 9	298	240 – 400	Calculated from vapor pressure	Pyrex cells with quartz windows. 100 cm
This work	T2P T2H T2Hep	0.2 – 3.0	298	270 – 410	Calculated from vapor pressure	Pyrex cells with quartz windows. 107 cm

a) T2P spectra

Only one previous determination of the gas-phase UV absorption spectrum of T2P exists in the literature (Kalalian et al., 2019). Figure III.6 displays all the UV absorption cross-sections determined for T2P.

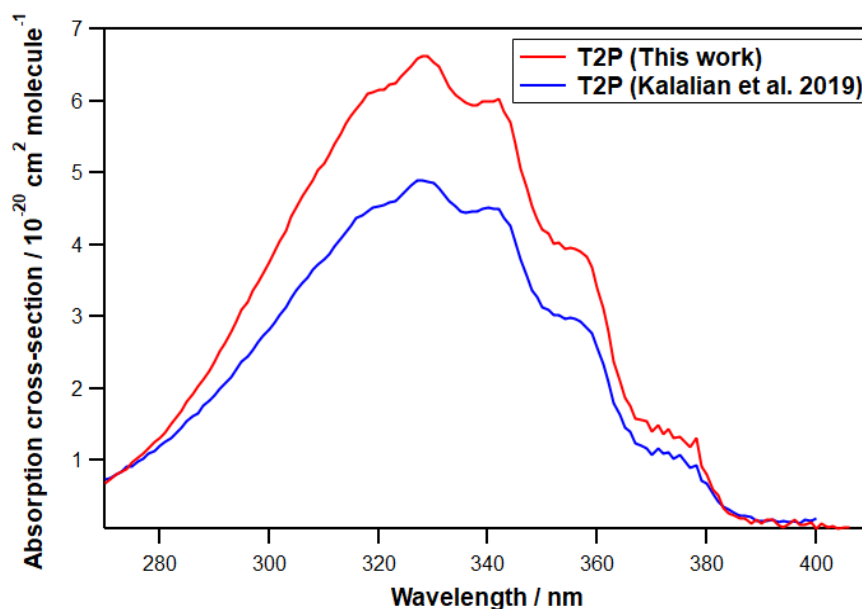


Figure III.6: Comparison of the UV spectrum of T2P determined in this work with literature data (Kalalian et al., 2019).

The maximum absorption position is 328 nm in this work and 330 nm in Kalalian et al., 2019. However, the cross-section at the maximum found in the present work ($\sigma_{\text{max}} = 6.62 \times 10^{-20} \text{ cm}^2 \text{ molecule}^{-1}$) is higher than the one determined by Kalalian et al., ($\sigma_{\text{max}} = 4.86 \times 10^{-20} \text{ cm}^2 \text{ molecule}^{-1}$) by about 27%. A bias can explain this difference due to measurement errors.

b) T2H spectra

Three measurements of the gas-phase UV absorption spectrum of T2H exist in the literature (O'Connor et al., 2006, Jiménez et al., 2007, Kalalian et al., 2019). Figure III.7 displays all the UV absorption cross-sections determined for T2H.

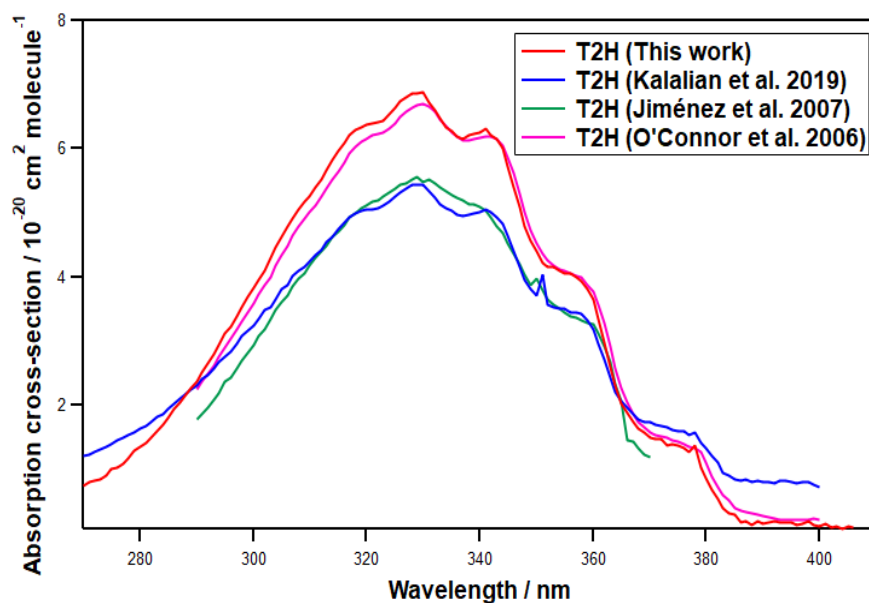


Figure III.7: Comparison of the UV spectrum of T2H determined in this work with literature data (O'Connor et al., 2006, Jiménez et al., 2007, Kalalian et al., 2019).

The absorption maximum of T2H in this work is located at 330 nm ($\sigma_{\max} = 6.88 \times 10^{-20} \text{ cm}^2 \text{ molecule}^{-1}$). This value is in very good agreement with the value determined by O'Connor et al. 2006 nm ($\sigma_{\max} = 6.70 \times 10^{-20} \text{ cm}^2 \text{ molecule}^{-1}$). However, a difference of 19% was observed with an absorption maximum of T2H found by Jiménez et al., 2007 ($\sigma_{\max} = 5.55 \times 10^{-20} \text{ cm}^2 \text{ molecule}^{-1}$) and Kalalian et al., 2019 ($\sigma_{\max} = 5.53 \times 10^{-20} \text{ cm}^2 \text{ molecule}^{-1}$). Considered the experimental conditions and the analytical techniques used in these two studies (Jiménez et al. and Kalalian et al.), no obvious difference between experimental set-ups of literature data was detected (see Table III.4). However, this difference remains in the uncertainty interval determined in this work.

The absorption maximum of T2Hep in this work was observed at 328 nm ($\sigma_{\max} = 6.09 \times 10^{-20} \text{ cm}^2 \text{ molecule}^{-1}$). No determination of the UV spectra for T2Hep was found in the literature. This work is the first determination of its UV spectrum in the range 270 – 410 nm at 298 K.

III.3.3.3 Structure effect

To evaluate the influence of a double bond in conjugation with the carbonyl group, the UV spectra of the C₃-C₇ unsaturated aldehydes are plotted with their saturated homologous aldehydes (from Figure III.8 to Figure III.12).

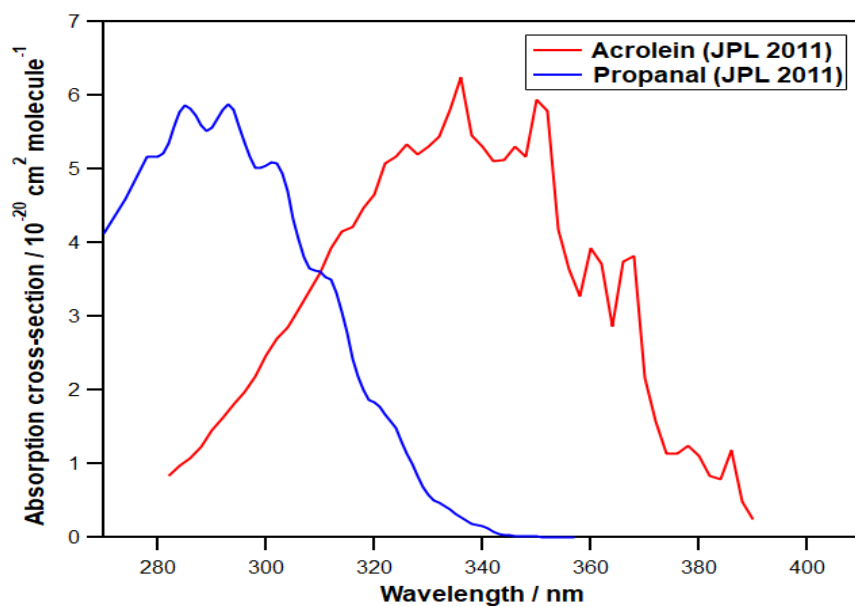


Figure III.8: Comparison between the UV spectra of acrolein (JPL 2011) and propanal (JPL 2011).

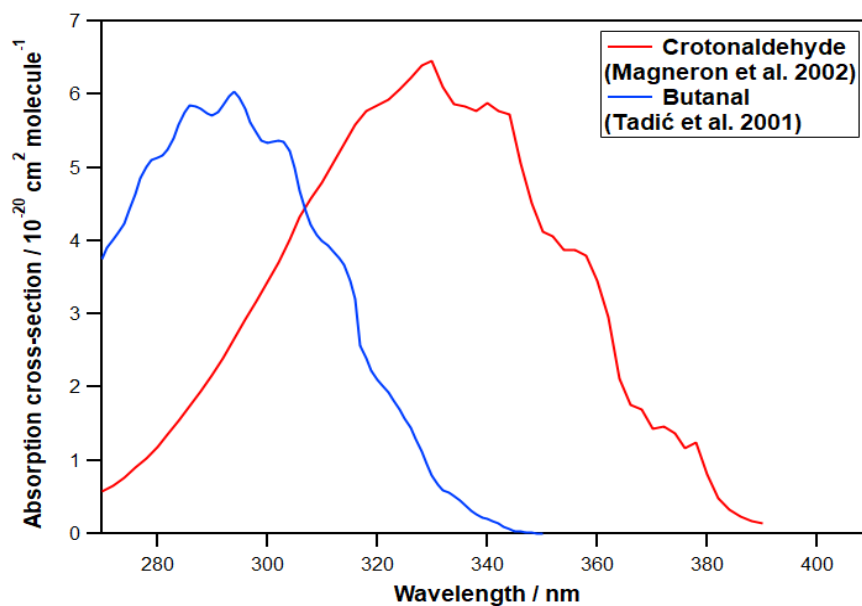


Figure III.9: Comparison between the UV spectra of crotonaldehyde (Magneron et al., 2002) and butanal (Tadić et al., 2001).

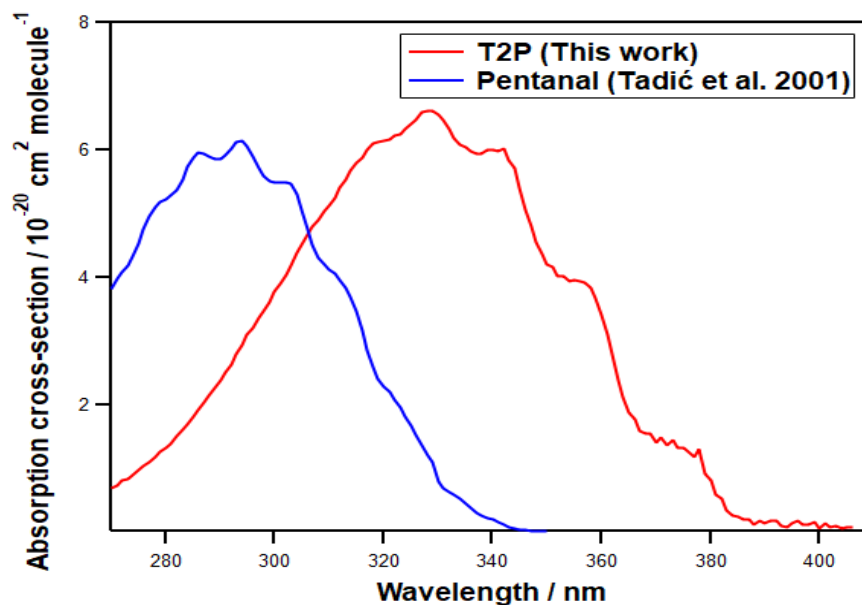


Figure III.10: Comparison between the UV spectra of T2P (this work) and pentanal (Tadić et al., 2001).

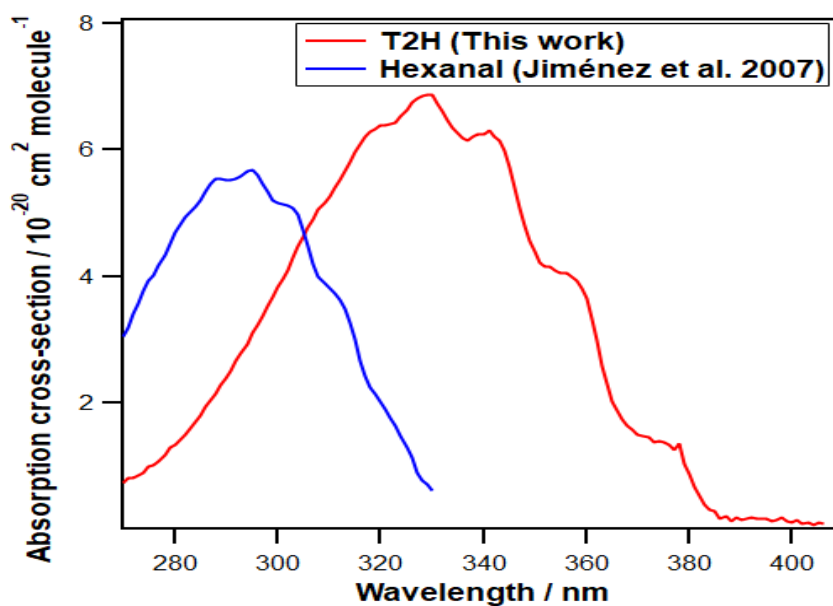


Figure III.11: Comparison between the UV spectra of T2H (this work) and hexanal (Jiménez et al., 2007).

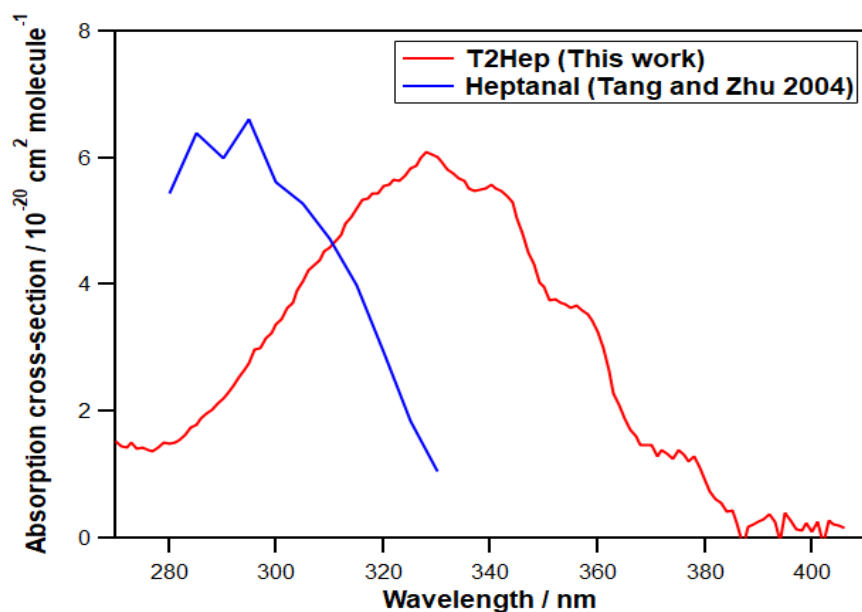


Figure III.12: Comparison between the UV spectra of T2Hep (this work) and heptanal (Tang and Zhu, 2004).

These figures show a shift of the absorption maximum to a longer wavelength (a so-called bathochromic effect that means the shift from lower to higher wavelength): the absorption maximum is shifted from (293 – 295) nm for C₃-C₇ saturated aldehydes to (328 – 336) nm for C₃-C₇ unsaturated aldehydes. The C=C double bond's conjugation can explain this shift with the C=O group leading to an easier excitation of the n and π electrons of the molecule.

III.3.3.4 Calculation of photolysis rate constants

In this work, photolysis rate constants $J(z, \theta)$ of the unsaturated aldehydes in the actinic region at a certain zenith angle (θ) and altitude (z), assuming a quantum yield (Φ) of unity, were determined as explained in section III.3.2.2. In this calculation, we used the calculated UV absorption cross-section $\sigma(\lambda)$ calculated in section 3.2.2. The solar spectral flux $F(z, \theta)$ at z for different zenith angles ($\theta = 20^\circ, 30^\circ, 40^\circ, 50^\circ, 60^\circ, 70^\circ$) were calculated using the TUV software (QUICK TUV CALCULATOR) for wavelengths in the range $290 < \lambda < 400$ nm (Table III.5). This software allows calculating the actinic flux $F(\lambda)$ at a specific zenith angle (θ).

Table III.5: Variation of the photolysis constant (J) of T2P, T2H, and T2Hep for $\theta = 20^\circ - 70^\circ$.

Compound	Photolysis constants (J) / s^{-1}					
	$\theta = 20^\circ$	$\theta = 30^\circ$	$\theta = 40^\circ$	$\theta = 50^\circ$	$\theta = 60^\circ$	$\theta = 70^\circ$
T2P	4.90×10^{-4}	4.55×10^{-4}	4.05×10^{-4}	3.38×10^{-4}	2.53×10^{-4}	1.54×10^{-4}
T2H	5.11×10^{-4}	4.75×10^{-4}	4.23×10^{-4}	3.53×10^{-4}	2.64×10^{-4}	1.61×10^{-4}
T2Hep	4.60×10^{-4}	4.28×10^{-4}	3.81×10^{-4}	3.18×10^{-4}	2.39×10^{-4}	1.46×10^{-4}

The previous table shows that T2H is the most photolyzable compound at all zenith angles with maximum photolysis constant varying between $1.61 \times 10^{-4} s^{-1}$ for $\theta = 70^\circ$ and $5.11 \times 10^{-4} s^{-1}$ for $\theta = 20^\circ$. These values represent higher limits since we note here that the quantum yields were set to 100% for all wavelengths.

On the other hand, O'Connor et al., 2006 observed fast photoisomerization of T2H at the photoreactor EUPHORE (Valencia, Spain) under solar light during summer and detected the presence of Cis-2-Hexanal. The latter was observed before by Magneron et al., 2002, who suggested the photoisomerization of Trans-Crotonaldehyde, in the same photoreactor, and identified its isomer's presence Cis-Crotonaldehyde.

III.4 Conclusion

In this work, experimental IR absorption cross-sections at room temperature of T2P, T2H, and T2Hep have been reported between 650 and 4000 cm^{-1} . The investigation of three studied compounds' IR spectra aims to quantify their concentrations accurately during their oxidation studies at UCLM University. The UV absorption spectra of T2P, T2H, and T2Hep have been determined at room temperature over the spectral range 270 – 410 nm. This work provides the first UV spectrum for T2Hep and the second for T2P. In the case of T2H, it helps to elucidate the existing discrepancy among previous experimental studies (O'Connor et al., 2006, Jiménez et al., 2007, Kalalian et al., 2019). The obtained UV absorption cross-sections show that photolysis may be an important loss process for unsaturated C₅-C₇ aldehydes if it occurs. Photolysis rates of the studied unsaturated aldehydes were calculated using a photolysis quantum yield $\Phi(\lambda)$ equal to 100%, and atmospheric photolysis lifetimes were shown to be theoretically lower than 1 hour (see section IV.2.1.4.4).

Additional studies of photolysis quantum yields are necessary to assess this process's effective role in the atmospheric degradation of unsaturated aldehydes. The results of this work will be published in a paper entitled "IR and UV absorption of C₅-C₇ unsaturated aldehydes: Contribution to the atmospheric transmission and tropospheric lifetimes".

IV Chapter IV: Oxidation of unsaturated aldehydes and alcohols: reaction with ozone

IV.1 Introduction

This chapter aims to display the oxidation of two series of unsaturated aldehydes and alcohols with one of the major diurnal atmospheric oxidants: ozone (O_3), and assess their impact degradation processes on the atmosphere.

This chapter is divided into two parts. The first part is dedicated to the investigation of the ozonolysis reactions of C_5 - C_6 unsaturated aldehydes (Trans-2-Pentenal (T2P) and Trans-2-Hexenal (T2H)) in terms of kinetics, mechanisms, and SOA formations. Besides, the second part deals with the kinetic measurements of the ozonolysis reactions of C_5 - C_8 unsaturated alcohols (Cis-2-Penten-1-ol (C2P-ol), Trans-2-Hexen-1-ol (T2H-ol), Trans-3-Hexen-1-ol (T3H-ol), Cis-3-Hexen-1-ol (C3H-ol), 1-Octen-3-ol (1O-3-ol) and Trans-2-Octen-1-ol (T2O-ol)). These compounds were selected for three main reasons.

Firstly, the selected compounds have been detected with an atmospheric concentration of the order of a few ppbv, particularly C_5 and C_6 compounds. These compounds are emitted from the vegetation into the atmosphere following the enzymatic oxidation of α -linolenic acid in response to biotic and abiotic stresses for microbiological defense purposes (Hatanaka, 1993, Kirstine et al., 1998, Karl et al., 2001, Nakamura and Hatanaka, 2002, Davis et al., 2007, Toome et al., 2010, Peñuelas and Staudt, 2010, Kleist et al., 2012) (see section I.3.2.2). This series of unsaturated alcohols and aldehydes can be formed in situ through almost all organic compounds' photooxidation.

Secondly, these compounds may have a key role in atmospheric chemistry because they undergo various chemical and photolytic reactions (see section I.4) (Johnson and Marston, 2008, Peñuelas and Staudt, 2010). Therefore, it is very important to decipher their Structure-Activity Relationship (SAR) with respect to the presence of a double bond, carbonyl group, and the length of their carbon chain.

Thirdly, the ozonolysis reaction databases for unsaturated aldehydes and alcohols in terms of kinetics, mechanistic studies, and SOA contributions are scattered, scarce or non-existent for the majority of compounds with more than five carbon atoms. The ozonolysis reactions of these unsaturated aldehydes have been fairly investigated in the literature (Table IV.1).

Only two previous measurements on the rate constant of the ozonolysis of T2P have been determined (Sato et al., 2004, Kalalian et al., 2017). Regarding the reaction between T2H and ozone, three rate constants are available in the literature (Atkinson et al., 1995, Grosjean and Grosjean, 1996, Kalalian et al., 2017). Table IV.1 displayed a summary of the rate constants, methods, and analytical techniques used in previous works for studying the kinetic of T2P + O₃ and T2H + O₃ reactions at 298 K.

Table IV.1: Summary of rate constants, methods, and analytical techniques used in previous works of the reactions between C₅-C₆ unsaturated aldehydes and ozone at 298 K.

Reaction	$k \times 10^{18} / \text{cm}^3 \text{ molecule}^{-1} \text{ s}^{-1}$	Method	Analytical technique	Reference
T2P + O ₃	1.59 ± 0.22	RM: Reference compounds: propylene and isobutene	FTIR spectroscopy	Sato et al. 2004
	1.24 ± 0.06	AM: Pseudo-first order: $[\text{O}_3]_0 / [\text{T2P}]_0 \geq 10$	FTIR spectroscopy	Kalalian et al. 2017
T2H + O ₃	2.00 ± 1.00	RM: Reference compound: trans-2-butene	GC-FID	Atkinson et al. 1995
	1.28 ± 0.28	AM: Pseudo-first order: $[\text{T2H}]_0 / [\text{O}_3]_0 \geq 10$	Ozone analyzer	Grosjean et al. 1996
	1.37 ± 0.03	AM: Pseudo-first order: $[\text{O}_3]_0 / [\text{T2H}]_0 \geq 10$	FTIR spectroscopy	Kalalian et al. 2017

RM: Relative Method; AM: Absolute Method.

The present work provides the rate constants of the ozonolysis reactions of T2P and T2H with and without adding an OH scavenger, not only in the batch system (ASC) but also in the continuous system (LFR). Also, the chemical mechanism of the C₅-C₆ unsaturated aldehydes ozonolysis was far from being completely understood.

In this chapter, I displayed a second mechanistic study for T2P + O₃ reaction (after the work done by Kalalian et al. 2018 in her thesis) and a third product study for T2H + O₃ reaction (after works done by Grosjean et al. 1996 and Kalalian et al. 2018).

Mechanism and product distribution of the O₃-initiated degradation of longer carbon chains such as Trans-2-Heptenal, Trans-2-Octenal, and Trans-2-Nonenal has been studied by (Gaona Colmán et al., 2017). The contribution of these ozonolysis reactions to the total particle budget was studied for the first time in the present work.

In the second part of this chapter, we worked on the ozonolysis reaction of a series of C₅-C₈ unsaturated alcohols to complete and enrich the kinetic databases. Studies of the atmospheric degradation of C₅-C₈ unsaturated alcohols are scattered (C2P-Ol, T2H-Ol, T3H-Ol, C3H-Ol), scarce (1O-3-Ol), or non-existent (T2O-Ol). A summary of the literature data is presented in Table IV.2.

Table IV.2: Summary of rate constants, methods, and analytical techniques of previous works of C₅-C₈ unsaturated alcohols and ozone reactions.

Reaction	$k \times 10^{17} / \text{cm}^3 \text{ molecule}^{-1} \text{ s}^{-1}$	Method	Analytical technique	Reference
C2P-Ol + O ₃	16.9 ± 2.5	AM: Pseudo-first order: [C2P-Ol] ₀ / [O ₃] ₀ ≥ 10	Ozone analyzer	Grosjean et al. 1994
	11.5 ± 0.66	AM: Pseudo-first order: [C2P-Ol] ₀ / [O ₃] ₀ ≥ 10	Ozone analyzer	Dwyer et al. 2010
	10.5 ± 1.99	RM: Reference compounds: 2,3-dimethyl-1,3-butadiene and 1-penten-3-ol	FTIR spectroscopy GC-FID	Kalalian et al. 2020
T2H-Ol + O ₃	5.98 ± 0.73	RM: Reference compounds:	FTIR spectroscopy	Gibilisco et al. 2015

		1,4-cyclohexadiene and isoprene		
	16.6 ± 2.2	AM: Pseudo-first order: $[T2H-OI]_0/[O_3]_0 \geq 10$	Ozone analyzer	Lin et al. 2016
T3H-OI + O ₃	5.83 ± 0.86	RM: Reference compounds: 1,4-cyclohexadiene and isoprene	FTIR spectroscopy	Gibilisco et al. 2015
	6.19 ± 0.72	AM: Pseudo-first order: $[T3H-OI]_0/[O_3]_0 \geq 10$	Ozone analyzer	Lin et al. 2016
	6.24 ± 1.37	RM: Reference compounds: 2,3-dimethyl-1,3- butadiene and 1-penten-3-ol	FTIR spectroscopy GC-FID	Kalalian et al. 2020
C3H-OI + O ₃	10.5 ± 0.7	AM: Pseudo-first order: $[C3H-OI]_0/[O_3]_0 \geq 10$	Ozone analyzer	Grosjean et al. 1993
	6.4 ± 1.7	RM: Reference compound: trans-2-butene	GC-FID	Atkinson et al. 1995
	6.04 ± 0.95	RM: Reference compounds: 1,4-cyclohexadiene and isoprene	FTIR spectroscopy	Gibilisco et al. 2015
	5.47 ± 0.71	AM: Pseudo-first order: $[C3H-OI]_0/[O_3]_0 \geq 10$	Ozone analyzer	Lin et al. 2016
	5.96 ± 0.35	AM: Pseudo-first order: $[C3H-OI]_0/[O_3]_0 \geq 10$	Ozone analyzer PTR-MS	Chen et al. 2016

		RM: Reference compounds: 1-choro-3-methyl-2- butene and isoprene		
10-3-0l + O ₃	1.91 ± 0.19	AM: Pseudo-first order: [10-3-0l] ₀ / [O ₃] ₀ ≥ 10	Ozone analyzer	Li et al. 2018
T20-0l + O ₃	NM			

RM: Relative Method; AM: Absolute Method; NM: Not Measured.

IV.2 Oxidation of unsaturated aldehydes with ozone

This work was done in collaboration with Wuppertal University, where experimental work was done together with a trainee during his master's internship (Mr. Jan Niklas Illmann). In this section, I present the kinetic measurements, the gas-phase products, and the formed particles for the ozonolysis reactions of C₅-C₆ unsaturated aldehydes (T2P and T2H). The kinetic measurements and the SOA formations for these oxidation reactions are done in D-ASC (IMT Lille Douai). Simultaneously, the gas-phase products of the ozonolysis of T2P and T2H are performed in QUAREC-ASC (Wuppertal University) and 3m-ASC (Wuppertal University), respectively.

IV.2.1 Determination of rate constants

Before studying the kinetics of C₅-C₆ unsaturated aldehydes' ozonolysis reactions, we started by calibrating the used reactants (aldehydes and ozone), estimating their wall losses onto the LFR and D-ASC wall's. The calibration of the used reagents is needed to determine an accurate concentration for both reagents since we used the absolute method for kinetic measurements.

IV.2.1.1 Preliminary experiments

This section displays the calibration curves for the reagents (T2P, T2H, and O₃) and their wall losses in LFR and D-ASC experiments. All the presented experiments were done at room temperature and atmospheric pressure.

IV.2.1.1.1 Calibration and wall losses of unsaturated aldehydes

a) In LFR

In the LFR set-up, analyses were performed using the GC-MS device. The calibration curves for T2P and T2H were completed within the range of concentrations $(0.5 - 2.5) \times 10^{14}$ molecule cm^{-3} and $(1 - 4) \times 10^{14}$ molecule cm^{-3} , respectively. The experimental procedure started by adding a flow of the studied aldehyde (T2P or T2H) from the prepared canister (see section II.2.2.1), mixing with zero air flow at the injecting head of the LFR. Three gas analyses were performed by GC-MS/FID device. In Figure IV.1, I showed a chromatogram of T2H measured in LFR.

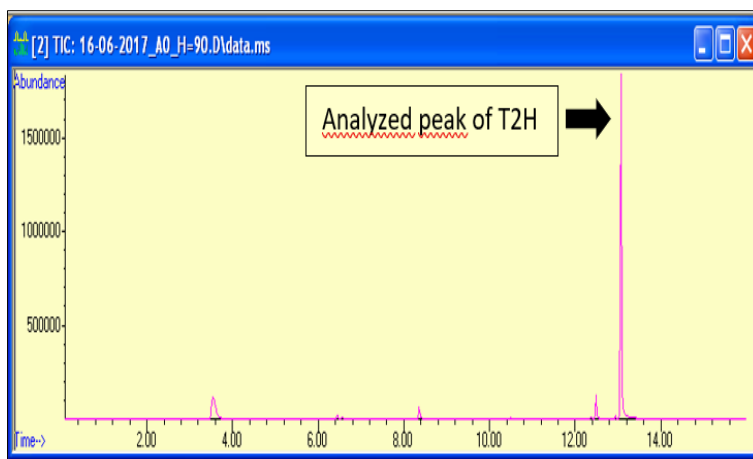


Figure IV.1: Chromatogram of T2H measured in LFR.

The averages of the major peak areas located at retention time (t_R) between 12 and 14 minutes were then plotted as a function of the calculated aldehyde concentration ($[\text{T2P}]_0$ or $[\text{T2H}]_0$) as shown in Figure IV.2.a and Figure IV.2.b for T2P and T2H, respectively.

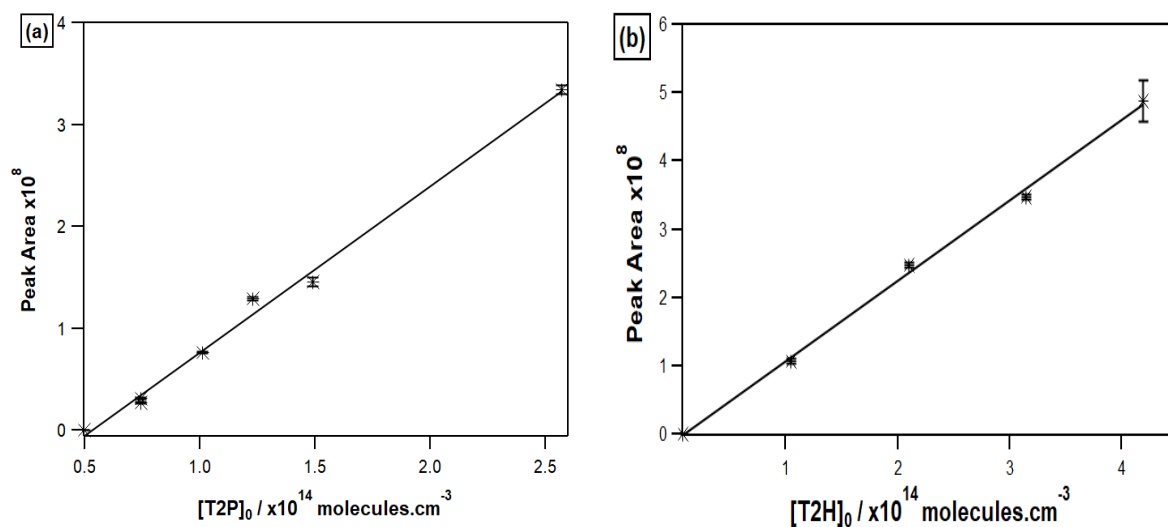


Figure IV.2: Peak Area measured by GC-MS/FID in LFR versus the calculated concentration of the aldehyde ((a) for T2P and (b) for T2H).

Both calibration curves (for T2P and T2H) have good linearity ($R^2 > 99.5\%$). These plots' slopes allow us to calculate the aldehydes' concentrations in the tested concentration ranges by analyzing their chromatogram using GC-MS.

To estimate the losses of both studied aldehyde on the LFR walls, we measured the area of their major peaks for 2 hours. The reported values reflect small fluctuations. Only a coefficient of variation (CV, expressed as the ratio of one standard deviation to the mean value for a specific measurement time) can be calculated. Both aldehydes were shown to be stable with a CV of about 2.05% and 4% for 2 hours of T2P and T2H concentrations, respectively.

b) In D-ASC

In the D-ASC set-up, analyses were done using the FTIR spectrometer. The calibrations of both studied aldehydes were prepared within the concentration ranges $(0.5 - 1.0) \times 10^{15}$ molecule cm⁻³ and $(1 - 7) \times 10^{14}$ molecule cm⁻³ for T2P and T2H, respectively. The Aldehyde was injected directly into the inlet of the D-ASC using a microsyringe (section II.2.1.2.1) through a flow of zero air, which allows the transport of the compound to the chamber. Three gas samples were taken online using the FTIR spectrometer.

The averages of the peak areas were then plotted as a function of the aldehyde concentration calculated theoretically. Figure IV.3 displays an example of the T2H spectrum measured in D-ASC.

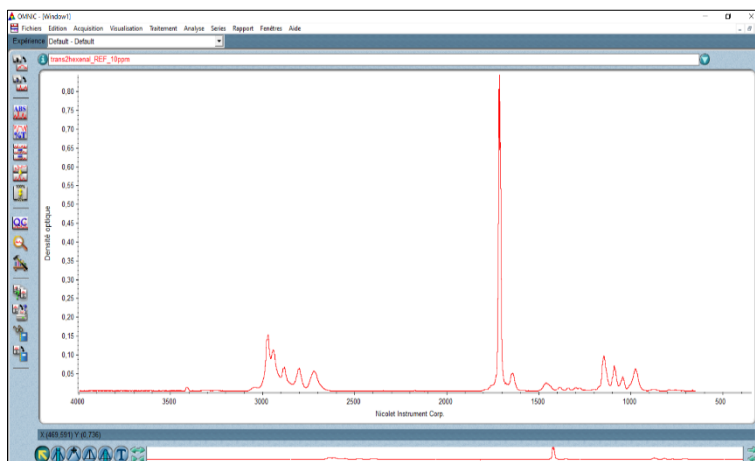


Figure IV.3: T2H spectrum measured in D-ASC in the range (650 – 4000 cm^{-1}).

The used band for T2P and T2H were (1117 – 1170 cm^{-1}) and (1114 – 1172 cm^{-1}), respectively. The average of three peak areas was plotted as a function of the studied aldehyde's calculated concentration. Figure IV.4.a and Figure IV.4.b displayed the calibration curves of T2P and T2H, respectively.

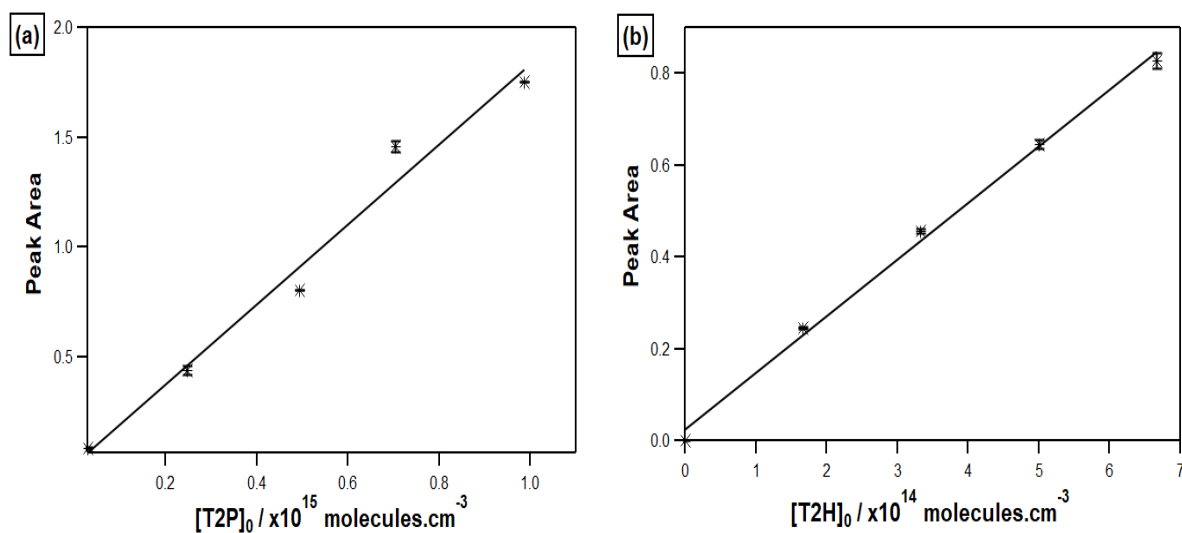


Figure IV.4: Peak Area measured by FTIR spectrometer in D-ASC versus the calculated concentration of the aldehyde ((a) for T2P and (b) for T2H).

The two calibration curves have good linearity ($R^2 > 98\%$). The slope of each plot allows calculating the aldehyde concentration as explained above for the aldehyde calibration in LFR using GC-MS. Wall losses of both compounds in D-ASC were also investigated to reduce the possible errors in calculating the aldehyde concentrations. A concentration of about 1×10^{15} molecule cm^{-3} and 2×10^{14} molecule cm^{-3} for T2P and T2H, respectively, are injected in D-ASC. For 6 hours of analysis, a coefficient of variation of T2P and T2H concentration was 0.39% and 1.04%, respectively. The possible losses of the studied aldehydes can be considered negligible during 1 hour of reaction time.

IV.2.1.1.2 Calibration and wall losses of ozone

It should be underlined that the measurement of ozone was done directly by O_3 , and no calibration curve is needed to know the O_3 concentrations in LFR and D-ASC. On the other hand, the measurement of ozone losses inside both reactors was mandatory to determine the T2P and T2H ozonolysis rate constant since we used the pseudo-first-order conditions (see section II.4.1.2.1).

a) In LFR

In LFR experiments, ozone was directly sent from the O_3 generator to the reactor's injection head via a zero airflow and measured using an O_3 analyzer. To analyze O_3 losses, I injected 14.8×10^{12} molecule cm^{-3} of ozone inside LFR (this concentration of O_3 was used in the kinetic study), and I measured the concentration of O_3 every 10 minutes during 40 minutes. The coefficient variation of ozone concentration was lower than 0.5% for 40 min. However, the reaction time in LFR did not exceed a few minutes. Therefore, the loss of ozone in the LFR was considered negligible.

b) In D-ASC

In D-ASC experiments, ozone was generated and analyzed as described above for LFR. The only difference here is that O_3 was injected using a syringe in a purified air flow (D-ASC is a batch system). The analysis of O_3 concentrations in the absence of aldehyde gives the O_3 decay in D-ASC. In Figure IV.5, I displayed the O_3 decay for 3 hours of measurement for 3.9×10^{12} molecule cm^{-3} of ozone in D-ASC.

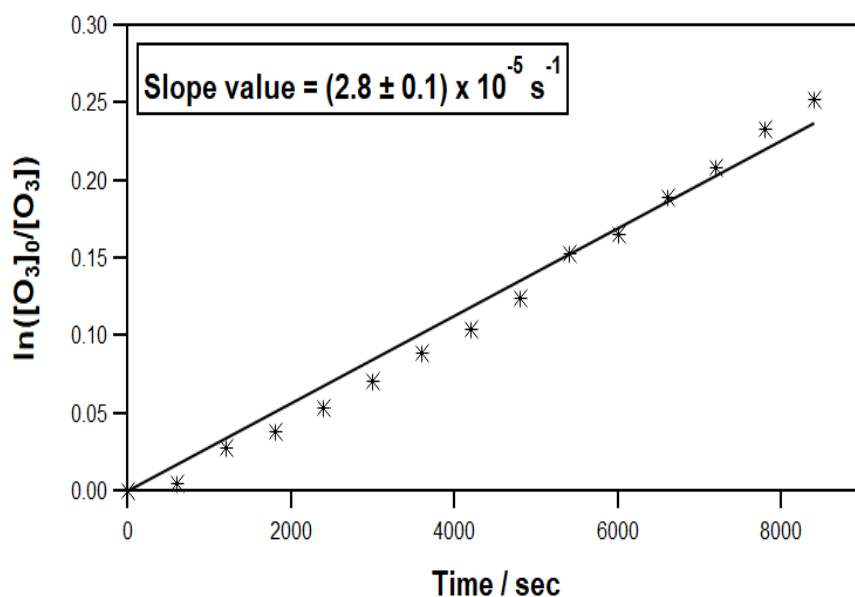


Figure IV.5: The plot of $\ln ([O_3]_0/[O_3])$ versus time for the wall losses of ozone ($[O_3]_0 = 3.9 \times 10^{12}$ molecule cm^{-3}) in D-ASC (the error is 2σ).

The rate constant of ozone loss onto D-ASC walls was $(2.8 \pm 0.1) \times 10^{-5} \text{ s}^{-1}$ for 3.9×10^{12} molecule cm^{-3} of ozone. This rate constant was considered in the measurement of T2P and T2H ozonolysis in D-ASC.

IV.2.1.2 Experimental conditions and protocols

All experiments were carried out at room temperature and atmospheric pressure using the absolute method under the pseudo-first-order condition ($[Ald]_0/[O_3]_0 > 10$). Kinetic studies were investigated for the first time in LFR (continuous system) and then in D-ASC (batch system). In LFR, the kinetic studies of the aldehydes ozonolysis reactions were done without adding an OH scavenger. On the other hand, D-ASC experiments were carried out without and with adding an OH scavenger (cyclohexane). The pseudo-first-order rate constants (k') and the rate constants (k_{Ald+O_3}) were determined as explained in section II.4.1.2.1. I will describe the kinetic studies' experimental protocols in LFR and D-ASC in the next two sections.

a) In LFR

A typical experiment was performed as follows: the unsaturated aldehyde was introduced from the canister to the injection head of LFR via a continuous flow of purified air. The mixture was allowed to homogenize and stabilize for 30 min. Four samples were taken online via the GC-MS/FID apparatus to determine the studied aldehyde's initial concentration $[Ald]_0$. Then, ozone was produced using an O_3 generator and added at the injection head via zero air flow. The reaction progress depends on the head position and the total flow rate. The remaining ozone is measured at each position of the reactor's head using an O_3 analyzer (see section II.2.2.2.1).

b) In D-ASC

The experiment procedure starts with injecting the studied aldehyde into D-ASC using a microsyringe in a purified air flow. The reaction mixture is allowed to homogenize for around 30 min. Three samples were then taken via online sampling to the FTIR spectrometer to determine the studied aldehyde's initial concentration $[Ald]_0$. OH radicals could be generated through Criegee intermediates formed during the oxidation of the unsaturated aldehydes.

Therefore, a part of D-ASC experiments was carried by adding an excess quantity of cyclohexane to trap the OH radicals (Aschmann et al., 1997, Alam et al., 2011). The reaction mixture (aldehyde+cyclohexane) was allowed to homogenize for 1 hour. The initial cyclohexane concentration was calculated as explained before (see section II.4.2.2). I mention that no estimation for OH yields was assumed in this section.

Three samples were analyzed by FTIR spectrometer to quantify the initial concentration of reactants and to verify if there was any possible interference between their analyzed IR bands. Finally, ozone was introduced into the reactor using a syringe, and continuous O_3 measurements were performed over time. All the experimental conditions used for kinetic studies of T2P and T2H ozonolysis are summarized in Table IV.3.

Table IV.3: Summary of experimental conditions used for the kinetic studies of T2P and T2H ozonolysis.

Reaction	Reactor	Number of experiments	[Ald] ₀ × 10 ¹⁴ /molecule cm ⁻³	[O ₃] ₀ × 10 ¹² /molecule cm ⁻³	[Cyclohexane] ₀ × 10 ¹⁵ /molecule cm ⁻³
T2P + O ₃	LFR	5	2 – 6.9	≈ 13.5	0
	D-ASC	5	0.9 – 2.9	2.7-10.8	0
		2	0.9 – 10.7	≈ 2.7	9.0 – 23.9
T2H + O ₃	LFR	6	1.6 – 6.2	≈ 13.5	0
	D-ASC	3	0.8 – 3.0	2.8-13	0
		2	1.0	≈ 2.7	9.9 – 21.7

Sigma Aldrich provided the used compound's purities: T2P (≥ 95%), T2H (98%), cyclohexane (≥ 99%), O-(2,3,4,5,6-Pentafluorobenzyl), hydroxylamine hydrochloride (PFBHA) (≥ 98%), and dimethyl ether (≥ 99.99%) and they were used without further purification. The bath gases were provided by Air Liquide: Air (> 99.9999%), O₂ (> 99.9999%), He (> 99.9999%).

IV.2.1.3 Results

IV.2.1.3.1 Rate constant of T2P + O₃

The decay of ozone was measured for different concentrations of T2P. Representative plots of $\ln([O_3]_0/[O_3])$ as a function of reaction time for different initial concentrations of T2P are presented in Figure IV.6.a (LFR), in Figure IV.7.a (D-ASC without an OH scavenger), and Figure IV.8.a (D-ASC with an OH scavenger). Data were fitted with linear regression lines. The slopes of $\ln([O_3]_0/[O_3])$ versus the reaction time give the pseud-first order rate constants (k'). The k' values are plotted as a function of the initial concentrations of T2P ($[T2P]_0$), which allows determining the second-order rate constant k_{T2P+O_3} of the reaction between T2P and O₃ in LFR (Figure IV.6.b) in D-ASC without an OH scavenger (Figure IV.7.b) and in D-ASC with an OH scavenger (Figure IV.8.b). The average rate constant was calculated, and the error on k_{T2P+O_3} is discussed below.

a) In LFR

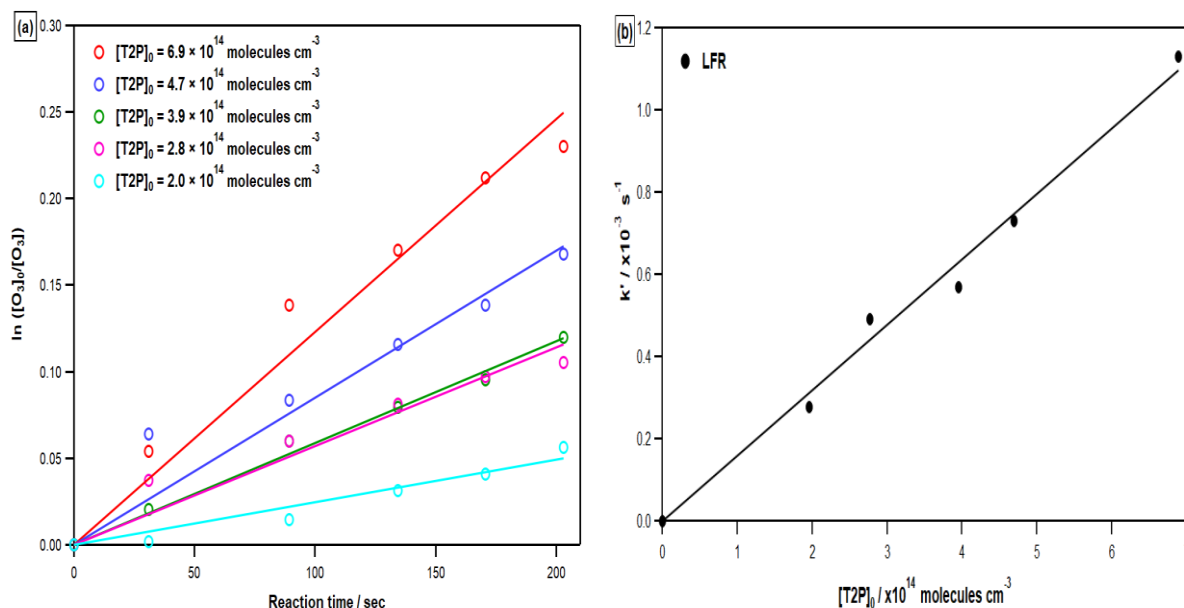


Figure IV.6: Kinetic measurement of T2P + O₃ reaction in LFR at 298 K: (a) plot of the ozone decay vs. reaction time and (b) plot of pseudo-order rate constant (k') vs. $[T2P]_0$.

Note that the reaction's extent is rather low (consumption of O₃ below 25% of its initial value) due to the limited reaction time in LFR.

b) In D-ASC without an OH scavenger

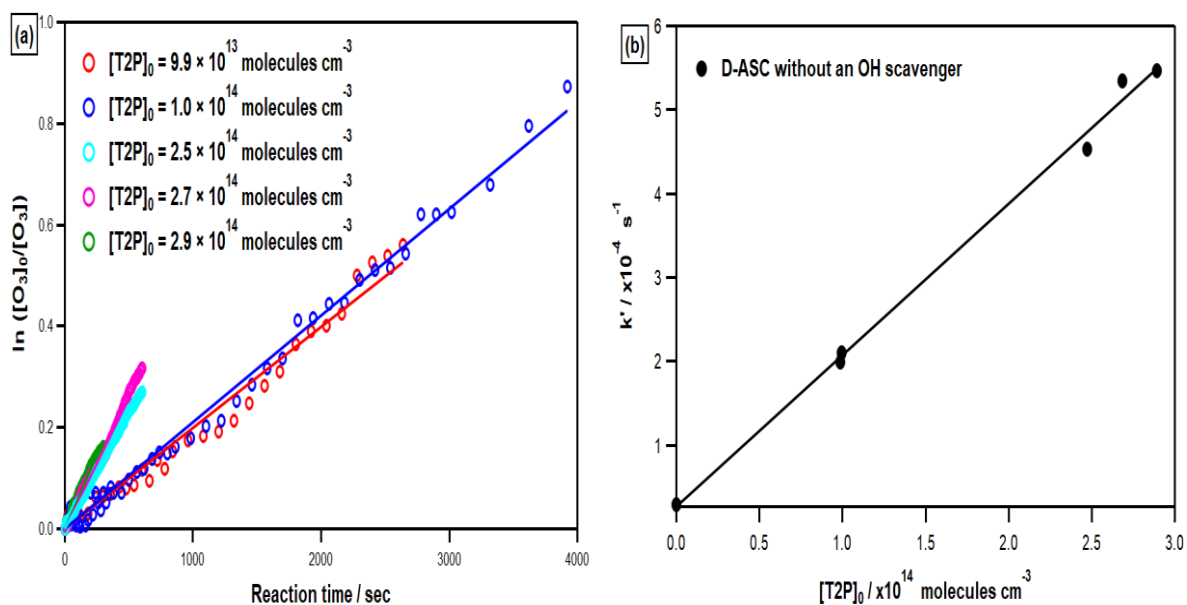


Figure IV.7: Kinetic measurement of T2P + O₃ reaction in D-ASC without an OH scavenger at 298 K: (a) plot of the ozone decay vs. reaction time and (b) plot of pseudo-order rate constant (k') vs. [T2P]₀.

c) In D-ASC with an OH scavenger

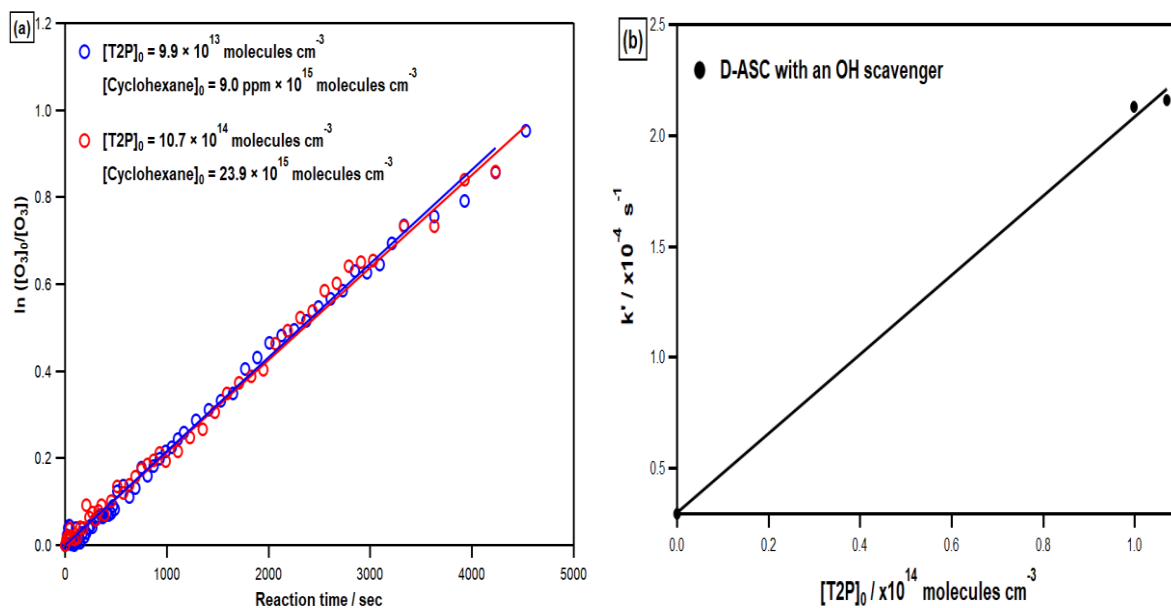


Figure IV.8: Kinetic measurement of T2P + O₃ reaction in D-ASC with an OH scavenger at 298 K: (a) plot of the ozone decay vs. reaction time and (b) plot of pseudo-order rate constant (k') vs. [T2P]₀.

All obtained second-order rate constants of the T2P + O₃ reaction were summarized in Table IV.4.

Table IV.4: Summary of determined rate constants for T2P ozonolysis.

Reactor	Scavenger	$k_{T2P+O_3} \times 10^{18} / \text{cm}^3 \text{ molecule}^{-1} \text{ s}^{-1}$
LFR	No	$1.59 \pm 0.08^{(a)}$
D-ASC	No	$1.80 \pm 0.12^{(a)}$
	Yes	$1.78 \pm 0.16^{(a)}$
Average		$1.72 \pm 0.23^{(b)}$

^(a) Uncertainty is 2 σ on the slope.

^(b) Uncertainty is 2 σ on the three rate constants studied in different set-ups.

As we can see, the rate constant of the T2P ozonolysis with the presence of an OH scavenger is only 1.1% lower than the one determined in the absence of an OH scavenger. Statistical errors on second-order rate constant k_{T2P+O_3} studied in different set-ups are (2σ) resulting from the fitting procedure on Figure IV.6.b – Figure IV.8.b. The global statistical error on k calculates as (2σ) on the three determined values and represents 13.4%. $[T2P]_0$ is determined with an uncertainty of about 10% arising from the calibration procedure. Then, propagating the error results in a global uncertainty on k_{T2P+O_3} of about 16.7% ($\sqrt{10^2 + 13.4^2}$).

IV.2.1.3.2 Rate constant of T2H + O₃

The analysis of T2H + O₃ kinetic measurements was done exactly as T2P + O₃ kinetic measurements (see section IV.2.1.3.1). I plotted the decay of ozone $\ln([O_3]_0/[O_3])$ versus the reaction time for different initial concentrations of T2H in Figure IV.9.a (LFR), Figure IV.10.a (D-ASC without an OH scavenger), and in Figure IV.11.a (D-ASC with an OH scavenger). Data were linearly fitted, and the slopes represent the pseudo-first-order rate constants (k'). The k' values are plotted as a function of the initial concentrations of T2H ($[T2H]_0$), which allows determining the second-order rate constant k_{T2H+O_3} of the reaction between T2H and O₃ in LFR (Figure IV.9.b) in D-ASC without an OH scavenger (Figure IV.10.b) and in D-ASC with an OH scavenger (Figure IV.11.b). The average rate constant was calculated, and the error on k_{T2H+O_3} is discussed below.

a) In LFR

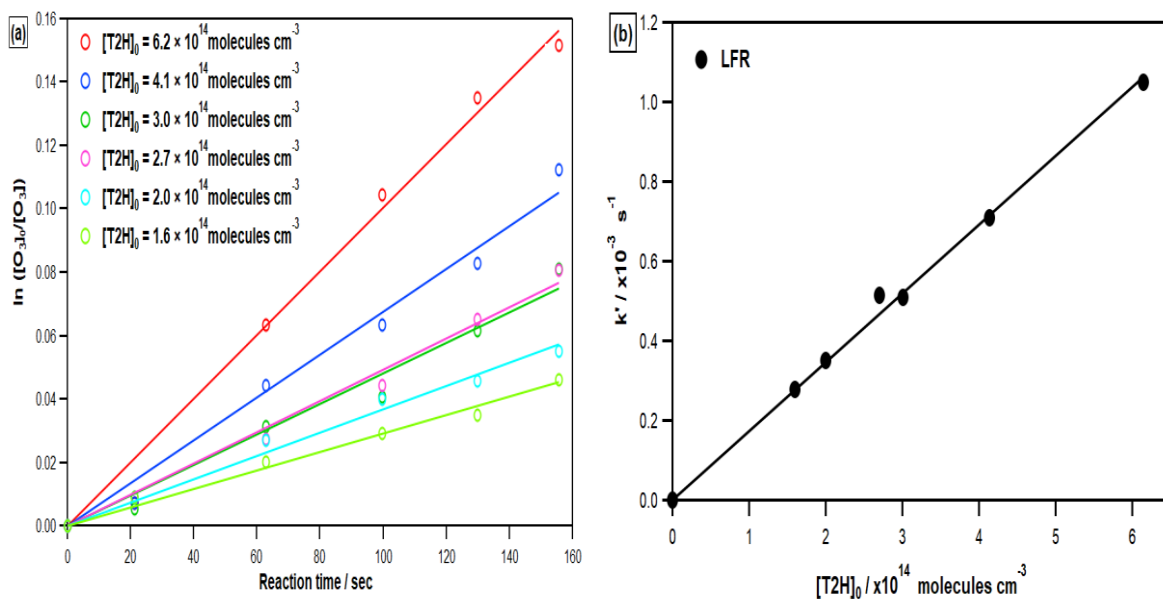


Figure IV.9: Kinetic measurement of T2H + O₃ reaction in LFR at 298 K: (a) plot of the ozone decay vs. reaction time and (b) plot of pseudo order rate constant (k') vs. $[T2H]_0$.

Note that the reaction's extent is rather low (consumption of O₃ below 20% of its initial value) due to the limited reaction time in LFR.

b) In D-ASC without an OH scavenger

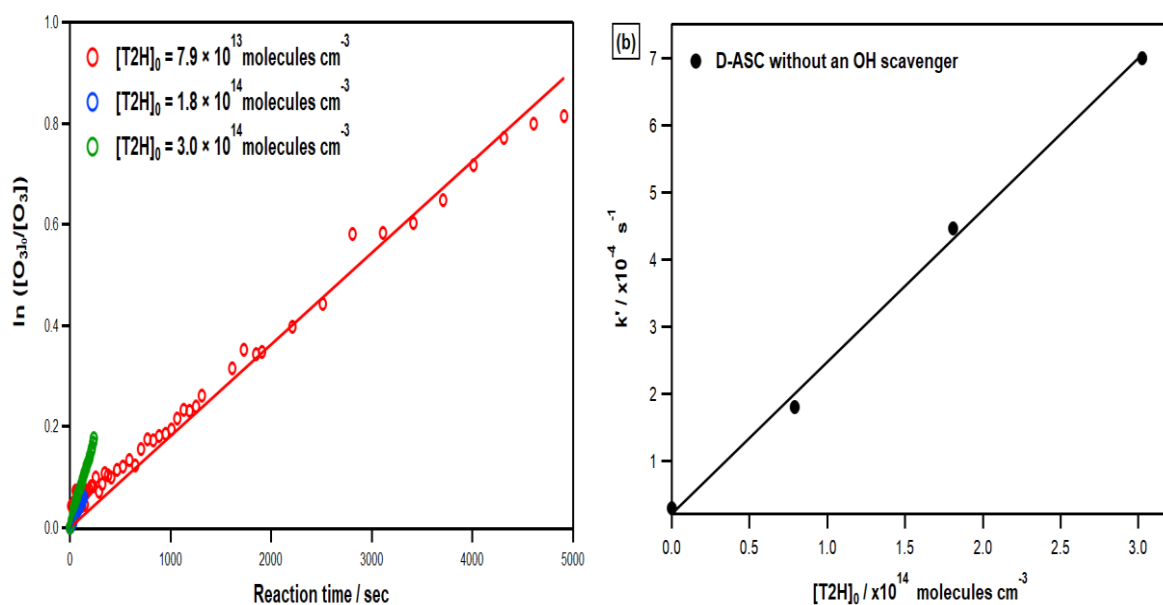


Figure IV.10: Kinetic measurement of T2H + O₃ reaction in D-ASC without an OH scavenger at 298 K: (a) plot of the ozone decay vs. reaction time and (b) plot of pseudo order rate constant (k') vs. [T2H]₀.

c) In D-ASC with an OH scavenger

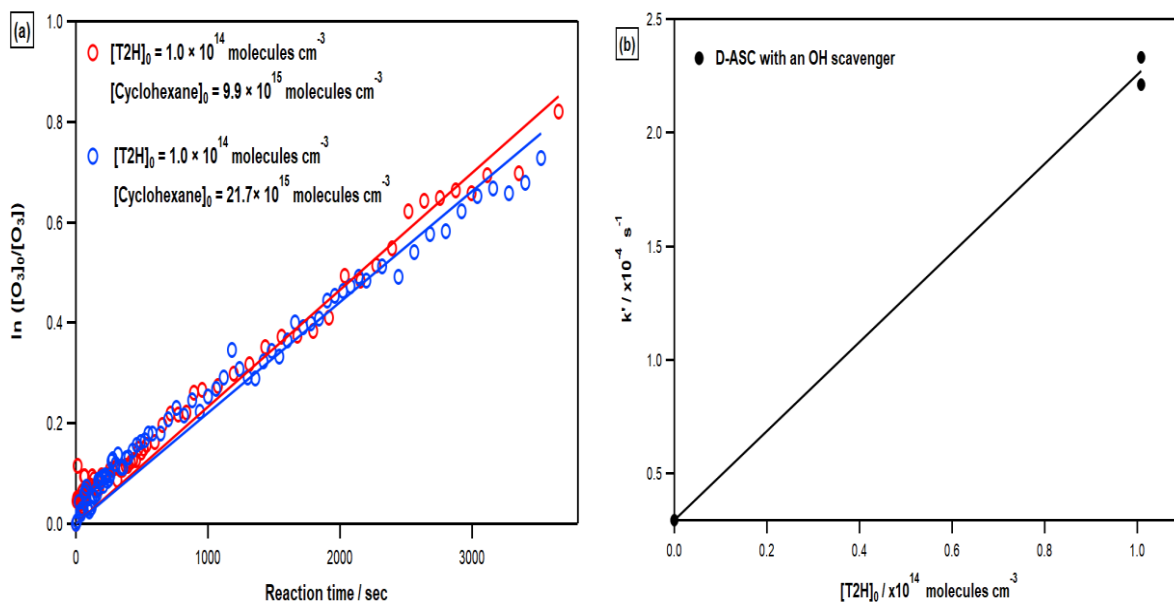


Figure IV.11: Kinetic measurement of T2H + O₃ reaction in D-ASC with an OH scavenger at 298 K: (a) plot of the ozone decay vs. reaction time and (b) plot of pseudo order rate constant (k') vs. [T2H]₀.

All obtained second-order rate constants of the T2H + O₃ reaction were summarized in Table IV.5.

Table IV.5: Summary of determined rate constants for T2H ozonolysis.

Reactor	Scavenger	$k_{\text{T2H+O}_3} \times 10^{18} / \text{cm}^3 \text{ molecule}^{-1} \text{ s}^{-1}$
LFR	No	$1.73 \pm 0.05^{(a)}$
D-ASC	No	$2.26 \pm 0.17^{(a)}$
	Yes	$1.96 \pm 0.20^{(a)}$
Average		$1.98 \pm 0.53^{(b)}$

^(a) Uncertainty is 2 σ on the slope.

^(b) Uncertainty is 2 σ on the three rate constants studied in different set-ups.

As we can see, the rate constant of the T2H ozonolysis with adding an OH scavenger is lower than the one determined without adding an OH scavenger with 13.3%. Statistical errors on second-order rate constant k_{T2H+O_3} studied in different set-ups are (2σ) resulting from the fitting procedure on Figure IV.9.b – Figure IV.11.b. The global statistical error (2σ) on k calculated on the three determined values is 26.8%. $[T2H]_0$ is determined with an uncertainty of about 10% arising from the calibration procedure. Then, propagating the error results in a global uncertainty on k_{T2H+O_3} leads to about 28.6% ($\sqrt{10^2 + 26.8^2}$).

IV.2.1.4 Discussion

IV.2.1.4.1 Comparison with literature data

The obtained rate constants for C₅-C₆ unsaturated aldehydes are compared to the ones measured in previous works. Two previous works studied the kinetic of T2P ozonolysis also in the simulation chamber. Sato et al., 2004 used the relative method and found $(1.59 \pm 0.22) \times 10^{-18} \text{ cm}^3 \text{ molecule}^{-1} \text{ s}^{-1}$. On the other hand, Kalalian et al., 2017 measured the rate constant of the reaction between T2P and ozone using the absolute method in the pseud-first order condition with an excess of ozone, and they got $(1.24 \pm 0.06) \times 10^{-18} \text{ cm}^3 \text{ molecule}^{-1} \text{ s}^{-1}$. The present work is in very good agreement with Sato et al. and is consistent with Kalalian et al., considering the uncertainties (Table IV.6).

Regarding the kinetic measurement of the rate constant of the T2H + O₃ reaction, the first determination was done by Atkinson et al., 1995 using the relative method, and they reported a value of $(2 \pm 1) \times 10^{-18} \text{ cm}^3 \text{ molecule}^{-1} \text{ s}^{-1}$. Grosjean et al., 1996 used pseudo-first-order conditions with T2H in excess (as in the present study) and obtained a value of $(1.28 \pm 0.28) \times 10^{-18} \text{ cm}^3 \text{ molecule}^{-1} \text{ s}^{-1}$. Kalalian et al., 2017 obtained $(1.37 \pm 0.03) \times 10^{-18} \text{ cm}^3 \text{ molecule}^{-1} \text{ s}^{-1}$ in absolute rate experiments with O₃ in excess. As can be seen, the present value agrees very well with Atkinson et al. and is consistent with Grosjean et al., and Kalalian et al., considering the reported uncertainties.

IV.2.1.4.2 Effect of the chain length and the C=C position

The rate constants determined for the T2P + O₃ and T2H + O₃ reactions are in the same order of magnitude as those of other 2-alkenals: crotonaldehyde (or 2-butenal, Grosjean and Grosjean 1998, Sato et al. 2004), Trans-2-Heptenal, Trans-2-Octenal and Trans-2-Nonenal (Colmán et al., 2015) as listed in Table IV.6. However, these C₄-C₉ 2-alkenals rate constants are significantly higher than those reported for acrolein (or 2-propenal, $\leq 3.6 \times 10^{-19}$ cm³ molecule⁻¹ s⁻¹, (Al Mulla et al., 2010)). The latter suggests that the electronic density of the C=C bond in acrolein is lower than in longer chain 2-alkenals.

The conjugation of the two π systems (C=O and C=C) in acrolein may be more important than other longer unsaturated aldehydes and yields lower rate constants with O₃. Quantum chemistry calculations on a series of 2-alkenals may help understand the origin of acrolein's lower reactivity towards O₃. Besides, the carbon chain length seems to have an activating effect on the rate constant of their ozonolysis reactions, especially if we compare C₄-C₅ unsaturated aldehydes vs. C₆-C₉ unsaturated aldehydes.

To better understand the C=C bond position effect, the rate constants of 2-alkenals have to be compared with similar 3-alkenals. Unfortunately, only one literature data was found: the rate constant of the ozonolysis of Cis-3-Hexenal $(35 \pm 2) \times 10^{-18}$ cm³ molecule⁻¹ s⁻¹ (Xing et al., 2012). This value is more than 17 times higher than the rate constant of the ozonolysis of T2H, which may indicate that the C=C bond closer to C=O has a deactivating effect on the reactivity of the molecule versus ozone. This result is not definitive since we miss having more data on 3-alkenals to better discuss this effect.

Table IV.6: Summary of the rate constants for the reactions of a series of C₃-C₉ alkenals with ozone at room temperature and atmospheric pressure.

Compound Linear formula	$k \times 10^{18} /$ cm ³ molecule ⁻¹ s ⁻¹	Reference
2-Propenal or Acrolein (CH ₂ =CH-CHO)	0.28 ± 0.05	Atkinson et al., 1981
	0.3 ± 0.04	Treacy et al., 1992
	0.26 ± 0.05	Grosjean et al., 1993
	0.36 ± 0.035	Al Mulla et al., 2010

2-Butenal or Crotonaldehyde (CH ₃ -CH=CH-CHO)	1.74 ± 0.20	Grosjean and Grosjean, 1998
	1.58 ± 0.23	Sato et al., 2004
Trans-2-Pentenal (T2P) (CH ₃ -CH ₂ -CH=CH-CHO)	1.59 ± 0.22	Sato et al., 2004
	1.24 ± 0.06	Kalalian et al., 2017
	1.72 ± 0.23	This work
Trans-2-Hexenal (T2H) (CH ₃ -CH ₂ -CH ₂ -CH=CH-CHO)	2.00 ± 1.00	Atkinson et al., 1995
	1.28 ± 0.28	Grosjean et al., 1996
	1.37 ± 0.03	Kalalian et al., 2017
	1.98 ± 0.53	This work
Trans-2-Heptenal (CH ₃ -CH ₂ -CH ₂ -CH ₂ -CH=CH-CHO)	2.47 ± 0.73	Colmán et al., 2015
Trans-2-Octenal (CH ₃ -CH ₂ -CH ₂ -CH ₂ -CH ₂ -CH=CH-CHO)	2.37 ± 0.68	Colmán et al., 2015
Trans-2-Nonenal (CH ₃ -CH ₂ -CH ₂ -CH ₂ -CH ₂ -CH ₂ -CH=CH-CHO)	2.05 ± 0.20	Colmán et al., 2015

IV.2.1.4.3 Effect of the carbonyl group

To better understand the effect of the carbonyl group on the reactivity of unsaturated aldehydes, the obtained rate constant for the ozonolysis of unsaturated aldehydes can be compared to the rate constants of the ozonolysis of alkenes such as Trans-2-Pentene ($162 \times 10^{-18} \text{ cm}^3 \text{ molecule}^{-1} \text{ s}^{-1}$) and Trans-2-Hexene ($155 \times 10^{-18} \text{ cm}^3 \text{ molecule}^{-1} \text{ s}^{-1}$) which Avzianova and Ariya, 2002 determined. The rate constant for the studied aldehyde is 100 times lower than its homologous alkene. A similar trend is observed for crotonaldehyde/Trans-2-Butene (Greene and Atkinson, 1992, Avzianova and Ariya, 2002, Wegener et al., 2007). The latter shows the strong deactivating effect of the carbonyl group on the reactivity of the C=C double bond towards ozone in the case of 2-alkenals. As noted above, this may be due to the conjugation of the two π systems.

Table IV.7: Summary of the rate constants for the reactions of a series of C₄-C₆ alkenes with ozone at room temperature and atmospheric pressure.

Compound Linear formula	$k \times 10^{18} /$ $\text{cm}^3 \text{ molecule}^{-1} \text{ s}^{-1}$	Reference
Trans-2-Butene ($\text{CH}_3\text{CH}=\text{CHCH}_3$)	217 ± 16 182 ± 1.1 125 ± 31	Greene and Atkinson, 1992 Avzianova and Ariya, 2002 Wegener et al., 2007
Trans-2-Pentene ($\text{CH}_3\text{CH}=\text{CHCH}_2\text{CH}_3$)	162 ± 0.6	Avzianova and Ariya, 2002
Trans-2-Hexene ($\text{CH}_3\text{CH}=\text{CHCH}_2\text{CH}_2\text{CH}_3$)	155 ± 0.6	Avzianova and Ariya, 2002

IV.2.1.4.4 Atmospheric implications

Atmospheric lifetimes (τ_{Oxi} and τ_{UV}) due to the oxidation of the C₅-C₇ unsaturated aldehydes or their photolysis were estimated using the equation (Eq.30) and (Eq.31), respectively, and both were displayed in section II.4.1.3. I note that not only atmospheric lifetimes of T2P and T2H were calculated here, but also the atmospheric lifetimes of Trans-2-Heptenal (T2Hep) (see chapter V). The oxidant concentrations of OH, Cl, O₃, and NO₃ were detailed in section II.4.1.3. The calculated atmospheric lifetimes were summarized in Table IV.8.

Table IV.8: Calculated atmospheric lifetimes of C₅-C₇ unsaturated aldehydes towards atmospheric oxidants (Cl, O₃, NO₃, and OH) and photolysis.

Compound	$\tau_{\text{Cl-high}}$ (h)	$\tau_{\text{Cl-low}}$ (days)	τ_{O_3} (days)	τ_{NO_3} (h)	τ_{OH} (h)	τ_{UV} (min)
T2P	11 (a)	47 (a)	8 (d)	32 (g)	8 (j)	35 (m)
T2H	11 (b)	44 (b)	7 (e)	32 (h)	7 (k)	34 (m)
T2Hep	9 (c)	36 (c)	5 (f)	17 (i)	8 (l)	38 (m)

(a) k (T2P + Cl) is the average of Rodríguez et al., 2005, Teruel et al., 2009 and this work (see chapter V).

(b) k (T2H + Cl) is the average of Rodríguez et al., 2005 and this work (see chapter V).

(c) k (T2Hep + Cl) is the average of Rodríguez et al., 2005 and this work (see chapter V).

(d) k (T2P + O₃) is the average of Sato et al., 2004, Kalalian et al., 2017, and this work (chapter IV).

^(e) $k(T2H + O_3)$ is the average of Atkinson et al., 1995, Grosjean et al., 1996, Kalalian et al., 2017, and this work (see chapter IV).

^(f) $k(T2Hep + O_3)$ is the value of Colmán et al., 2015.

^(g) $k(T2P + NO_3)$ is the average of Grosjean and Williams, 1992, Cabanas et al., 2001, Zhao et al., 2011, and Rayez et al., 2014.

^(h) $k(T2H + NO_3)$ is the average of Grosjean and Williams, 1992, Cabanas et al., 2001, Zhao et al., 2011, Kerdouci et al., 2012, and Rayez et al., 2014.

⁽ⁱ⁾ $k(T2Hep + NO_3)$ is the average of Cabanas et al., 2001, Zhao et al., 2011, Kerdouci et al., 2012, and Rayez et al., 2014.

^(j) $k(T2P + OH)$ is the average of Grosjean and Williams, 1992, Albaladejo et al., 2002, Davis et al., 2007, and this work (see chapter VI).

^(k) $k(T2H + OH)$ is the average of Grosjean and Williams, 1992, Atkinson et al., 1995, Albaladejo et al., 2002, Davis et al., 2007, Jiménez et al., 2007 and Gao et al., 2009.

^(l) $k(T2Hep + OH)$ is the average of Albaladejo et al., 2002 and Davis et al., 2007.

^(m) The photolysis constants of June 30 at 12 h for Paris are used to calculate the lifetime (zenith angle=26°) (see chapter III).

According to Table IV.8, unsaturated aldehydes are mainly removed in the troposphere by photolysis ($\tau_{uv} < 1h$). I mention that the lifetimes against photolysis correspond to an upper limit since the quantum yield was unity. For instance, the photolysis of T2H ($1.5 \times 10^{-4} s^{-1}$) was measured experimentally by O'Connor et al., 2006 upon sunlight photolysis at EUPHORE. It was 31% lower than the calculated value in this work. It should be noted that T2H showed photoisomerization into Cis-2-Hexenal (see section III.3.3.4).

Lifetimes of C₅-C₇ unsaturated aldehydes due to the OH oxidation are typically less than 8 hours ($\tau_{OH} \leq 8h$). Simultaneously, those due to the Cl reaction are similar only at the marine boundary layer's specific conditions where Cl concentration is high ($\tau_{Cl-High} \leq 11h$). At a typical Cl concentration, the atmospheric degradation of these compounds initiated by OH predominates those initiated by Cl atoms. Also, reactions with ozone at daytime ($\tau_{O_3} \leq 8$ days) and NO₃ radicals at night time ($\tau_{NO_3} \leq 2$ days) are ultimately responsible for the atmospheric removal of unsaturated aldehydes.

IV.2.2 Determination of gas-phase products

As with olefinic compounds, the reaction between unsaturated aldehydes and ozone is initiated by the electrophilic addition of ozone to the C=C double bond to form a primary ozonide. This primary ozonide is not stable and decomposes rapidly to give two primary carbonyl compounds (aldehyde or ketone) and two intermediates called "Criegee" intermediates. The mechanisms of ozone-alkene reactions in the gas phase are detailed elsewhere in different publications (Criegee, 1975, Finlayson-Pitts and Pitts Jr, 1986, Aschmann et al., 1997, Finlayson-Pitts and Pitts Jr, 1999, Johnson and Marston, 2008).

This part aims to identify and quantify the products formed through the ozonolysis of two unsaturated aldehydes (T2P and T2H) by identifying their gas-phase products using FTIR and GC analysis.

IV.2.2.1 Experimental conditions and protocols

Product studies were performed at room temperature and atmospheric pressure. Product studies of T2P ozonolysis and T2H ozonolysis were performed in QUAREC-ASC and 3m-ASC, respectively. For each experiment, the aldehyde was injected and left to stabilize for 30 min in the chamber. Then its initial concentration was checked using the FTIR spectrometer. The studied aldehyde's initial concentration was obtained using a calibration curve determined in preliminary experiments (see section IV.2.1.1.1). The ozonolysis reaction of the studied aldehyde started immediately after the ozone addition to the reaction mixture. A gas sample was taken from the reactor to the FTIR spectrometer each 5 min to identify and quantify the studied aldehyde and gas-phase products. Recorded spectra were compared with references available in IR databases at the Wuppertal University.

For QUAREC-ASC experiments, besides FTIR analysis, several GC analyses were done using an offline sampling on Carbotrap 202 cartridges using a flow rate of 0.5 L min^{-1} each 20 min. In 3m-ASC, Dimethyl Ether (DME) was added as an OH tracer only in the reaction mixture T2H + O₃ to quantify OH radicals' formation in the system. The experimental conditions used for the product studies are summarized in Table IV.9.

Table IV.9: Summary of experimental conditions used for the gas-phase product studies of T2P and T2H ozonolysis.

Reaction	Reactor	Number of experiments	[Ald] ₀ × 10 ¹³ /molecule cm ⁻³	[O ₃] ₀ × 10 ¹² /molecule cm ⁻³	[Cyclohexane] ₀ × 10 ¹⁵ /molecule cm ⁻³
T2P + O ₃	QUAREC-ASC	5	4.2 – 5.9	4.2 – 20	0
T2H + O ₃	3m-ASC	7	9.1 – 14	3.4 – 96	39 – 59

IV.2.2.2 Results

IV.2.2.2.1 Products of T2P + O₃

a) Temporal evolution of T2P and product concentrations

In QUAREC-ASC, five experiments were carried out without adding an OH tracer. I mention that no estimation for the formed OH radicals was done in the present section.

Glyoxal, propanal, and acetaldehyde were identified and quantified as the major primary products using the FTIR spectrometer. Ozone, T2P, and the identified products were monitored using the IR absorption bands: 1105 cm⁻¹ for O₃, 1170 – 1117 cm⁻¹ for T2P, 2764 – 2889 cm⁻¹ for glyoxal, 2857 – 3034 cm⁻¹ for propanal, and 2650 – 2750 cm⁻¹ for acetaldehyde. The quantification of glyoxal was done using absorption cross-sections determined by (Volkamer et al., 2005), whereas propanal and acetaldehyde were quantified using IR absorption cross-sections determined at Wuppertal University.

The analysis procedure is based on the calibrated reference spectra' iterative subtraction after eliminating the remaining reagents (T2P and O₃). Concentration-time profiles of the decay of T2P, the quantified products, and the calculated carbon balance are presented in Figure IV.12.

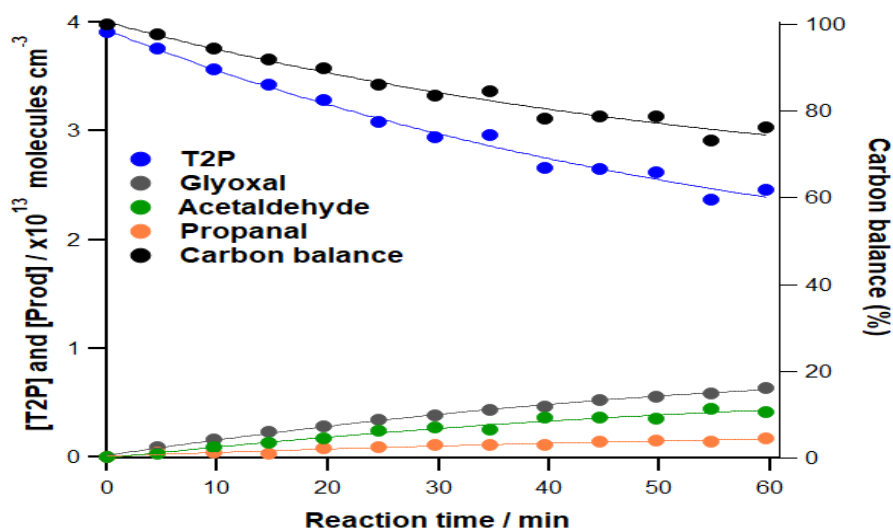


Figure IV.12: Temporal evolution of T2P, products identified by FTIR (left axis), and the carbon balance (right axis) are examples of the T2P ozonolysis experiment in QUAREC-ASC.

b) Product yields

Product yields Y_{Prod} were obtained from the plots of the product mixing ratios $[\text{Prod}]$ vs. aldehyde consumption, $\Delta[\text{T2P}]$ according to Eq.14 in chapter II. Glyoxal, propanal, and acetaldehyde yield plots are shown in Figure IV.13.

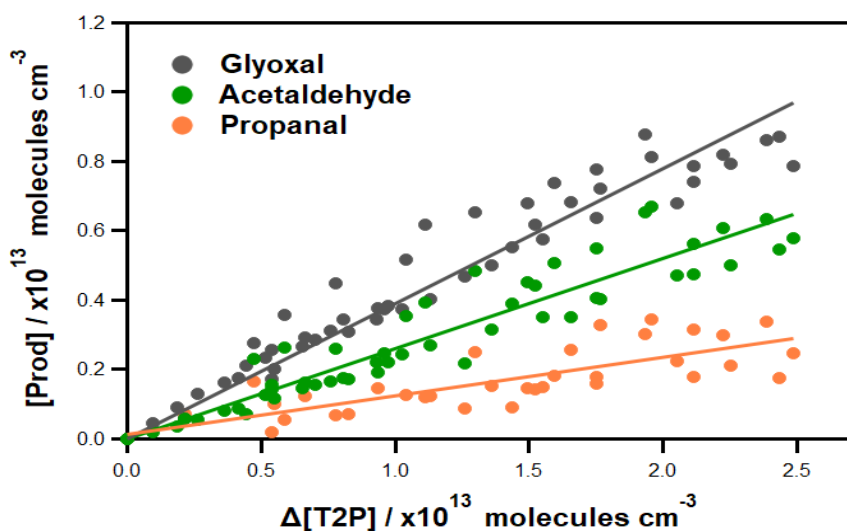


Figure IV.13: Plots of all reaction products (FTIR analysis) as a function of reacted T2P obtained in QUAREC-ASC (without OH scavenger).

These species were formed with an average yield of $(39 \pm 6)\%$ for glyoxal, $(26 \pm 4)\%$ for acetaldehyde, and $(12 \pm 2)\%$ for propanal. Errors represent an estimated total uncertainty of 15%. Indeed, uncertainties on Y_{Prod} were obtained by adding errors on $[T2P]$ (estimated at 10%) and errors on $[\text{Prod}]$ arising from uncertainties on both absorption cross-sections (5%) and subtraction procedure of the IR spectra (10%). Overall uncertainties on Y_{Prod} , calculated by error propagation, were of the order of 15%.

Besides, propanal and propanoic acid were detected by GC-MS. The quantification of these products was not possible due to the lack of standards. Although a significant increase was observed for the intensity of the specific absorptions attributed to CO and CO₂, their quantification is not possible under the present experimental setup. Indeed, the IR light beam interferes with the external atmosphere before going into the reactor; it was not possible to approximate the concentration of CO₂ in the reactor. A summary of the identified and quantified products in the present work is displayed in Table IV.10.

c) Mechanism of T2P ozonolysis

The identification and the quantification of gas-phase products based on IR and GC/MS techniques allow establishing a detailed mechanism for the ozonolysis of T2P. The first step in the T2P ozonolysis proceeds by the ozone's electrophilic addition on the aldehyde's double bond and produces an asymmetrical ozonide. This compound decomposes rapidly to give two primary carbonyl compounds and two intermediates called "Criegee" intermediates: the bi-radical $\text{CHOC}\cdot\text{HOO}\cdot$ and propanal from the channel (I) and the bi-radical $\text{CH}_3\text{CH}_2\text{C}\cdot\text{HOO}\cdot$ and glyoxal from the channel (II). Propanal and glyoxal were identified and quantified in this work as a major product.

The bi-radical $\text{CHOC}\cdot\text{HOO}\cdot$, resulting from the channel (I), can evolve into four different pathways (Figure IV.14):

- a. Stabilization and isomerization into glyoxylic acid. This compound was not detected in our experiments, which is consistent with the literature data (Kalalian, 2018). This pathway could be either minor or non-existent.

- b. Decomposition into formaldehyde and CO₂. Formaldehyde was observed neither in this work nor in Kalalian, 2018 thesis. A slight increase in the 2289 – 2388 cm⁻¹ characteristic band of CO₂ was observed but not quantified, as explained above.
- c. O(³P) atom ejection and glyoxal formation. According to (Finlayson-Pitts and Hemminger, 2000), this is a minor channel.
- d. Decomposition into OH and CHOCO•. The CHOCO• radical could evolve into CO₂ and CHO•, the latter reacting with O₂ to form HO₂ and CO. Carbon monoxide formation was observed by IR but not quantified for reasons mentioned above.

The decomposition of the bi-radical CHOC•HOO proceeds only via the two pathways (c) and (d). We envisage the determination of both CO and OH yields in a future study.

The bi-radical CH₃CH₂C•HOO•, resulting from the channel (II) could either be stabilized by collision or undergo fast unimolecular decomposition via 1,5-H shift and hydroperoxide formation CH₃CH=CH(OOH). The latter can evolve in four different pathways, as presented in Figure IV.14.

- a'. Rearrangement into and stabilization of a β-hydroxy carbonyl, which is 2-hydroxypropanal. Kalalian, 2018 detected the 2-hydroxypropanal and estimated a formation yield of 9%.
- b'. Formation of H₂ and methylglyoxal: the formation of methylglyoxal in the present study cannot be ruled out.
- c'. Decomposition into CHO• + α-hydroxyalkyl, the latter yielding acetaldehyde, quantified in the present work 12%. Acetaldehyde was identified and quantified with a formation yield of 11% in Kalalian, 2018. CHO• will yield HO₂ + CO; as mentioned above, CO formation was observed by IR but not quantified.
- d'. Release of an OH radical and formation of CH₃•CHCHO. In the presence of O₂, this radical will methylglyoxal.

In addition to the evolution routes mentioned above, the stabilized biradical CH₃CH₂C•HOO• can isomerize into a dioxy biradical and form propanoic acid.

Propanoic acid was detected in the experiments performed without OH scavenger, suggesting the existence of this channel.

In the present work, the sum of the yields of the identified compounds (glyoxal, propanal, and acetaldehyde) is 87%, which suggests that secondary pathways can produce only minor compounds. The decomposition of CI (I) was justified only by glyoxal formation (pathway c). At the same time, the evolution of CI (II) occurred via the formation of 2-hydroxypropanal (pathway a') (Kalalian, 2018) or the formation of acetaldehyde (pathway c'). The mechanism of T2P ozonolysis was established based on the identified products in IR and GC/MS (Figure IV.14).

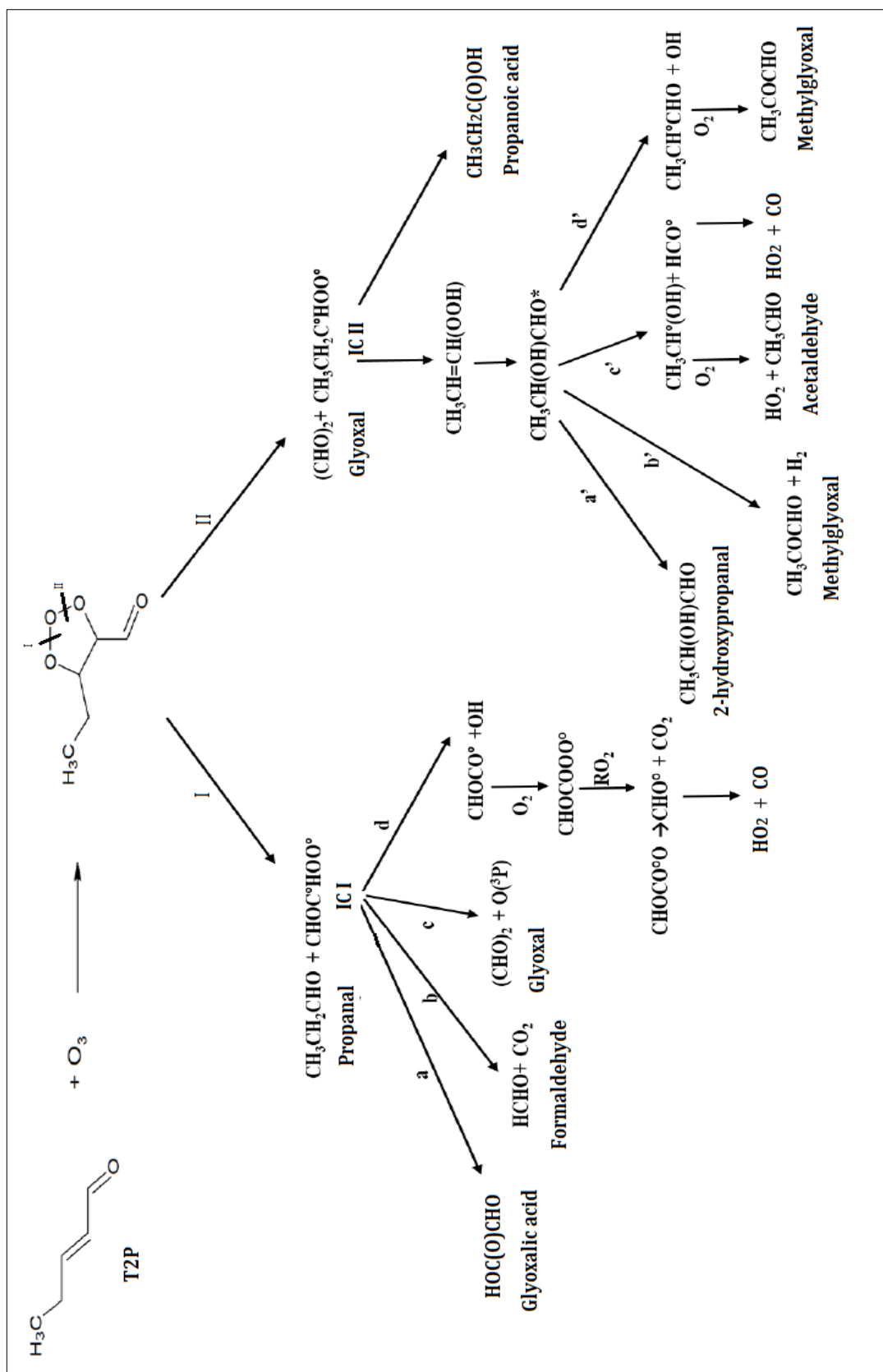


Figure IV.14: Proposed mechanistic scheme for the ozonolysis of T2P.

IV.2.2.2.2 Products of T2H + O₃

a) Temporal evolution of T2H and product concentrations

In 3m-ASC, seven experiments were performed, and three among them were carried out using Dimethyl Ether (DME) used as an OH radical tracer. An upper limit of 10^6 molecule cm^{-3} was estimated for OH radicals' concentration in the T2H + O₃ system. Glyoxal and butanal were identified and quantified as the major primary products using the FTIR spectrometer. Ozone, T2H, and the identified products were monitored using the IR absorption bands centered at 1105 cm^{-1} for ozone, 1150 and 2726 cm^{-1} for T2H, 2835 cm^{-1} for glyoxal, 1126 , and 2712 cm^{-1} for butanal. The quantification of glyoxal was done using absorption cross-sections determined by (Volkamer et al., 2005) whereas, butanal was quantified using tabulated IR absorption cross-sections determined in the 3m-ASC.

The analysis procedure is based on the iterative subtraction as described above (see section IV.2.2.2.1). Concentration-time profiles of T2H, butanal, and glyoxal are presented in Figure IV.15 together with the carbon balance.

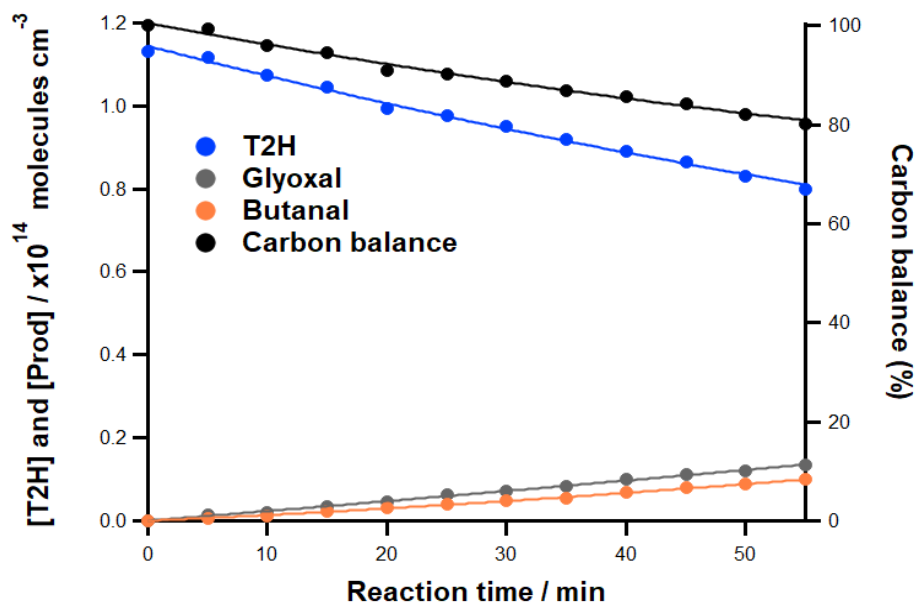


Figure IV.15: Temporal evolution of T2H, products identified by FTIR (left axis) and the carbon balance (right axis) for an example of T2H ozonolysis experiment in 3m-ASC.

b) Product yields

Product yields Y_{Prod} were obtained from the plot of the product mixing ratios $[\text{Prod}]$ vs. aldehyde consumption, $\Delta[\text{T2H}]$ as described above (see section IV.2.2.2.1). Yield plots of the concentrations of the primary products determined in 3m-ASC as a function of consumed T2H are shown in Figure IV.16.

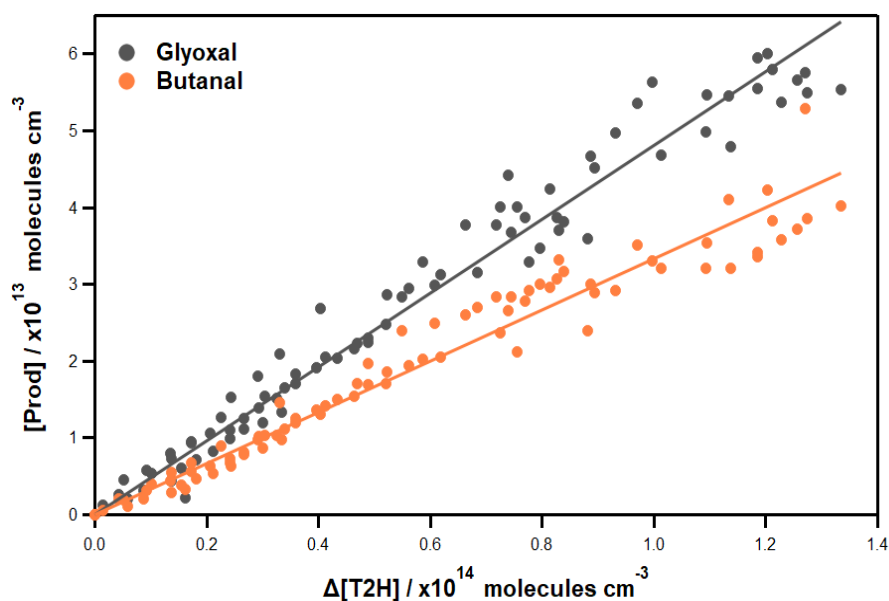


Figure IV.16: Plots of all reaction products' concentrations as a function of reacted T2H obtained in the 3m-ASC (without OH scavenger).

For butanal and glyoxal, molar yields of $33 \pm 7\%$ and $48 \pm 10\%$, respectively, were obtained, where the errors (2σ) represent estimated total uncertainties of $\sim 18\%$. Uncertainties on Y_{Prod} were obtained by adding errors on $\Delta[\text{T2H}]$ (estimated at 14%) and errors on $[\text{Prod}]$ arising from uncertainties on both absorption cross-sections (5%) and subtraction procedure of the IR spectra (10%). Overall uncertainties on Y_{Prod} calculated by error propagation were thus of the order of 18%. The formation of propanal and acetaldehyde was observed in the residual IR spectra of all experiments, but due to overlapping of absorption features, it could not be accurately quantified (Figure IV.17).

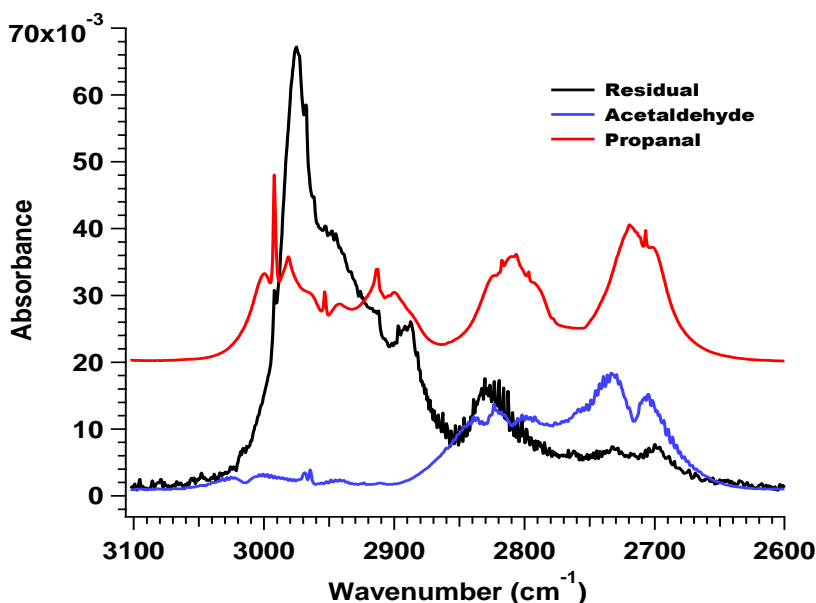


Figure IV.17: IR spectra obtained in the 3m-ASC in the range 2600 – 3100 cm^{-1} . Qualitative reference spectra for propanal (red) and acetaldehyde (blue) together with the residual spectrum after removing T2H, O_3 , butanal, and glyoxal.

An upper limit (molar yield) of 8% and 10% can be estimated using the absorption band centered at 2992 cm^{-1} for propanal and 1352 and 2706 cm^{-1} for acetaldehyde, respectively. The presence of butanoic acid in the spectra obtained from the 3m-ASC cannot be ruled out as its spectral features can be “hidden” under the unidentified residual absorptions (Figure IV.18).

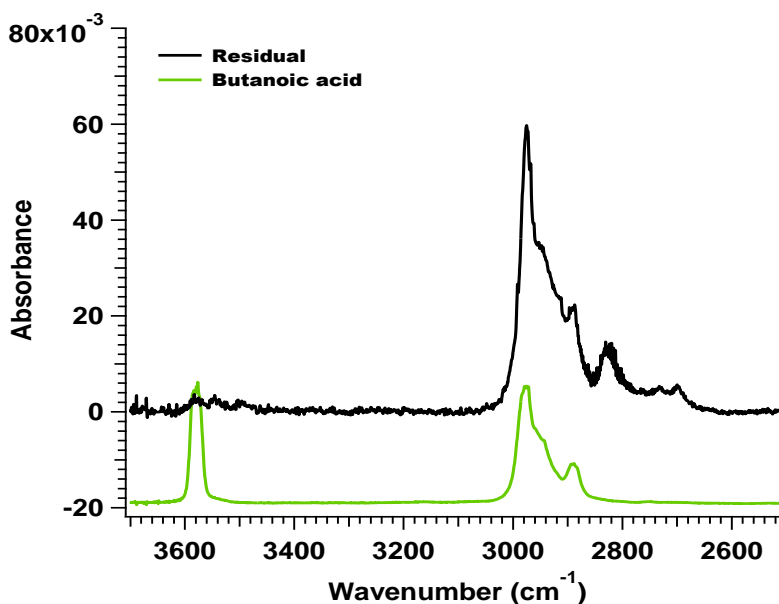


Figure IV.18: IR spectra obtained in the 3m-ASC in the range 2500 – 3700 cm^{-1} .

Qualitative reference spectrum for butanoic acid (green, absorbance $\times 10^{-2}$) together with the residual spectrum after removing T2H, O_3 , butanal, and glyoxal.

As mention in the $\text{T2P} + \text{O}_3$ reaction, a significant increase was observed for the intensity of the specific absorptions attributed to CO and CO_2 . However, unfortunately, we cannot quantify these two products, as explained in the T2P ozonolysis. A summary of the identified and quantified products in the present work is displayed in Table IV.10. Note that these yields were not corrected for potential OH reactions with both reactants and products since the evaluated OH concentration is too small to contribute significantly to the loss of these species. The ozonolysis of T2H in the 3m-ASC shows OH radicals' formation (10^5 - 10^6 molecule cm^{-3}), estimated based on the tracer (DME) consumption. This range of OH concentrations accounts for much less than 10% of the overall consumption of the T2H and indicates that the OH reaction plays a minor role. The latter is also supported by the good agreement between the yields of primary products determined in experiments performed in the presence and absence of a scavenger. The product yields can also be impacted by an OH scavenger, which may support the higher yields observed in the 3m-ASC.

c) Mechanism of T2H ozonolysis

Based on the product analysis results of T2H analysis done in 3m-ASC using IR spectrometer, we propose a detailed mechanism shown in Figure IV.19. The T2H ozonolysis reaction proceeds similarly as explained above for T2P ozonolysis. Channel (I) leads to the formation of the bi-radical $\text{CHOC}\cdot\text{HOO}\cdot$ and butanal and channel (II) leads to the formation of the biradical $\text{CH}_3\text{CH}_2\text{CH}_2\text{C}\cdot\text{HOO}\cdot$ and glyoxal. Butanal and glyoxal were identified and quantified in this work as a major product.

The bi-radical $\text{CHOC}\cdot\text{HOO}$ resulting from the channel (I) reacts exactly as described in the T2P mechanism. Therefore, pathways a, b, c, and d are the same as described in $\text{T2P} + \text{O}_3$ mechanism. According to these analyses, the bi-radical's ($\text{CHOC}\cdot\text{HOO}$) decomposition proceeds mainly via the pathway (d). We envisage the determination of both CO and OH yields as the object of a future study.

The bi-radical $\text{CH}_3\text{CH}_2\text{CH}_2\text{C}^\bullet\text{HOO}^\bullet$, resulting from the channel (II), can either be stabilized by collision or undergo fast unimolecular decomposition via 1,5-H shift and hydroperoxide formation $\text{CH}_3\text{CH}_2\text{CH}=\text{CH}(\text{OOH})$. The latter can evolve in four different pathways (a' – d'), as explained in the mechanistic study of T2P ozonolysis and displayed in Figure IV.19.

a'. Rearrangement and stabilization of a β -hydroxy carbonyl into 2-hydroxybutanal: Grosjean et al. 1996 could not distinguish between the 2-hydroxybutanal and 2-oxobutanal. However, Kalalian, 2018 detected the 2-hydroxybutanal and estimated a formation yield of 18%.

b'. Formation of H_2 and 2-oxobutanal: the formation of 2-oxobutanal in the present study cannot be ruled out.

c'. Decomposition into $\text{CHO}^\bullet + \alpha$ -hydroxyalkyl: The latter yielding propanal was observed in the present work but was not quantified. Propanal was identified and quantified with a formation yield of 19% in Kalalian, 2018 and 6.7% in Grosjean et al. 1996. CHO^\bullet will yield $\text{HO}_2 + \text{CO}$; as mentioned above, CO formation was observed by IR but not quantified.

d'. Release of an OH radical and formation of $\text{CH}_3\text{CH}_2^\bullet\text{CHCHO}$: In the presence of O_2 , this radical will form the oxy radical $\text{CH}_3\text{CH}_2\text{CHO}^\bullet\text{CHO}$ which may evolve toward the production of acetaldehyde, glyoxal, propanal, 2-oxobutanal, and CO. Acetaldehyde was identified and not quantified in our study. Kalalian 2018 quantified a formation yield of 11% of acetaldehyde.

In addition to the evolution routes mentioned above, the stabilized biradical $\text{CH}_3\text{CH}_2\text{CH}_2\text{C}^\bullet\text{HOO}^\bullet$ can isomerize into a dioxy biradical and form butanoic acid. No certain identification of butanoic acid is possible due to the IR absorption band overlapping in the residual spectra (see Figure IV.19). The sum of the identified compounds' yields (glyoxal and butanal) is 81% in the present work. The latter suggests that secondary pathways can produce only minor compounds. The decomposition of CI (I) was justified only by glyoxal formation (pathway c).

However, the evolution of CI (II) occurred via the formation of 2-hydroxybutanal (pathway a') (Kalalian, 2018), the formation of propanal (pathway c'), the formation of acetaldehyde and glyoxal (pathway d'-d'₁) or the formation of propanal (pathway d'-d'₂). The mechanism of T2H ozonolysis was established based on the identified products using an IR spectrometer (Figure IV.19).

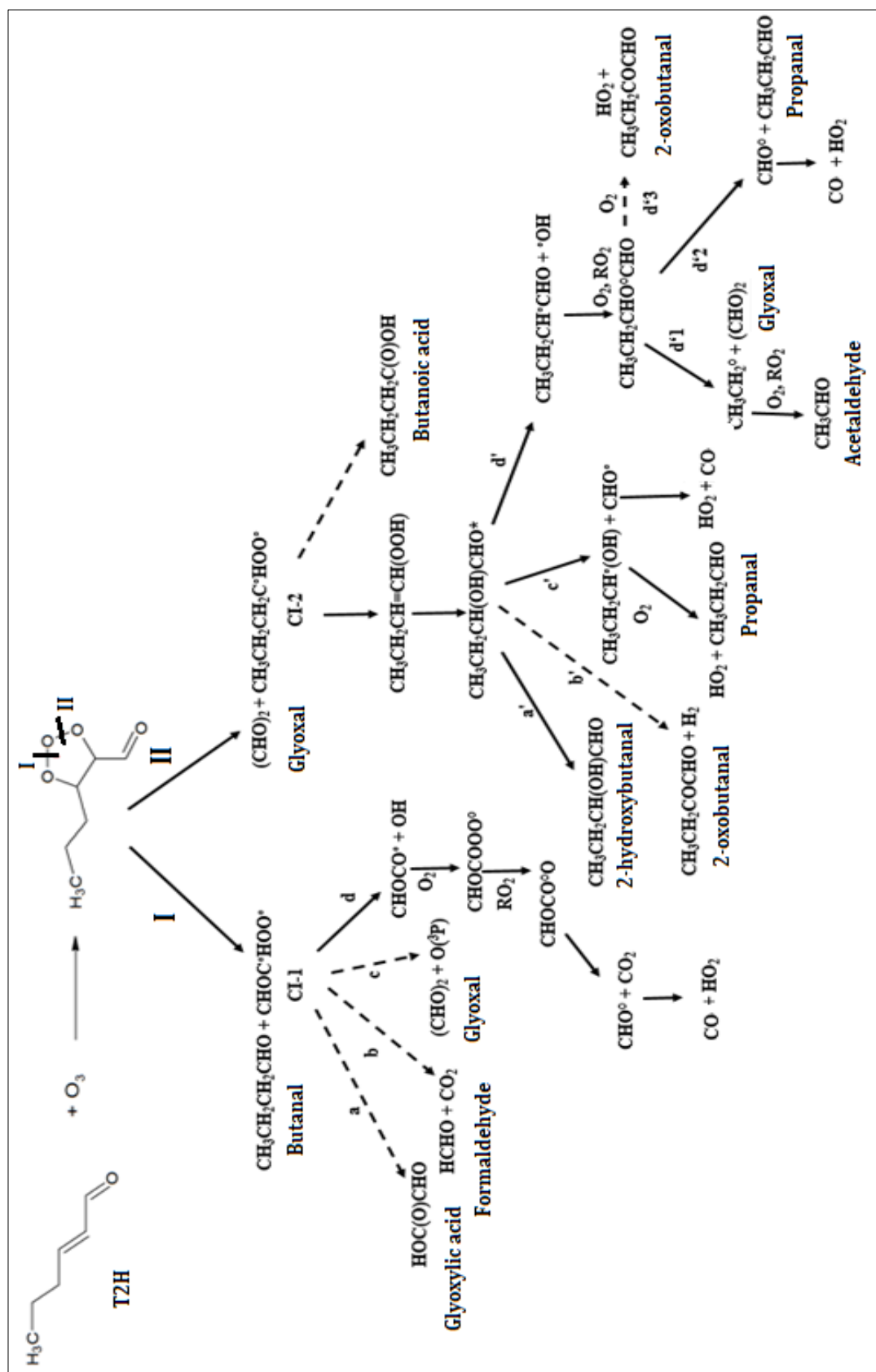


Figure IV.19: Proposed mechanistic scheme for the ozonolysis of T2H.

IV.2.2.3 Discussion

To better understand the mechanism of the Trans-2-alkenals ozonolysis, the studied mechanism for T2P and T2H ozonolysis were compared to other similar unsaturated aldehydes with shorter (2-propenal, 2-methyl-2-propenal, and 2-butenal) or longer (Trans-2-Heptenal, Trans-2-Nonenal, and Trans-2-Octenal) carbon chain. A summary of the product formation yields of the ozonolysis of a series of C₃-C₉ unsaturated aldehydes is displayed in Table IV.10.

Table IV.10: Summary of literature data and the present work for the product formation yields of the ozonolysis of a series of C₃-C₉ unsaturated aldehydes.

Compound Linear formula	Identified products	Yield (%)	References
2-Propenal CH ₂ =CH-CHO	Glyoxal	(c)	Grosjean et al., 1994a
	Formaldehyde		
	Glyoxylic acid		
2-Methyl-2-Propenal CH ₂ =C(CH ₃)-CHO	Methylglyoxal	58 ± 12	Daniel Grosjean et al., 1993b
	Formaldehyde	12 ± 2	
2-Butenal CH ₃ -CH=CH-CHO	Glyoxal	47 ± 2	Grosjean and Grosjean, 1997a
	Acetaldehyde	42 ± 3	
	Formaldehyde	8 ± 1	
	Cyclohexanone	2.8 ± 0.2	
Trans-2-Pentenal C ₂ H ₅ -CH=CH-CHO	Glyoxal	57 ± 8	Kalalian, 2018 (Thesis)
	Propanal	44 ± 16	
	Acetaldehyde	11 ± 6	
	2-hydroxypropanal (a)	9 ± 6	
	Glyoxal	39 ± 6	This work
	Propanal	26 ± 4	
	Acetaldehyde	12 ± 2	
	Propanoic acid	(c)	
2-Methyl-2-Pentenal C ₂ H ₅ -CH=C(CH ₃)-CHO	Methylglyoxal	52 ± 10	Kalalian, 2018 (Thesis)
	Propanal	45 ± 18	
	Acetaldehyde	9 ± 8	

	2-hydroxypropanal ^(a)	6 ± 4	
Trans-2-Hexenal $\text{C}_3\text{H}_7\text{-CH=CH-CHO}$	Glyoxal	52.7 ± 5.5	Grosjean et al., 1996b
	Butanal	55.9 ± 3.7	
	Acetaldehyde	10.9 ± 2	
	Propanal	6.7 ± 0.8	
	2-oxobutanal or 2-hydroxybutanal ^(b)	7.4 ± 0.6	
	Cyclohexanone	3.2 ± 0.3	
	Glyoxal	59 ± 15	Kalalian, 2018 (Thesis)
	Butanal	36 ± 9	
	Acetaldehyde	10 ± 3	
	Propanal	19 ± 5	
	2-hydroxybutanal ^(a)	18 ± 6	
	Glyoxal	48 ± 10	This work
	Butanal	33 ± 7	
	Acetaldehyde	^(c)	
	Propanal	^(c)	
	Butanoic acid	^(c)	
Trans-2-Heptenal $\text{C}_4\text{H}_9\text{-CH=CH-CHO}$	Glyoxal	49 ± 4	Gaona Colmán et al., 2017a
	Pentanal	34 ± 3	
Trans-2-Octenal $\text{C}_5\text{H}_{11}\text{-CH=CH-CHO}$	Glyoxal	41 ± 3	
	Hexanal	39 ± 3	
Trans-2-Nonenal $\text{C}_6\text{H}_{13}\text{-CH=CH-CHO}$	Glyoxal	45 ± 3	
	Heptanal	46 ± 3	

^(a) average of IR and SPME/GC-MS analysis.

^(b) Grosjean et al. 1996 could not distinguish between the two carbonyls (see text).

^(c) Not quantified.

a) The reaction 2-Propenal + O₃

Grosjean et al. 1994 studied the products formed during the ozonolysis of 2-propenal (acrolein). Their experiments have been carried out in a (3.5 – 3.7) m³ Teflon chamber at room temperature and atmospheric pressure in the presence of an OH scavenger.

The analysis was done using an HPLC device with UV detection based on an offline sampling on 2,4-dinitrophenylhydrazine (DNPH) cartridges. Primary observed carbonyls products were glyoxal, formaldehyde, and glyoxylic acid. No quantification was done, and only concentrations were presented (few ppbv).

b) The reaction 2-Methyl-2-Propenal + O₃

The ozonolysis of 2-methyl-2-propenal (methacrolein) was investigated (Daniel Grosjean et al., 1993b). The reaction ozonolysis of 2-methyl-2-propenal was studied in the same experimental conditions described above (2-propenal). This reaction yielded methylglyoxal (58%) and formaldehyde (12%). These results are consistent with those found later by (Grosjean et al., 1994b) for the ozonolysis of 2-propanal and prove that the methyl group (CH₃-) presence instead of hydrogen does not change the decomposition pathways. However, it generates methylglyoxal for 2-methyl-2-propenal oxidation instead of glyoxal for 2-propenal oxidation.

c) The reaction 2-Butenal + O₃

Grosjean et al.' group studied longer carbon chains such as 2-butenal (crotonaldehyde) (Grosjean and Grosjean, 1997b). The reaction ozonolysis of 2-butenal was studied in the same experimental conditions as described above for (2-propenal) and had provided the product formation yields of glyoxal (47%), acetaldehyde (42%), formaldehyde (8%), and cyclohexanone (2.8%). Cyclohexanone, a product of the OH-cyclohexane reaction, was identified, thus indicating that OH forms a product of the ozonolysis reaction of 2-butenal. However, cyclohexanone formation yields did not exceed 3%.

d) The reaction Trans-2-Pentenal + O₃

The mechanistic study of T2P ozonolysis was carried out by Kalalian, 2018 during her thesis work. This work was done at room temperature and atmospheric pressure in a Pyrex cell of (63L), adding cyclohexane as an OH scavenger. Products analyses were done by an FTIR spectrometer and GC/MS via an offline sampling on SMPE fiber. The identified and quantified products were glyoxal (57 ± 8)%, propanal (44 ± 16)%, acetaldehyde (11 ± 6)%, and 2-hydroxypropanal (9 ± 6)%.

In the present work, we investigated the same reaction, and we identified and quantified glyoxal (39 ± 6)%, propanal (26 ± 4)%, acetaldehyde (12 ± 2)%.

We also quantified propanoic acid in Carbotrap 202 cartridges analyses. The present work agrees well with Kalalian, 2018 in terms of the yield formation of acetaldehyde. However, a huge discrepancy was observed for glyoxal and propanal yields. Indeed, it was determined that aerosols represent a significant sink due to uptake on the surface or partitioning to the oxygenated organic aerosol phase (Hallquist et al., 2009, Knote et al., 2014, Shen et al., 2018). Therefore, these differences may be explained by: (i) the presence of an OH scavenger in Kalalian, 2018 set-up and/or (ii) the formation of aerosols in QUAREC-ASC (see section 1.3) and their absence in the reactor of Kalalian 2018 (since they used a continuous flow of O_3 which can destroy the first formed particles). To accept or reject this hypothesis, Kalalian, 2018 had to measure SOA formation, but unfortunately, this was not possible for them due to the lack of instrument (SMPS).

e) The reaction 2-Methyl-2-Pentenal + O_3

The ozonolysis of 2-methyl-2-pentenal was investigated by Kalalian, 2018 in the same experimental set-up and conditions as described for the ozonolysis of T2P above. Methylglyoxal (52%) and propanal (45%) were identified as primary products, and acetaldehyde (9%) and 2-hydroxybutanal (6%) were secondary products.

f) The reaction Trans-2-Hexenal + O_3

Grosjean et al. 1996 determined the products formed during the T2H ozonolysis using the same experimental set-up and conditions as explained for 2-propenal ozonolysis. Glyoxal (52.7 ± 5.5)% and butanal (55.9 ± 3.7)% were identified as primary products and propanal (6.7 ± 0.8)%, 2-oxobutanal (7.4 ± 0.6)%, acetaldehyde (10.9 ± 2.0)% and cyclohexanone (3.2 ± 0.3)% were identified as secondary products. Cyclohexanone observation confirms the OH radicals formation in the reactor, as explained above for 2-butenal ozonolysis (Grosjean and Grosjean, 1997b).

Kalalian, 2018 also investigated the mechanism of T2H ozonolysis. The same experimental set-up and conditions as explained for T2P ozonolysis.

Glyoxal (59 ± 15)%, butanal (36 ± 9)%, propanal (19 ± 5)%, acetaldehyde (10 ± 3)% and 2-hydroxybutanal (18 ± 6)% were identified and quantified. In the present work, T2H ozonolysis yielded glyoxal (48 ± 10)% and butanal (33 ± 7)% as primary products. Other products, such as propanal, acetaldehyde, and butanoic acid, were detected and not quantified. This work is consistent with Grosjean et al., 1996 and Kalalian, 2018 with respect to glyoxal and butanal yields. The differences can be due to an OH scavenger or SOA formation, as explained in T2P ozonolysis.

g) The reaction of Trans-2-Heptenal/ Trans-2-Octenal/ Trans-2-Nonenal + O₃

A recent study by (Gaona Colmán et al., 2017b), performed in QUAREC-ASC at room temperature and atmospheric pressure without an OH scavenger, has investigated the degradation of three unsaturated aldehydes: Trans-2-Heptenal, Trans-2-Octenal, and Trans-2-Nonenal with O₃. The yields of the primary products were: glyoxal (49 ± 4)% and pentanal (34 ± 3)% for Trans-2-Heptenal ozonolysis, glyoxal (41 ± 3) % and hexanal (39 ± 3)% for Trans-2-Octenal ozonolysis and glyoxal (45 ± 3)% and heptanal (46 ± 3)% for Trans-2-Nonenal ozonolysis.

This work provides additional information concerning trans-2-alkenals ozonolysis and contributes to a better understanding of unsaturated aldehydes' reactivity with ozone. In our study, the ozonolysis of T2P and T2H displays a slight preference for the channel giving the glyoxal as a primary product. Indeed, some studies such as Kalalian, 2018 (thesis) and Gaona Colmán et al., 2017 displayed the same preference. In contrast, other studies such as Grosjean and Grosjean, 1997 and Grosjean et al., 1996 have no preference in the primary ozonide decomposition pathways. The ozonolysis of asymmetric alkyl-substituted alkenes is known to favor the formation of the most substituted bi-radical due to hyperconjugation (Grosjean et al., 1996, Tuazon et al., 1997).

Furthermore, studies carried out on the ozonolysis of oxygenated alkenes indicate that the primary ozonide decomposition displays a preference for the pathway yielding an oxygenated carbonyl (Grosjean et al., 1994, Grosjean and Grosjean, 1997, Uchida et al., 2015). Hence, the formation of the alkyl-substituted bi-radical and the formation of glyoxal could be favored.

However, the limited number of reported data for the ozonolysis of C₃-C₉ trans-2-alkenals, Table IV.10 does not indicate a clear trend to support this observation.

IV.2.3 Particle-phase study

The formation of particles through the oxidation of BVOCs dominates the global burden of atmospheric SOAs (Hoffmann et al., 1997, Griffin et al., 1999, Peñuelas and Staudt, 2010). One of the major uncertainties of biogenic hydrocarbons' impact on atmospheric processes is the quantitative understanding of their ability to form organic aerosols. Efforts have been made to quantify the aerosol formation from terpenes. However, there is still a lack of knowledge concerning unsaturated carbonyls such as unsaturated aldehydes (Hoffmann et al., 1997, Lee et al., 2006, Ng et al., 2007). This section presented the contribution of the C₅-C₆ unsaturated aldehydes (T2P and T2H) ozonolysis reactions on the atmospheric SOA formation. To our knowledge, this work is the first investigation of the SOA formation from the C₅-C₆ unsaturated aldehydes reaction with ozone.

IV.2.3.1 Experimental conditions and protocols

Particle formation of C₅-C₆ unsaturated aldehydes ozonolysis was studied in the D-ASC at room temperature and atmospheric pressure in the absence of OH scavenger (Johnson and Marston, 2008, Ahmad et al., 2017b). All the technical details concerning the D-ASC set-up were reported in section II.2.1.2.1. The experimental steps are the same as explained in the gas-phase products studies for C₅-C₆ unsaturated aldehydes ozonolysis reactions (see section IV.2.2.1), and continuous SMPS measurements started after the ozone injection until the end of the experiment. The experimental conditions, including initial concentrations and analytical techniques, are summarized in Table IV.11.

Table IV.11: Summary of experimental conditions and analytical techniques used for the formed SOA through the ozonolysis of T2P or T2H.

Reaction	Reactor	Number of experiments	[Ald] ₀ × 10 ¹³ / molecule cm ⁻³	[O ₃] ₀ × 10 ¹³ / molecule cm ⁻³
T2P + O ₃	D-ASC	9	5.2 – 6.9	0.2 – 1.6
T2H + O ₃		6	3.9 – 4.4	0.2 – 1.6

To quantify the mass of SOA formed, the number particle size distribution of the SOA measured by the SMPS was converted to mass particle size distribution with the assumptions that particles were perfect spheres and the density of the generated particles was 1.4 g cm^{-3} (Hallquist et al., 2009).

Preliminary tests were performed to ensure that no particle formation occurred when either aldehyde or ozone was introduced alone in the chamber. The relatively high surface-to-volume (S/V) ratio of the reactor ($\sim 7 \text{ m}^{-1}$) inevitably led to semi-volatile gas and particle losses on the walls. The chamber's volume decreased about 40% of the initial volume along the reaction time due to the different samplings (SMPS: 0.6 L min^{-1} and IR analysis: $\sim 3 \text{ L}$ each sample), a constant aerosol wall loss rate could not be determined (the reactor S/V ratio increased with time). A rough estimation was done for some experiments using the aerosol mass concentration decrease after maximal aerosol formation, indicating an aerosol mass concentration loss of about 20% over one hour. The latter is consistent with the aerosol wall loss measured by Wang et al. 2018 in Teflon simulation chambers for $\sim 100 \text{ nm}$ particles. However, the aerosol mass concentrations measured in the present work were not corrected for wall losses. Besides, unaccounted losses of semi-volatile and low-volatile reaction products might reduce the final aerosol mass concentration observed (Krechmer et al., ES&T 2020, pp 12890).

IV.2.3.2 Results

IV.2.3.2.1 SOAs in T2P + O₃

a) Particle number concentrations

Typical time evolution of the particle number size distribution during $\sim 2 \text{ h}$ of reaction time for the ozonolysis of T2P is presented in Figure IV.20.

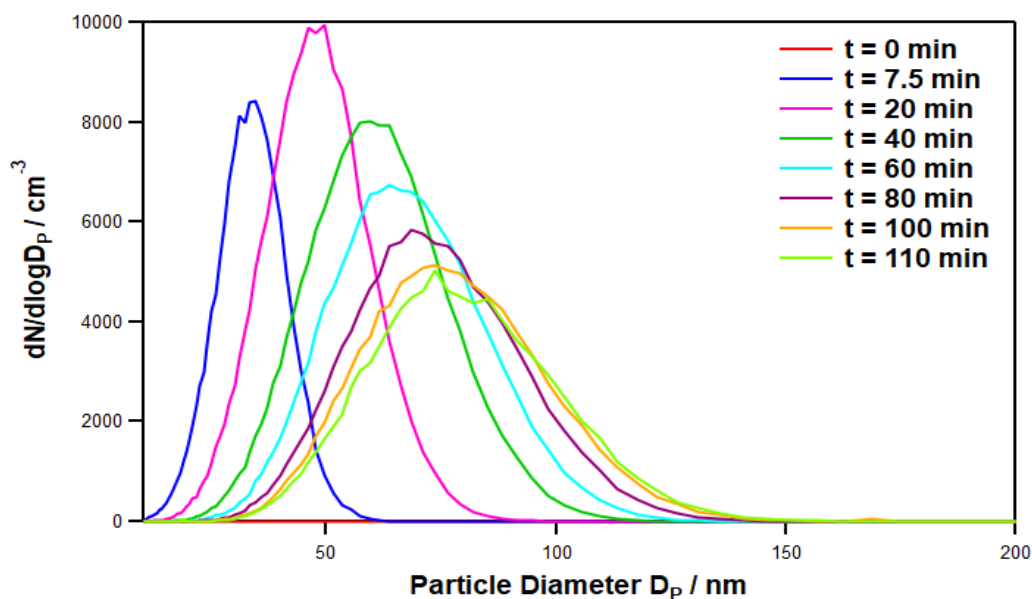


Figure IV.20: Evolution of the SOA number size distribution with reaction time (t) during ozonolysis of T2P (initial reactant mixing ratios $[T2P]_0 = 5.4 \times 10^{13}$ molecule cm^{-3} and $[O_3]_0 = 9.5 \times 10^{12}$ molecule cm^{-3}) in D-ASC. No aerosol was present at $t = 0$ (the corresponding size distribution is flat).

The maximum particle concentration ($N_{p\text{max}}$) was around 1.0×10^4 particles/ cm^3 at about 50 nm, which was reached after 20 min of the reaction. During the reaction, the total particle concentration decreases due to the particles' coagulation, whose diameter increases due to coagulation and condensation of reaction products at the particle's surface. After 2 hours of reaction time, the size distribution stabilizes at the steady-state phase with the following characteristics: $D_{\text{Steady state}} = 75$ nm and $N_{p\text{steady state}} = 5 \times 10^3$ particles/ cm^3 .

b) Particle mass concentrations

Total SOA mass concentrations M_0 were calculated assuming a particle density of 1.4 g cm^{-3} and spherical geometry. The temporal mass evolution of the SOAs formed through the ozonolysis of T2P is displayed in Figure IV.21.

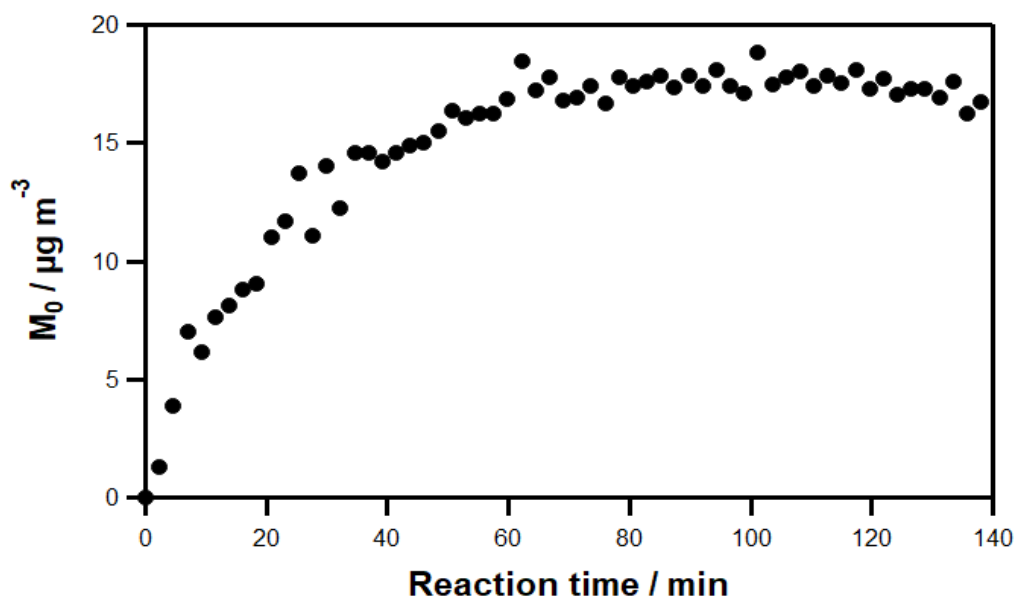


Figure IV.21: SOA formation as a function of time for T2P ozonolysis in D-ASC (initial reactant mixing ratios $[\text{T2P}]_0 = 5.4 \times 10^{13} \text{ molecule cm}^{-3}$ and $[\text{O}_3]_0 = 9.5 \times 10^{12} \text{ molecule cm}^{-3}$).

According to Figure IV.21, the particle formation was very fast and occurred as soon as the ozone was injected in D-ASC. SOA mass concentrations started to reach a plateau after roughly 80 min reaction time, where M_0 starts to decrease due to particle wall losses slowly.

c) Aerosol yields

The SOA yield (Y_{SOA}) is defined as the ratio of the formed SOA mass and the consumed aldehyde (see chapter II, Eq.16). In Figure IV.22, the aerosol yields (Y_{SOA}) were plotted versus the maximum mass (M_{max}) and fitted using the one-product model from (Odum et al., 1996) (see chapter II, Eq.20).

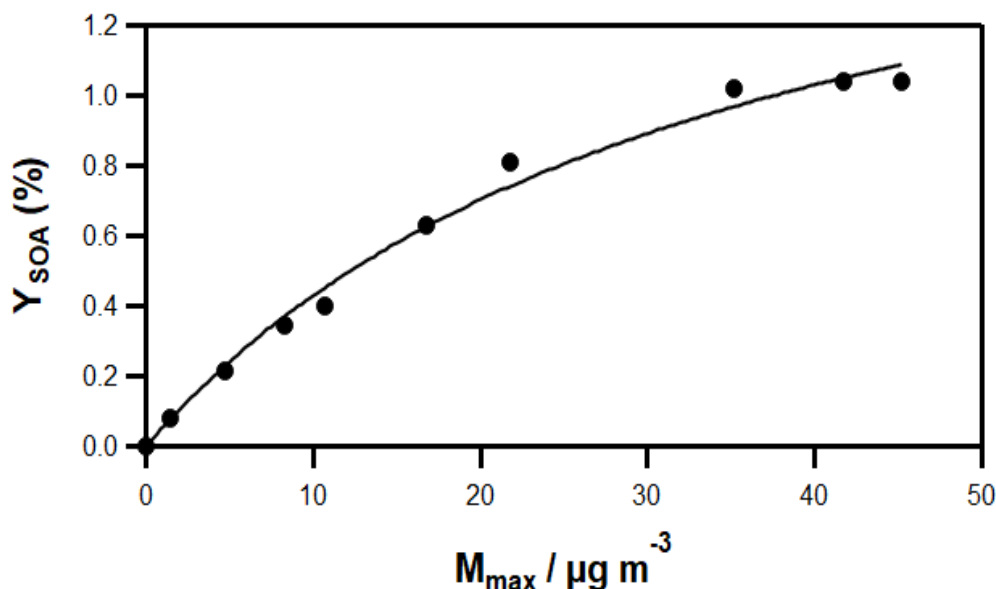


Figure IV.22: SOA formation yields vs. aerosol mass concentrations for T2P in D-ASC.

The fit is carried out using Odum's one-product model (Odum et al., 1996).

The oxidation of about $(5.2 - 6.9) \times 10^{13}$ molecule cm^{-3} of T2P by increasing the amounts of ozone from $(0.2 - 1.6) \times 10^{13}$ molecule cm^{-3} led to SOA yields varying from 0.1% to 1.2% at an SOA mass concentrations M_{\max} up to $45 \mu\text{g m}^{-3}$ in D-ASC. It should be reminded that since no wall loss correction was applied, the SOA yields obtained in the present work represent lower limits. A least-square regression on the data yields according to the one-product model from Odum et al. 1996 (see chapter II, Eq.20) gives the following parameters: $\alpha = (1.93 \pm 0.18)\%$ and $K_p = (2.9 \pm 0.5) \times 10^{-2} \text{ m}^3 \mu\text{g}^{-1}$. Uncertainties represent two standard deviations (2σ). The first indicates that Y_{SOA} could rise to 1.93% if M_{SOA} were extremely high, reaching infinity, whereas the obtained K_p shows that the vapor phase of the generated semi-volatile product is more important than the condensed phase.

IV.2.3.2.2 SOAs in T2H + O₃

a) Particle number concentrations

Typical time evolutions of the particle number size distribution during ~ 2 h of reaction are presented in Figure IV.23.

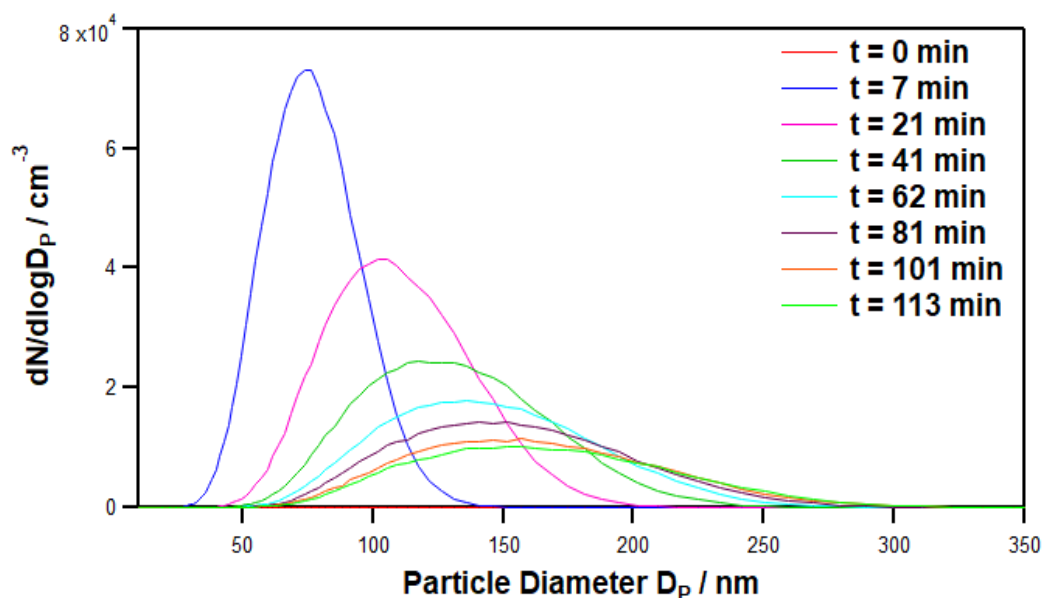


Figure IV.23: Evolution of the SOA number size distribution with reaction time (t) during ozonolysis of T2H ($[T2H]_0 = 9.3 \times 10^{13}$ molecule cm^{-3} and $[O_3]_0 = 9.6 \times 10^{12}$ molecule cm^{-3}) in D-ASC. No aerosol was present at $t = 0$ (the corresponding size distribution is flat).

The maximum particle concentration ($N_{p\text{max}}$) was around 8.0×10^4 particles/ cm^3 at 50 nm, which was reached after 2.5 min of the reaction. During the reaction, the total particle concentration decreases due to the particles' coagulation, and the particle diameter increases due to both coagulation and condensation of reaction products at the surface of the particle. After 2 hours of the reaction time, the size distribution stabilizes at the steady-state phase with the following characteristics: $D_{\text{Steady state}} = 170$ nm and $N_{p\text{steady state}} = 9 \times 10^3$ particles/ cm^3 .

b) Particle mass concentrations

Total SOA mass concentrations M_0 have been calculated assuming a particle density of 1.4 g cm^{-3} and spherical geometry. Figure IV.24 shows particle formation, in terms of mass concentration M_0 , as a function of time in the D-ASC.

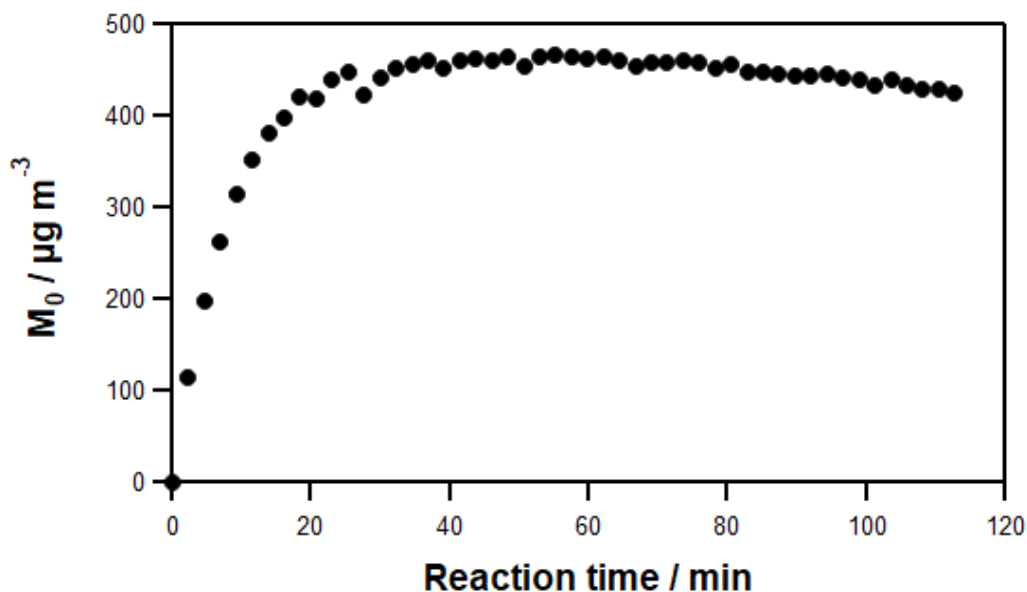


Figure IV.24: SOA formation as function of time for T2H ozonolysis in D-ASC ($[\text{T2H}]_0 = 9.3 \times 10^{13} \text{ molecule cm}^{-3}$ and $[\text{O}_3]_0 = 9.6 \times 10^{12} \text{ molecule cm}^{-3}$).

According to Figure IV.24, particle formation in D-ASC is very fast and occurred as soon as ozone is injected. SOA mass concentrations started to reach a plateau after roughly 40 min reaction time, where M_0 starts to slowly decrease due to particle wall losses.

c) Aerosol yields

According to the maximum of SOA mass concentrations and the corresponding T2H consumption, aerosol yields can be determined. Figure IV.25 displays the aerosol yield as a function of aerosol mass concentration for the experiments carried out in D-ASC.

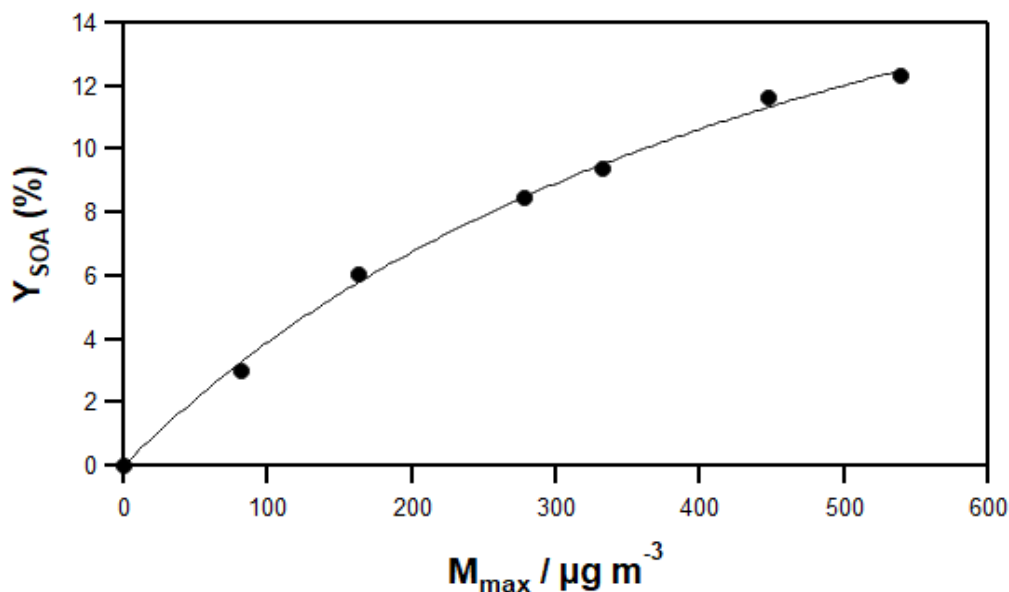


Figure IV.25: SOA formation yields Y_{SOA} vs. aerosol mass concentrations for T2H in D-ASC. The fit is carried out using Odum's one-product model (Odum et al., 1996).

The oxidation of $(3.9 - 4.4) \times 10^{13} \text{ molecule cm}^{-3}$ of T2H by increasing ozone amounts from $(0.2 - 1.6) \times 10^{13} \text{ molecule cm}^{-3}$ led to SOA yields of 2.5% to 12.3% at SOA mass concentrations M_{\max} up to $550 \mu\text{g m}^{-3}$. It should be reminded that since no wall loss correction was applied, the SOA yields obtained in the present work represent lower limits. A least-square regression on the data yields according to Eq. 4 gives the following parameters: $\alpha = (24.98 \pm 1.78)\%$ and $K_p = (1.85 \pm 0.3) \times 10^{-3} \text{ m}^3 \mu\text{g}^{-1}$. Uncertainties represent two standard deviations (2σ). The first indicates that Y_{SOA} could rise to 24.98% if M_{SOA} were extremely high, reaching infinity, whereas the obtained K_p shows that the vapor phase of the generated semi-volatile product is more important than the condensed phase.

IV.2.3.3 Discussion

The present study demonstrates for the first time that ozonolysis reactions of unsaturated aldehydes produce aerosols. SOA also was known to be a major contributor to the tropospheric particles. The SOA yields determined in this work under room temperature and atmospheric pressure for the ozonolysis of T2P and T2H range between 0.1 – 1.2% and 2.5 – 12.3%, respectively.

The difference between the two studies may be due to the formation of less volatile products in the T2P ozonolysis than those obtained in the T2H ozonolysis that contributes to the SOA formation. The formation of SOA in the reaction system could be affected by several conditions. Indeed, the structure of the oxidized compounds and their ability to dissociate into fewer volatile products is the most important parameter on the SOA formation. Moreover, it seems that the presence of NO_x in the system could affect the SOA formation. However, the latter's impact is not well understood until now since multiple studies show contradictory results, as summarized in (Chan et al., 2010). Moreover, other factors may affect the SOA yields, such as the temperature and the relative humidity seeing their hygroscopic properties (Massoli et al., 2010).

IV.3 Oxidation of unsaturated alcohols with ozone

In this section, I displayed the kinetic measurements of the C_5 - C_6 unsaturated aldehydes reactions with ozone. These experiments have been done in D-ASC (IMT Lille Douai). The selected compounds were Cis-2-Penten-1-ol (C2P-ol), Trans-2-Hexen-1-ol (T2H-ol), Trans-3-Hexen-1-ol (T3H-ol), Cis-3-Hexen-1-ol (C3H-ol), 1-Octen-3-ol (1O-3-ol), and Trans-2-Octen-1-ol (T2O-ol). The rate constants of the O_3 reaction of these C_5 to C_8 unsaturated alcohols have been determined at 296 K using the absolute kinetic method. The rate constants of C2P-ol, T2H-ol, T3H-ol, C3H-ol, 1O-3-ol ozonolysis reactions were done together with a trainee (Miss. Oumaya Bejaoui) during her master's internship at IMT Lille Douai.

The rate constant of T2O-ol ozonolysis was determined by a trainee during her master's internship (Miss. Nouha Aloui). The results will help to resolve the inconsistencies noted above on the rate constants and better understand the atmospheric impacts of such compounds in the context of increasing O_3 background concentrations and climate change. Further, developing structure-activity relationships (SAR) for atmospheric chemistry models needs consistent and extended kinetic databases. The present work aims to explain the contribution of the double bond position vs. the $-\text{OH}$ function.

IV.3.1 Determination of rate constants

IV.3.1.1 Experimental conditions and protocols

The used experimental set-up and protocol are the same as described above in section IV.2.1.2 for the ozonolysis of studied aldehydes. Experiments were performed in D-ASC at room temperature and under atmospheric pressure of purified air. Liquid aliquots of alcohols were first vaporized in the chamber under a stream of pure air, and the mixture was let stabilized for ~ 1 hour.

Ozone was added to the reaction mixture using a gas-syringe, which starts the reaction pool. Alcohol concentrations were measured using the FTIR spectrometer, and ozone decay was monitored using the O₃ analyzer. Preliminary tests were performed to study alcohol stability in the reactor. Also, their calibration curves were carefully determined to monitor their concentration in each reaction. Wall losses of alcohols appeared negligible under the used conditions (loss rate < 3% per hour for all alcohols). Preliminary tests showed that the investigated alcohols were not absorbing at the wavelength of the ozone instrument. Pseudo-first order conditions were set up with alcohol initial concentrations [ROH]₀ in excess over that of ozone [O₃]₀ (at least 10 times higher), as reported in Table IV.12.

It should be stressed out that any OH radicals formed will react with the alcohol but would not affect the ozone decay significantly at the high initial alcohol/ozone concentration ratios employed. Therefore, no OH scavenger was used in the present work, except for 1-Octen-3-ol (10-3-ol), for which two experiments were performed with an excess of cyclohexane. In these two experiments, about 90% of the OH was scavenged by cyclohexane (this estimation was calculated as explained in section II.4.2.2).

Table IV.12: Summary of experimental conditions used for the kinetic studies of C₅-C₈ unsaturated alcohols ozonolysis.

Reaction	Number of experiments	[Alc] ₀ × 10 ¹⁴ /molecule cm ⁻³	[O ₃] ₀ × 10 ¹² /molecule cm ⁻³	[Cyclohexane] ₀ × 10 ¹⁵ /molecule cm ⁻³
C2P-Ol + O ₃	6	0.6 – 1.3	2.8 – 3.3	0
T2H-Ol + O ₃	13	0.4 – 3.3	2.0 – 5.6	0
T3H-Ol + O ₃	10	0.66 – 1.5	2.9 – 7.5	0
C3H-Ol + O ₃	9	1.0 – 2.6	3.0 – 4.7	0
10-3-Ol + O ₃	5	0.34 – 0.91	2.8 – 17	0
	2	0.59 – 0.74	2.8 – 3.7	4.2 – 23.7
T2O-Ol + O ₃	20	0.94 – 3.6	1.4 – 9.4	0

The following chemicals were used as received: C2P-Ol (≥96%, Aldrich), T2H-Ol (≥ 95%, Aldrich), T3H-Ol (97%, Aldrich), C3H-Ol (> 98%, Fluka), 10-3-Ol (≥ 98%, Aldrich), and T2O-Ol (97%, Aldrich). Extra pure zero air was produced with a pure air generator (AZ-2020, Claimed, Italy) with relative humidity (RH) < 2 ppm and CO and CO₂ < 80 ppb. N₂ was from Messer France (99.999%, RH < 3 ppm).

IV.3.1.2 Results

C2P-Ol, T2H-Ol, T3H-Ol, C3H-Ol, 10-3-Ol, and T2O-Ol were measured in the following IR ranges, respectively: 960 – 1081 cm⁻¹, 956 – 1032 cm⁻¹, 934 – 1000 cm⁻¹, 997 – 1096 cm⁻¹, 913 – 940 cm⁻¹ and 900 – 1050 cm⁻¹. Primary products from reactions of unsaturated compounds with O₃ are mainly carbonyls (Johnson and Marston, 2008). Potential interferences from these carbonyls in the O₃ analyzer are expected to be negligible since (i) the ozone decay analysis is restricted to the first minutes where at most half of the initial ozone concentration has reacted, thus limiting product formation, and (ii) the absorption cross-section ratios between ozone and carbonyls at 253.7 nm (photolysis

wavelength of the O_3 analyzer) are in the range of 400 to 4000 (Turnipseed et al., 2017). Hence, carbonyl absorption in the used range of concentrations will be negligible compared to that of ozone.

The ozone decay was measured as a function of time. Kinetic plots representing the pseudo-first-order rate constant (k') as a function of the initial concentration of the studied alcohol ($[Alc]_0$) are displayed in Figure IV.26 – Figure IV.31 for the six investigated compounds. All plots show very good linearity.

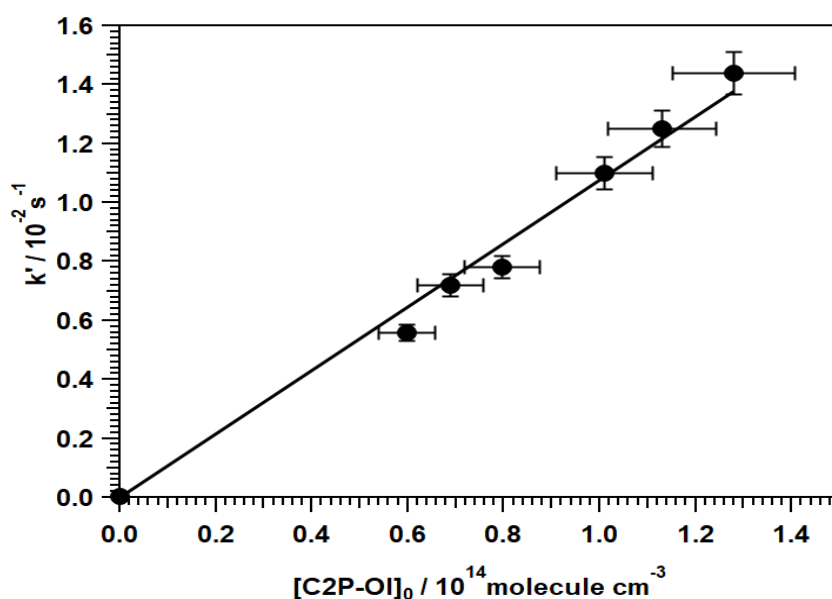


Figure IV.26: The kinetic plot of C2P-Ol ozonolysis.

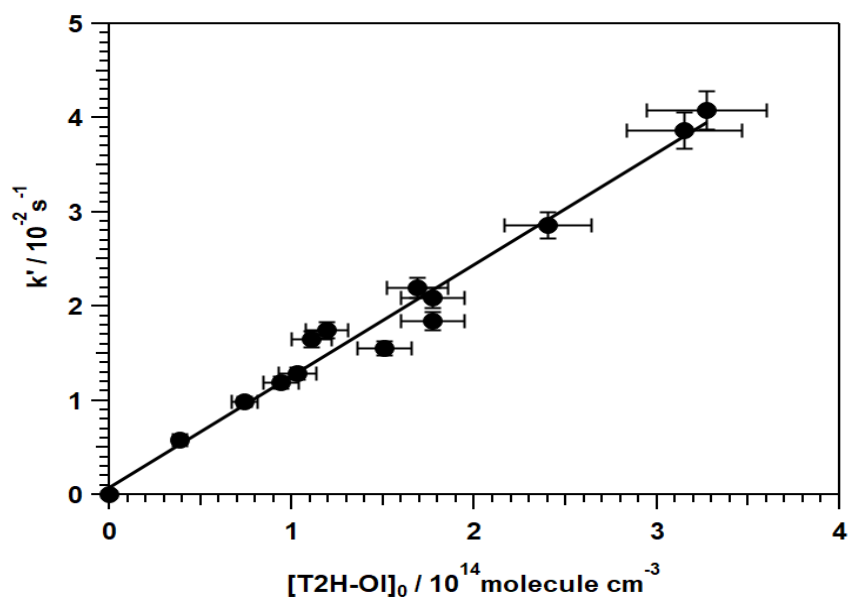


Figure IV.27: The kinetic plot of T2H-Ol ozonolysis.

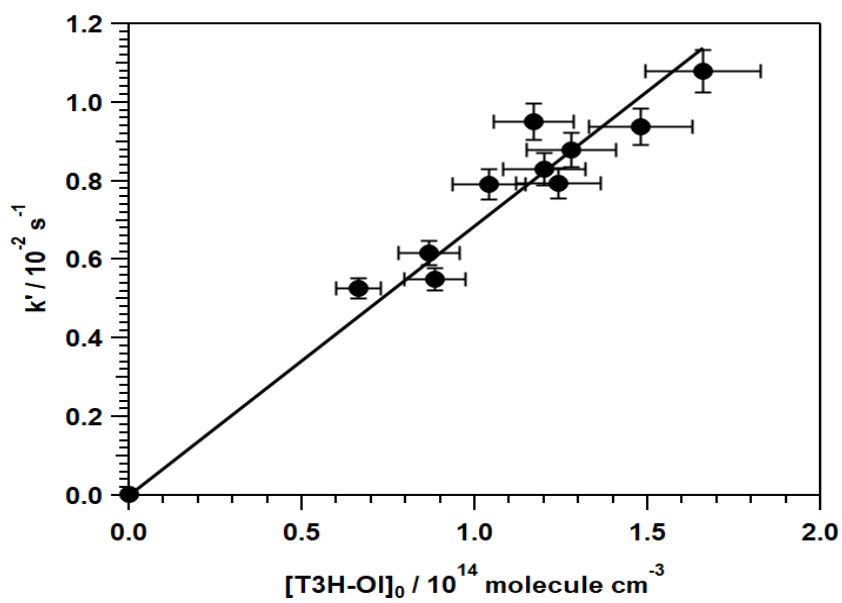


Figure IV.28: The kinetic plot of T3H-Ol ozonolysis.

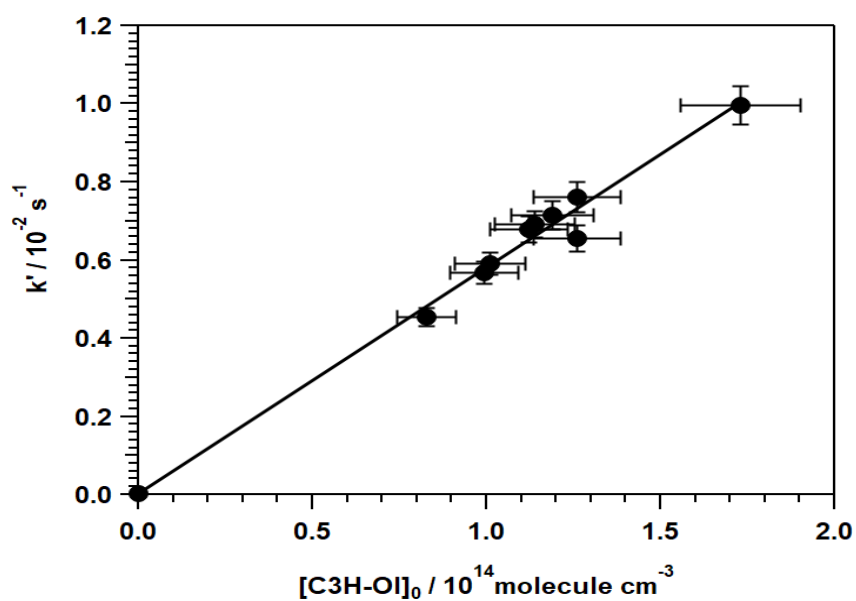


Figure IV.29: The kinetic plot of C3H-OI ozonolysis.

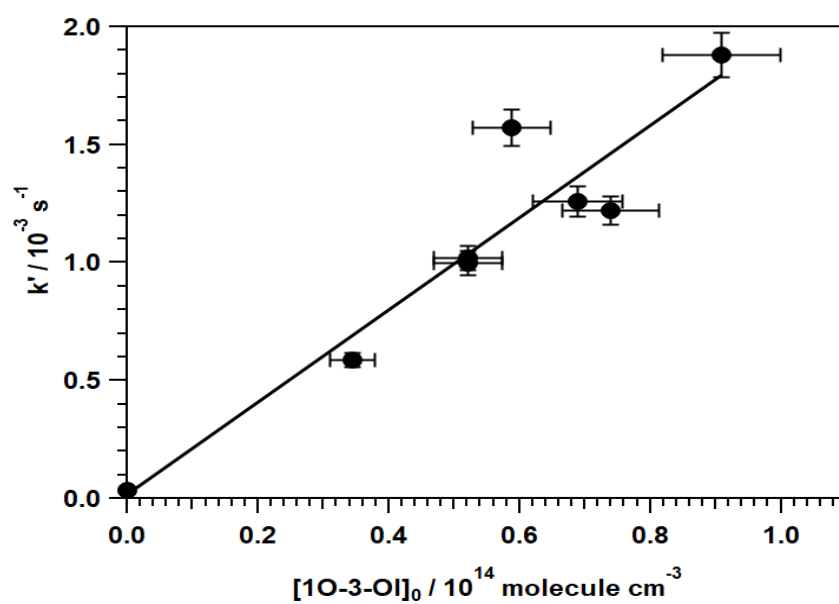


Figure IV.30: The kinetic plot of 10-3-OI ozonolysis.

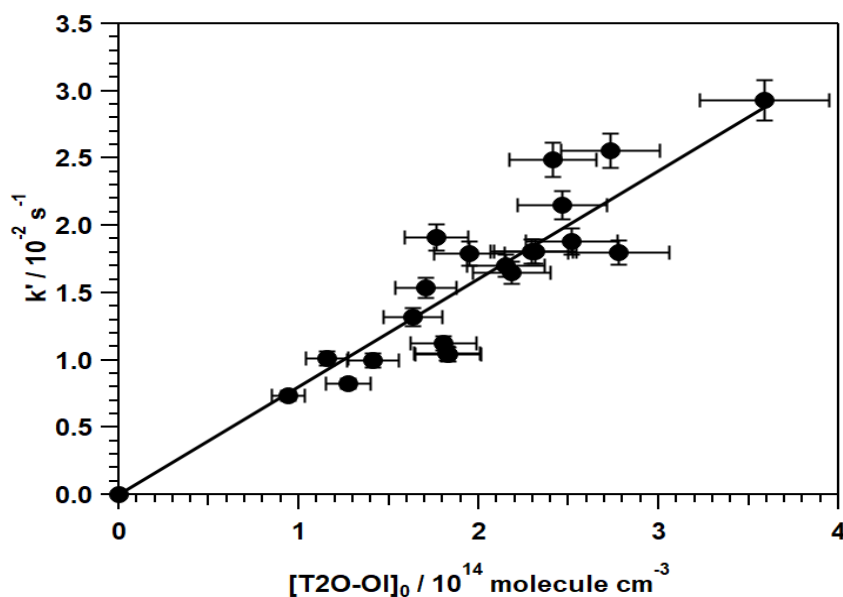


Figure IV.31: The kinetic plot of T2O-ol ozonolysis.

All plots show very good linearity with close to zero intercepts. The ozone rate constants obtained from the slope of these plots are ($\times 10^{-17} / \text{cm}^3 \text{ molecule}^{-1} \text{ s}^{-1}$): (11.3 ± 1.1) for C2P-ol, (11.9 ± 1.2) for T2H-ol, (6.4 ± 1.0) for T3H-ol, (5.8 ± 0.6) for C3H-ol, (2.0 ± 0.6) for 10-3-ol and (8.4 ± 1.3) for T2O-ol. Table IV.13 summarizes all the experimental conditions and rate constants obtained in the present work compared with literature data. Quoted uncertainties are two standard deviations and represent the statistical error on the ozone decays (from 10 – 30 %) combined with the uncertainty coming from alcohol concentrations (of the order of 15%). The final uncertainty on k , $\Delta(k)$, was calculated using the propagation of the error method (see section II.4.1.2.1) and ranges from 18 to 34% for each alkenol rate constant.

IV.3.1.3 Discussion

IV.3.1.3.1 Rate constants

a) Comparison with literature data

A rate constant was obtained for C2P-ol equal to $(11.3 \pm 1.1) \times 10^{-17} \text{ cm}^3 \text{ molecule}^{-1} \text{ s}^{-1}$, about 33% lower than the study of Grosjean and Grosjean, 1994, while in excellent agreement with the determination of Dwyer et al., 2010 and Kalalian et al., 2020 who

found $11.5 \times 10^{-17} \text{ cm}^3 \text{ molecule}^{-1} \text{ s}^{-1}$ and $10.5 \times 10^{-17} \text{ cm}^3 \text{ molecule}^{-1} \text{ s}^{-1}$, respectively. It should be noted that Kalalian et al., relative kinetic methods, while Dwyer et al. and Grosjean and Grosjean used absolute methods. Grosjean and Grosjean carried out only three experiments with no variation of the initial alkenol concentration, leading to probably less reliable results.

For T2H-Ol, the obtained rate constant of $(11.9 \pm 1.2) \times 10^{-17} \text{ cm}^3 \text{ molecule}^{-1} \text{ s}^{-1}$ is in reasonable agreement with the last study by Lin et al., 2016 (28% of difference), while significantly larger than Gibilisco et al., 2015 who found $(5.98 \pm 0.73) \times 10^{-17} \text{ cm}^3 \text{ molecule}^{-1} \text{ s}^{-1}$. Experimental evidence for a series of C₄-C₅ alkenols (Gai et al., 2011) and C₆ alkenols (Lin et al., 2016) supported a higher rate constant when the double bond is in the α carbon to the -OH function.

Indeed, for T3H-Ol and C3H-Ol where the double bond is farther from the -OH group compared to T2H-Ol, lower rate constants are obtained in the present work, $(6.4 \pm 1.0) \times 10^{-17}$ and $(5.8 \pm 0.9) \times 10^{-17} \text{ cm}^3 \text{ molecule}^{-1} \text{ s}^{-1}$, respectively, in excellent agreement with literature data. It should be noted that both 3-Hexen-1-Ol isomers (Trans- and Cis-) display a similar reactivity towards O₃, while literature reviews on alkene + O₃ kinetics indicate that Trans- isomers are generally more reactive than Cis- due to a higher pre-exponential factor (Grosjean and Grosjean, 1996, Treacy et al., 1992).

Only three experiments were performed by Grosjean et al., 1993, with no variation of the initial alkenol concentration, which probably led to less reliable results. The latter may explain the discrepancies observed for $k_{\text{C3H-Ol}+\text{O}_3}$ between Grosjean et al., on the one hand, and the other studies (including the present work), on the other hand.

For 10-3-Ol, our value is in excellent agreement with the only literature data from (Li et al., 2018). Finally, no literature data is available for T2O-Ol. The determined rate constant values, both with all literature data, were summarized in Table IV.13.

b) Effect of the degree of substitution

As observed in previous studies on alkenes + O₃ reaction kinetics (Avzianova and Ariya, 2002, Leather et al., 2010), a higher degree of substitution of the double bond generally

leads to a higher rate constant, which is also the case of alkenols considering all rate constants known for alkenols + O₃ (Table IV.13). Note that the highest *k* value of unsaturated alcohol is for 3-methyl-2-buten-1-ol ($> 4.39 \times 10^{-16} \text{ cm}^3 \text{ molecule}^{-1} \text{ s}^{-1}$) tri-substituted compound. This phenomenon can be explained by an inductive effect produced via enhancing the π -orbital electron density for higher substituted compounds, leading to a lower activation energy.

c) Effect of the OH function

In principle, the hydroxyl function is expected to induce an attractive effect on the adjacent bonds, thus lowering the double bond's electronic density and reducing the unsaturated compound's reactivity. Nevertheless, comparing the O₃ reactivity of alkenols with that of the corresponding alkene where -OH is replaced by -H displays a puzzling picture, as displayed in Figure IV.32.

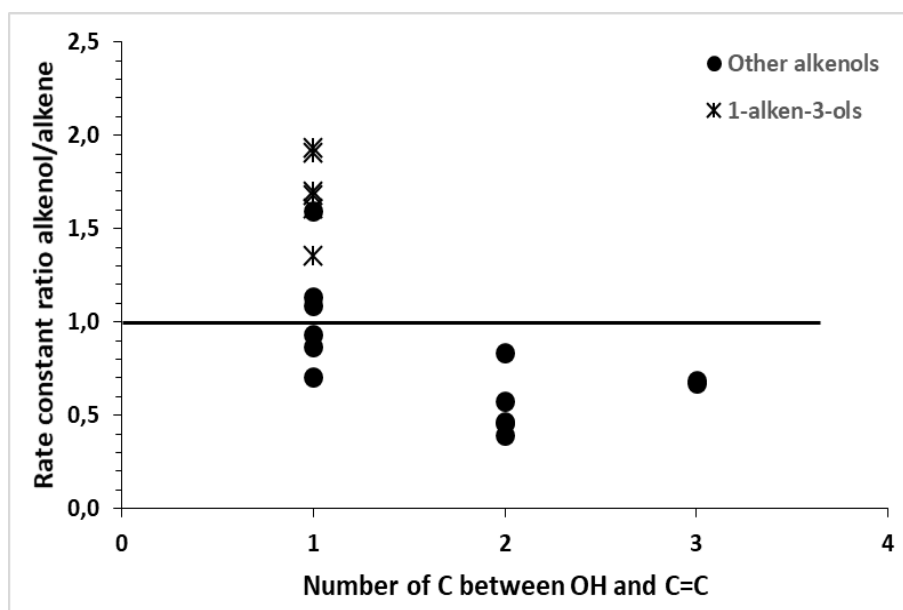


Figure IV.32: Relationship between O₃ rate constant ratio and the number of carbon atoms between OH and C=C (for example, C2P-Ol has one carbon atom between OH and C=C). Stars (*) represent data for 1-alken-3-ols, circles (●) represent other alkenols.

Several compounds have a ratio ($k(\text{O}_3 + \text{alkenol})/k(\text{O}_3 + \text{alkene})$) lower than 1, as expected. For many others, the reverse is observed. The highest ratio of about 2 is calculated for the pairs 10-3-Ol/1-octene and 1-nonen-3-ol/1-nonene.

Note that ratios > 1 are only obtained for compounds where the OH group is attached to the C in α -position and, more specifically, only for 1-alken-3-ols (except 2-buten-1-ol for which only one determination is available in the literature). The used rate constants for this comparison were summarized in Table IV.13.

Table IV.13: Summary of the rate constants for the reactions of a series of alkenols with ozone at room temperature and atmospheric pressure.

Compound	$k \times 10^{17} / \text{cm}^3 \text{ molecule}^{-1} \text{ s}^{-1}$	Reference
1-propen-3-ol	1.44 ± 0.2	Grosjean et al., 1993
	1.8 ± 0.2	Le Person et al., 2009
	1.63 ± 0.03	Parker and Espada-Jallad, 2009
1-buten-3-ol	1.62 ± 0.07	Grosjean et al. 1994
1-buten-4-ol	0.49 ± 0.04	Grosjean et al., 1993
2-methyl-3-buten-2-ol	0.83 ± 0.10	Klawatsch-Carrasco et al. 2004
	0.86 ± 0.29	Fantechi et al., 1998
	1.00 ± 0.03	Grosjean and Grosjean, 1994
1-penten-3-ol	1.68 ± 0.32	Kalalian et al., 2020
	1.64 ± 0.15	Dwyer et al., 2010
	1.79 ± 0.18	Grosjean and Grosjean, 1994
1-penten-4-ol	0.488 ± 0.08	Gai et al., 2011
3-methyl-1-penten-3-ol	0.515 ± 0.03	McGillen et al., 2011
1-nonen-3-ol	1.89 ± 0.20	Li et al., 2018
1-nonen-4-ol	0.83 ± 0.08	Li et al., 2018
2-buten-1-ol (cis and trans)	25.1 ± 4.1	Grosjean and Grosjean, 1994
Cis-2-penten-1-ol (C2P-ol)	10.5 ± 2.0	Kalalian et al., 2020
	16.9 ± 2.5	Grosjean and Grosjean, 1994
	11.5 ± 0.7	Dwyer et al., 2010
	11.3 ± 1.1	This work
Trans-2-hexen-1-ol (T2H-ol)	5.98 ± 0.73	Gibilisco et al., 2015
	16.6 ± 2.2	Lin et al., 2016

	11.9 ± 1.2	This work
Cis-2-hexen-1-ol	7.44 ± 1.03	Lin et al., 2016
Trans-3-hexen-1-ol (T3H-OL)	6.24 ± 1.37 5.83 ± 0.86 6.19 ± 0.72 6.4 ± 1.0	Kalalian et al., 2020 Gibilisco et al., 2015 Lin et al., 2016 This work
Cis-3-hexen-1-ol (C3H-OL)	10.5 ± 0.7 6.4 ± 1.7 6.04 ± 0.95 5.47 ± 0.71 5.8 ± 0.6	Grosjean et al., 1993 Atkinson et al., 1995 Gibilisco et al., 2015 Lin et al., 2016 This work
Trans-4-hexen-1-ol	7.09 ± 0.91	Lin et al., 2016
Cis-4-hexen-1-ol	10.5 ± 1.4	Lin et al., 2016
Cis-3-hepten-1-ol	5.12 ± 0.30	Chen et al., 2016
1-octen-3-ol (1O-3-OL)	1.91 ± 0.19 2.0 ± 0.6	Li et al., 2018 This work
Cis-3-octen-1-ol	5.66 ± 0.52	Chen et al., 2016
Trans-2-octen-1-ol (T2O-OL)	8.4 ± 1.3	This work
3-methyl-2-buten-1-ol	≥ 43.9 ± 3.70	E. Grosjean and Grosjean, 1999

IV.3.1.3.2 Structure-Activity Relationship (SAR)

Rate constants can be evaluated theoretically using the group-additivity approach, based on the earlier work of McGillen et al., 2008 alkenes and extended by McGillen et al., 2011 to heteroatomic unsaturated VOCs. In the reported SAR, an x_H index is calculated, taking into account inductive and steric effects through the following equation:

$$x_H = y \times S + I_x \quad (\text{Eq.1})$$

where y is a negative constant of -4.04, S is the total steric effect, and I_x is the total inductive effect.

For C2P-Ol, T2H-Ol, and C3H-Ol, x_H values were already calculated and reported by McGillen et al., 2011 in their Table. 2: 2.68, 2.55, and 1.43, respectively. T3H-Ol has the same x_H value of 1.43 as its *cis*- isomer. We calculated a slightly different S value for T2H-Ol ($S = 0.085$) compared to McGillen et al., 2011, who found ($S = 0.10$). However, as underlined by McGillen et al., 2011, the steric effect is of small importance in the final x_H value, where inductive effects play the main role. Using an S value of 0.085 yields $x_H = 2.61$ for T2H-Ol, representing an increase of only 2.3%. For 1O-3-Ol and T2O-Ol, we calculated an x_H value of 0.63 ($S = 0.085$ and $I_x = 0.975$) and 2.61 ($S = 0.085$ and $I_x = 2.95$), respectively. Predicted ozonolysis rate constants are then obtained from the following equation:

$$k_{298} = e^{x_H \times 1.08 - 39.66} \quad (\text{Eq.2})$$

SAR-derived rate constants for C2P-Ol, T2H-Ol, T3H-Ol, C3H-Ol, 1O-3-Ol, and T2O-Ol with O_3 are (\times in $\text{cm}^3 \text{ molecule}^{-1} \text{ s}^{-1}$): 11×10^{-17} , 10×10^{-17} (9.4×10^{-17} if using the x_H value from McGillen et al.), 2.8×10^{-17} , 2.8×10^{-17} , 1.2×10^{-17} and 1.0×10^{-17} , respectively. Thus, a very satisfactory estimate is obtained for C2P-Ol, T2H-Ol, and T2O-Ol, with an agreement between 5% and 19%. For the other alkenols, experimental to the calculated rate constant ratios vary between 1.7 and 2.3.

The strongest disagreement is obtained for C3H-Ol and *Trans*- isomers, for which rate constants ratios are 2.1 and 2.3, respectively, suggesting that the impact of $-OH$ in β -position on the reactivity of the double bond may be underestimated in the SAR method. Additional experiments on 3-alkenols are needed to clarify if higher inductive effects should be considered in the SAR.

Ozonolysis rate constants were also computed for a range of alkenols using the same SAR, and values are reported in Figure IV.33 as a function of experimental ones (data are from Table IV.13). Besides the compounds already included by McGillen et al., 2011 analysis (with updated values from (Kalalian et al., 2020) and the present work), four new compounds were added: 1-penten-4-ol (Gai et al., 2011b), *cis*-3-hepten-1-ol (Chen et al., 2016), *cis*-3-octen-1-ol (Chen et al., 2016) and 3-methyl-2-buten-1-ol (E. Grosjean and Grosjean, 1999).

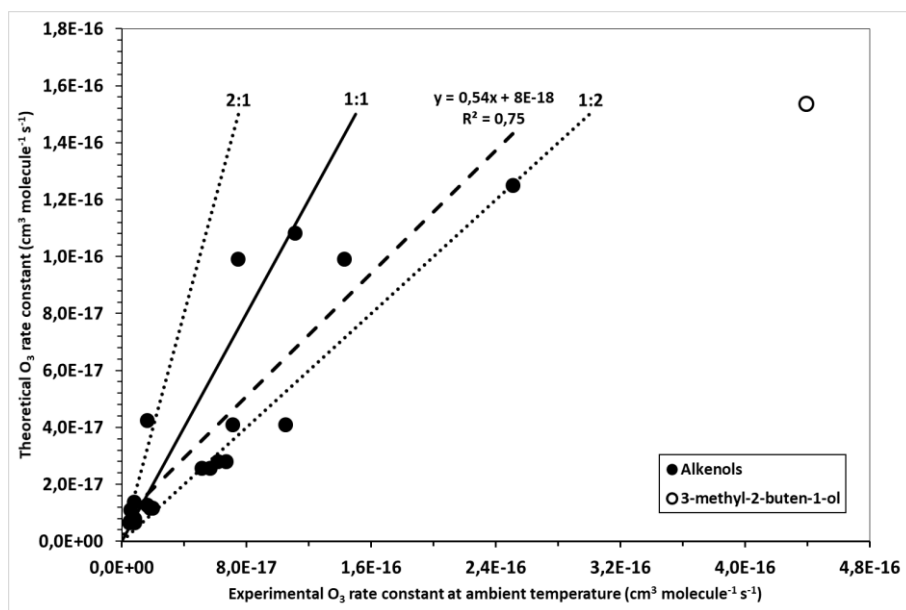


Figure IV.33: Ozonolysis of alkenols: rate constants calculated by SAR vs. those determined experimentally (see Table IV.14). The dashed line is a linear regression on all the data except for 3-methyl-2-buten-1-ol (open circle).

It can be seen that calculated (or theoretical) rate constants from the group-additivity approach are within a factor of 2 of the experimental rate constants. A linear regression through the data yields a coefficient of 0.54 with an R^2 of 0.72, indicating that calculated rate constants are mostly lower than experimental ones.

One compound, 3-methyl-2-buten-1-ol, is excluded from the linear regression. This compound is tri-substituted unsaturated alcohol, for which the unique experimental value ($> 4.39 \times 10^{-16} \text{ cm}^3 \text{ molecule}^{-1} \text{ s}^{-1}$ from (E. Grosjean and Grosjean, 1999)) is about three times higher than the calculated one. Additional experiments are needed for 3-methyl-2-buten-1-ol and other tri-substituted compounds to include them in the SAR developed by (McGillen et al., 2011a).

IV.3.1.3.3 Atmospheric implications

Atmospheric lifetimes (τ_{O_3}) due to the oxidation of the C₅-C₈ unsaturated alcohols or their photolysis were calculated using the equation (Eq.30) displayed in section II.4.1.3. The oxidant concentrations of Cl, O₃, NO₃, and OH were detailed in section II.4.1.3. The calculated atmospheric lifetimes were summarized in Table IV.14.

Table IV.14: Calculated atmospheric lifetimes of C₅-C₈ unsaturated alcohols towards atmospheric oxidants (OH, O₃, Cl, and NO₃).

Compound	$\tau_{\text{Cl-high}}$ (h)	$\tau_{\text{Cl-low}}$ (days)	τ_{O_3} (h)	τ_{NO_3} (h)	τ_{OH} (h)
C2P-Ol	9 ^(a)	39 ^(a)	2 ^(e)	2 ^(k)	4 ⁽ⁿ⁾
T2H-Ol	8 ^(b)	34 ^(b)	2 ^(f)	4 ^(l)	3 ^(o)
T3H-Ol	9 ^(b)	36 ^(b)	4 ^(g)	1 ^(l)	3 ^(p)
C3H-Ol	9 ^(b)	38 ^(b)	3 ^(h)	2 ^(m)	2 ^(q)
10-3-Ol	7 ^(c)	29 ^(c)	12 ⁽ⁱ⁾	(d)	(d)
T2O-Ol	(d)	(d)	3 ^(j)	(d)	(d)

^(a) k (C2P-Ol + Cl) is the average of (Rodríguez et al., 2010) and this work (see chapter V).

^(b) k (T2H-Ol + Cl), k (T3H-Ol + Cl), k (C3H-Ol + Cl) are the average of (Gibilisco et al., 2014) and this work (see chapter V).

^(c) k (10-3-Ol + Cl) is the value of this work (see chapter V).

^(d) Not measured.

^(e) k (C2P-Ol + O₃) is the average of (Grosjean and Grosjean, 1994) (Dwyer et al., 2010b) (Kalalian et al., 2020), and this work (Grira et al., 2020, chapter IV).

^(f) k (T2H-Ol + O₃) is the average of Gibilisco et al., 2015, Lin et al., 2016, and this work (Grira et al., 2020, chapter IV).

^(g) k (T3H-Ol + O₃) is the average of Gibilisco et al., 2015, Lin et al., 2016, Kalalian et al., 2020, and this work (Grira et al., 2020, chapter IV).

^(h) k (C3H-Ol + O₃) is the average of (Daniel Grosjean et al., 1993a) Atkinson et al., 1995, Gibilisco et al., 2015, Lin et al., 2016 Chen et al., 2016 and this work (Grira et al., 2020, chapter IV).

⁽ⁱ⁾ k (10-3-Ol + O₃) is the average of Li et al., 2018, and this work (Grira et al., 2020, chapter IV).

^(j) k (T2O-Ol + O₃) is the value of this work (Grira et al., 2020, chapter IV).

^(k) k (C2P-Ol + NO₃) is the value of (Zhao et al., 2011)

^(l) k (T2H-Ol + NO₃) and k (T3H-Ol + NO₃) are the values of Pfrang et al., 2006.

^(m) k (C3H-Ol + NO₃) is the average of Atkinson et al., 1995 and Pfrang et al., 2006.

⁽ⁿ⁾ k (C2P-Ol + OH) is the value of Davis et al., 2011.

^(o) k (T2H-Ol + OH) is the average of Davis et al., 2011 and Gibilisco et al., 2013.

^(p) k (T3H-Ol + OH) is the average of Gibilisco et al., 2013, Peirone et al., 2014, and Gibilisco et al., 2015.

^(q) k (C3H-Ol + OH) is the average of Atkinson et al., 1995, Jimenez et al., 2009, Davis et al., 2011, and Gibilisco et al., 2013.

The estimated atmospheric lifetimes of the studied alcohols during their reactions with the atmospheric oxidants range from 1 to 12 h, except for Cl atoms' reactions, for which much higher lifetimes (29 to 39 days) were found in a continental background atmosphere. Thus, C₅-C₈ unsaturated alcohols are rapidly removed in the gas phase by O₃, NO₃, or OH and disappear closely to their emission sources. However, it is worth stressing that, in the marine boundary layer and coastal areas, the Cl-initiated oxidation of alkenols can become competitive compared to other oxidants with lifetimes on the order of a few hours. In addition to the marine boundary layer and coastal areas, specific continental areas were recently shown to display even higher Cl atom concentrations (Lee et al., 2018, Faxon and Allen, 2013, Breton et al., 2018). The present results will help in better understanding the atmospheric chemistry in these regions.

IV.4 Conclusion

In this chapter, the reactivity of a series of C₅-C₆ unsaturated aldehydes with O₃ has been investigated experimentally in terms of kinetics and reaction mechanisms in the absence of OH scavenger. The kinetics of C₅-C₆ unsaturated aldehydes with ozone has been investigated for the first time using a flow reactor (LFR). Additional experiments using a static atmospheric simulation chamber (D-ASC) were performed. Both experimental setups yield consistent results and show very good agreement with the literature data. C₅-C₆ unsaturated aldehydes' ozonolysis leads to the formation of multifunctional compounds such as bicarbonyl like glyoxal, hydroxycarbonyls like 2-hydroxypropanal, and saturated aldehydes such as propanal, butanal, and acetaldehyde.

A slight preference for the formation pathway of bicarbonyls (glyoxal) was observed. The present work suggests that O₃-initiated oxidation of unsaturated aldehydes is initiated by electrophilic addition of ozone to the double bond to form a primary ozonide. Compared with literature data (Kalalian, 2018), where cyclohexane was used as an OH scavenger, the yields of glyoxal and propanal (T2P + O₃) glyoxal and butanal (T2H + O₃) did not differ

significantly with the present work, within the error limits, which suggests that secondary OH processes are of minor importance.

A detailed chemical reaction mechanism for each ozonolysis reaction ($\text{T2P} + \text{O}_3$ and $\text{T2H} + \text{O}_3$) is proposed upon the identified reaction products. Finally, the present study constitutes the first investigation of aerosol formation from a trans-2-alkenal species' ozonolysis to the best of our knowledge. Both T2P and T2H ozonolysis are shown to participate in particle loadings in the atmosphere. Further work is needed to improve our understanding of SOA contribution from trans-2-alkenal compounds, which are ubiquitous species emitted by the vegetation. These results on the C₅-C₆ alkenals both with (Kalalian 2018) complete the missing puzzle data of previous studies of C₃-C₉ trans-2-alkenals.

The estimation of the C₅-C₇ unsaturated aldehydes lifetimes shows that these carbonyls are mainly removed by photodissociation ($\tau_{\text{uv}} < 1\text{h}$). Their OH and Cl atoms' reactions at the marine boundary layer compete with a lifetime lower than 11h. On the other hand, lifetimes of the reaction between C₅-C₇ unsaturated aldehydes with respect to the atmospheric oxidants O₃ NO₃ vary in the range of 1 to 8 days. Those results were divided into two publications. The first article, entitled "Gas-phase ozonolysis of trans-2-hexenal: Kinetics, products, mechanism and SOA formation", has been submitted to "Atmospheric Environment". The second article, entitled "Gas-phase ozonolysis of trans-2-pentenal: Kinetics, products, mechanism and SOA formation", is in preparation.

In the second part of this chapter, I focused on measuring the rate constants of the ozonolysis of a series of C₅-C₈ unsaturated alcohols at room temperature using the absolute method. The rate constant of the ozonolysis of unsaturated alcohol decreases as a function of the substitution degrees. The lifetimes of the reaction between C₅-C₈ unsaturated alcohols with respect to the atmospheric oxidants O₃, OH, and NO₃ vary in the range of 1 to 12 hours. However, their lifetimes with Cl atoms are in the range of 29 to 39 days. To better understand these carbonyls' impact, detailed studies on their gas-phase products and their contribution to the SOA budget in the troposphere have to be done. Those results are gathered in one publication, entitled "Ozone reaction kinetics of C₅-C₈ unsaturated alcohols of biogenic interest", which is in preparation.

V Chapter V: Oxidation of unsaturated aldehydes and alcohols: reaction with Cl

V.1 Introduction

This chapter investigates the oxidation of two series of unsaturated aldehydes and alcohols ($\geq C_5$) with chlorine atom (Cl) and to assesses the impact of their degradation process on the atmosphere. The first section of this chapter is focused on the oxidation reactions of C_5 - C_7 unsaturated aldehydes, which are Trans-2-Pentenal (T2P), Trans-2-Hexenal (T2H), and Trans-2-Heptenal (T2Hep) with chlorine (Cl) in term of kinetics, gas-phase products, and SOA formations. The second section deals with the kinetics of the reaction between C_5 - C_8 unsaturated alcohols, namely: Cis-2-Penten-1-ol (C2P-ol), Trans-2-Hexen-1-ol (T2H-ol), Trans-3-Hexen-1-ol (T3H-ol), Cis-3-Hexen-1-ol (C3H-ol), and 1-Octen-3-ol (1O-3-ol) with chlorine (Cl). These compounds were chosen for the same reasons discussed in the previous chapter (see section IV.1).

The rate constants of the reactions between C_5 - C_7 unsaturated aldehydes (T2P, T2H, and T2Hep) and chlorine (Cl) were measured by Rodríguez et al., 2005 using a relative method at room temperature and atmospheric pressure. The T2P + Cl reaction rate was calculated using the structure Activity Relationships (SARs) method (Teruel et al., 2009). Table V.1 displayed a summary of the rate constants calculated and measured in previous works for T2P + Cl, T2H + Cl, and T2Hep + Cl reactions.

Table V.1: Summary of rate constants, methods, and analytical techniques used in previous works of C_5 - C_7 unsaturated aldehydes and chlorine reactions.

Reaction	$k \times 10^{-10} / \text{cm}^3 \text{ molecule}^{-1} \text{ s}^{-1}$	Method	Analysis technique	Reference
T2P + Cl	3.47	SAR Estimation		Teruel et al., 2009
	1.31 ± 0.19	RM: Reference compounds: Ethane Propene 1-butene	GC-FID	Rodríguez et al., 2005
T2H + Cl	1.92 ± 0.22			
T2Hep + Cl	2.4 ± 0.29			

RM: Relative Method.

On the other hand, neither mechanistic data nor SOA quantification for the C₅-C₇ unsaturated aldehydes with Cl is available in the literature. The second part of this chapter displayed the kinetic measurements of C₅-C₈ unsaturated alcohols (C2P-Ol, T2H-Ol, T3H-Ol, C3P-Ol, and 10-3-Ol) reactions with chlorine (Cl).

The rate constant of the C2P-Ol + Cl reaction was measured by Rodríguez et al., 2005, using the relative method and the kinetic studies of C₆ alcohols (T2H-Ol, T3H-Ol, and C3H-Ol) reactions with chlorine were investigated by Gibilisco et al. 2014 using the relative method. However, no determination of the reaction rate constant between 10-3-Ol+Cl can be found in the literature. Table V.2 displayed a summary of the rate constants measured in previous works for C₅-C₈ unsaturated alcohols with chlorine.

Table V.2: Summary of rate constants, methods, and analytical techniques used in previous works of the reactions between C₅-C₈ unsaturated alcohols and Cl atoms.

Reaction	$k \times 10^{-10} / \text{cm}^3 \text{ molecule}^{-1} \text{ s}^{-1}$	Method	Analysis technique	Reference
C2P-Ol + Cl	3.00 ± 0.49	RM: Reference compounds: Octane Propene Cyclohexane	GC-FID	Rodríguez et al., 2010
T2H-Ol + Cl	3.49 ± 0.82	RM: Reference compounds: Isobutene 1-butene	FTIR spectroscopy	Gibilisco et al., 2014
T3H-Ol + Cl	3.42 ± 0.79			
C3H-Ol + Cl	2.94 ± 0.72			
10-3-Ol + Cl	NM			

RM: Relative Method.

AM: Absolute Method.

NM: Not measured.

V.2 Oxidation of unsaturated aldehydes with chlorine atoms

This work was done in collaboration with UCLM University, where experimental work was done with a postdoctoral researcher (Dr. Maria Antinolo). In this section, I displayed the kinetic measurements, the gas-phase, and the SOA formations of the reaction between chlorine atoms and C₅-C₇ unsaturated aldehydes (T2P, T2H, and T2Hep). The determination of the rate constant of the reaction between T2P + Cl was done in both D-ASC (IMT Lille Douai) and 16L-ASC (UCLM, Spain), whereas the kinetic measurements of T2H + Cl and T2Hep + Cl were done in D-ASC (IMT Lille Douai) and 16L-ASC (UCLM), respectively. Gas-phase products of the three reactions (T2P + Cl, T2H + Cl, and T2Hep + Cl) were done in 16L-ASC and CR-ASC (UCLM). Finally, the particle-phase investigations for the T2P, T2H, and T2Hep oxidations were done in CR-ASC. All experiments were carried out at 296 ± 2 K and 730 ± 20 Torr of purified air (D-ASC) and synthetic air (16L-ASC and CR-ASC).

V.2.1 Determination of rate constants

V.2.1.1 Experimental conditions and protocols

The kinetic studies of chlorine's reaction and the three studied aldehydes (T2P, T2H, and T2Hep) were carried out using the relative method in two atmospheric simulation chambers: D-ASC and/or 16L-ASC. Technical specifications on both chambers are described in chapter II, whereas experimental conditions and protocols are described below. The kinetic measurements of the rate constants of T2P + Cl and T2Hep + Cl reactions were done based on FTIR analyses of the aldehyde and the reference compound concentrations. On the other hand, the T2H + Cl rate constant was determined using a Proton-Transfer Reaction Time-of-Flight Mass Spectrometry (PTR-ToF-MS Kore) analysis. The experimental protocol of the kinetic measurements of the three studied reactions in both reactors is the same. The procedure started by injecting the studied aldehyde in the reactor and following its concentration for 15 min in the dark. Then, a reference compound was added to the reactor and allowed for homogenization for 30 min. After 30 min of photolysis, lights were turned off, and molecular chlorine was added to the reaction mixture and left for 30 min in the chamber. At the end of each experiment,

the reactor was cleaned by filling with air and pumping up several times. We measured the loss rate constants corresponding to both reactants during all the described steps to check for any possible dark reaction, photolysis, or adsorption on the cell walls. The initial concentration of the unsaturated aldehyde and the reference compound was obtained either from partial pressure measurements or by subtracting the studied compound's absorption band in each IR spectrum, taking into account calibrated reference spectra. Those for the reference compounds and Cl₂ were obtained from partial pressure measurements. For T2H experiments, no wall losses were observed in PTR-ToF-MS measurements, fluctuations were calculated as the ratio of one standard deviation to the mean value, was estimated for T2H and isoprene in D-ASC for 45 min of measurements. The experimental conditions, reactants' initial concentrations, and loss rate constants are summarized in Table V.3.

Table V.3: Experimental conditions, initial reactant concentrations in the kinetic measurements, and measured loss rate constants.

Reaction	Reactor	Lamps	Compound	Initial concentration range / $\times 10^{13}$ molecule cm ⁻³	$k_L \pm 2\sigma / \times 10^{-5} \text{ s}^{-1}$
T2P + Cl	D-ASC (FTIR)	1-2	T2P	5.0 – 15.1	(1.85±0.20) – (6.43±0.42)
			Isoprene	5.9 – 14.8	(0.54±0.32) – (2.68±0.24)
			Cl ₂	25.0 – 37.3	NM
	16L-ASC (FTIR)	4	T2P	46.2 – 93.0	(2.95±0.26) – (3.57±0.14)
			Cyclohexane	57.6 – 66.0	(0.11±0.18) – (1.07±0.42)
			Ethanol	74.4 – 110	(1.72±0.14) – (2.08±0.80)
			Cl ₂	66.0 – 132	NM
T2H + Cl	D-ASC (PTR)	2	T2H	5.9 – 11.6	Fluctuations ≤ 1.1
			Isoprene	6.40 – 13.3	Fluctuations ≤ 1.1
			Cl ₂	14.5 – 58.3	NM
T2Hept + Cl	16L-ASC (FTIR)	3	T2Hep	23.0 – 83.6	(3.05±0.90) – (4.38±0.57)
			Isoprene	10.5 – 13	(0.77±0.39) – (6.18±0.24)
			Propene	18.1 – 25.2	(2.79±0.96) – (6.61±1.09)
			Cl ₂	82.9 – 101	NM

NM: Not Measured.

The purities of T2P, T2H, and T2Hep were the same, as mentioned in chapter III. On the other hand, the rest of the reagents were obtained from the following sources: isoprene (99%, Sigma-Aldrich), cyclohexane (99.9%, Sigma-Aldrich), ethanol ($\geq 99.5\%$, Sigma-Aldrich), Cl_2 (10% in N_2 , Air Products) at IMT Lille Douai and Cl_2 (99.8%, Sigma-Aldrich) at UCLM. All experiments were carried out in synthetic air (purity 99.999%, Air Liquide). As it can be seen in the previous table that the T2P losses in the 16L-ASC are lower than its losses in the D-ASC, this can be explained by the difference of the reactor material where D-ASC is made from Teflon and 16L-ASC is made from Pyrex.

a) Rate constants of the used reference compounds

The relative rate constant of the gas-phase reaction of T2P with Cl was measured in the presence of three reference compounds: isoprene, cyclohexane, ethanol. On the other hand, the kinetic measurements of the T2H + Cl reaction were run using isoprene. The determination of the rate constant of T2Hep and Cl was done using isoprene and propene. The used Cl-rate constant of isoprene k_{Isoprene} is $(4.80 \pm 1.25) \times 10^{-10} \text{ cm}^3 \text{ molecule}^{-1} \text{ s}^{-1}$. This value is the average of three data found in the literature. The used Cl-rate constant $k_{\text{Cyclohexane}}$ is $(2.77 \pm 1.12) \times 10^{-10} \text{ cm}^3 \text{ molecule}^{-1} \text{ s}^{-1}$, an average of 6 data found in the literature. The used Cl-rate constants of ethanol ($(1.0 \pm 0.2) \times 10^{-10} \text{ cm}^3 \text{ molecule}^{-1} \text{ s}^{-1}$) and propene ($(2.7 \pm 0.3) \times 10^{-10} \text{ cm}^3 \text{ molecule}^{-1} \text{ s}^{-1}$) were taken from IUPAC, 2006 and IUPAC, 2003, respectively. All uncertainties of the reference compounds (Δk_{Ref}) are 2σ , whereas no specification was mentioned for the uncertainties of k_{Ethanol} (IUPAC, 2006) and k_{Propene} (IUPAC, 2003). The summary of all rate constants is displayed in Table V.4.

Table V.4: Summary of rate constants of the used reference compounds (isoprene, cyclohexane, ethanol, and propene).

Compound	$k_{\text{Ref}} \times 10^{10} / \text{cm}^3 \text{ molecule}^{-1} \text{ s}^{-1}$	Reference
Isoprene	4.6 ± 0.5	Ragains and Finlayson-Pitts, 1997
	5.5 ± 1.0	Fantechi et al., 1998
	4.3 ± 0.6	Orlando et al., 2003
	4.80 ± 1.25	The used value (average)
Cyclohexane	2.0 ± 0.2	Davis et al., 1970

	3.11 ± 0.14	Atkinson and Aschmann, 1985
	3.61 ± 0.15	Wallington et al., 1988
	2.4 ± 0.3	Rowley et al., 1992
	3.08 ± 0.12	Aschmann and Atkinson, 1995
	2.91 ± 0.31	Li and Pirasteh, 2006
	2.3 ± 0.09	Anderson et al., 2007
	2.77 ± 1.12	The used value (average)
Ethanol	1.0 ± 0.2	The used value (IUPAC, 2006)
Propene	2.7 ± 0.3	The used value (IUPAC, 2003)

b) Determination of the rate constant k_{Ald} and the overall error Δk_{Ald}

Relative rate constants were obtained for each reference compound by plotting $\ln([Ald]_0/[Ald]_t) - k_{L,Ald}t$ vs. $\ln([Ref]_0/[Ref]_t) - k_{L,Ref}t$. Using the reference compound + Cl rate constant (k_{Ref}), we calculated the rate constant of the aldehyde + Cl (k_{Ald}). The overall error Δk_{Ald} comprises statistical errors Δk_{Ald} (stat) and systematic errors Δk_{Ald} (syst). Statistical errors Δk_{Ald} (stat) and systematic errors Δk_{Ald} (syst) are estimated to 10% (see section II.4.1.2.2).

V.2.1.2 Results

V.2.1.2.1 Rate constant of T2P + Cl

The consumption of the reactants (T2P and isoprene) in the D-ASC was monitored as a function of time, using the following IR spectral features: $1175 - 1115 \text{ cm}^{-1}$ and $942 - 855 \text{ cm}^{-1}$ for T2P and isoprene, respectively. In the 16L-ASC, the used IR spectral features were $1750 - 1700 \text{ cm}^{-1}$ for T2P, $2890 - 2830 \text{ cm}^{-1}$ for cyclohexane, and $930 - 840 \text{ cm}^{-1}$ ethanol. The rate constants of the reagent losses were measured for each experiment and taken into account in calculations (Table V.4). Figure V.1 shows the relative loss of T2P versus the reference compounds in Cl atoms' presence.

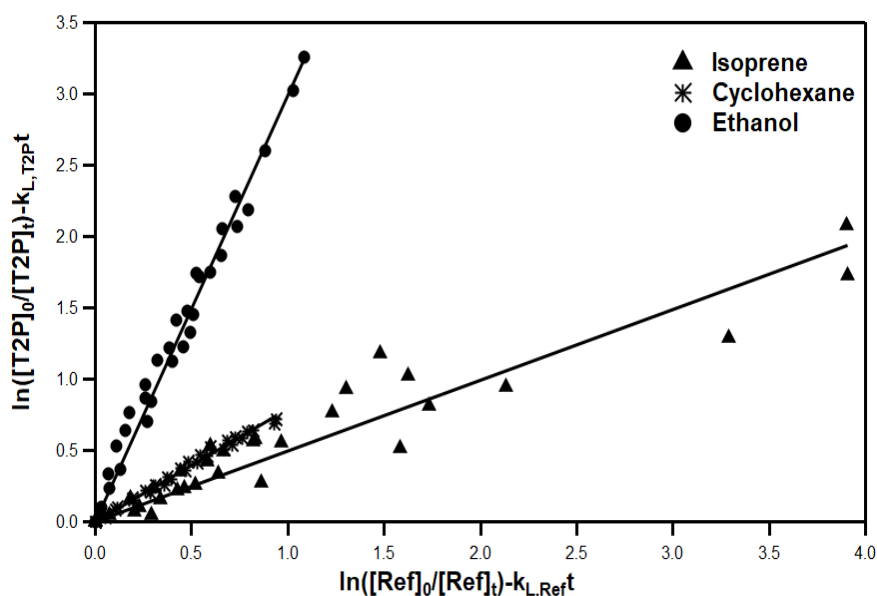


Figure V.1: Decays of T2P vs. reference in the presence of Cl atoms.

The good linearity with a correlation coefficient greater than 98% and an intercept close to zero for all the reference compounds indicates no secondary reactions other than those corrected losses are occurring. The slope $\left(\frac{k_{T2P}}{k_{Ref}}\right)$ Relative rate constants (k_{T2P}) were obtained for each reference compound, and a total average was calculated. All these data are summarized in Table V.5.

Table V.5: Rate constants for the reaction of T2P with Cl atoms.

Reactor	Reference compound	$\frac{k_{T2P}}{k_{Ref}} \pm \Delta \left(\frac{k_{T2P}}{k_{Ref}}\right)^a$	$k_{T2P} \pm \Delta k_{T2P}^b$ ($\times 10^{-10} \text{ cm}^3 \text{ molecule}^{-1} \text{ s}^{-1}$)
D-ASC	Isoprene (6 runs)	0.50 ± 0.04	2.40 ± 0.82
16L-ASC	Cyclohexane (2 runs)	0.79 ± 0.01	2.19 ± 0.92
	Ethanol (3 runs)	2.99 ± 0.08	2.99 ± 0.69
Average			2.53 ± 0.83^a

^a two standard deviations.

^b uncertainty calculated according to equations 11-12 (see section II.4.1.2.2).

The overall error Δk_{T2P} in the individual rate constant values ranges from 24 to 42%.

V.2.1.2.2 Rate constant of T2H + Cl

The initial concentrations of reactants (T2H and isoprene) were determined using the FTIR spectrometer. The IR spectral features were: 1182 – 1116 cm^{-1} and 943 – 844 cm^{-1} for T2H and isoprene, respectively. The decay of both compounds' concentrations was measured using a PTR-ToF-MS Kore, which allows the measurement of the mass-to-charge ratio (m/z) of the product fragments. The used fragments were ($\text{C}_2\text{HO.H}^+$, $m/z = 57$) and ($\text{C}_6\text{H}_{10}\text{O.H}^+$, $m/z = 99$) for T2H and ($\text{C}_5\text{H}_8.\text{H}^+$, $m/z = 69$) for isoprene. Concentration profiles of both reagents have not shown any decay due to wall losses or photolysis of reactants. Only fluctuations of less than 1.1% were observed for T2H and isoprene over 45 min. Figure V.2 displays the relative loss of T2H versus the reference compounds in Cl atoms' presence.

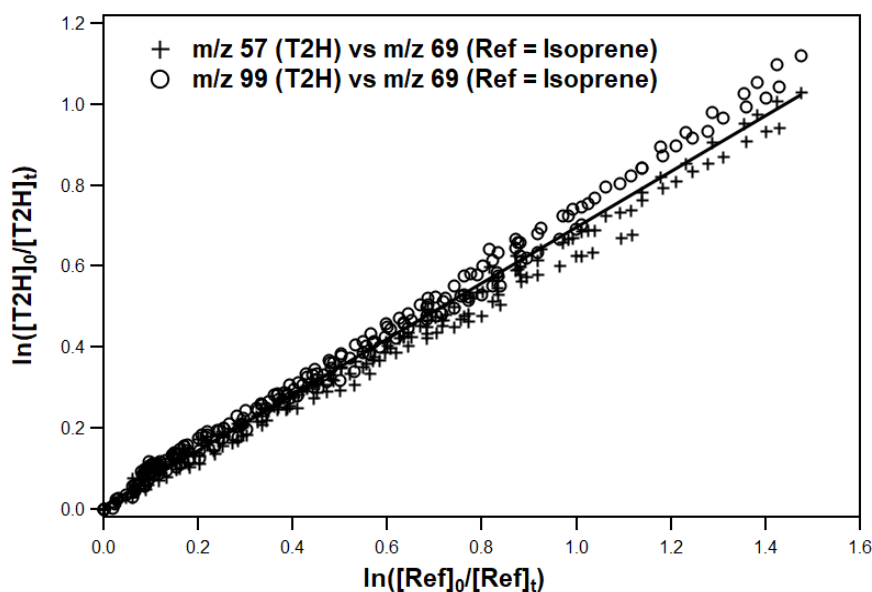


Figure V.2: Decays of T2H vs. reference in the presence of Cl.

The good linearity with a correlation coefficient greater than 99% and an intercept close to zero. Both the slope ($\frac{k_{\text{T2H}}}{k_{\text{Ref}}}$) and the relative rate constant (k_{T2H}) were calculated. All these data are summarized in Table V.6.

Table V.6: Rate constant for the reaction of T2H with Cl atoms.

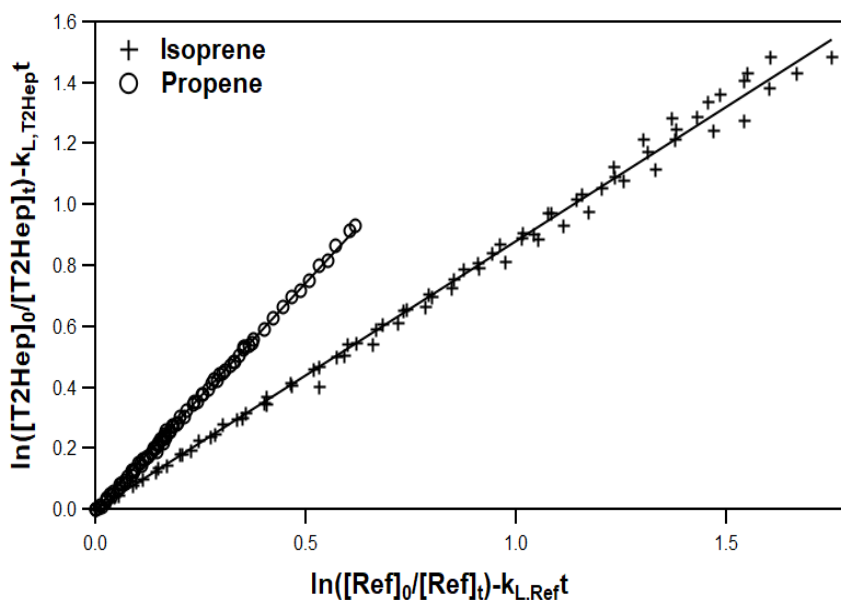
Reactor	Reference compound	$\frac{k_{T2H}}{k_{Ref}} \pm \Delta \left(\frac{k_{T2H}}{k_{Ref}} \right)^a$	$k_{T2H} \pm \Delta k_{T2H}^b$ ($\times 10^{-10} \text{ cm}^3 \text{ molecule}^{-1} \text{ s}^{-1}$)
D-ASC	Isoprene (6 runs)	0.69 ± 0.02	3.31 ± 0.96

^a two standard deviations.^b uncertainty calculated according to equations 11-12 (see section II.4.1.2.2).

The overall error Δk_{T2H} in the individual rate constant value is 29%.

V.2.1.2.3 Rate constant of T2Hep + Cl

The consumption of the reactants (T2Hep, isoprene, and propene) in 16L-ASC were monitored as a function of time, using IR spectral features: 1170 – 1120 cm^{-1} , 950 – 850 cm^{-1} , and 915 – 850 cm^{-1} for T2Hep, isoprene, and propene. The rate constants of the reagent losses were measured for each experiment and taken into account in calculations (Table V.7). Figure V.3 shows the consumption of T2Hep as a function of the reference compound's consumption in the presence of Cl.

**Figure V.3:** Decays of T2Hep vs. reference in the presence of Cl atoms.

The good linearity with a correlation coefficient greater than 99% and an intercept close to zero.

The slope $\left(\frac{k_{T2Hep}}{k_{Ref}}\right)$ and the relative rate constants (k_{T2Hep}) were obtained for each reference compound, and a total average was calculated. All these data are summarized in Table V.7.

Table V.7: Rate constants for the reaction of T2Hep with Cl atoms.

Reactor	Reference compound	$\frac{k_{T2Hep}}{k_{Ref}} \pm \Delta\left(\frac{k_{T2Hep}}{k_{Ref}}\right)^a$	$k_{T2Hep} \pm \Delta k_{T2Hep}^b$ ($\times 10^{-10} \text{ cm}^3 \text{ molecule}^{-1} \text{ s}^{-1}$)
16L-ASC	Isoprene (3 runs)	0.88 ± 0.02	4.00 ± 0.51
	Propene (3 runs)	1.48 ± 0.02	4.22 ± 1.20
Average			4.11 ± 0.32^a

^a two standard deviations.

^b uncertainty calculated according to equations 11-12 (see section II.4.1.2.2).

The overall error Δk_{T2Hep} in the individual rate constant values is in the range of 13 to 28%.

V.2.1.3 Discussion

a) Comparison with literature data

The measured rate constants of C₅-C₇ unsaturated aldehydes are compared to literature data listed in Table V.8. The kinetic measurement of the reaction between T2P and Cl was obtained in two previous works: a rate constant estimated using the SAR method, $3.47 \times 10^{-10} \text{ cm}^3 \text{ molecule}^{-1} \text{ s}^{-1}$ (Teruel et al., 2009) and an experimental value $(1.31 \pm 0.19) \times 10^{-10} \text{ cm}^3 \text{ molecule}^{-1} \text{ s}^{-1}$ (Rodríguez et al., 2005).

The rate constant of the reaction of T2P with Cl atoms estimated by Teruel et al., 2009, using the SAR method is 25% higher than that determined in the present work. The source of this discrepancy is probably the uncertainties of the SAR method that aims to estimate rate constants based on the reactivity of other compounds considering only their structure. On the other hand, the rate constant determined in the present work is 51% higher than that provided by Rodríguez et al., 2005. The source of this discrepancy with Rodríguez et al.'s work is not clear.

Moreover, the latter difference was also observed for T2H + Cl and T2Hep + Cl, where the rate constants determined in the present work are 58% times higher than those provided by Rodríguez et al. 2005 (Table V.8). In Rodríguez et al.'s work, the losses of aldehydes (T2P, T2H, and T2Hep) and the reference compounds (ethane, propene, and 1-butene) were monitored by GC-FID detection.

First, the Cl-rate constants for the reference compounds used by Rodríguez et al. cannot explain this discrepancy. Indeed, a re-evaluation of the value obtained by Rodríguez et al. for k_{T2P} , k_{T2H} and k_{T2Hep} using the rate constants recommended by IUPAC, 2006 for ethane and propene gives rate constants which remain as the one calculated by Rodríguez et al. ($k_{T2P} = 1.39 \times 10^{-10} \text{ cm}^3 \text{ molecule}^{-1} \text{ s}^{-1}$, $k_{T2H} = 2.04 \times 10^{-10} \text{ cm}^3 \text{ molecule}^{-1} \text{ s}^{-1}$ and $k_{T2Hep} = 2.54 \times 10^{-10} \text{ cm}^3 \text{ molecule}^{-1} \text{ s}^{-1}$). The difference between the reported rate constants here and that provided by Rodríguez et al., 2005 may be due to possible secondary losses that were not corrected in the Rodríguez et al.'s work.

Table V.8: Summary of the rate constants for the reactions of a series of C₃-C₇ alkenals with Cl atoms at room temperature and atmospheric pressure.

Compound Linear formula	$k \times 10^{-10} /$ $\text{cm}^3 \text{ molecule}^{-1} \text{ s}^{-1}$	Reference
2-Propenal or Acrolein (CH ₂ =CH-CHO)	2.2 ± 0.3	Thévenet et al., 2000
	2.2 ± 0.3	Canosa-Mas et al., 2001
	1.8 ± 0.3	Ullerstam et al., 2001
	2.5 ± 0.7	Wang et al., 2002
	2.2 ± 0.4 ^a	Average
2-Methyl-2-Propenal or Methacrolein (CH ₂ =C(CH ₃)-CHO)	2.9 ± 0.8	Wang et al., 2002
Trans-2-Butenal or Crotonaldehyde (E-CH ₃ -CH=CH-CHO)	2.6 ± 0.3	Thévenet et al., 2000
	2.2 ± 0.4	Ullerstam et al., 2001
	3.2 ± 0.9	Wang et al., 2002
	2.7 ± 0.7 ^a	Average
Trans-2-Methyl-2-Butenal (E-CH ₃ -CH=C(CH ₃)-CHO)	2.45 ± 0.32	Antiñolo et al., 2020

3-Methyl-2-Butenal or β,β -dimethylacrolein $((\text{CH}_3)_2\text{-C=CH-CHO})$	2.48 ± 0.71	Blanco et al., 2010
Trans-2-Pentenal $(\text{E-CH}_3\text{-CH}_2\text{-CH=CH-CHO})$	1.31 ± 0.19 3.47 2.53 ± 0.83	Rodríguez et al., 2005 Teruel et al., 2009 This work
Trans-2-Hexenal $(\text{E-CH}_3\text{-CH}_2\text{-CH}_2\text{-CH=CH-CHO})$	1.92 ± 0.22 3.31 ± 0.96	Rodríguez et al., 2005 This work
Trans-2-Heptenal $(\text{E-CH}_3\text{-CH}_2\text{-CH}_2\text{-CH}_2\text{-CH=CH-CHO})$	2.4 ± 0.29 4.11 ± 0.32	Rodríguez et al., 2005 This work

^a uncertainties are 2σ .

b) Effect of chain length and the presence of methyl group

The rate constants of Cl reactions with C₃-C₅ unsaturated aldehydes seem to be fairly dependent on the chain length. This is consistent with Blanco et al., 2010, who mentions that C₃-C₄ unsaturated aldehydes' reactivity towards Cl is dependent on the substitution of the olefinic carbons. However, if we compare the rate constants of longer carbon such as C₅-C₇ unsaturated aldehydes, we found that the hydrocarbon chain length has a slight activating effect on chlorine reactions as noticed recently by Antiñolo et al., 2020 for C₅-C₇ unsaturated aldehydes.

Comparing the Cl reactivity of the linear unsaturated aldehyde 2-Propenal and Trans-2-Butenal with respect to their branched unsaturated aldehyde Trans-2-Methyl-2-Propenal and Trans-2-Methyl-2-Butenal, indicate that the presence of the methyl group has no clear effect on the reactivity. These two trends are not well understood because of the lack of data; therefore, more studies would be needed for similar carbonyls.

c) Effect of the carbonyl group

It is interesting to compare the reactivity on the studied unsaturated aldehydes towards Cl atoms with the corresponding alkenes since they postulated that they react via similar addition mechanisms (Mellouki et al., 2003). Unfortunately, no data is available in the literature for the reaction of Cl with Trans-2-Pentene, Trans-2-Hexene, and Trans-2-Heptene, which are the corresponding alkene of T2P, T2H, and T2Hep, respectively.

Therefore, we compared the rate constants of 2-Propenal and Trans-2-Butenal with their corresponding alkenes (propene and Trans-2-Butene). The rate constants for the reactions of listed alkenes with Cl atoms are summarized in Table V.9.

Table V.9: Summary of the rate constants for two C₃-C₄ alkenes' reactions with Cl atoms at room temperature and atmospheric pressure.

Compound Linear formula	$k \times 10^{-10} /$ $\text{cm}^3 \text{ molecule}^{-1} \text{ s}^{-1}$	Reference
Propene (CH ₂ =CH-CH ₃)	2.7 ± 0.4	Kaiser and Wallington, 1996
Trans-2-Butene (CH ₃ -CH=CH-CH ₃)	3.58 ± 0.23	Kaiser et al., 2007

The average of the rate constants of the reactions of Cl with 2-Propenal and Trans-2-Butenal were ($2.2 \times 10^{-10} \text{ cm}^3 \text{ molecule}^{-1} \text{ s}^{-1}$) and ($2.7 \times 10^{-10} \text{ cm}^3 \text{ molecule}^{-1} \text{ s}^{-1}$), respectively. Those data are 19% and 25% lower than Cl-rate constants of propene and Trans-2-Butene, respectively. The latter may be due to the carbonyl-containing group's negative inductive effect, which may deactivate the Cl atom addition's double bond. However, this decrease in reactivity due to the electron-withdrawing effect may be compensated by the CHO group's reactive nature. The latter was discussed in the study carried out by Thévenet et al., 2000. This shows that the -CHO group is a reactive site, although H abstraction from the -CHO group remains a minor channel compared to the Cl-addition to the double bond, which is likely to be the major one as stated by these authors. As will be discussed in the next section, we confirm that the reaction of C₅-C₇ unsaturated aldehydes with Cl proceeds via both abstraction and addition channels.

V.2.2 Determination of gas-phase products

This part aims to identify and quantify the gas-phase products of the reaction between the C₅-C₇ unsaturated aldehydes and chlorine at $296 \pm 2 \text{ K}$ and $740 \pm 20 \text{ Torr}$. To our knowledge, no information has been found in the literature on the mechanisms of Cl atoms' reactions with the studied aldehydes.

V.2.2.1 Experimental conditions and protocols

The gaseous products for the three studied reactions were determined in two reactors were used 16L-ASC and CR-ASC depending on the detection techniques: FTIR spectroscopy, SPME/GC-MS, and PTR-ToF-MS. The products formed during the gas-phase reactions of T2P and T2H with Cl were identified and quantified using FTIR spectroscopy and SPME/GC-MS coupled to the 16L-ASC and the CR-ASC, respectively. On the other hand, the investigation of the products formed through T2Hep reaction towards Cl was achieved using the SPME/GC-MS technique and PTR-ToF-MS instrument both coupled to the CR-ASC (FTIR spectroscopy was used only to measure the initial concentration of T2Hep). All technique details were explained in chapter II. The experimental procedure started with the injection of the studied aldehyde in the reactor. After stabilization for 30 min, its initial concentration was checked using the FTIR spectrometer based on reagents' calibration spectra (see section III.2.2.2). A sample was done on SMPE fiber (for T2P + Cl, T2H + Cl, and T2Hep + Cl experiments) and on PTR-ToF-MS device (for T2Hep + Cl experiments). Molecular chlorine was added to the reactor and the reaction mixture (synthetic air+aldehyde+Cl₂) left to stabilize for 30 min in the dark. Then, samples of the used analysis techniques were taken to check the reaction mixture's stability in the dark. The gaseous products were monitored for 60 min of UV light exposure, and samples were taken continuously. The experimental conditions of each aldehyde used for the mechanistic studies are summarized in Table V.10.

Table V.10: Experimental conditions and techniques used during the product study.

Reaction	Reactor (Number of experiments)	Analysis technique for products	Lamps	Compound	Initial concentration range $\times 10^{14}$ / molecule cm ⁻³
T2P + Cl	16L-ASC (4 runs)	FTIR spectrometer	3	T2P	2.78 – 5.91
				Cl ₂	8.34 – 9.97
	CR-ASC (2 runs)	SPME/GC-MS	8	T2P	9.05 – 9.64
				Cl ₂	8.34 – 8.76

T2H + Cl	16L-ASC (7 runs)	FTIR spectrometer	3	T2H	4.67 – 21.89
				Cl ₂	3.83 – 12.62
	CR-ASC (2 runs)	SPME/GC- MS	8	T2H	6.20 – 6.32
				Cl ₂	4.08 – 4.10
T2Hep + Cl	CR-ASC (3 runs)	PTR-ToF-MS SPME/GC- MS	8	T2Hep	1.10 – 3.10
				Cl ₂	1.00 – 1.40

The overall errors on the formation yields are due to systematic errors (σ_{syst}) mentioned above (section V.2.2.1) and to statistical errors that result from a least-squares analysis of the $[\text{Product}]_t$ vs. $\Delta[\text{Aldehyde}]$ plots.

V.2.2.2 Results and discussion

V.2.2.2.1 Products of T2P + Cl

a) Temporal evolution of T2P and product concentrations

▪ Detection by FTIR spectroscopy

The FTIR spectra recorded during the T2P + Cl reaction showed features of four abundant products, which were HCl, CO, HC(O)OH (formic acid), and propanal by comparison with the reference spectra (Figure V.4). The used IR features were: 1180 – 1120 cm⁻¹ for T2P, 2600 – 3100 cm⁻¹ for HCl, 2060 – 2230 cm⁻¹ for CO, 1780 – 1840 cm⁻¹ for HC(O)OH, and 817 – 875 cm⁻¹ for propanal (Figure V.4). The residual IR spectrum, presented in Figure V.4, shows that additional products were formed that could not be identified and quantified. This is mainly due to overlap and the lack of standards of the products expected to be formed.

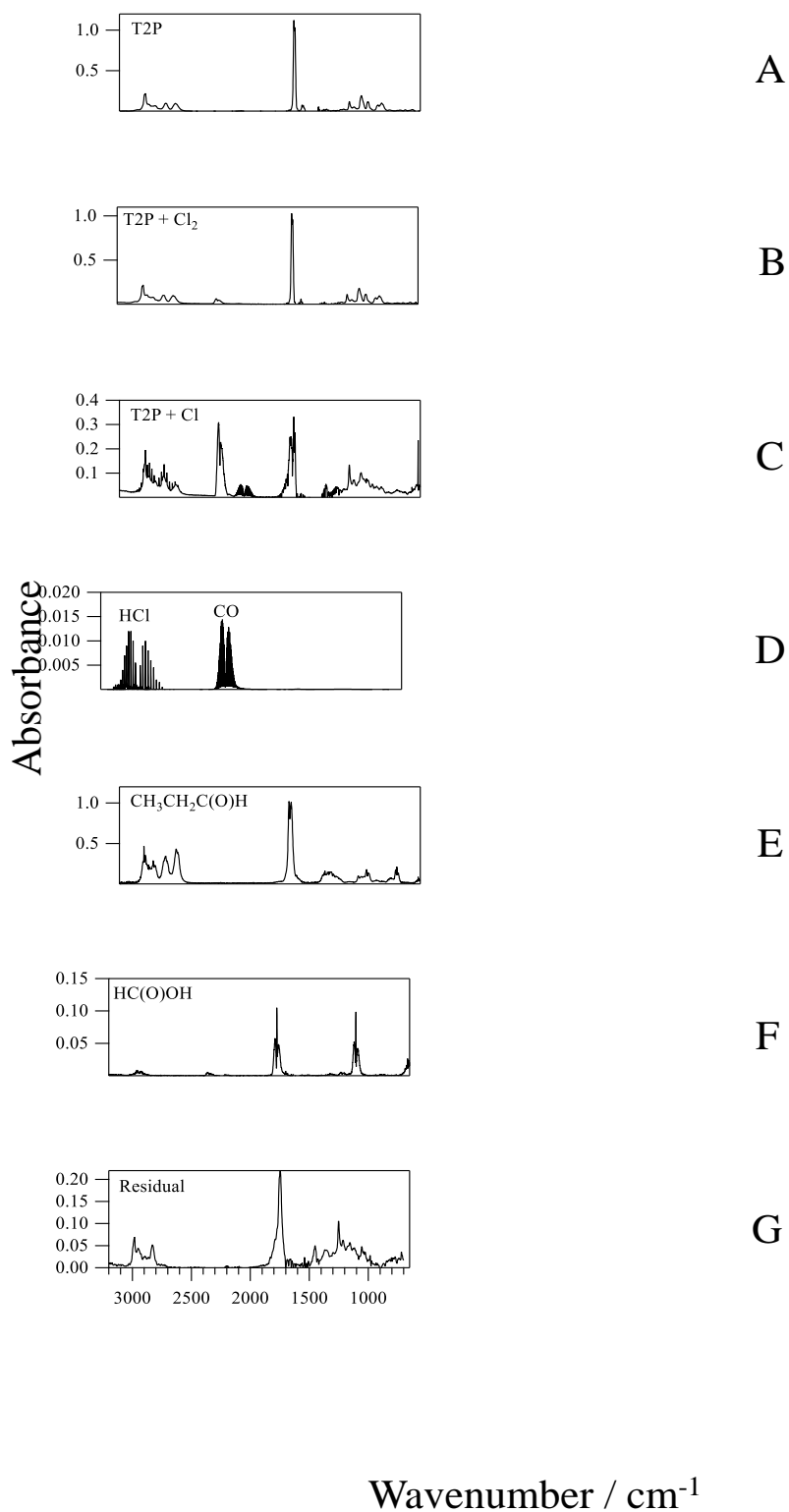


Figure V.4: IR spectra: Panel A: T2P in the dark. Panel B: after adding Cl_2 to T2P in the dark. Panel C: under irradiation after 12 min. Panels D, E, and F: spectra of HCl and CO,

propanal, and HC(O)OH. Panel G: residual IR spectrum after removing T2P, HCl, CO, HC(O)OH, and propanal.

The identification and the quantification of the products were done using standard reference libraries of IR spectra. Figure V.5 shows typical concentration vs. time profiles for the consumption of T2P and the formation of products.

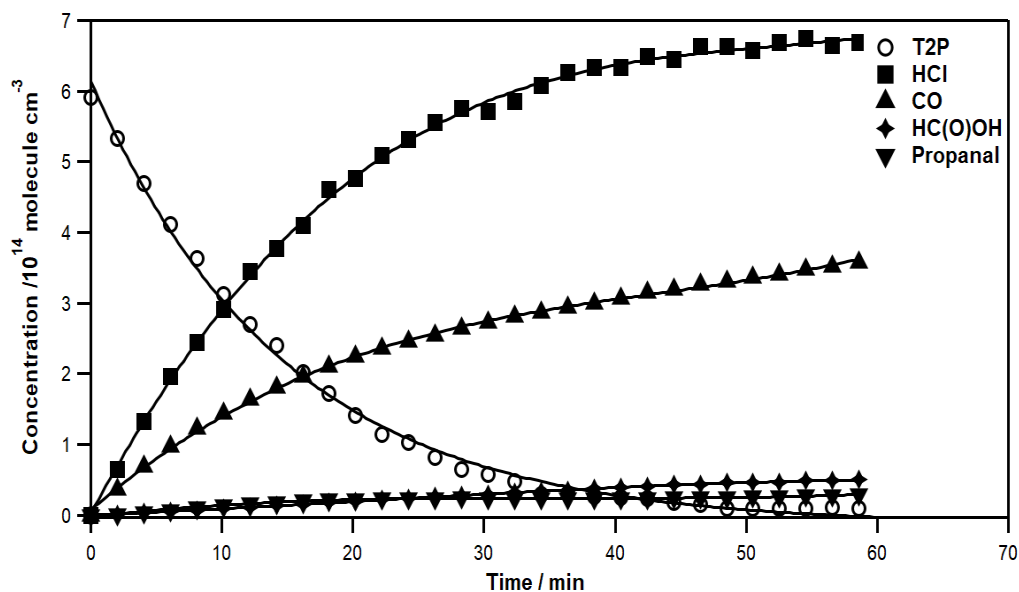


Figure V.5: Concentration-time profile for T2P and the major products using $[T2P]_0 = 5.9 \times 10^{14} \text{ molecule cm}^{-3}$ and $[Cl_2]_0 = 9.1 \times 10^{14} \text{ molecule cm}^{-3}$.

▪ Detection by SPME/GC-MS

Figure V.6 shows an example of the chromatogram obtained after 60 min of irradiation. The peak corresponding to T2P was observed at a retention time (RT) of 4.5 min. The detected products were 2-chlorobutanal (RT = 4.03 min), chlorinated compound (RT = 5.09 min) and 2-pentenoic acid (RT = 6.18 min). The identified peaks were not quantified due to the lack of their standards. Other small peaks in the chromatogram were due to the SPME fiber's degradation and the GC column.

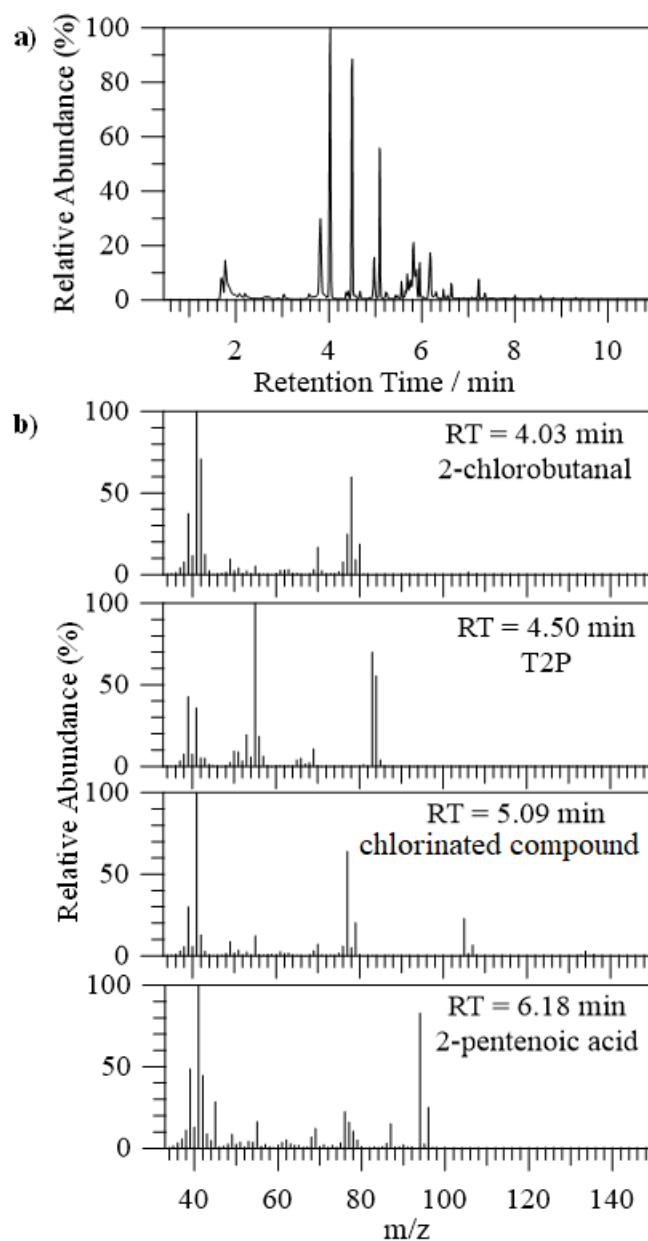


Figure V.6: Examples of (a) chromatogram for the gas mixture after 60 min of the reaction of T2P + Cl, (b) determining mass spectra of T2P and the identified products.

b) Molar yields of reaction products

The product yields were calculated based on the quantified concentrations of T2P and products in the FTIR spectroscopy analyses. The plots of the product concentration at a time t ($[Product]_t$) vs. the consumed concentration of T2P at a time t ($\Delta[T2P]$) for the identified products are shown in Figure V.7.

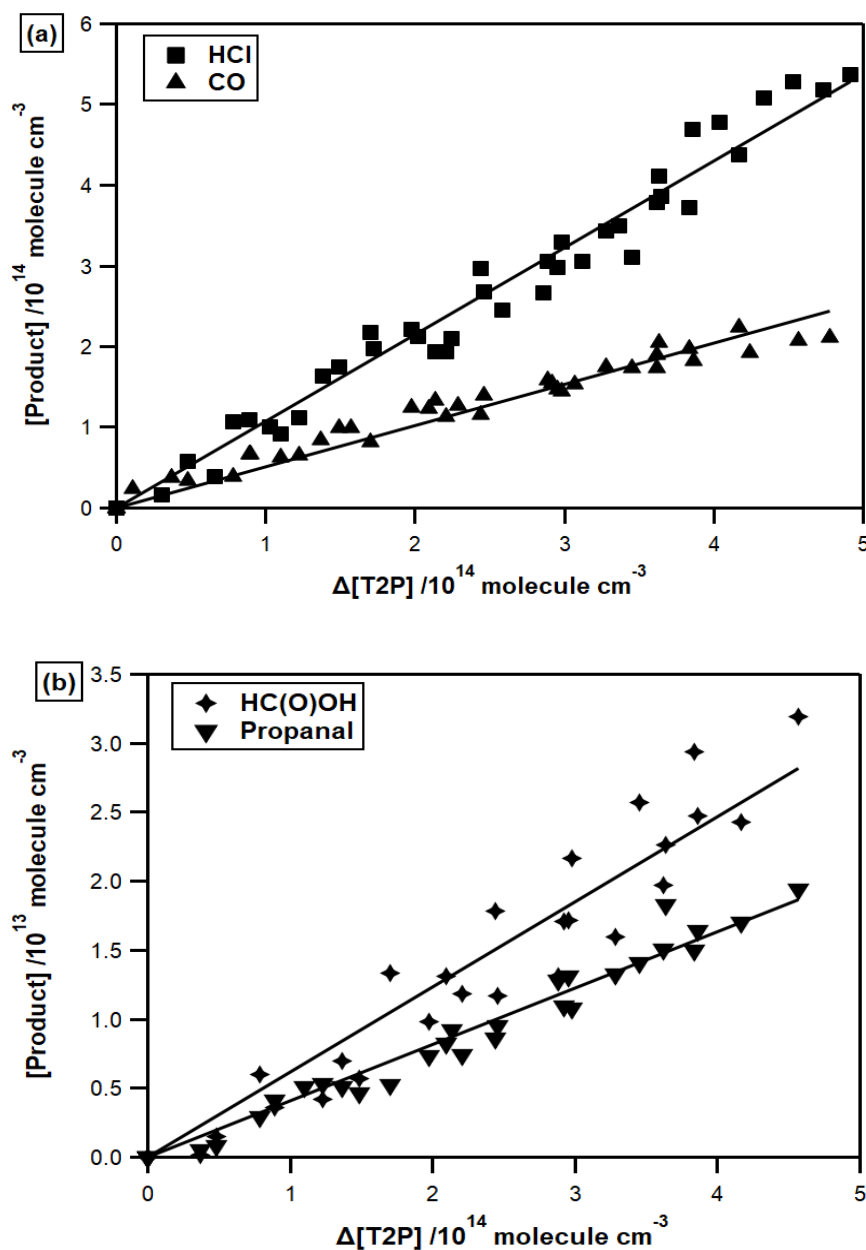


Figure V.7: Product yields for (a) HCl and CO and (b) HC(O)OH and propanal.

The molar yields obtained from the slopes of the plot depicted in Figure V.7 are $(107 \pm 11)\%$, $(51 \pm 2)\%$, $(6.2 \pm 0.4)\%$ and $(4.1 \pm 0.2)\%$, for HCl, CO, HC(O)OH and propanal, respectively. CO is expected to be formed as a primary product and a final product from the studied reaction and may be generated in the mechanism's oxidation of other species. Propanal is expected to be formed as a primary product from the reaction of T2P with Cl.

Its fast consumption by reaction with Cl constitutes an additional source of HCl. HC(O)OH may be produced as a consequence of heterogeneous reactions on the chamber walls. The reaction products detected by GC-MS were 2-chlorobutanal and 2-pentenoic acid and a chlorinated product that could not be identified at 5.09 min retention time (Figure V.7). The quantification of these products was not possible due to the lack of standards. The carbon balance was calculated considering only the quantified products. The obtained value was shown to not exceed 33% at the end of the reaction showing that additional oxidation products could not be detected or quantified.

c) Proposed reaction mechanism

As other unsaturated aldehydes (Canosa-Mas et al., 2001, Orlando and Tyndall, 2002, Magneron et al., 2002), the degradation of T2P initiated by Cl atoms are expected to proceed via two basic mechanisms: abstraction of the hydrogen atom from the -CHO group (Figure V.8.c) and/or addition to the C=C double bond. In Figure V.8, the reaction pathways that may justify the observed products are shown. The addition of a Cl atom may occur on two sites of the C=C double bond: adjacent to the -C(O)H group (α) (Figure V.8.a) or on the double-bonded carbon furthest from the aldehydic group (β) (Figure V.8.b).

As seen in Figure V.8.a, the α -addition forms the $\text{CH}_3\text{CH}_2\text{CHCHClC(O)H}$ radical, which will react with O_2 followed by reaction with RO_2 to lead to the corresponding chloroalkoxy radical $\text{CH}_3\text{CH}_2\text{C(O)HCHClC(O)H}$. The decomposition of this chloroalkoxy radical may proceed via two channels. The first one leads to the formation of propanal ($\text{CH}_3\text{CH}_2\text{C(O)H}$), 2-oxoacetylchloride (ClC(O)C(O)H), formyl chloride HC(O)Cl and CO. Propanal may further react with Cl atoms to form HCl and $\text{CH}_3\text{CH}_2\text{C(O)}$ radicals (Le Crâne et al., 2004). The second channel leads to the formation of chloromalonaldehyde (C(O)HCHClC(O)H) and acetaldehyde $\text{CH}_3\text{C(O)H}$. Among these products, only propanal and CO were observed and quantified in this work.

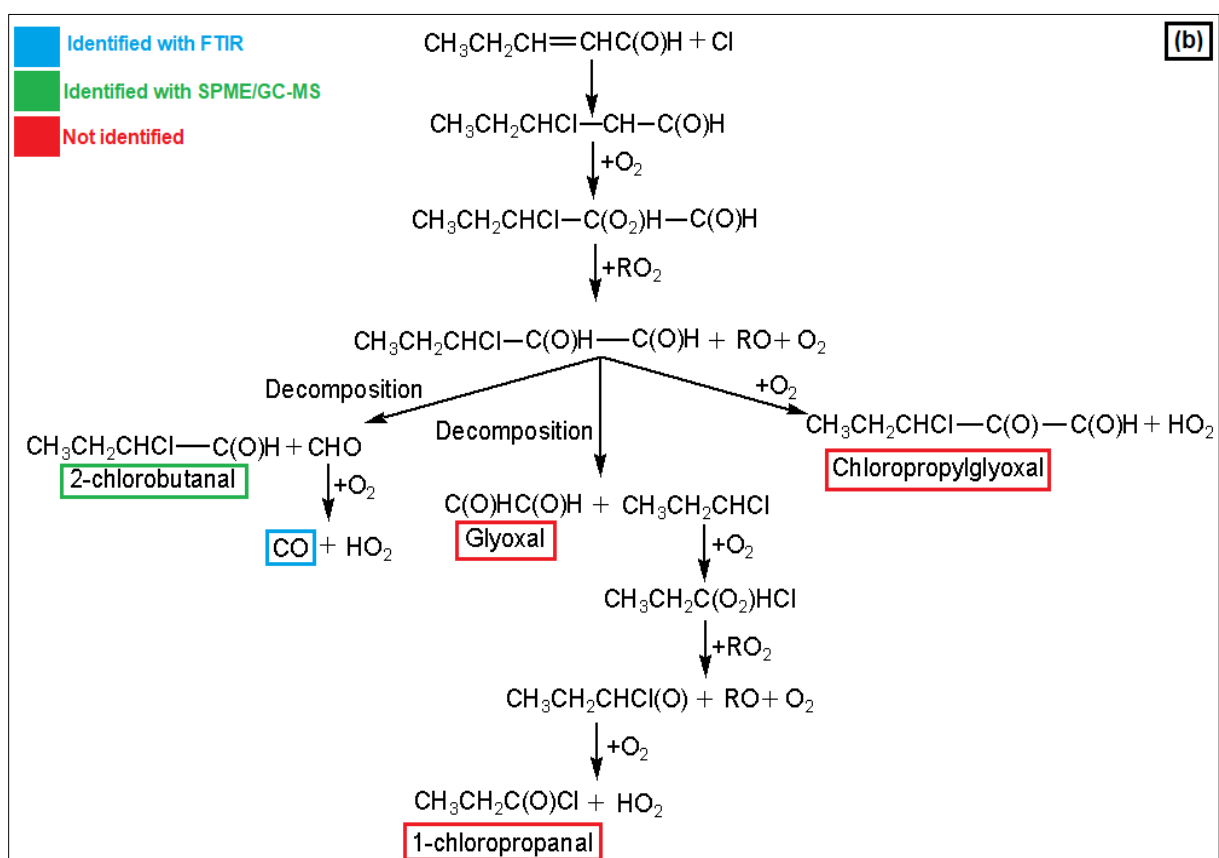
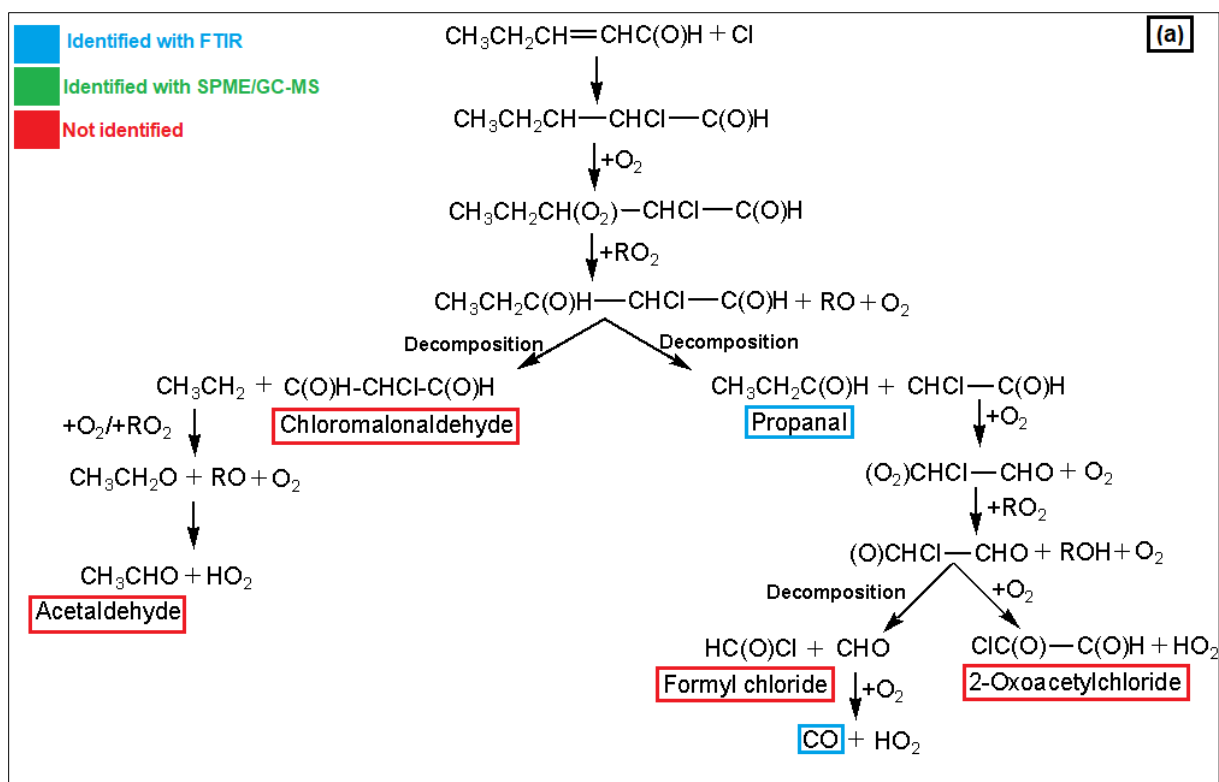
In Figure V.8.b, the β -addition mechanism proceeds through the $\text{CH}_3\text{CH}_2\text{CHClCHC(O)H}$ radical, which will react with O_2 followed by the reaction with RO_2 to lead to the $\text{CH}_3\text{CH}_2\text{CHClC(O)HC(O)H}$ radical.

This radical may decompose to lead to the formation of 2-chlorobutanal ($\text{CH}_3\text{CH}_2\text{CHClC}(\text{O})\text{H}$) identified by GC-MS, but not quantified and further to the formation of CO identified and quantified by FTIR.

The decomposition of the $\text{CH}_3\text{CH}_2\text{CHClCOHC}(\text{O})\text{H}$ radical may also lead to the formation of glyoxal ($\text{C}(\text{O})\text{HC}(\text{O})\text{H}$) and 1-chloropropanal ($\text{CH}_3\text{CH}_2\text{C}(\text{O})\text{Cl}$) after the conversion of the reaction of the chloroperoxy radical $\text{CH}_3\text{CH}_2\text{C}(\text{O}_2)\text{HCl}$ with RO_2 . Glyoxal ($\text{C}(\text{O})\text{HC}(\text{O})\text{H}$) and 1-chloropropanal were not observed in this work, suggesting that this channel either does not occur in the timescale of the experiments or is a minor route in the mechanism. Note also that glyoxal may be readily photolyzed under UV irradiation. The $\text{CH}_3\text{CH}_2\text{CHClC}(\text{O})\text{HC}(\text{O})\text{H}$ radical may react with O_2 to form chloropropyl glyoxal ($\text{CH}_3\text{CH}_2\text{CHClC}(\text{O})\text{C}(\text{O})\text{H}$). This product may be the unidentified one observed by GC-MS but could not be confirmed.

In Figure V.8.c, the H-abstraction from the $-\text{C}(\text{O})\text{H}$ group may proceed to form the $\text{CH}_3\text{CH}_2\text{CHCHC}(\text{O})$ radical and HCl. HCl was quantified as a major product by FTIR with a molar yield of $(107 \pm 11)\%$. In the presence of O_2 , the $\text{CH}_3\text{CH}_2\text{CHCHC}(\text{O})$ radical may be converted to the peroxy radical $\text{CH}_3\text{CH}_2\text{CHCHC}(\text{O})\text{O}_2$, which generates 2-pentenoic acid ($\text{CH}_3\text{CH}_2\text{CHCHC}(\text{O})\text{OH}$) and ozone in the presence of HO_2 . 2-pentenoic acid was detected in SPMS/GC-MS analysis. On the other hand, the $\text{CH}_3\text{CH}_2\text{CHCHC}(\text{O})\text{O}_2$ radicals may also react with RO_2 and generates the $\text{CH}_3\text{CH}_2\text{CHCHC}(\text{O})\text{O}$ radical. This radical can decompose to carbon dioxide (CO_2) and ethyl vinyl radical ($\text{CH}_3\text{CH}_2\text{CHCH}$), which is converted to the $\text{CH}_3\text{CH}_2\text{CHCH}(\text{O}_2)$ radical in the presence of O_2 . This later reaction with RO_2 may lead to the formation of butanal ($\text{CH}_3\text{CH}_2\text{CH}_2\text{C}(\text{O})\text{H}$) not observed in this work. The reaction of $\text{CH}_3\text{CH}_2\text{CHCH}(\text{O}_2)$ with RO_2 may also lead to propanal and CO formation, both quantified by FTIR in this work.

CO was formed from the three channels, and propanal was observed in the α -addition and the H-abstraction channels. Indeed, those compounds were not considered as a key compound in this mechanism. However, 2-chlorobutanal were observed only in β -addition, and HCl and 2-pentenoic acid were observed only in H-abstraction. Those compounds could better explain the relative contribution of addition and abstraction channels in the suggested mechanism, provided that they will be all quantified.



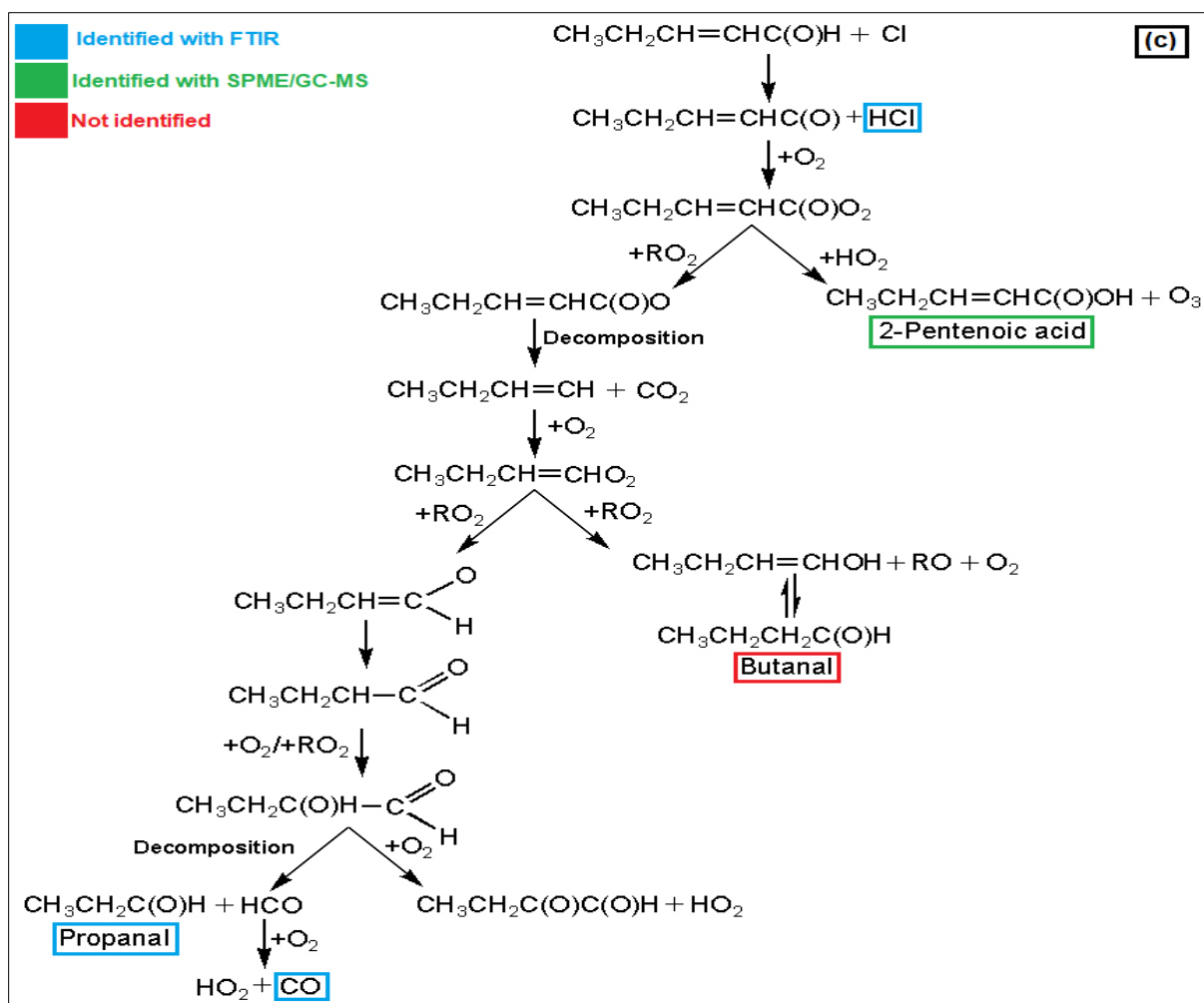


Figure V.8: Proposed mechanism for the reaction of T2P with Cl atom: α -addition (a), β -addition (b), and H-abstraction (c).

V.2.2.2.2 Products of T2H + Cl

a) Temporal evolution of T2H and product concentrations

▪ Detection by FTIR spectroscopy

The FTIR spectra of the T2H+Cl reaction displayed features of four abundant products: HCl, CO, HC(O)OH, and propanal by comparison with the reference spectra (Figure V.9). The IR spectral features used for this analysis were as follows: 1610 – 1750 cm^{-1} for T2H, 2600 – 3100 cm^{-1} for HCl, 2039 – 2239 cm^{-1} for CO, 2870 – 2950 cm^{-1} for HC(O)OH, and 817 – 875 cm^{-1} for propanal.

The identification and the quantification of the products were done using standard reference libraries of IR spectra. Figure V.9 shows typical concentration vs. time profiles for the consumption of T2H and the formation of products.

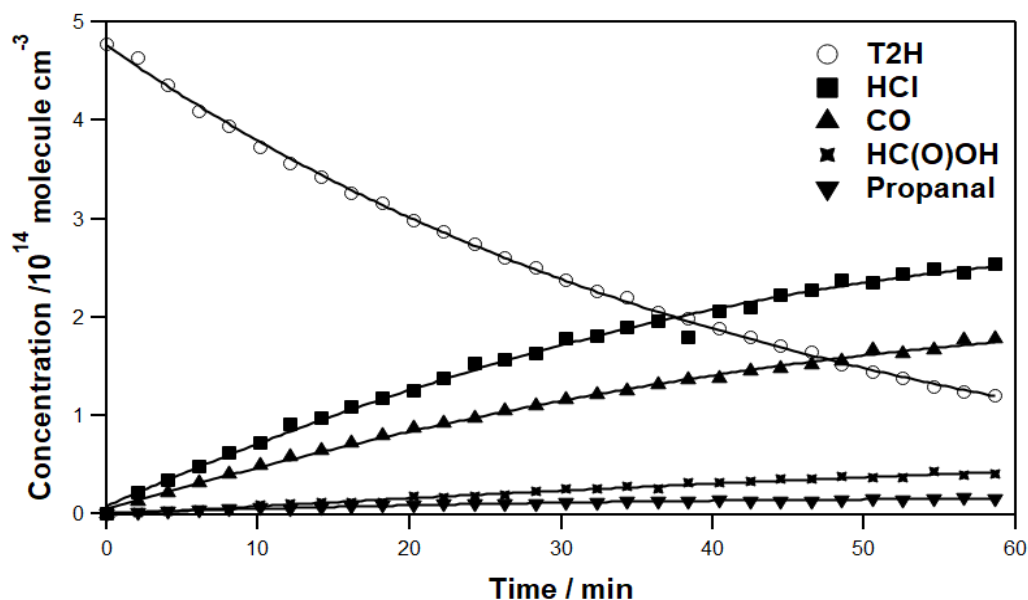


Figure V.9: Concentration-time profile for T2H and the major products using $[T2H]_0 = 4.7 \times 10^{14} \text{ molecule cm}^{-3}$ and $[Cl_2]_0 = 3.9 \times 10^{14} \text{ molecule cm}^{-3}$.

▪ Detection by SPME/GC-MS

The peak corresponding to T2H was observed at a retention time (RT) of 5.31 min. The reaction products detected by GC-MS were butanal (RT = 2.88 min), 2-chloropentanal (RT = 4.84 min) and 2-hexenoic acid (RT = 6.36 min). The identified peaks were not quantified due to the lack of their standards.

b) Molar yields of reaction products

The product yields were calculated based on the quantified concentrations of T2H and products in the FTIR spectroscopy. The plots of the product concentration at a time t ($[Product]_t$) vs. the consumed concentration of T2H at a time t ($\Delta[T2H]$) for the identified products are shown in Figure V.10.

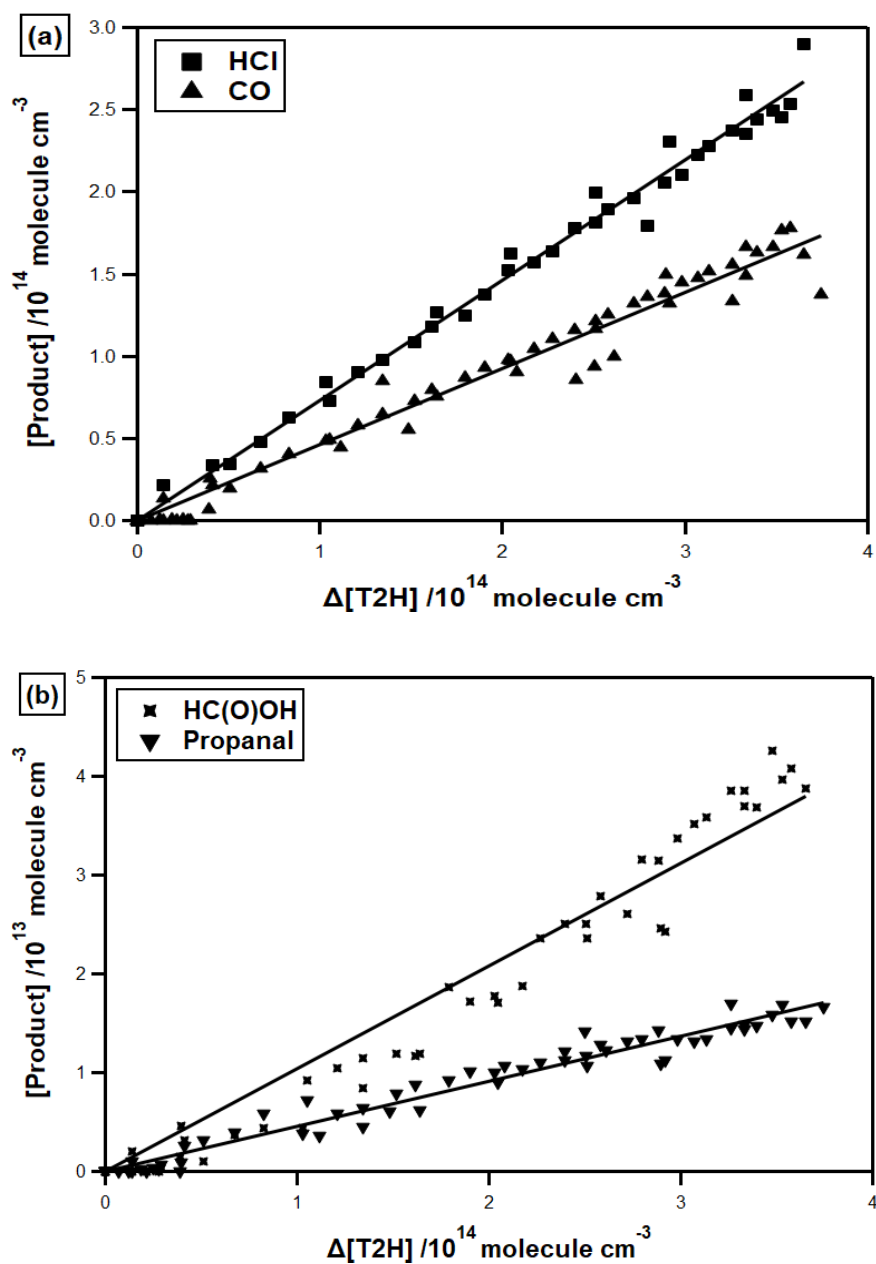


Figure V.10: Product yields for (A) HCl and CO and (B) HC(O)OH and propanal.

The molar yields obtained from the slope of the plot depicted in Figure V.10 were: $(73 \pm 1.2)\%$, $(46 \pm 1.2)\%$, $(10 \pm 0.4)\%$ and $(4.6 \pm 0.1)\%$, for HCl, CO, HC(O)OH and propanal, respectively. The formation of HCl, CO, HC(O)OH, and propanal is expected to derive from the same pathways discussed in section V.2.2.2.1. for the T2P + Cl reaction. The reaction products detected by SPME/GC-MS were butanal, 2-chloropentanal, and 2-hexenoic acid. The quantification of these products was not possible due to a lack of standards.

The carbon balance was calculated to not exceed 24% taking into account only the quantified products at the end of the reaction.

c) Proposed reaction mechanism

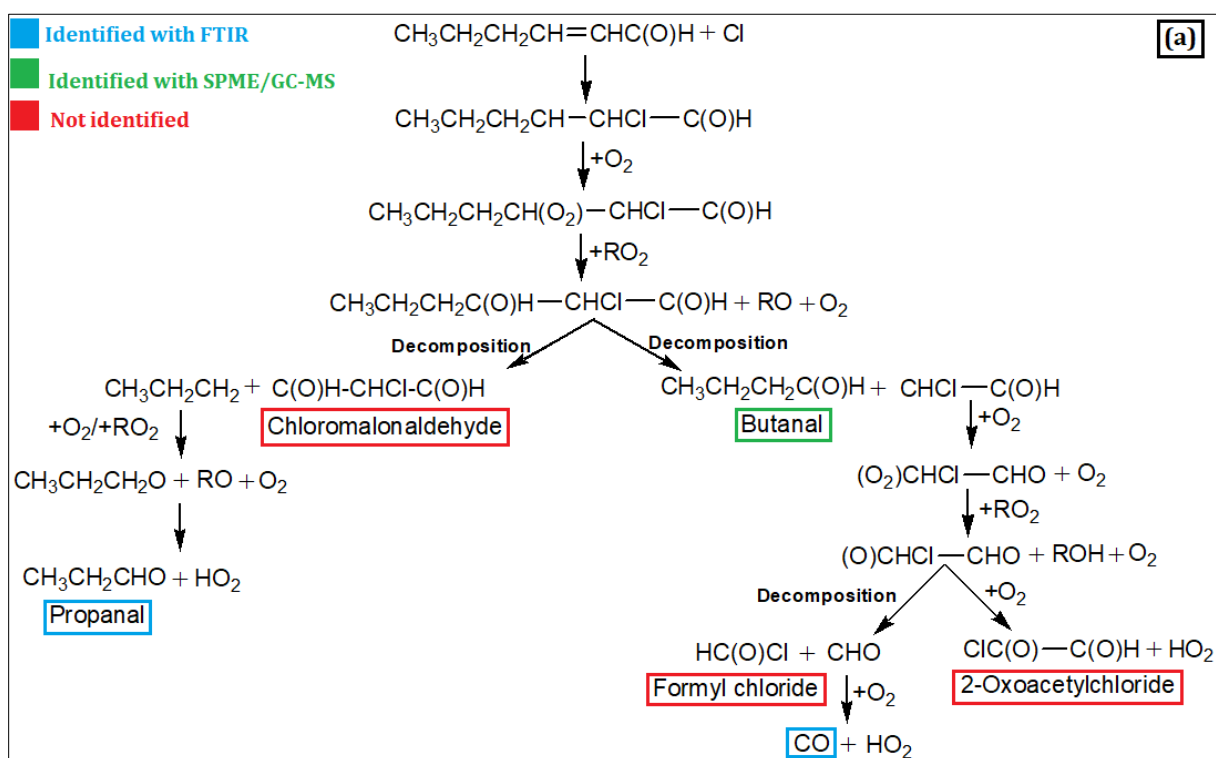
I mention that the T2H compound has the same structure as T2P except for an additional (CH_2 -) group. Therefore, this molecule reacts similarly to T2P and products common compounds as T2P+Cl mechanism. In this section, I displayed only the way of differences between both mechanisms. In Figure V.11, the reaction pathways that may justify the observed products are shown.

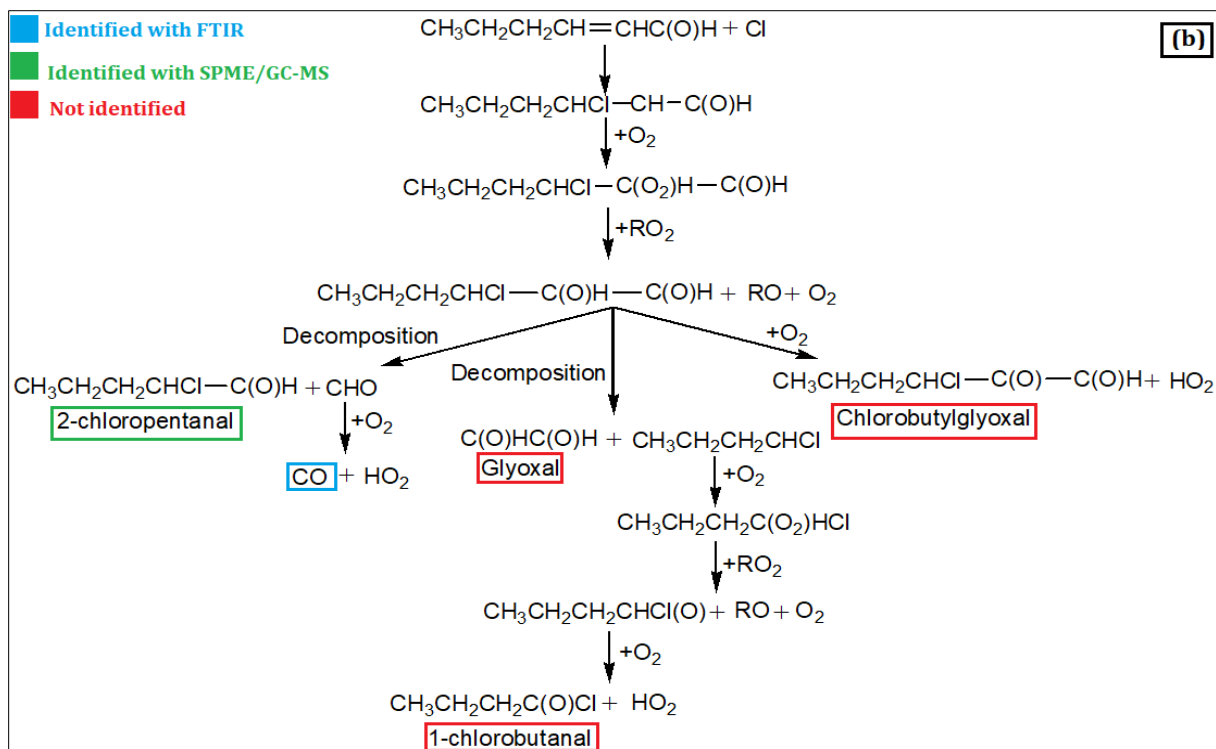
As seen in Figure V.11.a, the α -addition forms the $\text{CH}_3\text{CH}_2\text{CH}_2\text{CHCHClC(O)H}$ radical, which will react with O_2/RO_2 to lead to the corresponding chloroalkoxy radical $\text{CH}_3\text{CH}_2\text{CH}_2\text{C(O)HCHClC(O)H}$. The decomposition of this radical leads to the formation of butanal ($\text{CH}_3\text{CH}_2\text{CH}_2\text{C(O)H}$) and the same group of products as for the T2P + Cl mechanism (2-oxoacetylchloride (ClC(O)C(O)H), formyl chloride HC(O)Cl and CO) as the first channel of decomposition. The second channel leads to the formation of propanal $\text{CH}_3\text{CH}_2\text{C(O)H}$ and chloromalonaldehyde (C(O)HCHClC(O)H) (the same product as for T2P+Cl). Among these products, only propanal, butanal, and CO were detected in this work.

In Figure V.11.b, the β -addition mechanism proceeds through the $\text{CH}_3\text{CH}_2\text{CH}_2\text{CHClCHC(O)H}$ radical, which will react with O_2/RO_2 to lead to the $\text{CH}_3\text{CH}_2\text{CH}_2\text{CHClC(O)HC(O)H}$ radical. This radical may decompose to lead to the formation of 2-chloropentanal ($\text{CH}_3\text{CH}_2\text{CH}_2\text{CHClC(O)H}$) identified by GC-MS, but not quantified and further to the formation of CO identified and quantified by FTIR. The $\text{CH}_3\text{CH}_2\text{CH}_2\text{CHClC(O)HC(O)H}$ radical may also lead to the formation of glyoxal (C(O)HC(O)H) (not identified) and 1-chlorobutanal ($\text{CH}_3\text{CH}_2\text{CH}_2\text{C(O)Cl}$) (not identified). The $\text{CH}_3\text{CH}_2\text{CH}_2\text{CHClC(O)HC(O)H}$ radical may react with O_2 to form chlorobutyl glyoxal ($\text{CH}_3\text{CH}_2\text{CH}_2\text{CHClC(O)C(O)H}$), which was not identified.

In Figure V.11.c, the H-abstraction leads to the formation of $\text{CH}_3\text{CH}_2\text{CH}_2\text{CHCHC(O)}$ radical and HCl, quantified by FTIR as a major compound ($73 \pm 1.2\%$). In the presence of O_2/HO_2 , the $\text{CH}_3\text{CH}_2\text{CH}_2\text{CHCHC(O)}$ radical produces 2-hexenoic acid ($\text{CH}_3\text{CH}_2\text{CHCHC(O)OH}$) (identified in GC-MS) and ozone.

In the presence of O_2/RO_2 , the $CH_3CH_2CH_2CHCHC(O)H$ radical generates pentanal (not identified), butanal (identified with GC-MS), and CO (identified and quantified with FTIR). CO was formed from the three channels, and butanal was observed in the α -addition and the H-abstraction channels. Those compounds were not considered as key compounds in this mechanism. However, propanal was observed only in α -addition, 2-chloropentanal was observed only in β -addition, and HCl and 2-hexenoic acid were observed only in H-abstraction. Those compounds could better explain the relative contribution of addition and abstraction channels in the suggested mechanism, provided that they will be all quantified.





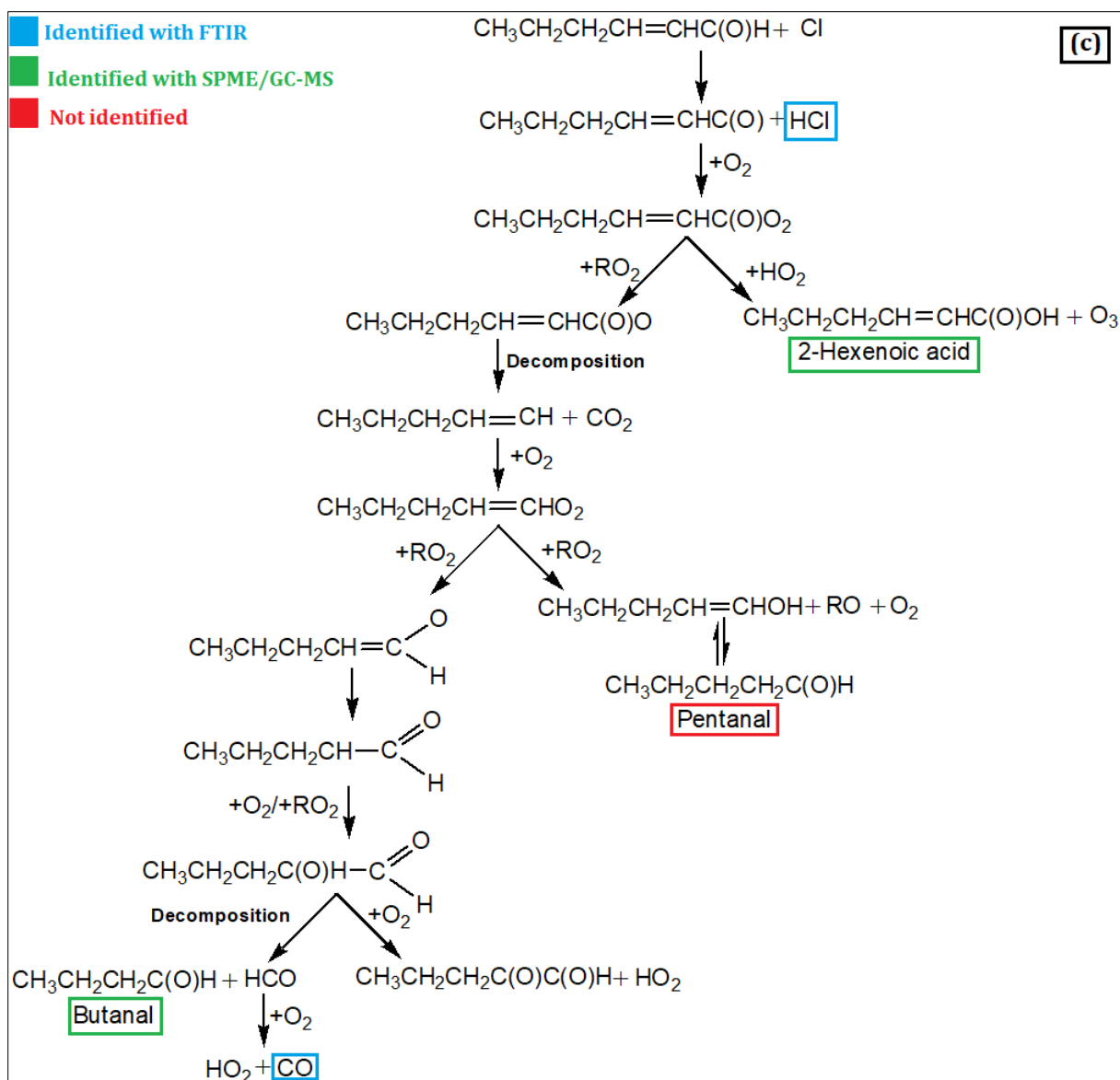


Figure V.11: Proposed mechanism for the reaction of T2H with Cl atom: α -addition (a), β -addition (b), and H-abstraction (c).

V.2.2.2.3 Products of T2Hep + Cl

a) Identification of products

In this part, I displayed preliminary results on the study of the T2Hep + Cl reaction products. Only the identification of gaseous products using SPME/GC-MS and PTR-ToF-MS techniques are presented. FTIR will be carried out in future experiments.

▪ Detection by SPME/GC-MS

The peak corresponding to T2Hep was observed at a retention time (RT) of 6.1 min. The reaction products detected by SPME/GC-MS were butanal (RT = 2.88 min), 2-chlorohexanal (RT = 5.8 min) and 2-heptenoic acid (RT = 7.11 min). The identified peaks were not quantified due to the lack of their standards.

▪ Detection by PTR-ToF-MS

The PTR-ToF-MS detects protonated molecular ions for non-chlorinated organic compounds. T2Hep was monitored via its protonated ion $C_7H_{12}OH^+$ ($m/z = 113$). Product identifications using PTR-ToF-MS were butanal ($C_4H_8OH^+$, $m/z = 73.06$) and pentanal ($C_5H_{10}OH^+$, $m/z = 87.08$). I mention that SPME/GC-MS also detected butanal.

b) Proposed reaction mechanism

I mention that the T2Hep compound has the same structure as T2P except for an additional (CH_2-CH_2-) group. Therefore, this molecule reacts similarly to T2P and products common compounds as T2P+Cl mechanism. In this section, I displayed only the way of differences between both mechanisms. In Figure V.12, the reaction pathways that may justify the observed products are shown.

As seen in Figure V.12.a, the α -addition forms the $CH_3CH_2CH_2CH_2CHCHClC(O)H$ radical, which will react with O_2/RO_2 to lead to the corresponding chloroalkoxy radical $CH_3CH_2CH_2CH_2C(O)HCHClC(O)H$. The decomposition of this radical leads to the formation of pentanal ($CH_3CH_2CH_2CH_2C(O)H$) and the same group of products as for the T2P + Cl mechanism (2-oxoacetylchloride ($ClC(O)C(O)H$), formyl chloride $HC(O)Cl$ and CO) as the first channel of decomposition. The second channel leads to the formation of butanal $CH_3CH_2CH_2C(O)H$ and chloromalonaldehyde ($C(O)HCHClC(O)H$) (the same product as for T2P+Cl). Among these products, only butanal and pentanal were detected in this work.

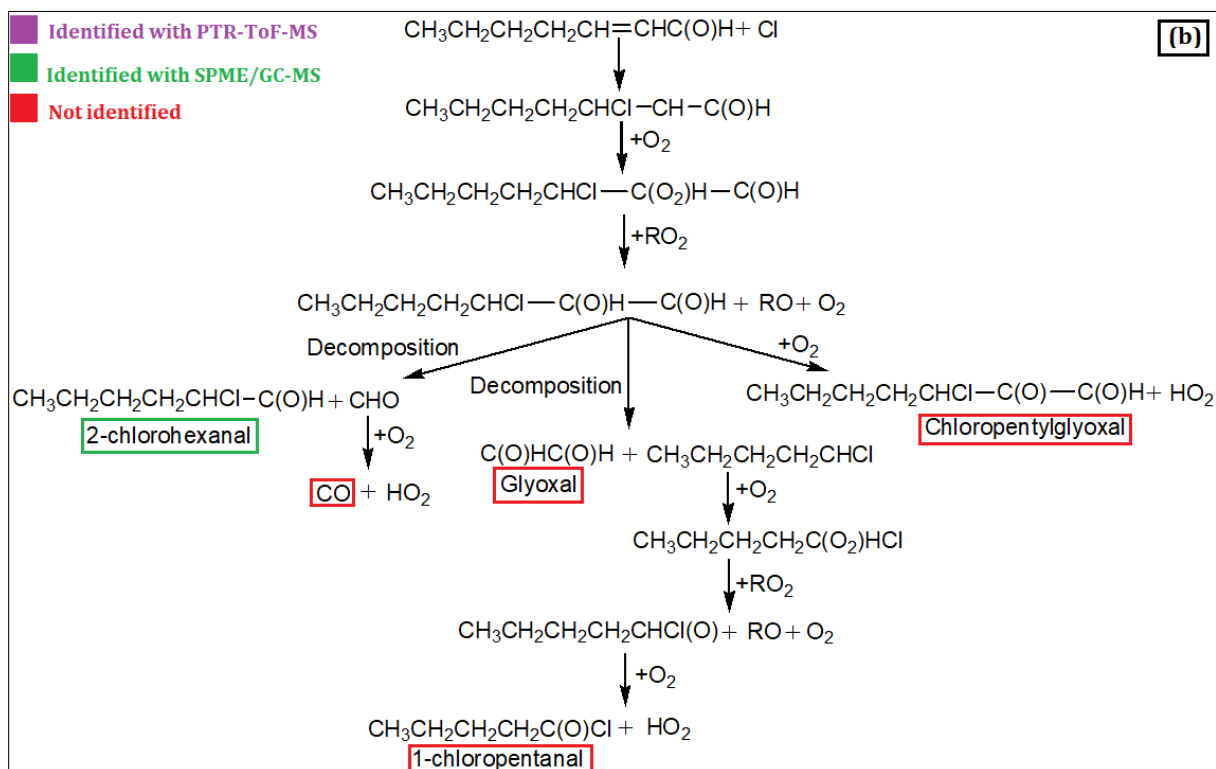
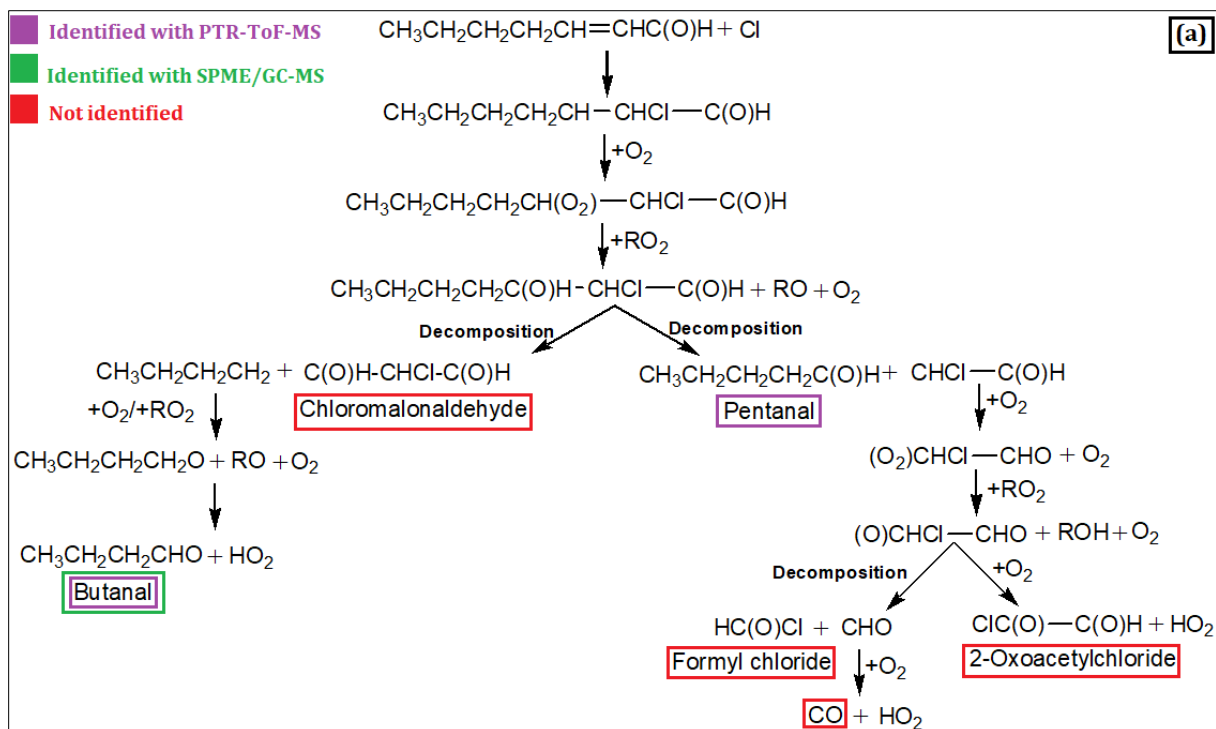
In Figure V.12.b, the β -addition mechanism proceeds through the $CH_3CH_2CH_2CH_2CHClCHC(O)H$ radical, which will react with O_2/RO_2 to lead to the $CH_3CH_2CH_2CH_2CHClC(O)HC(O)H$ radical.

This radical may decompose to lead to the formation of 2-chlorohexanal ($\text{CH}_3\text{CH}_2\text{CH}_2\text{CH}_2\text{CHClC}(\text{O})\text{H}$) identified by GC-MS, but not quantified, and further to the formation of CO (not identified).

The $\text{CH}_3\text{CH}_2\text{CH}_2\text{CH}_2\text{CHClC}(\text{O})\text{HC}(\text{O})\text{H}$ radical may also lead to the formation of glyoxal ($\text{C}(\text{O})\text{HC}(\text{O})\text{H}$) (not identified) and 1-chlorobutanal ($\text{CH}_3\text{CH}_2\text{CH}_2\text{C}(\text{O})\text{Cl}$) (not identified). The $\text{CH}_3\text{CH}_2\text{CH}_2\text{CH}_2\text{CHClC}(\text{O})\text{HC}(\text{O})\text{H}$ radical may react with O_2 to form chloropentylglyoxal ($\text{CH}_3\text{CH}_2\text{CH}_2\text{CH}_2\text{CHClC}(\text{O})\text{C}(\text{O})\text{H}$), which was not identified.

In Figure V.12.c, the H-abstraction leads to the formation of $\text{CH}_3\text{CH}_2\text{CH}_2\text{CH}_2\text{CHCHC}(\text{O})$ radical and HCl (not identified). In the presence of O_2/HO_2 , the $\text{CH}_3\text{CH}_2\text{CH}_2\text{CH}_2\text{CHCHC}(\text{O})$ radical produces 2-heptenoic acid ($\text{CH}_3\text{CH}_2\text{CH}_2\text{CHCHC}(\text{O})\text{OH}$) (identified by GC-MS) and ozone. In the presence of O_2/RO_2 , the $\text{CH}_3\text{CH}_2\text{CH}_2\text{CH}_2\text{CHCHC}(\text{O})$ radical generates pentanal (identified by PTR-ToF-MS), CO, and hexanal (not identified).

Pentanal was observed in the α -addition and the H-abstraction channels. The latter was not considered as a key compound in this mechanism. However, butanal was observed only in α -addition, 2-chlorohexanal was observed only in β -addition, and 2-heptenoic acid was observed only in H-abstraction. Those compounds could better explain the relative contribution of addition and abstraction channels in the suggested mechanism, provided that they will be all quantified.



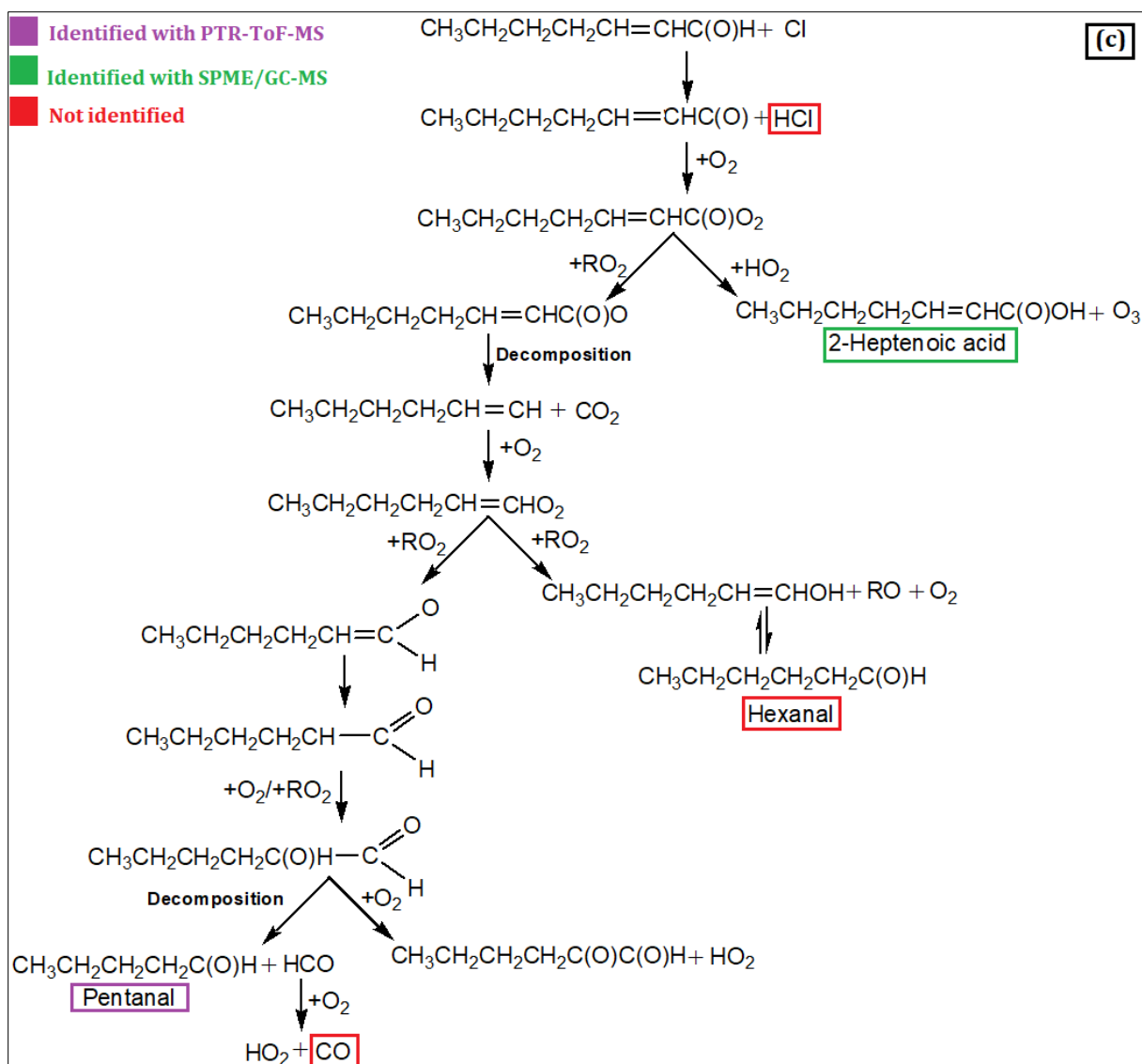


Figure V.12: Proposed mechanism for the reaction of T2Hep with Cl atom: α -addition (a), β -addition (b), and H-abstraction (c).

V.2.3 Particle-phase study

The important role of aldehyde chemistry in SOA formation has been highlighted in several previous works (Jang et al., 2002, Kroll and Seinfeld, 2008, Chan et al., 2010). The molecular structure of the aldehyde determines the amount of SOA formation, as the SOA mass yields are the highest for aldehydes that are α , β -unsaturated aldehyde and contain an additional methyl group on the α -carbon (Chan et al., 2010). The formation of particles from acrolein, crotonaldehyde, and methacrolein has been studied by Chan et al. Recently, the reaction between trans-2-methyl-2-butenal and chlorine to the total budget of particles in the atmosphere have been studied by (Antiñolo et al., 2020). However, the formation of SOAs of the reactions between C₅-C₇ unsaturated aldehydes and chlorine has been studied in the 16L-ASC and CR-ASC, connected by a Teflon tube (UCLM University). As far as we know, this work represents the first data on the particle phase studies on the oxidation reactions of C₅-C₇ unsaturated aldehydes through chlorine.

V.2.3.1 Experimental conditions and protocols

Particle-phase studies for the T2P + Cl, T2H + Cl, and T2Hep + Cl reactions were done at 296 ± 2 K and 730 ± 20 Torr of synthetic air in the 16L-ASC and CR-ASC using the Fast Mobility Particle Sizer (FMPS) spectrometer. All the technical details concerning the D-ASC set-up were reported in section II.2.1.2.6.

The gas mixture from the CR-ASC entered in the FMPS through a 1 μ m cut cyclone. A 10 L min⁻¹ filtered exhaust flow rate from the FMPS was then directed to the 16L-ASC and then again to the CR-ASC in closing the circuit allows the gases to mix in the system. Data were recorded with the FTIR spectrometer every 2 min and the FMPS spectrometer every 1 s (although they were averaged for 1 min in the present work).

The total timescale of the experiment was 80 min, as follows. In the first 10 min, the reaction mixture (synthetic air+aldehyde+Cl₂) stabilized in the dark. During that, the aldehyde losses and the possible reaction with Cl₂ were tested (no Cl reaction was taking place). The lamps were then turned on, and the Cl reaction started, monitoring aldehyde loss and SOAs formation for 60 min.

The loss of the formed SOAs by wall loss or through the filters of the FMPS were evaluated after the end of the reaction for 20 min in the dark. The two tests' two tests provide both $k_{L,Ald}$, and $k_{L,SOA}$, the rate constants of the aldehyde (Ald), and SOA losses. Initial concentrations of reactants and experimental techniques of the particle-phase studies are summarized in Table V.11.

Table V.11: Summary of experimental conditions and analytical techniques used for the formed SOA through the T2P + Cl, T2H + Cl, and T2Hep + Cl reactions.

Reaction	Reactor	Lamps	Compound	Initial concentration range / $\times 10^{14}$ molecule cm^{-3}
T2P + Cl	16L-ASC CR-ASC	8	T2P	1.6 – 9.2
			Cl ₂	1.6 – 15.8
T2H + Cl			T2H	0.8 – 2.7
			Cl ₂	13.4 – 77.2
T2Hep + Cl			T2Hep	0.8 – 2.3
			Cl ₂	0.3 – 3.4

Mass concentrations of particles (M_{SOA}) have been calculated assuming a particle density of 1.4 g cm^{-3} (recommended value by Hallquist et al., 2009) and spherical geometry.

V.2.3.2 Results

V.2.3.2.1 SOAs in T2P + Cl

a) Preliminary tests

Figure V.13 displays an example of these decays for an initial concentration of 6.5×10^{14} molecule cm^{-3} and 11.4×10^{14} molecule cm^{-3} for T2P and Cl₂, respectively.

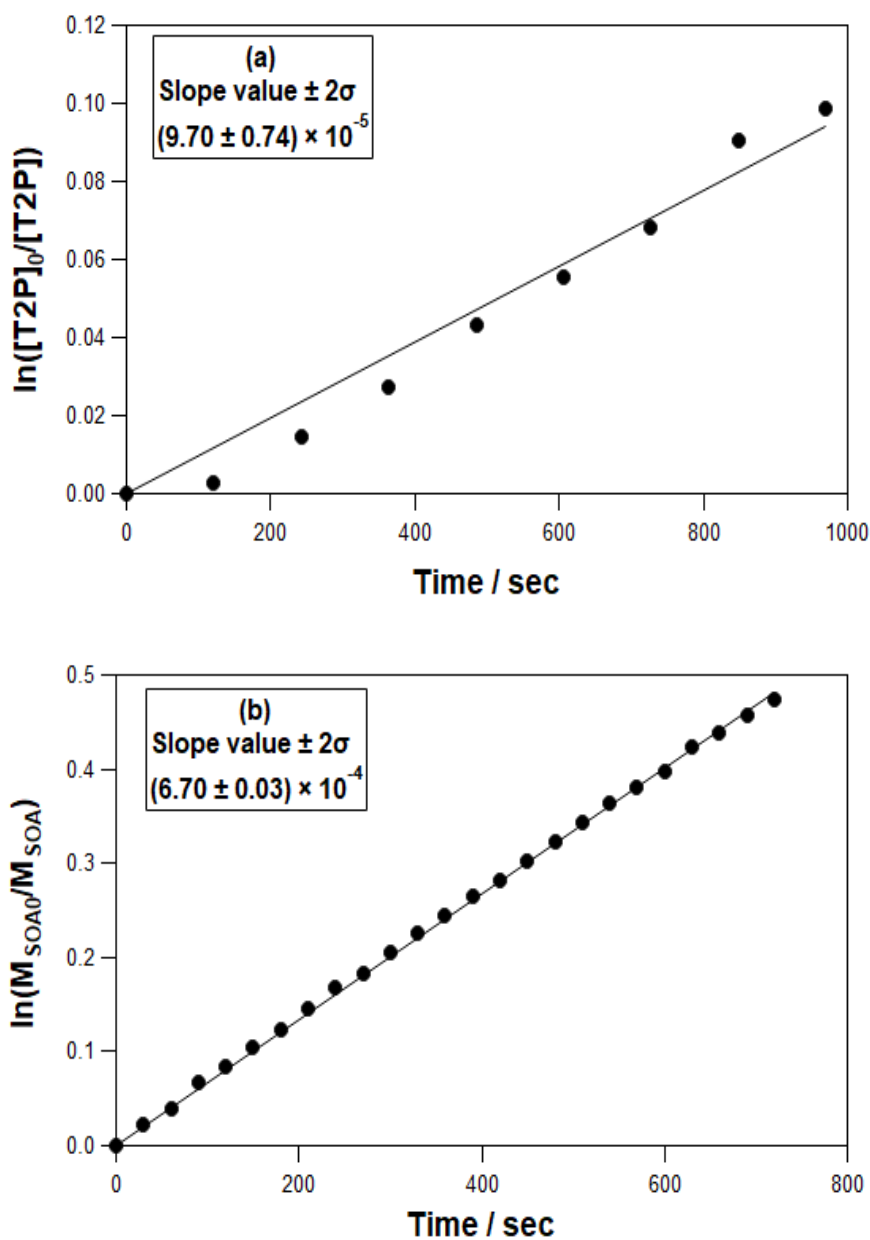


Figure V.13: Wall losses of T2P (a) and SOA (b). $[T2P]_0 = 6.5 \times 10^{14}$ molecule cm^{-3} and $[\text{Cl}_2]_0 = 11.4 \times 10^{14}$ molecule cm^{-3} .

The initial concentrations of T2P and Cl_2 are summarized in Table V.12. The rate constant of T2P losses ($k_{L,T2P}$) and aerosol losses ($k_{L,SOA}$) for all experiments was $(1.2 - 20.8) \times 10^{-4} \text{ s}^{-1}$ range and $(5.5 - 7.0) \times 10^{-4} \text{ s}^{-1}$ range, respectively. As shown, the rate constant of the aldehyde and the aerosol losses are highly dependent on the initial concentrations of the reagents.

b) Particle number concentrations

An example of the particle size's temporal evolution in terms of the normalized particle number concentrations ($dN/d\log D_p$) for a given initial concentration of T2P and Cl_2 is displayed in Figure V.14.

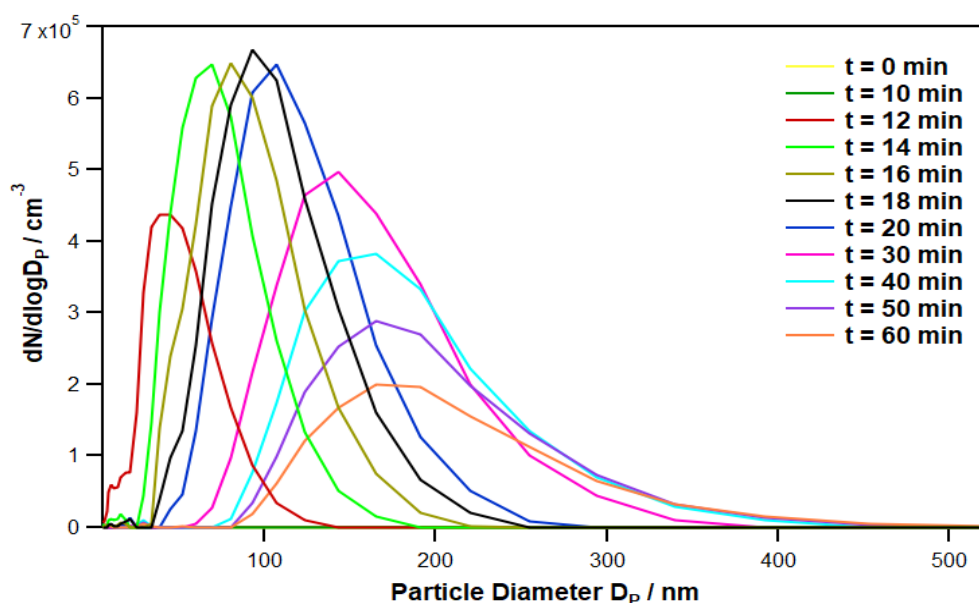


Figure V.14: Number-weighted particle size distributions for SOA measured by FMPS at several reaction times of the T2P oxidation initiated by Cl. $[\text{T2P}]_0 = 4.7 \times 10^{14}$ molecule cm^{-3} and $[\text{Cl}_2]_0 = 10.3 \times 10^{14}$ molecule cm^{-3} .

The temporal evolutions are sequentially displayed with different colors. From $t = 0$ min to $t = 10$ min, no particles were observed. At $t = 12$ min, the first particles have appeared with a maximum particle concentration ($N_{p_{\max}}$) around 4.4×10^5 particles/ cm^3 observed at 45.3 nm of diameter. From $t = 12$ min to $t = 20$ min, $N_{p_{\max}}$ stabilized at 6.5×10^5 particles/ cm^3 with an evolution of the diameter from 69.8 nm to 107.5 nm. Finally, from $t = 20$ min to $t = 60$ min (end of the reaction), the $N_{p_{\max}}$ declined to 1.9×10^5 particles/ cm^3 at 191.1 nm. The particle diameter growth versus time was explained by the small particles' coagulation, which caused the number of particles to be reduced at longer times.

c) Particle mass concentrations

The measured mass concentrations of particles (M_{SOA}) were corrected using the rate constant of their losses onto the wall set-up and the FMPS filter.

An example of the temporal mass evolution of the formed SOAs through the reaction between T2P and Cl atoms is displayed in Figure V.15.

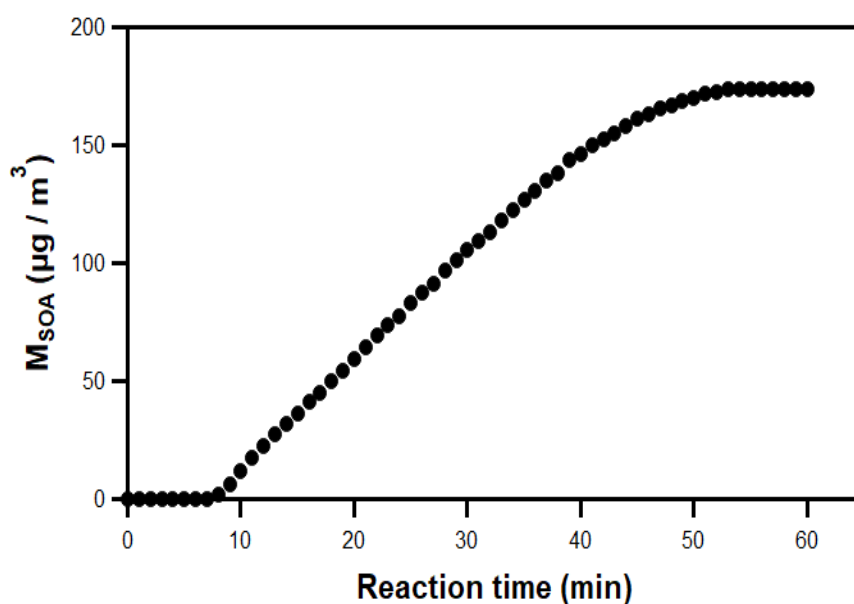


Figure V.15: Mass concentration of SOA as function of reaction time between T2P and Cl atoms. $[\text{T2P}]_0 = 6.6 \times 10^{14} \text{ molecule cm}^{-3}$ and $[\text{Cl}_2]_0 = 2.0 \times 10^{14} \text{ molecule cm}^{-3}$.

According to Figure V.15, the particle formation started 8 min after the reaction's initiation (lamps on). Besides, SOA mass concentrations reached a plateau after roughly 55 min reaction time up to the reaction's end (60 min). On the other hand, the plot of the maximum mass of SOA ($M_{\text{SOA, max}}$) versus the initial concentration of T2P for two similar concentrations of Cl_2 (Figure V.16.a) and the plot of the maximum mass of SOA ($M_{\text{SOA, max}}$) versus the initial concentration of Cl_2 for two similar concentrations of T2P (Figure V.16.b), shows the influence of each reagent on the amount of SOAs formed.

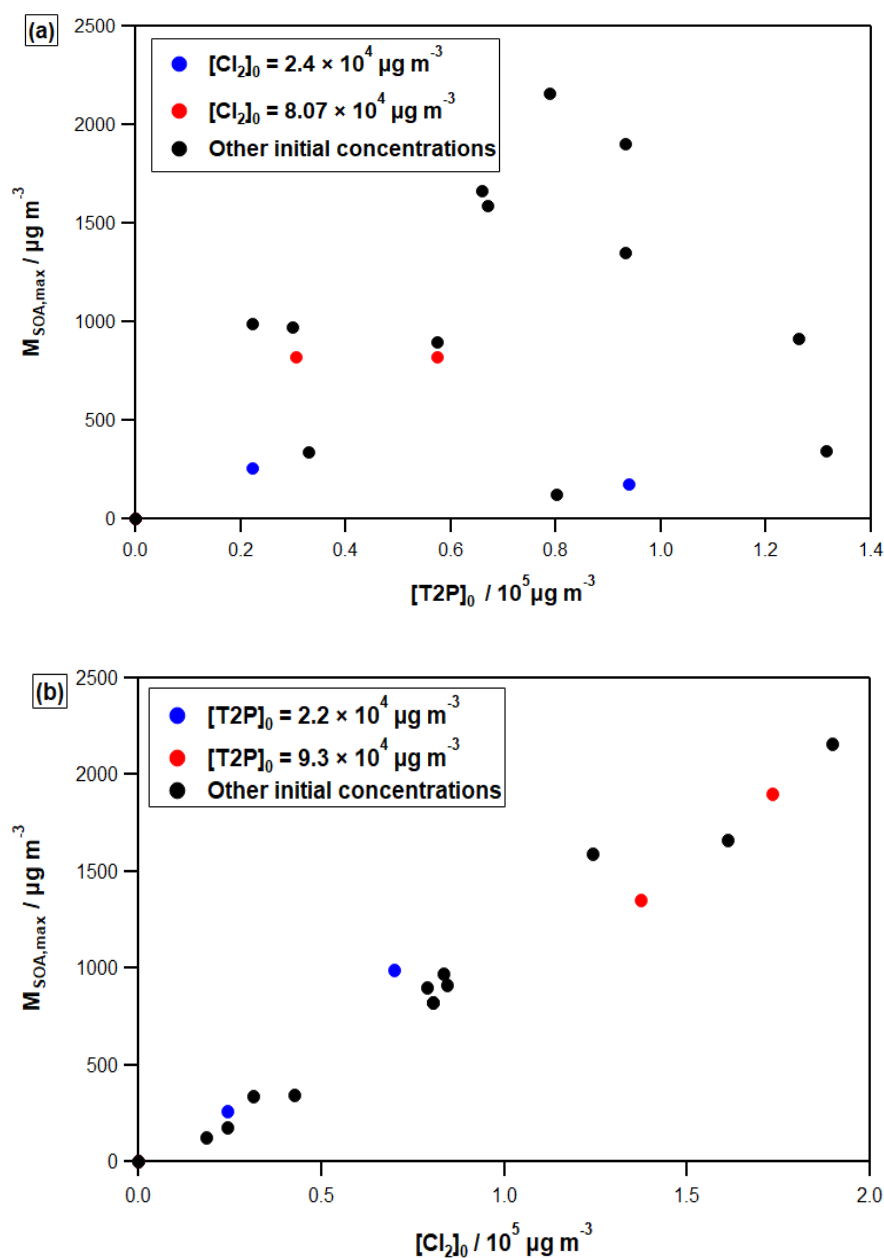


Figure V.16: (a) The plot of $M_{\text{SOA,max}}$ versus $[\text{T2P}]_0$ and (b) the plot of $M_{\text{SOA,max}}$ versus the $[\text{Cl}_2]_0$.

Figure V.16 shows a clear dependency of $M_{\text{SOA,max}}$ on the amount of Cl_2 introduced in the system, whereas no obvious correlation can be identified with the initial concentration of T2P.

d) Aerosol yields

The SOA yield Y_{SOA} is defined as described in section II.4.3. The initial concentrations of T2P and Cl_2 ($[\text{T2P}]_0$ and $[\text{Cl}_2]_0$), the reacted T2P ($\Delta[\text{T2P}]$), the maximum SOA mass concentration observed ($M_{\text{SOA,max}}$), and the SOA yields (Y_{SOA}) are summarized in Table V.12 together with the experimental conditions.

Table V.12: Experimental conditions and results obtained for the SOA study.

$[\text{T2P}]_0 \times 10^4$ / $\mu\text{g m}^{-3}$	$[\text{Cl}_2]_0 \times 10^4$ / $\mu\text{g m}^{-3}$	$\Delta[\text{T2P}] \times 10^4$ / $\mu\text{g m}^{-3}$	$M_{\text{SOA,max}} \times 10^2$ / $\mu\text{g m}^{-3}$	% $Y_{\text{SOA}} \pm 2\sigma$
8.0	1.9	1.8	1.2	0.8 ± 0.1
9.4	2.4	1.8	1.8	1.2 ± 0.1
13.1	4.3	3.1	3.4	1.3 ± 0.1
3.3	3.2	1.6	3.4	2.1 ± 0.1
12.6	8.5	4.8	9.1	2.2 ± 0.1
2.2	2.4	0.9	2.6	2.5 ± 0.1
5.8	8.1	3.4	8.2	2.6 ± 0.1
3.1	8.1	1.7	8.2	2.8 ± 0.1
3.0	8.3	1.6	9.7	3.8 ± 0.1
5.8	7.9	2.2	9.0	3.8 ± 0.1
9.3	13.7	2.8	13.5	4.3 ± 0.1
6.7	12.4	4.3	15.9	4.6 ± 0.3
2.2	7.0	1.4	9.9	4.8 ± 0.3
7.9	19.0	4.9	21.6	5.2 ± 0.4
6.6	16.1	4.4	16.6	5.2 ± 0.5
9.3	17.3	2.5	19.0	6.2 ± 0.1

The slope of the plot of M_{SOA} versus $\Delta[\text{T2P}]$ gives the SOA formation yield, as displayed in Figure IV.17.

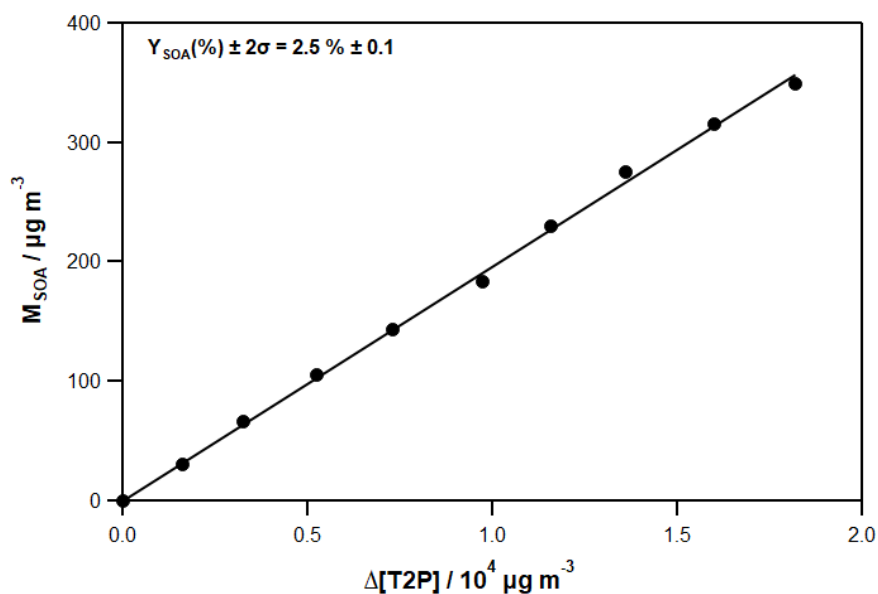


Figure V.17: SOA mass concentration M_{SOA} produced from the T2P+Cl reaction as function of the consumed T2P. $[\text{T2P}]_0 = 2.2 \times 10^{14} \text{ molecule cm}^{-3}$ and $[\text{Cl}_2]_0 = 2.4 \times 10^{14} \text{ molecule cm}^{-3}$. The SOA yield Y_{SOA} is obtained from the linear least-squares analysis.

Figure V.18 displays the plot of Y_{SOA} vs. $M_{\text{SOA,max}}$, and the fit using the one product model from Odum et al. 1996 (see chapter II, Eq.20).

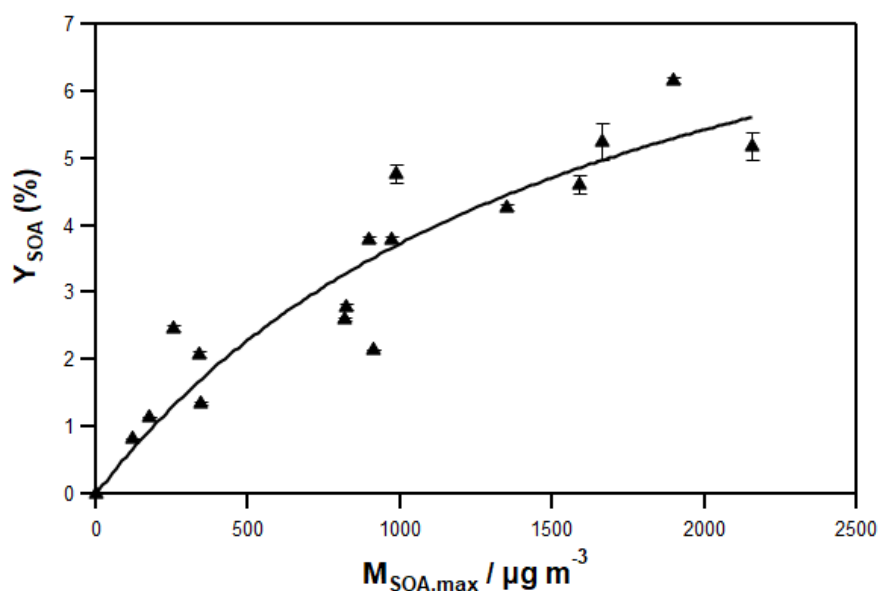


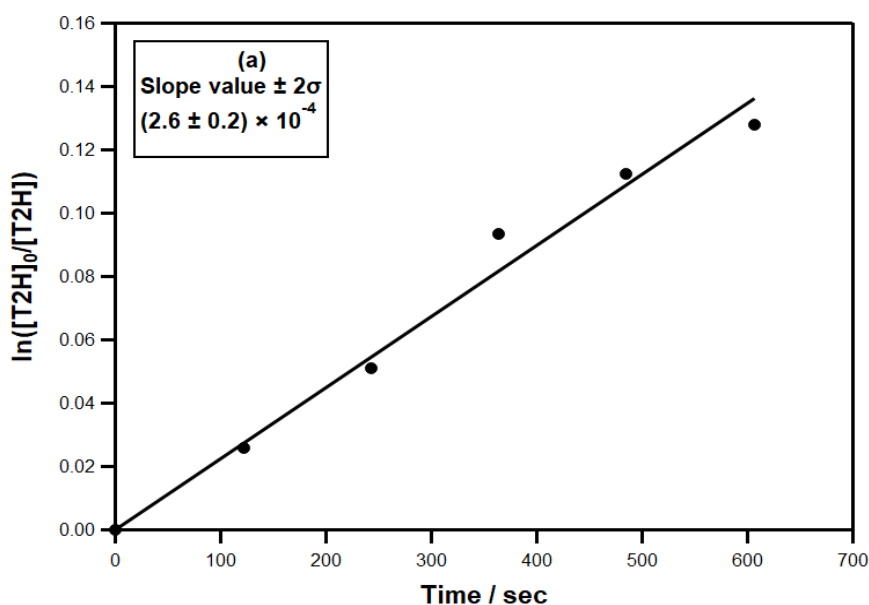
Figure V.18: The SOA plot yield Y_{SOA} as a function of $M_{\text{SOA,max}}$ for the reaction between T2P and Cl considering a particle mass density equal to 1.4 g cm^{-3} .

Despite the relative scattering in the data (Figure V.18), the calculated Y_{SOA} seems to fit the one-product model reasonably well. A least-square regression on the data gives the following parameters: $\alpha = (10.0 \pm 2.5)\%$ and $K_p = (6.0 \pm 2.7) \times 10^{-4} \text{ m}^3 \mu\text{g}^{-1}$. Uncertainties represent two standard deviations (2σ). The mass-based stoichiometric coefficient (α) indicates that Y_{SOA} tends towards 10% at very high M_{SOA} values. On the other hand, the equilibrium partitioning coefficient (K_p) indicates that the semi-volatile species that produce the SOA formation are mostly in the vapor phase rather than the condensed phase.

V.2.3.2.2 SOAs in T2H + Cl

a) Preliminary tests

T2H and SOA masses' wall losses are estimated as described above for T2P (section V.2.3.2.1). Figure V.19 displays an example of these decays for initial concentrations of 2.5×10^{14} and $6.0 \times 10^{14} \text{ molecule cm}^{-3}$ for T2H and Cl_2 , respectively.



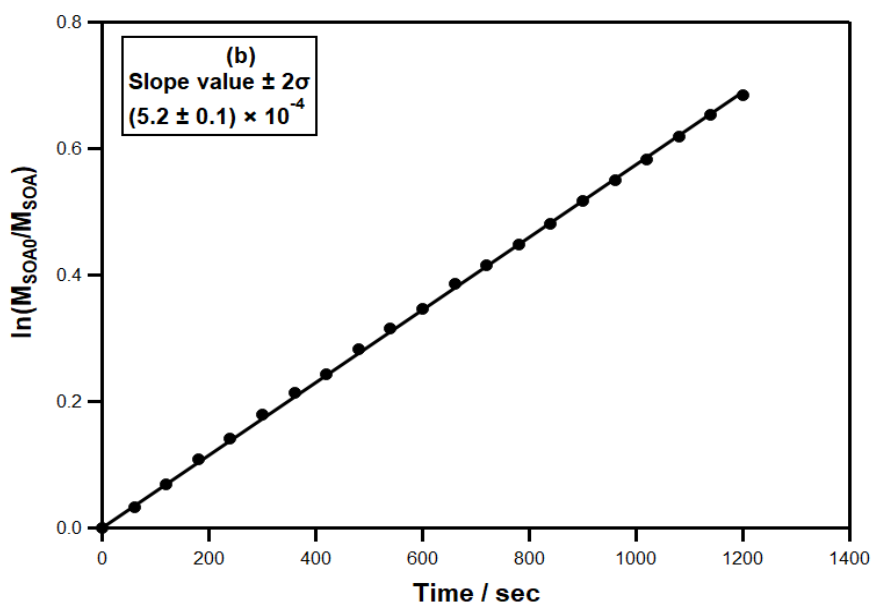


Figure V.19: Wall losses of T2H (a) and SOA masses (b). $[T2H]_0 = 2.5 \times 10^{14}$ molecule cm^{-3} and $[Cl_2]_0 = 6.0 \times 10^{14}$ molecule cm^{-3} .

The initial concentrations of T2H and Cl_2 used in the SOA study were listed in Table V.12. The rate constant of T2H losses, $k_{L,T2H}$, and M_{SOA} losses, $k_{L,SOA}$, for all experiments were in the $(0.008 - 2.25) \times 10^{-4} \text{ s}^{-1}$ range, and the rate constant of SOA losses, $k_{L,SOA}$, was in the $(4.35 - 6.18) \times 10^{-4} \text{ s}^{-1}$ range. As discussed above in section V.2.3.2.1, T2H and aerosols losses depend on the used initial concentration for T2H and Cl_2 .

b) Particle number concentrations

The temporal evolution of the size in terms of normalized particle number concentrations ($dN/d\log D_p$) for given initial concentrations of T2H and Cl_2 is displayed in Figure V.20.

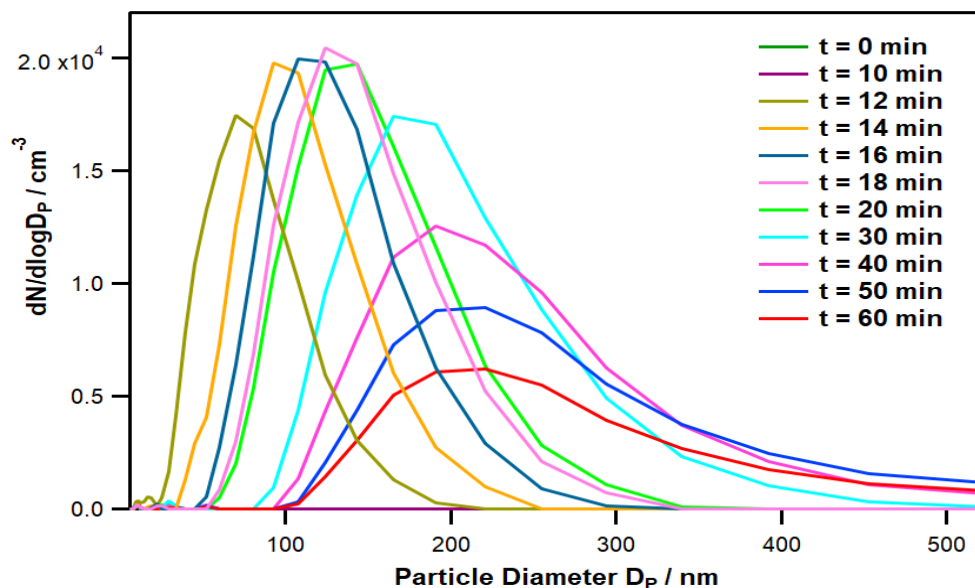


Figure V.20: Number-weighted particle size distributions for SOA measured by FMPS at several reaction times of the T2H oxidation initiated by Cl. $[T2H]_0 = 2.7 \times 10^{14}$ molecule cm^{-3} and $[Cl_2]_0 = 6.5 \times 10^{14}$ molecule cm^{-3} .

The temporal evolutions are sequentially displayed with different colors. From $t = 0$ min to $t = 10$ min, no particles were observed. At $t = 12$ min, the first particles have appeared with a maximum particle concentration ($N_{p_{\max}}$) around 1.7×10^4 particles/ cm^3 observed at 69.8 nm of diameter. From $t = 12$ min to $t = 20$ min, $N_{p_{\max}}$ stabilized at 2.0×10^4 particles/ cm^3 with an evolution of the diameter from 93.1 nm to 143.3 nm. Finally, from $t = 20$ min to $t = 60$ min (end of the reaction), the $N_{p_{\max}}$ declined down to 0.6×10^5 particles/ cm^3 at 220.7 nm. The particle diameter growth versus time was explained by the small particles' coagulation, which caused the number of particles to be reduced at longer times.

c) Particle mass concentrations

The measured mass concentrations of particles (M_{SOA}) were corrected using the rate constant of their losses onto the wall set-up and the FMPS filter. An example of the temporal mass evolution of the formed SOAs through the reaction between T2H and Cl atoms is displayed in Figure V.21.

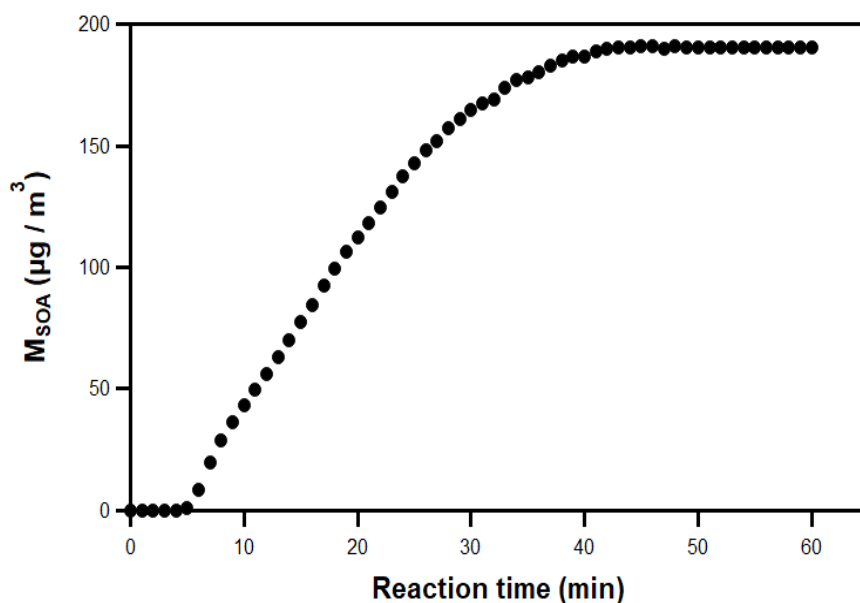


Figure V.21: SOA formation as function of reaction time between T2H and Cl atoms.

$[\text{T2H}]_0 = 1.3 \times 10^{14} \text{ molecule cm}^{-3}$ and $[\text{Cl}_2]_0 = 1.4 \times 10^{14} \text{ molecule cm}^{-3}$.

According to Figure V.21, the particle formation started after 6 minutes of starting the T2H and Cl reaction. Also, SOA mass concentrations reached a plateau after roughly 45 minutes of reaction time up to the reaction's end (60 min). To better understand the influence of each reagent on the amount of SOAs formed, I plotted the maximum mass of SOA ($M_{\text{SOA,max}}$) versus the initial concentration on one of the reagents (T2H or Cl_2) as explained in section V.2.3.2.1 (Figure V.22).

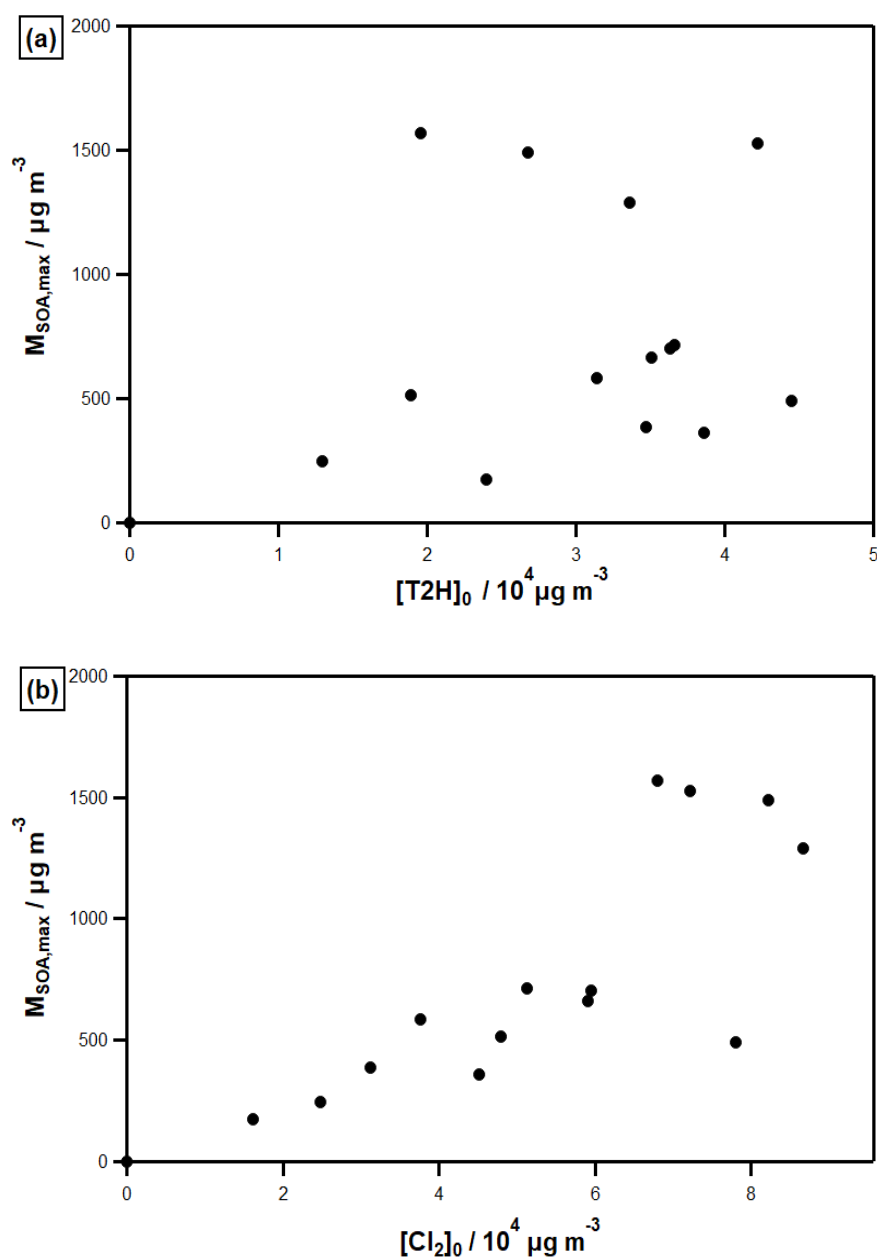


Figure V.22: (a) The plot of $M_{SOA,max}$ versus $[T2H]_0$ and (b) the plot of $M_{SOA,max}$ versus the $[Cl_2]_0$.

Figure V.22 shows a clear dependency of $M_{SOA,max}$ on the amount of Cl_2 introduced in the system, whereas no obvious correlation can be identified with the initial concentration of T2H.

d) Aerosol yields

The initial concentrations of T2H and Cl₂ ([T2H]₀ and [Cl₂]₀), the reacted T2H (Δ [T2H]), the maximum SOA mass concentration observed ($M_{\text{SOA,max}}$), and the SOA yields (Y_{SOA}) are summarized together with the used experimental conditions in Table V.13.

Table V.13: Experimental conditions and results obtained for the SOA study.

$[\text{T2H}]_0 \times 10^4$ / $\mu\text{g m}^{-3}$	$[\text{Cl}_2]_0 \times 10^4$ / $\mu\text{g m}^{-3}$	$\Delta[\text{T2H}] \times 10^3$ / $\mu\text{g m}^{-3}$	$M_{\text{SOA,max}} \times 10^2$ / $\mu\text{g m}^{-3}$	% $Y_{\text{SOA}} \pm 2\sigma$
2.4	1.6	1.9	1.8	5.1 ± 0.8
3.5	3.1	3.8	3.9	9.8 ± 1.1
1.3	2.5	2.8	2.5	10.5 ± 0.4
3.1	3.8	2.7	5.9	13.0 ± 2.4
3.7	5.1	3.4	7.1	15.3 ± 1.0
3.9	4.5	2.2	3.6	16.9 ± 1.4
3.6	6.0	2.8	7.0	20.7 ± 5.5
4.5	7.8	1.7	4.9	27.7 ± 4.8
4.2	7.2	4.2	15.3	29.9 ± 4.2
3.5	5.9	1.2	6.6	31.0 ± 4.6
2.0	6.8	2.9	15.7	31.1 ± 5.8
3.4	8.7	2.4	12.9	33.1 ± 2.8
1.9	4.8	1.1	5.2	33.1 ± 7.5
2.7	8.2	3.5	14.9	37.5 ± 4.4

The slope of the plot of M_{SOA} versus the reacted aldehyde ($\Delta[\text{T2H}]$) gives the yield formation of SOAs (Y_{SOA}) as displayed in Figure V.23.

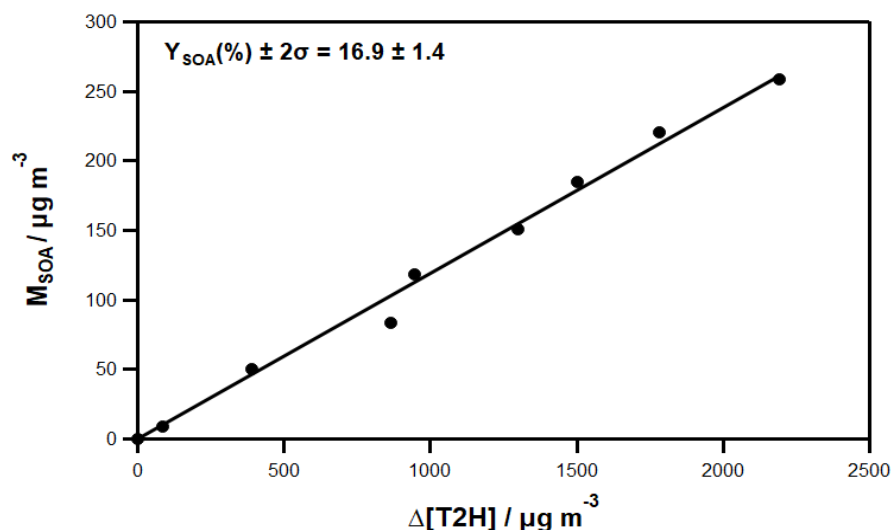


Figure V.23: SOA mass concentration M_{SOA} produced from the T2H + Cl reaction as a function of the consumed T2H. $[\text{T2H}]_0 = 3.9 \times 10^{14} \text{ molecule cm}^{-3}$ and $[\text{Cl}_2]_0 = 4.5 \times 10^{14} \text{ molecule cm}^{-3}$. The SOA yield Y_{SOA} is obtained from the linear least-squares analysis.

Figure V.24 shows the plot of Y_{SOA} versus $M_{\text{SOA,max}}$, and the fit using the one-product model from Odum et al.1996 (see chapter II, Eq.20).

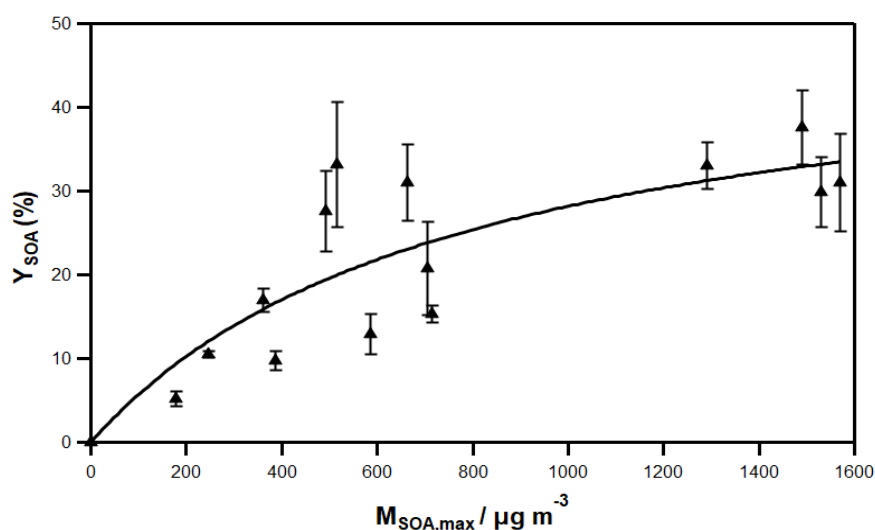


Figure V.24: The SOA plot yield Y_{SOA} as a function of $M_{\text{SOA,max}}$ for the reaction between T2H and Cl considering a particle mass density equal to 1.4 g cm^{-3} .

A least-square regression on the data gives the following parameters: $\alpha = (50.0 \pm 13.5)\%$ and $K_p = (1.3 \pm 0.7) \times 10^{-3} \text{ m}^3 \mu\text{g}^{-1}$. Uncertainties represent two standard deviations (2σ). The mass-based stoichiometric coefficient (α) indicates that Y_{SOA} tends towards 50% at very high M_{SOA} values. On the other hand, the equilibrium partitioning coefficient (K_p) indicates that the semi-volatile species that produce the SOA formation are mostly in the vapor phase rather than the condensed phase.

V.2.3.2.3 SOAs in T2Hep + Cl

a) Preliminary tests

The wall losses of T2Hep and SOA masses are estimated as described above for T2P (see section V.2.3.2.1). Figure V.25 displays an example of these decays for initial concentrations of 1.0×10^{14} and $3.4 \times 10^{14} \text{ molecule cm}^{-3}$ for T2Hep and Cl_2 , respectively.

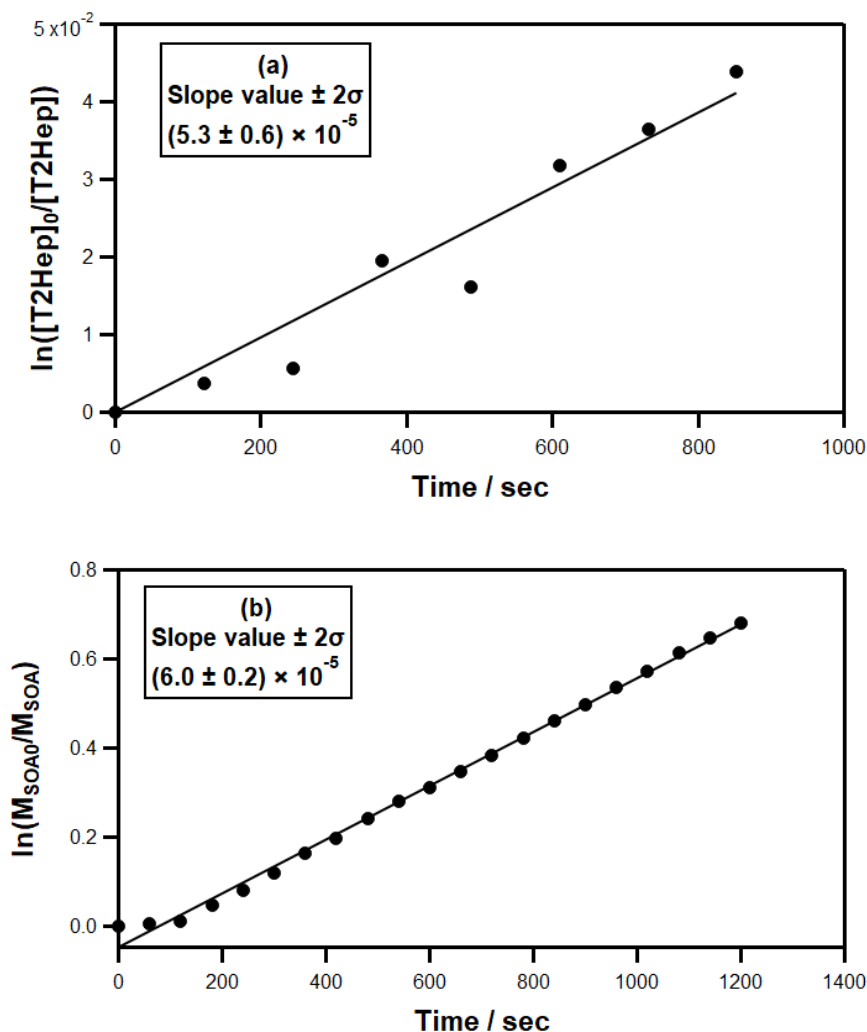


Figure V.25: Wall losses of T2Hep (a) and SOA (b) masses. $[T2Hep]_0 = 1.0 \times 10^{14}$ molecule cm^{-3} and $[Cl_2]_0 = 3.4 \times 10^{14}$ molecule cm^{-3} .

The initial concentrations of T2Hep and Cl_2 used in the SOA study were summarized in Table V.12. The aldehyde rate constant was within the $(0.15 - 5.33) \times 10^{-5} \text{ s}^{-1}$ range. On the other hand, the rate constant of SOA losses was in the $(5.40 - 6.61) \times 10^{-4} \text{ s}^{-1}$ range.

b) Particle number concentrations

The temporal evolution of the size in terms of the normalized particle number concentrations ($dN/d\log D_P$) for given initial concentrations of T2Hep and Cl_2 is displayed in Figure V.26.

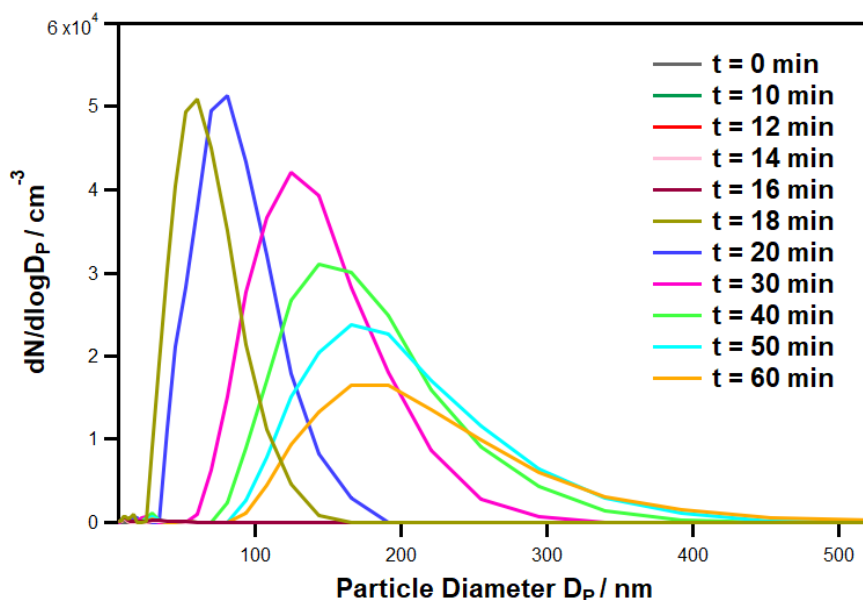


Figure V.26: Number-weighted particle size distributions for SOA measured by FMPS at several reaction times of the T2Hep oxidation initiated by Cl atoms. $[T2Hep]_0 = 1.0 \times 10^{14}$ molecule cm^{-3} and $[Cl_2]_0 = 3.4 \times 10^{14}$ molecule cm^{-3} .

The temporal evolutions are sequentially displayed with different colors. From $t = 0$ min to $t = 16$ min, no particles were observed. At $t = 18$ min, the first particles have appeared with a maximum particle concentration ($N_{p\max}$) around 5.0×10^4 particles/ cm^3 observed at 60.4 nm of diameter. From $t = 18$ min to $t = 20$ min, $N_{p\max}$ stabilized at 5.1×10^4 particles/ cm^3 with an evolution of the diameter from 60.4 nm to 80.6 nm.

Finally, from $t = 20$ min to $t = 60$ min (end of the reaction), the $N_{p_{\max}}$ declined down to 1.6×10^4 particles/cm³ at 191.1 nm.

c) Particle mass concentrations

The measured mass concentrations of particles (M_{SOA}) were corrected using the rate constant of their losses onto the wall set-up and the FMPS filter. An example of the temporal mass evolution of the formed SOAs through the reaction between T2Hep and Cl atoms is displayed in Figure V.27.

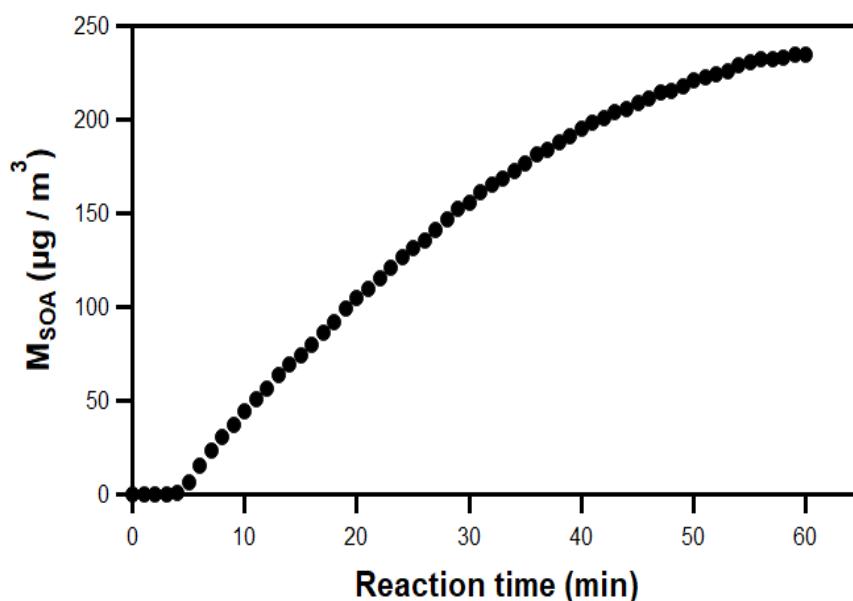


Figure V.27: Mass concentration of SOA as function of reaction time between T2Hep and Cl atoms. $[\text{T2Hep}]_0 = 1.4 \times 10^{14}$ molecule cm⁻³ and $[\text{Cl}_2]_0 = 1.4 \times 10^{14}$ molecule cm⁻³.

According to Figure V.27, the particle formation started 4 min after the reaction's initiation (lamps on). Besides, SOA mass concentrations started to reach a plateau after roughly 55 min reaction time up to the reaction's end (60 min). To better understand the influence of each reagent on the amount of SOAs formed, I plotted the maximum mass of SOA ($M_{\text{SOA,max}}$) versus the initial concentration on one of the reagents (T2Hep or Cl₂) as explained in section V.2.3.2.1 (Figure V.28)

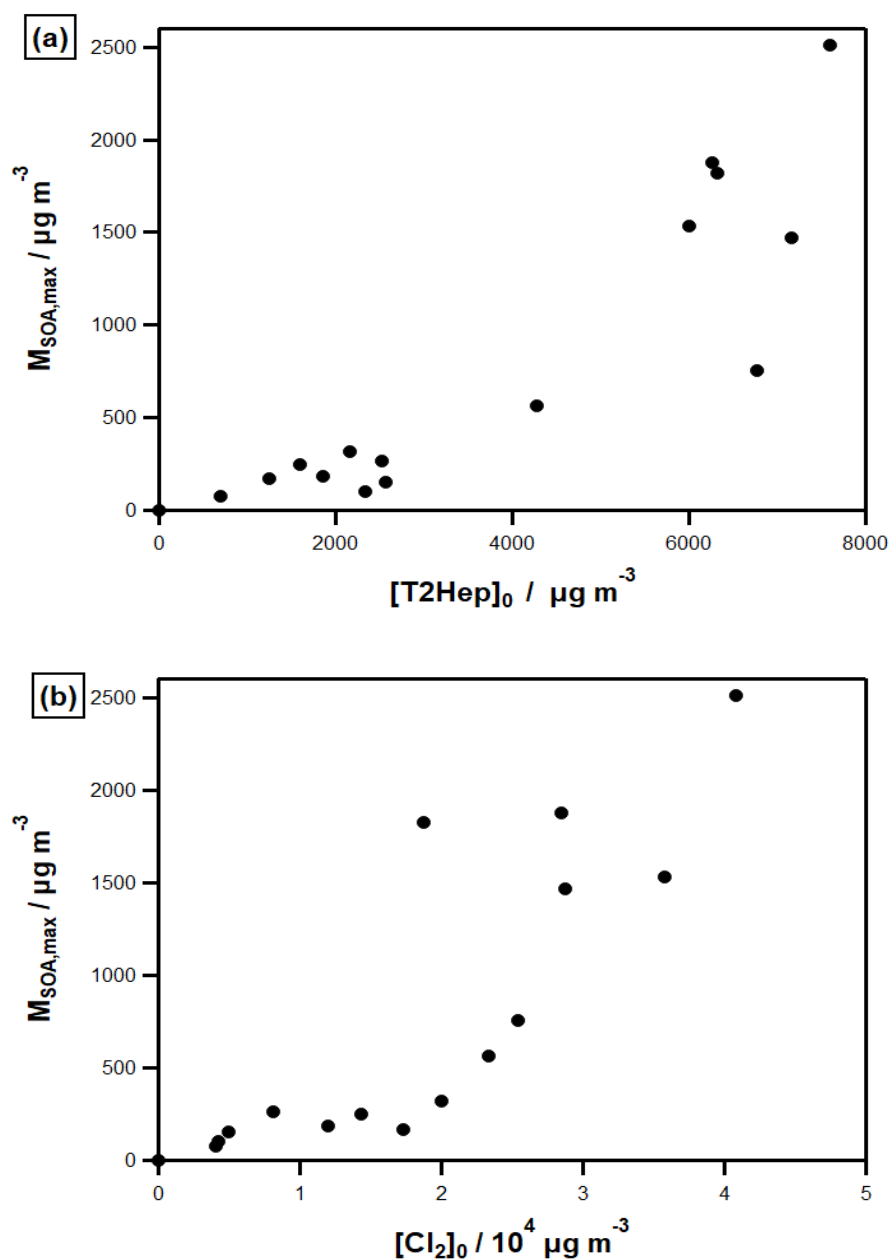


Figure V.28: (a) The plot of $M_{\text{SOA,max}}$ versus $[\text{T2Hep}]_0$ and (b) the plot of $M_{\text{SOA,max}}$ versus the $[\text{Cl}_2]_0$.

Figure V.28 shows a dependency of $M_{\text{SOA,max}}$ on the initial concentrations of both reagents T2Hep and Cl_2 .

d) Aerosol yields

The initial concentrations of T2Hep and Cl_2 ($[\text{T2Hep}]_0$ and $[\text{Cl}_2]_0$), the reacted T2Hep ($\Delta[\text{T2Hep}]$), the maximum SOA mass concentration observed ($M_{\text{SOA,max}}$), and the SOA

yields (Y_{SOA}) are summarized together with the used experimental conditions in Table V.14.

Table V.14: Experimental conditions and results obtained for the SOA study.

$[\text{T2Hep}]_0 \times 10^4$ / $\mu\text{g m}^{-3}$	$[\text{Cl}_2]_0 \times 10^4$ / $\mu\text{g m}^{-3}$	$\Delta[\text{T2Hep}] \times 10^3$ / $\mu\text{g m}^{-3}$	$M_{\text{SOA,max}} \times 10^2$ / $\mu\text{g m}^{-3}$	% $Y_{\text{SOA}} \pm 2\sigma$
4.2	0.4	2.4	1.0	3.6 ± 0.4
3.0	0.5	2.6	1.5	5.1 ± 0.2
2.9	0.4	2.5	2.6	8.7 ± 0.7
1.5	0.4	6.9	0.8	9.4 ± 1.1
4.1	2.5	6.8	7.6	10.4 ± 0.3
4.3	1.2	1.9	1.8	10.7 ± 0.9
2.8	2.3	4.3	5.7	11.5 ± 0.4
2.6	2.0	2.2	3.2	11.8 ± 1.2
2.6	1.7	1.3	1.7	12.8 ± 1.8
2.0	1.4	1.6	2.5	15.4 ± 1.0
1.1	2.9	7.2	14.7	22.0 ± 0.1
2.0	3.6	6.0	15.3	26.2 ± 0.1
1.7	1.9	6.3	18.2	29.9 ± 0.1
2.0	2.9	6.3	18.8	31.8 ± 0.1
2.0	4.1	7.6	25.1	34.3 ± 0.1

The slope of the plot of M_{SOA} versus the reacted aldehyde ($\Delta[\text{T2Hep}]$) gives the yield formation of SOAs (Y_{SOA}) as displayed in Figure V.29.

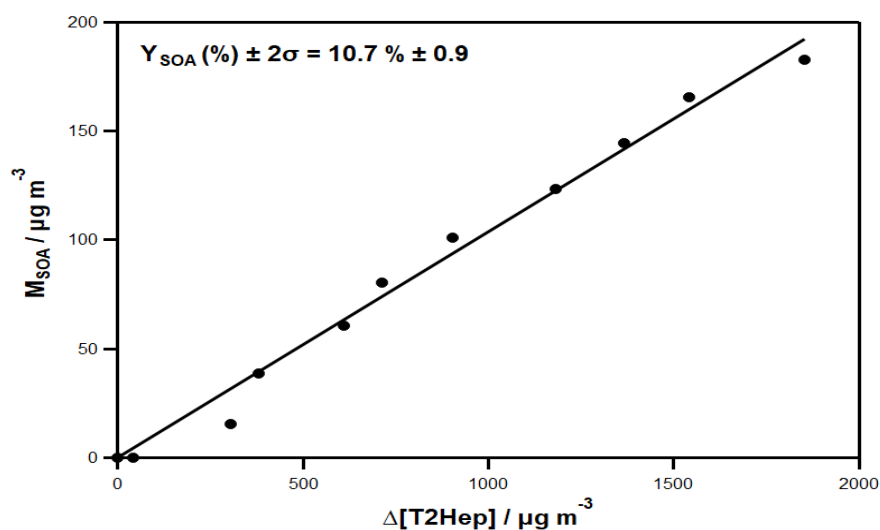


Figure V.29: SOA mass concentration M_{SOA} produced from the T2Hep + Cl reaction as a function of the consumed T2Hep. $[\text{T2Hep}]_0 = 4.3 \times 10^{14} \text{ molecule cm}^{-3}$ and $[\text{Cl}_2]_0 = 1.2 \times 10^{14} \text{ molecule cm}^{-3}$. The SOA yield Y_{SOA} is obtained from the linear least-squares analysis.

Figure V.30 displays the plot of Y_{SOA} versus $M_{\text{SOA,max}}$, and the fit using the one-product model from Odum et al.1996 (see chapter II, Eq.20).

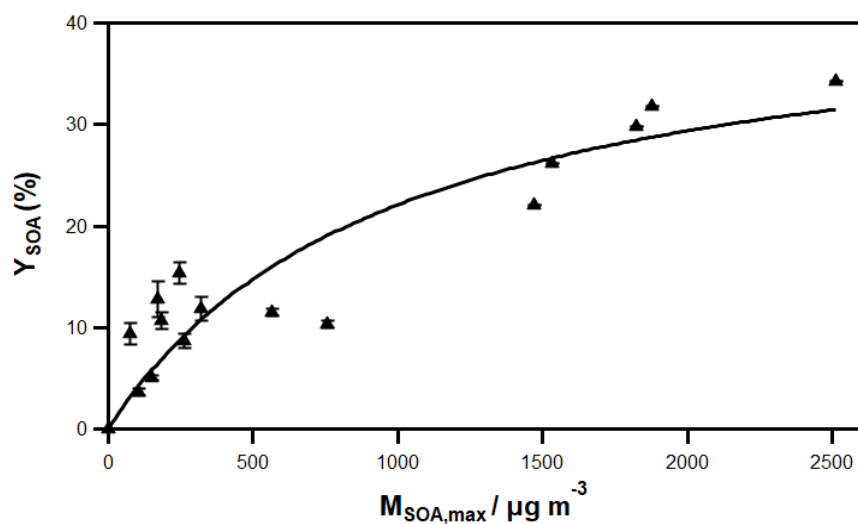


Figure V.30: SOA plot yields Y_{SOA} as a function of $M_{\text{SOA,max}}$ for the reaction between T2Hep and Cl considering a particle mass density equal to 1.4 g cm^{-3} .

A least-square regression on the data gives the following parameters: $\alpha = (43.8 \pm 16.1)\%$ and $K_p = (1.0 \pm 0.8) \times 10^{-3} \text{ m}^3 \mu\text{g}^{-1}$. Uncertainties represent two standard deviations (2σ).

The mass-based stoichiometric coefficient (α) indicates that Y_{SOA} tends towards 43.8% at very high M_{SOA} values. On the other hand, the equilibrium partitioning coefficient (K_p) indicates that the semi-volatile species that produce the SOA formation are mostly in the vapor phase rather than the condensed phase.

V.2.3.3 Discussion

For the first time, the present study demonstrates SOA production through the reaction of Cl atoms with C₅-C₇ unsaturated aldehydes. Under the listed initial concentrations of aldehyde and Cl₂ (Table V.14). The obtained yield for the T2P + Cl reaction ranges from 0.8 to 6.2%, with a maximum mass concentration ranges from 120 – 2160 $\mu\text{g m}^{-3}$. Regarding the T2H + Cl reaction, the obtained yield ranges from 5.1 to 37.5%, with a maximum mass concentration ranges from 180 – 1530 $\mu\text{g m}^{-3}$. On the other hand, the obtained yield ranges from 3.6 to 34.3%, with a maximum mass concentration ranges from 80 – 2510 $\mu\text{g m}^{-3}$. Thus, the SOA formation from C₅ unsaturated aldehyde (T2P) is much lower than that of C₆ and C₇ unsaturated aldehydes. The latter is consistent with the SOA formation observed in the ozonolysis of C₅-C₆ unsaturated aldehydes.

The present study could be compared to the SOA study of Trans-2-Methyl-2-Butenal (T2M2B) oxidation in the same experimental set-up as the present work (Antiñolo et al., 2020), where similar initial concentrations were used. Also, the rate constant of the T2M2B + Cl reaction is $(2.45 \pm 0.32) \times 10^{-10} \text{ cm}^3 \text{ molecule}^{-1} \text{ s}^{-1}$, which is in the same order of magnitude of T2P + Cl reaction $(2.53 \pm 0.83) \times 10^{-10} \text{ cm}^3 \text{ molecule}^{-1} \text{ s}^{-1}$. The SOA yield for the T2M2B + Cl reaction ranges from 0.26 to 1.65%, with a maximum mass concentration ranges from 27.4 to 863 $\mu\text{g m}^{-3}$. The presence of a methyl group on the second carbon of T2M2B seems to produce a deactivating effect of the particle formations with respect to the T2P structure. The length of the carbon chain has an activating effect only between C₅ and C₆ unsaturated aldehydes. However, no obvious effect of the carbon chain was observed for unsaturated aldehydes.

V.3 Oxidation of unsaturated alcohols with chlorine atoms

In this part, I measured the kinetics of the C₅-C₈ unsaturated alcohol reactions with chlorine. These experiments have been done in D-ASC (IMT Lille Douai).

The selected compounds were Cis-2-Penten-1-Ol (C2P-Ol), Trans-2-Hexen-1-Ol (T2H-Ol), Trans-3-Hexen-1-Ol (T3H-Ol), Cis-3-Hexen-1-Ol (C3H-Ol), and 1-Octen-3-Ol (1O-3-Ol). Cl reaction rate constants with these unsaturated alcohols have been determined at room temperature (296 ± 2 K) in zero air at atmospheric pressure (760 Torr) using the relative method. These experiments were done together with a Ph.D. (Miss. Cornelia Amarandei) from Iasi University (Romania) during her IMT Lille Douai internship. Those results are gathered in one publication, entitled “Kinetic Measurements of Cl Atom Reactions with C₅–C₈ Unsaturated Alcohols, 2020” published in “Atmosphere”.

V.3.1 Determination of rate constants

V.3.1.1 Experimental conditions and protocols

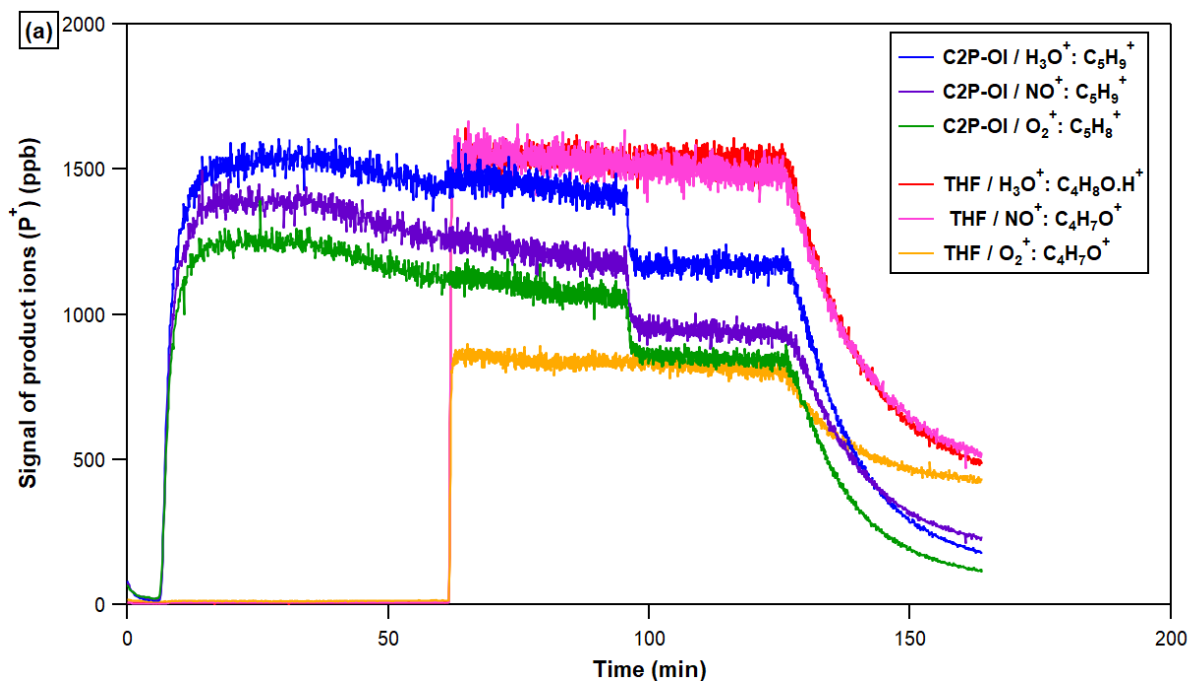
Rate constants of the reaction between five unsaturated alcohols (C2P-Ol, T2H-Ol, T3H-Ol, C3H-Ol, 1O-3-Ol) with chlorine atoms were measured using the THALAMOS-ASC coupled to SIFT-MS (Voice200® Syft Technologies, New Zealand) apparatus. Technical details on THALAMOS-ASC and SIFT-MS instrument were displayed in section II.2.1.2.2 and section II.3.1.2, respectively.

The relative method was used to measure the rate constants of the alcohols + Cl reactions. Tetrahydrofuran (THF), propan-1-ol, and octane were used as reference compounds. Chlorine atoms were produced by the photolysis of molecular chlorine (Cl₂) using broadband actinic lamps. In the present work, initial concentrations of reactants range from $(1.7 - 3.7) \times 10^{13}$ molecule cm⁻³ for both alcohols and reference compounds and around 4.2×10^{13} molecule cm⁻³ for molecular chlorine.

The experimental procedure started by cleaning the reaction chamber for 2 h at 323 K using a flow rate of about 20 L min⁻¹ of zero air. Once the reactor's temperature dropped to room temperature, the reactor's cleanliness was evaluated by measuring the background levels of the selected ions for both alcohol and reference compound using the SIFT-MS over 10 min. The background levels for all the selected ions never exceeded 5% of their initial experimental concentrations.

Each reaction started by injecting the studied alcohol into the chamber. Then, product ions (P^+) were recorded for 30 to 45 min until signal stabilization was achieved. The reference compound was then added to the reaction mixture and left to stabilize in the dark for 15 min. Afterward, Cl_2 was introduced into the reactor, and the mixture was left again for 20 min in the dark. Finally, the UV lamps were turned on for 30 min to monitor the reaction initiated by Cl atoms.

A chamber sample was introduced in a loop circuit, joining the THALAMOS-ASC and the SIFT-MS device using a dry Teflon diaphragm pump and reinjected into the reaction chamber with a flow rate of 4 L min^{-1} . A flow of 10 mL min^{-1} was analyzed by the SIFT-MS, allowing the decays of the reactants (alcohols and reference compounds) to be recorded. In Figure V.31, I present an example of the time evolution of product ions (P^+) for the C2P-Ol and the three reference compounds (THF (a), propan-1-ol (b), and octane (c)).



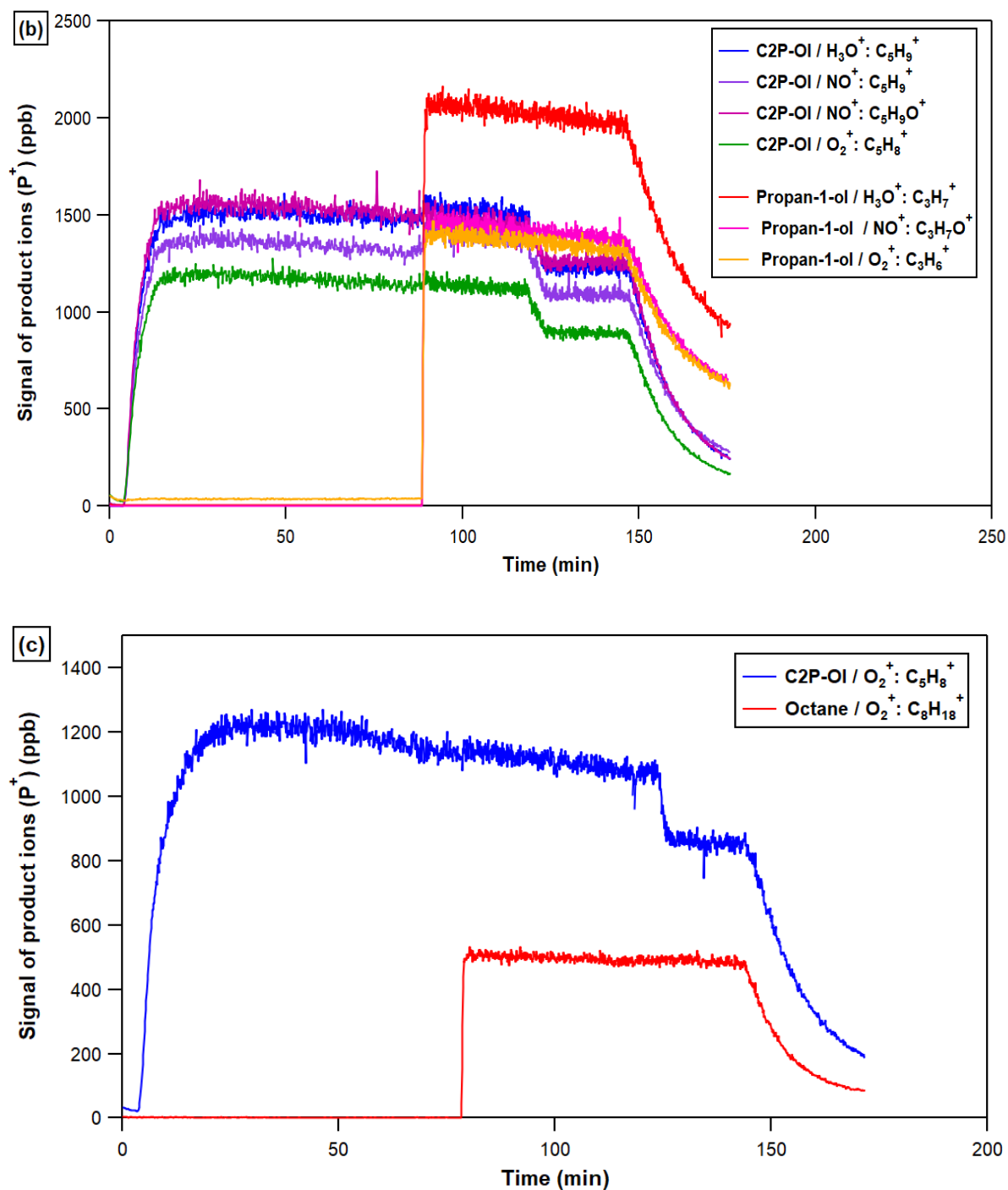


Figure V.31: Temporal evolution of the C2P-Ol and the reference compounds (THF (a), propan-1-ol (b), and octane (c)).

In Figure V.31, we observe the studied alcohol injection (C2P-Ol), the reference compound (THF, propan-1-ol, or octane).

Using the three reference compounds, the injection of Cl_2 was noticed by a sudden decrease only for the signal of product ions related to the alcohol (C2P-OI) at 100 min, 120 min, and 140 min for THF, propan-1-ol, or octane, respectively.

The same C_5 - C_8 alcohols as detailed in section IV.3 were used. Besides, the following chemicals were used as received: THF (99.9%, Acros), propan-1-ol (98.9%, Aldrich), and octane (> 99%, Aldrich). Molecular chlorine (Cl_2) was from Air Products ($(10 \pm 0.5)\%$ Cl_2 in $(90 \pm 0.2)\%$ N_2).

V.3.1.2 Preliminary experiments: Generation of ion product (P^+)

The SIFT-MS measurement process is initiated by the production of reagent ions (R^+ : H_3O^+ , NO^+ , and O_2^+), which were reacted with the gas mixture containing a component (A) (either alcohol or reference compound). These reactions generate ion products (P^+) and neutral products (N). Details on the SIFT-MS efficiency in measuring unsaturated alcohols (including those investigated in the present study) and about the ion reaction mechanisms were reported by Schoon et al., 2007. Table V.15 summarizes all the product ions (P^+) observed for alcohols and references.

Table V.15: Product ion distributions of the H_3O^+ , NO^+ , and O_2^+ reactions with the studied unsaturated alcohols and reference compounds (BR – branching ratios of product ions). (Data come from the SIFT-MS library).

Compound	M / g mol ⁻¹	H_3O^+			NO^+			O_2^+		
		m/z	Ion	BR/ %	m/z	Ion	BR/ %	m/z	Ion	BR/%
C2P-OI ($\text{C}_5\text{H}_{10}\text{O}$)	86	69	C_5H_9^+	100	68	C_5H_8^+	4	44	$\text{C}_2\text{H}_4\text{O}^+$	7
					69	C_5H_9^+	24	56	$\text{C}_3\text{H}_4\text{O}^+$	3
					85	$\text{C}_5\text{H}_9\text{O}^+$	68	57	$\text{C}_3\text{H}_5\text{O}^+$	56
					86	$\text{C}_5\text{H}_{10}\text{O}^+$	4	68	C_5H_8^+	15
								71	$\text{C}_4\text{H}_7\text{O}^+$	4

								86	C ₅ H ₁₀ O ⁺	9
									others	6
T2H-OI (C₆H₁₂O)	100	83	C ₆ H ₁₁ ⁺	100	83	C ₆ H ₁₁ ⁺	31	44	C ₂ H ₄ O ⁺	6
					99	C ₆ H ₁₁ O ⁺	55	56	C ₃ H ₄ O ⁺	5
					100	C ₆ H ₁₂ O ⁺	10	57	C ₃ H ₅ O ⁺	44
						others	4	67	C ₅ H ₇ ⁺	5
								71	C ₄ H ₇ O ⁺	7
								72	C ₄ H ₈ O ⁺	4
								82	C ₆ H ₁₀ ⁺	15
								10 0	C ₆ H ₁₂ O ⁺	5
									others	9
T3H-OI (C₆H₁₂O)	100	83	C ₆ H ₁₁ ⁺	65	71	C ₅ H ₁₁ ⁺	5	67	C ₅ H ₇ ⁺	20
		101	C ₆ H ₁₂ O.H ⁺	35	72	C ₄ H ₈ O ⁺	5	69	C ₅ H ₉ ⁺	10
					82	C ₆ H ₁₀ ⁺	25	70	C ₄ H ₆ O ⁺	10
					99	C ₆ H ₁₁ O ⁺	50	82	C ₆ H ₁₀ ⁺	50
					100	C ₆ H ₁₂ O ⁺	15	83	C ₆ H ₁₁ ⁺	5
								10 1	C ₆ H ₁₂ O.H ⁺	5
C3H-OI (C₆H₁₂O)	100	83	C ₆ H ₁₁ ⁺	90	71	C ₄ H ₇ O ⁺	10	67	C ₅ H ₇ ⁺	30
		101	C ₆ H ₁₂ O.H ⁺	10	72	C ₄ H ₈ O ⁺	30	69	C ₅ H ₉ ⁺	5
					82	C ₆ H ₁₀ ⁺	30	70	C ₄ H ₆ O ⁺	10
					99	C ₆ H ₁₁ O ⁺	20	82	C ₆ H ₁₀ ⁺	45
					100	C ₆ H ₁₂ O ⁺	10	83	C ₆ H ₁₁ ⁺	8

								10 1	C ₆ H ₁₂ O.H ⁺	2
10-3-OI (C₈H₁₆O)	128	69	C ₅ H ₉ ⁺	8	69	C ₄ H ₅ O ⁺	2	57	C ₃ H ₅ O ⁺	28
		111	C ₈ H ₁₅ ⁺	83	99	C ₆ H ₁₁ O ⁺	7	68	C ₅ H ₈ ⁺	4
		129	C ₈ H ₁₆ O.H ⁺	9	111	C ₈ H ₁₅ ⁺	29	71	C ₄ H ₇ O ⁺	3
					127	C ₈ H ₁₅ O ⁺	57	72	C ₄ H ₈ O ⁺	24
						others	5	81	C ₆ H ₉ ⁺	3
								82	C ₆ H ₁₀ ⁺	4
								85	C ₅ H ₉ O ⁺	7
								99	C ₆ H ₁₁ O ⁺	6
								11 0	C ₈ H ₁₄ ⁺	4
									others	17
THF (C ₄ H ₈ O)	72	73	C ₄ H ₈ O.H ⁺	100	71	C ₄ H ₇ O ⁺	100	42	CH ₂ CO ⁺ or C ₃ H ₆ ⁺	40
								43	CH ₃ CO ⁺ or C ₃ H ₇ ⁺	5
								71	C ₄ H ₇ O ⁺	55
Propan-1-ol (C ₃ H ₈ O)	60	43	C ₃ H ₇ ⁺	90	59	C ₃ H ₇ O ⁺	100	31	CH ₃ O ⁺	90
		61	C ₃ H ₉ O ⁺	10				42	C ₃ H ₆ ⁺	10
Octane (C ₈ H ₁₈)	114	113	C ₈ H ₁₇ ⁺	100	113	C ₈ H ₁₇ ⁺	80	11 4	C ₈ H ₁₈ ⁺	30

V.3.1.3 Preliminary tests

V.3.1.3.1 Interference tests between product ions

For each studied alcohol, six tests for the possible overlap of product ions of alcohol and the reference. In each test, only the compound of interest (either the alcohol or the reference) and Cl_2 were present and mixed with purified air in the THALAMOS-ASC. Gas samples were analyzed by SIFT-MS, selecting all the product ions arising from alcohols and references under dark and photolysis conditions.

The ions (either the alcohol or the reference) used for the kinetic analysis were selected based on the absence of any possible overlap arising from other chemical processes happening simultaneously with the studied reaction. In the section below, I chose to present an example of those tests for the possible overlap between C2P-Ol and reference compounds. These tests were also done for the other studied unsaturated alcohols (T2H-Ol, T3H-Ol, C3H-Ol, and 10-3-Ol).

a) Test 1: Injection of C2P-Ol and Cl_2 and controlling all fragments of THF

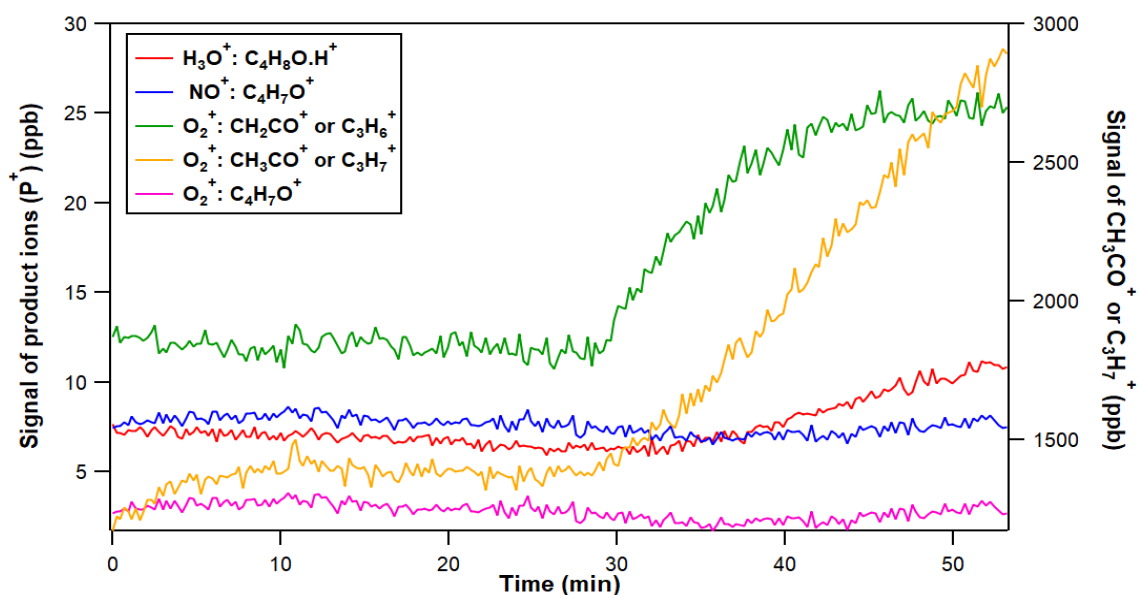


Figure V.32: Time evolution of THF product ions with only C2P-Ol and Cl_2 injected in THALAMOS-ASC.

This test showed that the product ion of THF + H_3O^+ reaction ($\text{C}_4\text{H}_8\text{O.H}^+$), the product ion of THF + NO^+ reaction ($\text{C}_4\text{H}_7\text{O}^+$), and the product ion of THF + O_2^+ reaction ($\text{C}_4\text{H}_7\text{O}^+$) were stable in the dark and under photolysis condition ($t \approx 30$ min). On the other hand, two product ions from the THF + O_2^+ reaction (CH_2CO^+ or C_3H_6^+ and CH_3CO^+ or C_3H_7^+) were stable in the dark displayed an increase when lamps were turned on. Therefore, these two product ions of THF (CH_2CO^+ or C_3H_6^+ and CH_3CO^+ or C_3H_7^+) were not considered to measure the rate constant of C2P-Ol + Cl using THF.

b) Test 2: Injection of C2P-Ol and Cl_2 and controlling all fragments of propan-1-ol

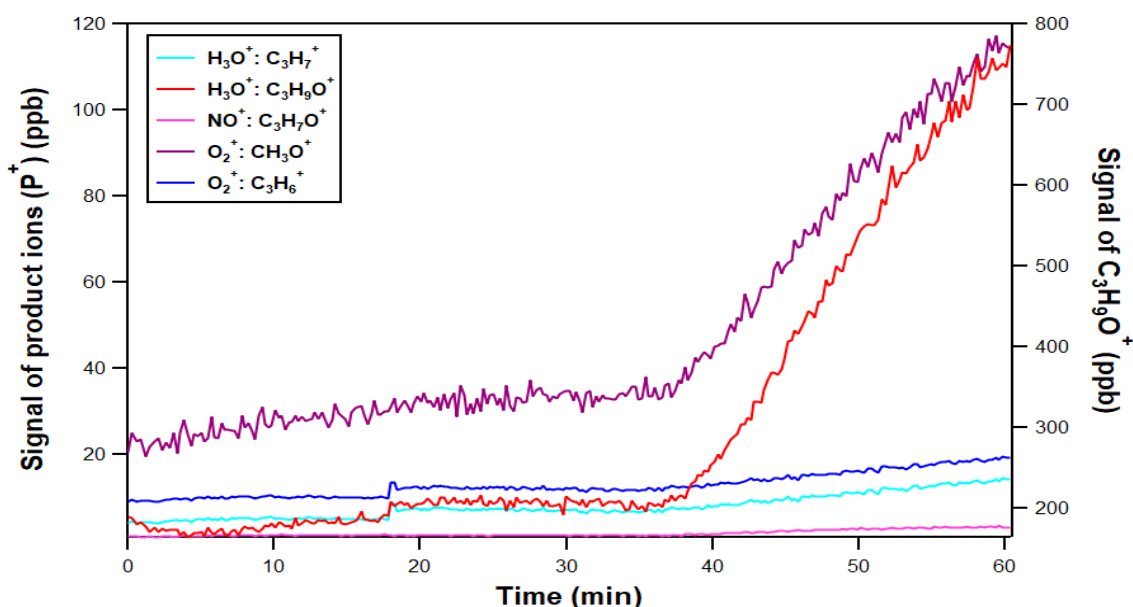


Figure V.33: Time evolution of propan-1-ol product ions with only C2P-Ol and Cl_2 injected in THALAMOS-ASC.

This test showed that the product ion formed from propan-1-ol + H_3O^+ reaction ($\text{C}_3\text{H}_9\text{O}^+$) and the product ion formed from propan-1-ol + O_2^+ reaction (CH_3O^+) were eliminated from the analysis of kinetic between C2P-Ol and Cl atom using propan-1-ol since they displayed an increase when lamps were turning on ($t \approx 35$ min) onto of C2P-Ol + Cl_2 mixture.

c) Test 3: Injection of C2P-Ol and Cl_2 and controlling all fragments of octane

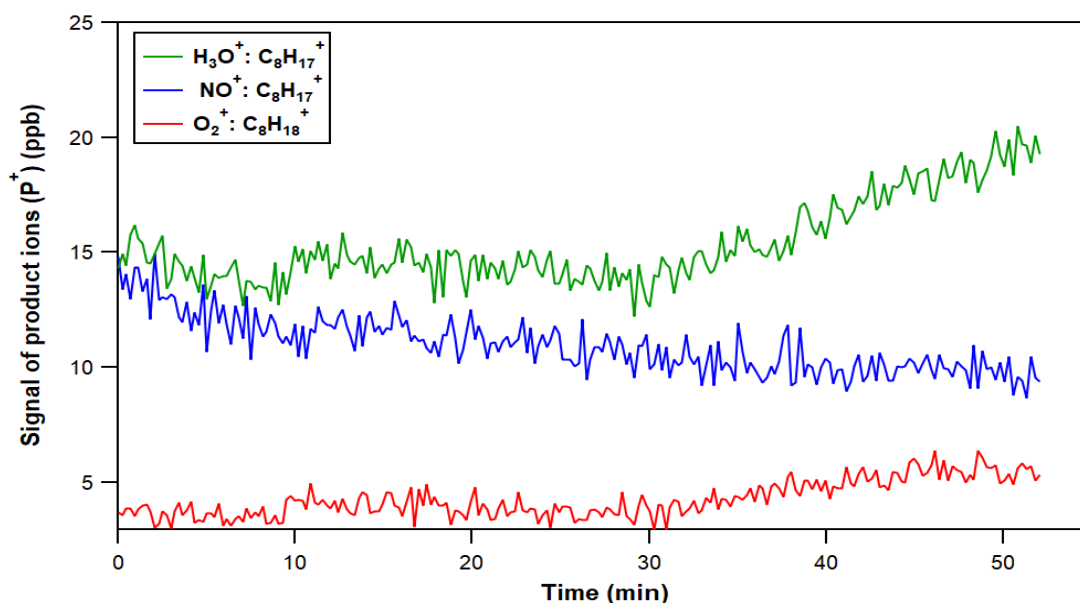


Figure V.34: Time evolution of octane product ions with only C2P-Ol and Cl₂ injected in THALAMOS-ASC.

This test displayed that $\text{C}_8\text{H}_{17}^+$ (formed from the octane + H_3O^+ reaction) was eliminated from the kinetic analysis between C2P-Ol and Cl atom using octane since it displayed an increase when lamps were turning on ($t \approx 30$ min) onto of C2P-Ol + Cl₂ mixture. The $\text{C}_8\text{H}_{17}^+$ (formed from octane + NO^+ reaction) presented an unstable signal with all the fragments formed from C2P-Ol + NO^+ . Despite that it was stable during this test, it was not considered in the kinetic analysis of C2P-Ol + Cl using octane. The product ion $\text{C}_8\text{H}_{18}^+$ (formed from the octane + O_2^+ reaction) displayed a small increase when lamps were on, but it remains stable for all the tests, so it was considered kinetic measurement.

d) Test 4: Injection of THF and Cl₂ and controlling all fragments of C2P-Ol

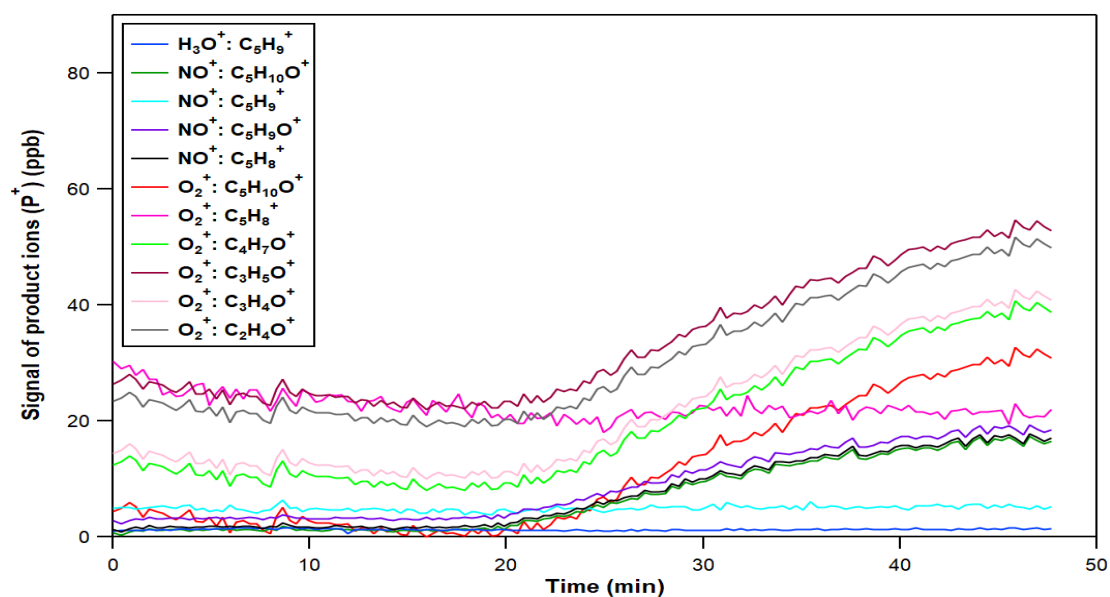


Figure V.35: Time evolution of C2P-Ol product ions with only THF and Cl₂ injected in THALAMOS-ASC.

All the fragments with the except of C₅H₉⁺ (formed from C2P-Ol + H₃O⁺ and C2P-Ol + NO⁺ reactions) and C₅H₈⁺ (formed from C2P-Ol + O₂⁺ reaction) were eliminated from the analysis of kinetic between C2P-Ol and Cl atoms using THF since they displayed an increase when lamps were turning on (t ≈ 20 min) onto of THF + Cl₂ mixture.

e) Test 5: Injection of propan-1-ol and Cl₂ and controlling all fragments of C2P-Ol

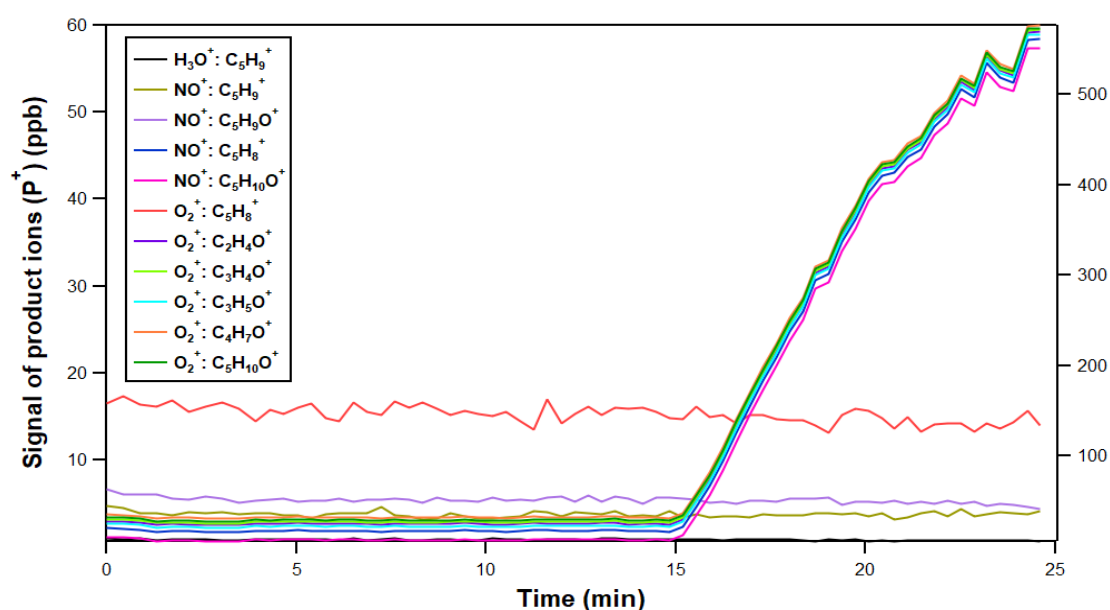


Figure V.36: Time evolution of C2P-Ol product ions with only propan-1-ol and Cl₂ injected in THALAMOS-ASC.

All the fragments with the except of C₅H₉⁺ (formed from C2P-Ol + H₃O⁺ and C2P-Ol + NO⁺ reactions), C₅H₉O⁺ (formed from C2P-Ol + NO⁺ reaction), and C₅H₈⁺ (formed from C2P-Ol + O₂⁺ reaction) were eliminated from the analysis of kinetic between C2P-Ol and Cl atoms using propan-1-ol since they displayed an increase when lamps were turning on (at ≈ 15 min) onto of propan-1-ol + Cl₂ mixture.

f) Test 6: Injection of octane and Cl₂ and controlling all fragments of C2P-Ol

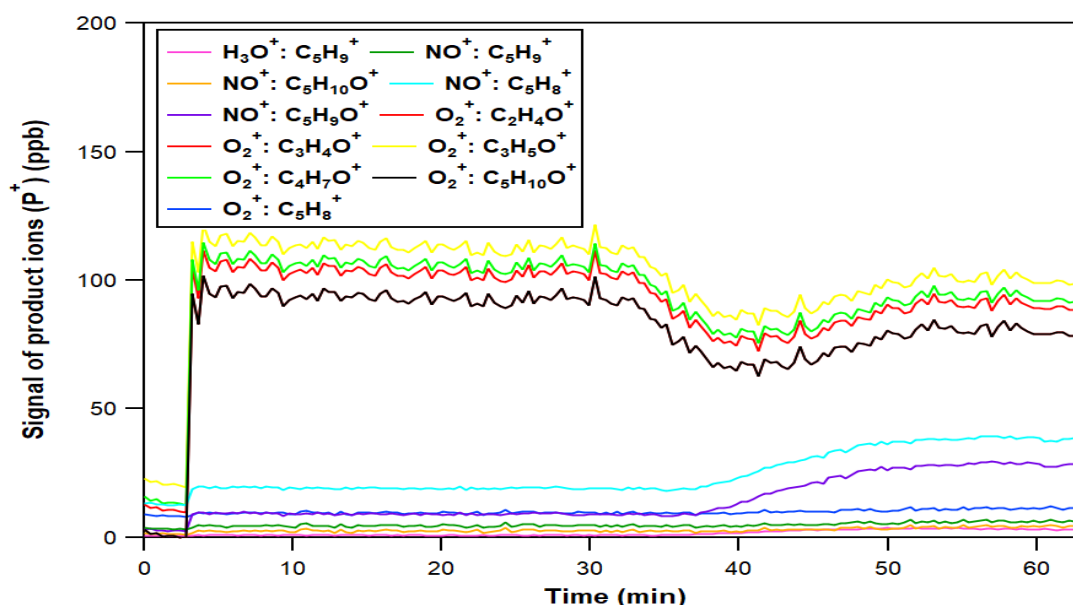


Figure V.37: Time evolution of C2P-Ol product ions with only octane and Cl₂ injected in THALAMOS-ASC.

All the ion products except C₅H₈⁺ (formed from C2P-Ol + O₂⁺ reaction) were eliminated from the kinetic analysis between C2P-Ol and Cl atoms using octane. They displayed an increase when lamps were turning on (t ≈ 30 min) onto of octane + Cl₂ mixture. The rest of the fragments formed from C2P-Ol + H₃O⁺ and C2P-Ol + NO⁺ reactions were unusable, even if they were stables because octane fragments from H₃O⁺ and NO⁺ were unstable and then unusable for the kinetic study of C2P-Ol with Cl atoms using octane.

V.3.1.3.2 Stability of product ions

a) Test 1: Stability of product ions at the moment of Cl₂ injection

At the moment of Cl₂ injection in the dark, the alcohol concentration showed a sudden decay in its concentration in the first 2 – 3 min, which was immediately followed by stabilization by staying at the final level (Figure V.37). Alcohol decays were of the order of 5 – 10% for 10-3-Ol, 15 – 20% for C2P-Ol, and about 30% for the C₆ alcohols. In the experimental set-up, the inlet and outlet ports are relatively close to each other (20 cm) and, therefore, it is believed that Cl₂ concentrations inside the injection port could be for a while up to 10⁴ times higher than their final values in the chamber (see section II.2.1.2.2). These very high local concentrations of Cl₂ may accelerate the reaction with the studied alcohol within the first few minutes after Cl₂ injection. Details concerning such dark reactions were already reported in previous studies for similar structurally unsaturated compounds (Finlayson-Pitts and Pitts Jr 1999, Rodríguez et al. 2007, Rodríguez et al. 2008, Rodríguez et al. 2010, Gibilisco et al. 2014). Nevertheless, these suspected side reactions are not expected to modify the kinetic measurements since (1) alcohol concentrations were stabilized a few minutes (2 – 3 min) after the Cl₂ injection and before starting the alcohol + Cl reaction, and (2) studied kinetics between unsaturated alcohols and Cl atoms are very fast compared to the kinetics of these side reactions.

b) Test 2: Stability tests of product ions in the dark and under photolysis conditions

Wall losses of the alcohols and the reference compounds in the dark were investigated in preliminary experiments, and negligible contributions were determined for these processes. Fluctuations of the recorded signal values were lower than 2.7%. The reported values reflect small fluctuations in the instrument's performances, such as small variations in the precursor ion concentrations, the instrument core's temperature, etc. The stability of the alcohols and reference compounds under UV-A irradiation was also tested, and all compounds were shown to be stable (Fluctuations < 2.8% over 30 min).

V.3.1.4 Results

Rate constant values for the Cl atom-initiated oxidation of the reference compounds used in the present work (THF, propan-1-ol, and octane) are well known and are (in $10^{-10} \text{ cm}^3 \text{ molecule}^{-1} \text{ s}^{-1}$) 2.39 ± 0.57 for THF + Cl (Giri and Roscoe, 2010, Alwe et al., 2013, Andersen et al., 2016), 1.60 ± 0.07 for propan-1-ol + Cl (Atkinson et al., 2006a), and 3.91 ± 0.63 for octane + Cl (Aschmann and Atkinson, 1995, Hooshiyar and Niki, 1995, Iannone et al., 2005, Li and Pirasteh, 2006, Anderson et al., 2007). Reported uncertainties on the rate constants of THF + Cl and octane + Cl (k_{THF} and k_{octane}) are 2σ , whereas no specification was mentioned for the uncertainty of $k_{\text{propan-1-ol}}$ (Atkinson et al. 2006).

Table V.16: Summary of rate constants of the used reference compounds (THF, propan-1-ol, and octane).

Compound	$k_{\text{Ref}} \times 10^{10} / \text{cm}^3 \text{ molecule}^{-1} \text{ s}^{-1}$	Reference
THF	2.71 ± 0.34	Giri and Roscoe, 2010
	2.50 ± 0.39	Alwe et al., 2013
	1.96 ± 0.24	Andersen et al., 2016
	2.39 ± 0.57	The used value (average)
1-propan-1-ol	1.60 ± 0.07	The used value (Atkinson et al. 2006)
Octane	4.05 ± 0.12	Aschmann and Atkinson, 1995
	4.09 ± 0.12	Hooshiyar and Niki, 1995
	4.38 ± 0.41	Iannone et al., 2005
	3.22 ± 0.36	Li and Pirasteh, 2006
	3.82 ± 0.18	Anderson et al., 2007
	3.91 ± 0.61	The used value (average)

To determine the relative rate constants, pairs of representative product ions from the alcohol and reference compound were selected and used to plot the reactant decays according to the relative-rate kinetic approach. For each reference, using the determined slope ($b = k_{\text{Alc}}/k_{\text{Ref}}$) and the known k_{Ref} (Table V.16).

The rate constant k_{Alc} , its uncertainty Δk_{Alc} , the final rate constant k_{Average} , and its uncertainty $\Delta k_{\text{Average}}$ were calculated as explained in section II.4.1.2.2.

V.3.1.4.1 Rate constant of C2P-Ol + Cl

Three experiments were performed for the C2P-Ol reaction with Cl atoms in zero air. Each experiment was done with one of the three reference compounds (THF, propan-1-ol, and octane). This strategy finally led to three distinct determinations. The kinetic plots for C2P-Ol using THF, propan-1-ol, and octane as reference compounds are displayed in Figure V.38.

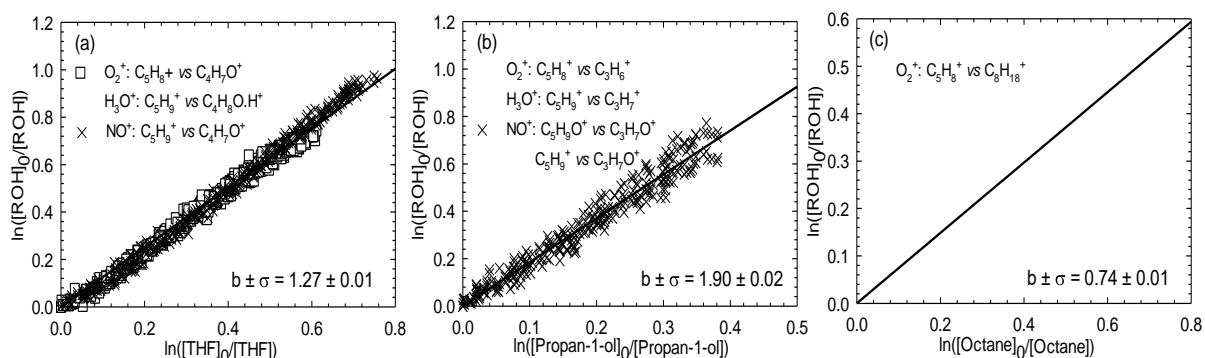


Figure V.38: Relative loss of C2P-Ol vs. that of tetrahydrofuran (THF) (a), propan-1-ol (b), and octane (c) in the Cl atom-initiated reaction.

All the $k_{\text{Alc}}/k_{\text{Ref}}$ ratios and the corresponding rate constants for each reference compound are reported in Table V.17. The average rate constant for the Cl atom reaction with C2P-Ol at 296 K was $(2.99 \pm 0.53) \times 10^{-10} \text{ cm}^3 \text{ molecule}^{-1} \text{ s}^{-1}$.

V.3.1.4.2 Rate constant of T2H-Ol + Cl

Kinetics of Cl atom T2H-Ol was investigated using the same reference compounds as those used for C2P-Ol (THF, propan-1-ol and octane). One experiment per reference was carried out. Figure V.39 shows the kinetic plots for the Cl reaction of T2H-Ol.

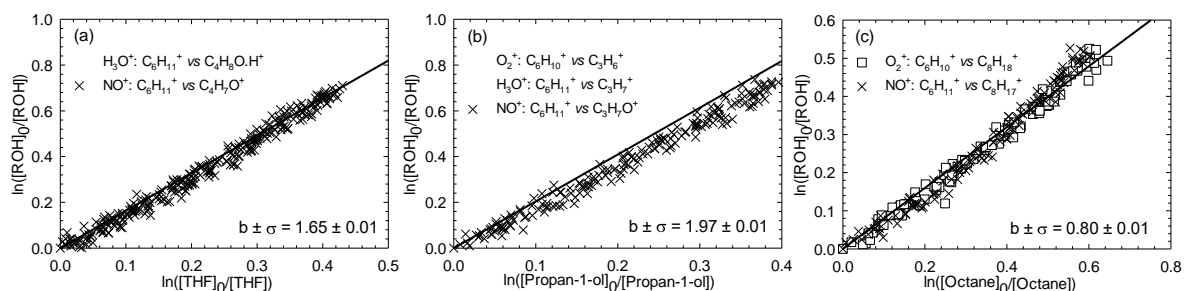


Figure V.39: Relative loss of T2H-Ol vs. that of THF (a), propan-1-ol (b), and octane (c) in the Cl atom-initiated reaction.

All the $k_{\text{Alc}}/k_{\text{Ref}}$ ratios and the corresponding rate constants for each reference compound are reported in Table V.17. The average rate constant for the Cl atom reaction with T2H-Ol at 296 K was $(3.41 \pm 0.65) \times 10^{-10} \text{ cm}^3 \text{ molecule}^{-1} \text{ s}^{-1}$.

V.3.1.4.3 Rate constant of T3H-Ol + Cl

Kinetics of Cl atom T3H-Ol was investigated using the same reference compounds as those used for C2P-Ol (THF, propan-1-ol, and octane). One experiment per reference was carried out. Figure V.40 displays the kinetic plots for the Cl reaction of T3H-Ol.

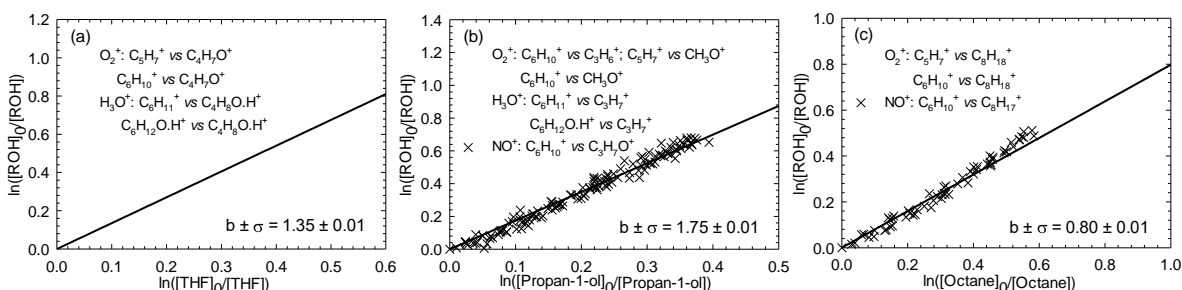


Figure V.40: Relative loss of T3H-Ol vs. that of THF (a), propan-1-ol (b), and octane (c) in the Cl atom-initiated reaction.

All the $k_{\text{Alc}}/k_{\text{Ref}}$ ratios and the corresponding rate constants for each reference compound are reported in Table V.17. The average rate constant for the Cl atom reaction with T3H-Ol at 296 K was $(3.05 \pm 0.50) \times 10^{-10} \text{ cm}^3 \text{ molecule}^{-1} \text{ s}^{-1}$.

V.3.1.4.4 Rate constant of C3H-Ol + Cl

Kinetics of Cl atom C3H-Ol was investigated using the same reference compounds as in C2P-Ol (THF, propan-1-ol, and octane). One experiment per reference was carried out. Figure V.41 displays the kinetic plots for the Cl reaction of C3H-Ol.

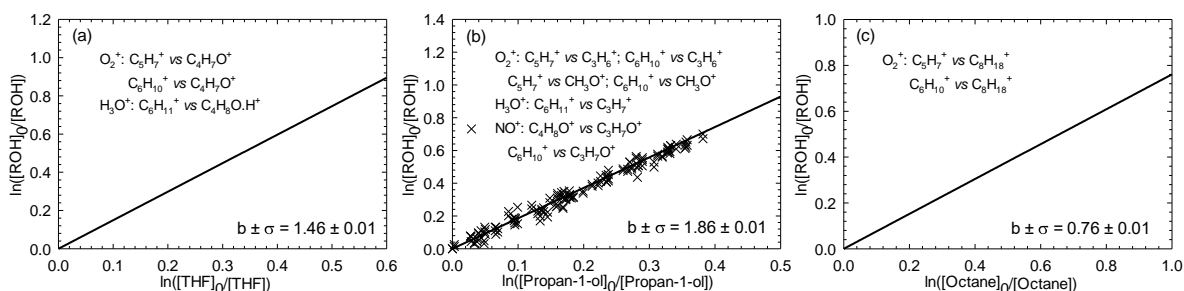


Figure V.41: Relative loss of C3H-Ol vs. that of THF (a), propan-1-ol (b), and octane (c) in the Cl atom-initiated reaction.

All the k_{Alc}/k_{Ref} ratios and the corresponding rate constants for each reference compound are reported in Table V.17. The average rate constant for the Cl atom reaction with C3H-Ol at 296 K was $(3.15 \pm 0.58) \times 10^{-10} \text{ cm}^3 \text{ molecule}^{-1} \text{ s}^{-1}$.

V.3.1.4.5 Rate constant of 10-3-Ol + Cl

Six experiments were carried out for 10-3-Ol (two experiments for each reference compound used in the present study). Figure V.42 displays the kinetic plots corresponding to the performed experiments.

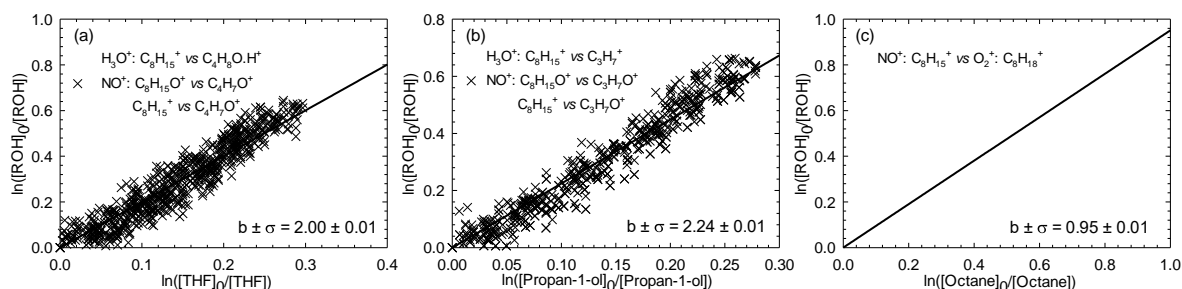


Figure V.42: Relative loss of 10-3-Ol vs. that of THF (a), propan-1-ol (b), and octane (c) in the Cl atom-initiated reaction.

All the k_{Alc}/k_{Ref} ratios and the corresponding rate constants for each reference compound are reported in Table V.17.

The average rate constant for the Cl atom reaction with 10-3-Ol at 296 K was $(4.03 \pm 0.77) \times 10^{-10} \text{ cm}^3 \text{ molecule}^{-1} \text{ s}^{-1}$. The obtained rate constants ($10^{-10} \text{ cm}^3 \text{ molecule}^{-1} \text{ s}^{-1}$) are summarized in Table V.17.

Table V.17: Summary of all the rate constants for alcohols' reactions with Cl atoms (all rate constants are expressed in $10^{-10} \text{ cm}^3 \text{ molecule}^{-1} \text{ s}^{-1}$).

Compound	Reference Compound						k _{average}
	THF		Propan-1-ol		Octane		
	$\frac{k_{\text{Alc}}}{k_{\text{Ref}}}$	k _{Alc}	$\frac{k_{\text{Alc}}}{k_{\text{Ref}}}$	k _{Alc}	$\frac{k_{\text{Alc}}}{k_{\text{Ref}}}$	k _{Alc}	
C2P-Ol	1.27±0.01	3.04±0.75	1.90±0.02	3.04±0.17	0.74±0.01	2.89±0.51	2.99±0.53
T2H-Ol	1.65±0.01	3.94±0.96	1.97±0.01	3.15±0.15	0.80±0.01	3.13±0.54	3.41±0.65
T3H-Ol	1.35±0.01	3.23±0.79	1.75±0.01	2.80±0.14	0.80±0.01	3.13±0.62	3.05±0.59
C3H-Ol	1.46±0.01	3.49±0.86	1.86±0.01	2.98±0.15	0.76±0.01	2.97±0.52	3.15±0.58
10-3-Ol	2.00±0.01	4.78±1.16	2.24±0.01	3.58±0.17	0.95±0.01	3.71±0.64	4.03±0.77

V.3.1.5 Discussion

The relative rate plots show very good linearity with zero intercepts, indicating the absence of secondary reactions. Use of the known reference rate constants k_{Ref} allows k_{Alc} to be determined for each investigated reaction.

V.3.1.5.1 Comparison with literature data

Table V.18 listed a synthesis of all the known rate constants of unsaturated alcohol + Cl from C₃ to C₈. The comparison of these data could help to better understand the relationships between molecular structure and rate constants.

Table V.18: Rate constants for Cl atoms' reactions with unsaturated alcohols at 298 K and atmospheric pressure.

Compound Linear formula	$k \times 10^{-10} /$ $\text{cm}^3 \text{ molecule}^{-1} \text{ s}^{-1}$	Reference
2-propen-1-ol ($\text{CH}_2=\text{CH}-\text{CH}_2\text{OH}$)	1.72 ± 0.19	Finlayson-Pitts and Pitts Jr, 1999
2-methyl-2-propen-1-ol ($\text{CH}_2=\text{C}(\text{CH}_3)\text{CH}_2\text{OH}$)	2.17 ± 0.39	Rodríguez et al., 2007
2-buten-1-ol ($\text{CH}_3\text{CH}=\text{CHCH}_2\text{OH}$)	3.12 ± 0.64	Rodríguez et al., 2007
	3.90 ± 0.35	Wayne et al., 1990
3-buten-1-ol ($\text{CH}_2=\text{CHCH}_2\text{CH}_2\text{OH}$)	2.63 ± 0.25	Wayne et al., 1990
3-buten-2-ol ($\text{CH}_2=\text{CHCH}(\text{OH})\text{CH}_3$)	1.44 ± 0.17	Finlayson-Pitts and Pitts Jr, 1999
1-penten-3-ol ($\text{CH}_2=\text{CHCH}(\text{OH})\text{CH}_2\text{CH}_3$)	2.35 ± 0.31	Rodríguez et al., 2010
Cis-2-Penten-1-Ol (C2P-Ol) $\text{CH}_3\text{CH}_2\text{CH}=\text{CHCH}_2\text{OH}$	3.00 ± 0.49	Rodríguez et al., 2010
	2.99 ± 0.53	This work
Trans-2-Hexen-1-Ol (T2H-Ol) $\text{CH}_3\text{CH}_2\text{CH}_2\text{CH}=\text{CHCH}_2\text{OH}$	3.49 ± 0.82	Gibilisco et al., 2014
	3.41 ± 0.65	This work
Trans-3-Hexen-1-Ol (T3H-Ol) $\text{CH}_3\text{CH}_2\text{CH}=\text{CHCH}_2\text{CH}_2\text{OH}$	3.42 ± 0.79	Gibilisco et al., 2014
	3.05 ± 0.50	This work
Cis-3-Hexen-1-Ol (C3H-Ol) $\text{CH}_3\text{CH}_2\text{CH}=\text{CHCH}_2\text{CH}_2\text{OH}$	2.94 ± 0.72	Gibilisco et al., 2014
	3.15 ± 0.58	This work
Cis-3-Hepten-1-Ol $\text{CH}_3\text{CH}_2\text{CH}_2\text{CH}=\text{CHCH}_2\text{CH}_2\text{OH}$	3.80 ± 0.86	Gibilisco et al., 2014
Cis-3-Octen-1-Ol $\text{CH}_3\text{CH}_2\text{CH}_2\text{CH}_2\text{CH}=\text{CHCH}_2\text{CH}_2\text{OH}$	4.13 ± 0.68	Gibilisco et al., 2014
1-Octen-3-Ol (10-3-Ol) $\text{CH}_2=\text{CHCH}_2\text{CH}_2\text{CH}_2\text{CH}(\text{OH})\text{CH}_2\text{CH}_3$	4.03 ± 0.77	This work

The C2P-Ol and Cl atom reaction, Rodríguez et al., 2010 reported a constant rate value determined by the relative-rate kinetic method with CCl_3COCl as the Cl atom precursor. In this study, octane, propene, and cyclohexane were used as reference compounds. The average value between the three determinations of Rodríguez et al., 2010 was $3.00 \times 10^{-10} \text{ cm}^3 \text{ molecule}^{-1} \text{ s}^{-1}$. This value is in excellent agreement with the value determined in the present study ($2.99 \times 10^{-10} \text{ cm}^3 \text{ molecule}^{-1} \text{ s}^{-1}$). A series of reactions between Cl atoms and several unsaturated alcohols was investigated by Gibilisco et al., 2014 using the relative method (the used reference compounds were isobutene and 1-butene) and Cl_2 source of Cl atoms. The three studied hexenols in the present research were also studied by Gibilisco et al., The obtained rate constants are in good agreement with Gibilisco et al., 2014, with the relative differences between our determinations and Gibilisco et al.,'s determinations being of the order of 11% or less for all hexenols. For 10-3-Ol, no other measurements are available in the literature.

V.3.1.5.2 Effect of the chain length

For a group of alcohols with the alcohol function located on the first carbon atom (alken-1-ol) and a C=C bond placed at the second or third carbon atom, data are presented in Figure V.43 for comparison purposes.

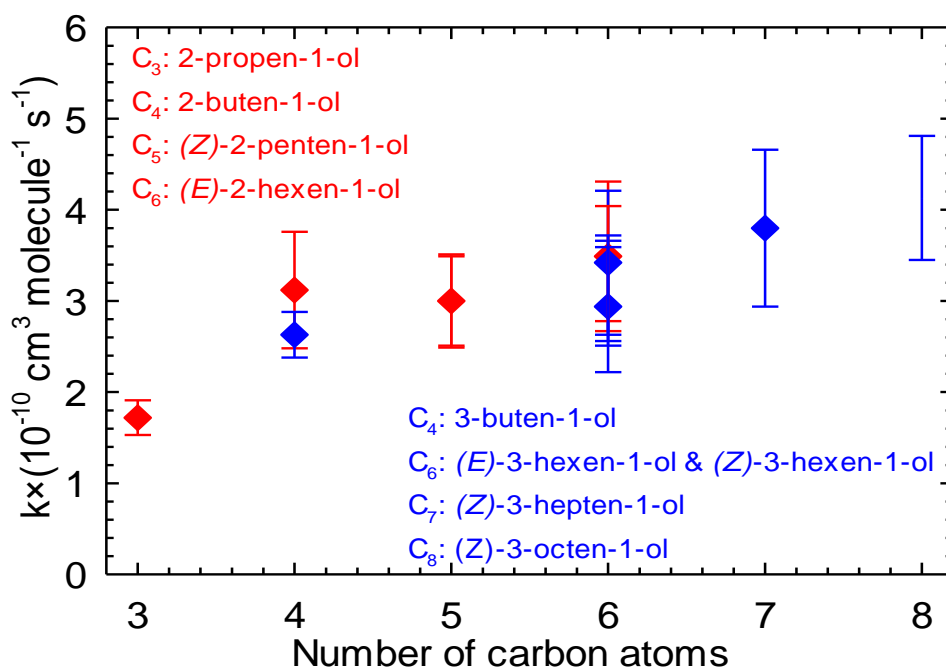


Figure V.43: Rate constants of the reaction of Cl atoms with 2-alken-1-ols (red) and 3-alken-1-ols (blue) vs. the number of carbon atoms (the open circles represent the values of the current study).

Considering the series of 2-alken-1-ols (red) with 2-propen-1-ol (Rodríguez et al. 2007), 2-buten-1-ol (Rodríguez et al., 2008), C2P-Ol (Rodríguez et al., 2010, and this work), and T2H-Ol (Gibilisco et al., 2014, and this work), the increase in chain length seems to lead to higher rate constants. A similar trend is also observable for the reaction of Cl with the series of 3-alken-1-ols (blue), namely: 3-buten-1-ol (Liang et al., 2011), T3H-Ol, C3H-Ol (Gibilisco et al., 2014, and this work), cis-3-hepten-1-ol, and cis-3-octen-1-ol (Gibilisco et al., 2014). The activation effect of the chain length on the rate constants was also observed in previous works for the reaction of Cl atoms with linear alcohols (Nelson et al., 1990) and alkenes (Ezell et al., 2002, Atkinson and Aschmann, 1985, Coquet and Ariya, 2000, Walavalkar et al., 2013).

V.3.1.5.3 Effect of the OH group

To better understand the OH group's role in the unsaturated alcohol chains, the rate constants for the reaction of the studied unsaturated alcohols with Cl atoms were compared to the rate constants of their corresponding alkenes reaction with Cl atoms. Table V.19 lists the rate constants for Cl atoms' reactions with a series of alkenes, i.e., propene, 1-butene, 1-pentene, cis-3-hexene, and 1-octene.

Table V.19: Rate constants for Cl atoms' reactions with alkenes at 298 K and atmospheric pressure.

Compound	$k \times 10^{-10} / \text{cm}^3 \text{ molecule}^{-1} \text{ s}^{-1}$	Reference
propene	2.70 ± 0.40	Coquet and Ariya, 2000
1-butene	3.52 ± 0.07	Nelson et al., 1990
1-pentene	3.97 ± 0.36	Ezell et al., 2002
(Z)-3-hexene	4.13 ± 0.51	Anderson et al., 2007b
1-octene	5.50 ± 0.90	Atkinson and Aschmann, 1985

To see the differences between the rate constant of Cl atoms with the studied alkenols and their corresponding alkenes, I plotted the rate constants for their Cl-reaction vs. the number of carbon atoms (Figure V.44).

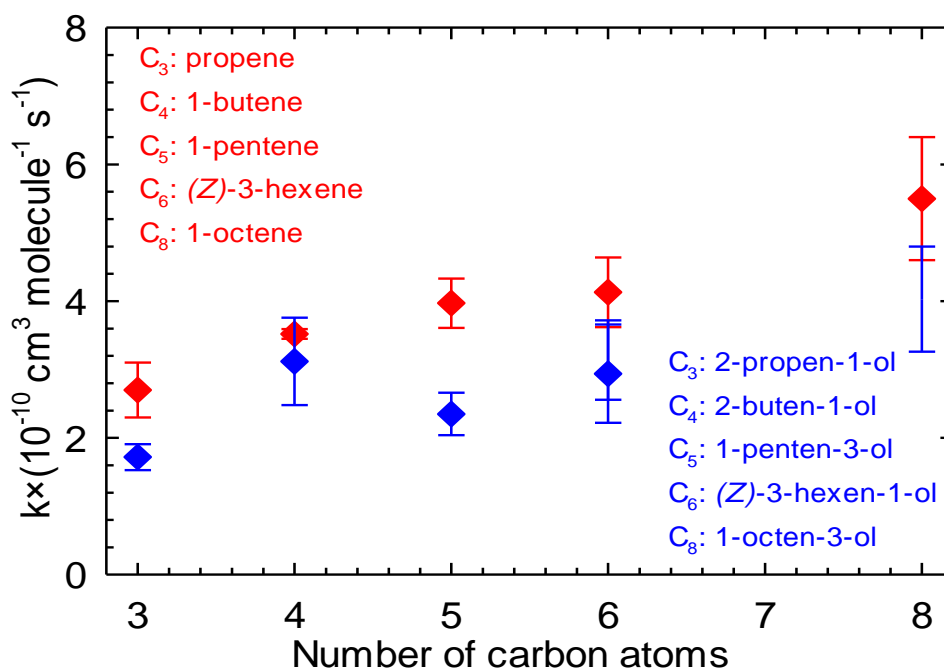


Figure V.44: The rate constant of the reaction of Cl atoms with a series of alkenes (red) and alken-1-ols (blue) vs. the number of carbon atoms (the open circles represent the values of the current study).

As shown in Figure V.44, the rate constants for Cl atoms' reactions with alkenes are higher than the rate constants for Cl atoms' reactions with alkenols. Here, the present work data also prove that the hydroxyl group's presence in the molecular structure has a deactivating effect on unsaturated alcohols' kinetics with Cl atoms through a negative inductive influence.

Moreover, Gibilisco et al., 2014 suggested a stronger deactivating effect of the OH group for α -alkenols than β -alkenols based on literature data. The present results do not confirm this assumption, probably because the measured rate constants are close to the collision rate. Finally, it can be underlined that an activating effect of the OH group was observed for OH radical addition to alkenols (Papagni et al., 2001), suggesting different reaction mechanisms.

The reactions between unsaturated VOCs and Cl atoms proceed mainly via the addition to the double bond to produce a chlorine-containing alkyl radical. Addition occurs preferably on the least substituted carbon, thus forming the most stable radical (Wayne et al., 1990). This chlorinated alkyl radical adds O₂ to form a chlorinated peroxy radical whose further reactions lead to oxygenated chlorine-containing compounds (Finlayson-Pitts and Pitts Jr, 1999). A second pathway is the abstraction of the allylic hydrogen from the C–H bond. For example, very recent work showed that the reaction of (Z)-3-hexene proceeds via both Cl atom addition and hydrogen abstraction with branching ratios of around 70% and 30%, respectively (Barbosa et al., 2017).

V.4 Conclusion

In the first part of this chapter, we investigated the reactions between three structurally similar unsaturated aldehydes, including T2P, T2H, and T2Hep and Cl atoms in terms of kinetics, products, and SOA formations. This work was carried out in collaboration with UCLM University. Investigations were performed in a D-ASC, 16L-ASC, and CR-ASC at 296 ± 2 K and 740 ± 20 Torr of zero air. The relative-rate kinetic approach was used to determine rate constant values of the target unsaturated aldehydes with Cl atoms using an FTIR spectrometer, SPME/GC-MS, and PTR-ToF-MS to control both reagents and products. The rate constant values determined in the present work are higher than the literature data (Rodríguez et al., 2005).

The source of these differences remains unclear. The degradation mechanism of each reaction has been proposed based on the analysis results of the gas-phase products. Particle formation was measured for the C₅-C₇ unsaturated aldehydes, and SOA yields were determined for the first time. Those results were divided into three publications. The first article, entitled “An experimental study of the gas-phase reaction between Cl atoms and trans-2-pentenal: kinetics, products, and SOA formation”, have been submitted to “Chemosphere”. Two other articles, entitled “An experimental study of the gas-phase reaction between Cl atoms and trans-2-hexenal: kinetics, products, and SOA formation” and “An experimental study of the gas-phase reaction between Cl atoms and trans-2-hexenal: kinetics, products, and SOA formation”, are in preparation.

In the second part of the present chapter, the Cl-initiated reactions with five structurally similar unsaturated alcohols, including C2P-Ol, T2H-Ol, T3H-Ol, C3H-Ol, and 10-3-Ol, were investigated. Investigations were performed in a 600-L Teflon reaction chamber at 296 ± 2 K and 1 atm zero air.

The relative-rate kinetic approach was used to determine the rate constant values of the target unsaturated alcohols with Cl atoms using SIFT-MS. The constant rate values determined in the present work agree with literature data within the experimental error limits. For the first time, the present work reports the rate of a constant value for the reaction between 10-3-Ol and Cl atoms.

VI Chapter VI: Oxidation of unsaturated aldehydes: reaction with OH

VI.1 Introduction

This chapter aims to investigate the reaction between C₅-C₆ unsaturated aldehydes (Trans-2-Pentenal (T2P), Trans-2-Hexenal (T2H)) through hydroxyl radicals (OH). OH radical is considered the essential oxidant in Earth's lower atmosphere and the tropospheric detergent (Thompson, 1992).

The first part of this chapter is dedicated to T2P and OH radical reaction's kinetic study at 296 ± 2 K and different pressures (7 – 471 Torr). These experiments were done using the Cryocell system, coupled to the Pulsed Laser Photolysis-Laser Induced Fluorescence (PLP-LIF) technique (IPR, Université de Rennes). The rate is constant of the T2P + OH reaction was determined experimentally in two previous works (Albaladejo et al., 2002) Davis et al., 2007) with a difference of about 45%. Two other works (Grosjean and Williams, 1992, Upendra et al., 2012) obtained the rate constant of T2P + OH reaction by theoretical calculations based on the Structure-Activity Relationship (SAR) method. For Grosjean and Williams, the value was situated between Albaladejo et al. and Davis et al. values. However, Upendra et al.'s values were the lowest one. Table VI.1 displayed a summary of the rate constants, experimental conditions, and analytical techniques used in previous works for studying the kinetic of T2P + OH reaction at 298 K.

Table VI.1: Summary of the rate constants, experimental conditions, and analytical techniques used in previous works for studying the kinetic of T2P + OH reaction at 298 K.

Reaction	P _T / Torr	k × 10 ¹¹ / cm ³ molecule ⁻¹ s ⁻¹	Analytical technique	Reference
T2P + OH	760	2.90	Estimated	Grosjean and Williams, 1992
	100 – 400	2.35 ± 0.32	PLP-LIF	Albaladejo et al., 2002
	23 – 150	4.30 ± 0.6	PLP-LIF	Davis et al., 2007
	760	1.64	Estimated	Upendra et al., 2012

Since the literature data were scattered, the present work provided an additional value of the rate constant of T2P + OH reaction in a larger pressure range (7 – 471 Torr). This work helps to reduce the observed dispersion between literature data.

Experiments on the temperature dependence of the rate constant for the reaction of T2P + OH over the temperature range 254 – 323 K are in progress. Those experimental results will be published later, together with theoretical calculation of the rate constant of the reaction T2P+OH, done at the Bharathiar University in India. The gas-phase products and the SOA formation of two unsaturated aldehydes (T2P and T2H) with hydroxyl radicals (OH) were studied in QUAREC-ASC (Wuppertal University) at 296 ± 2 K and 740 ± 20 Torr. As far as we know, this work displayed the first data on mechanistic and particle-phase studies. I mention that for the products and SOAs formation, only preliminary results were presented in this chapter since experiments and analyses are still in progress.

VI.2 Oxidation of unsaturated aldehydes with OH

VI.2.1 Determination of rate constant

VI.2.1.1 Experimental conditions and protocols

The rate constant of the T2P + OH reaction was measured at 296 ± 2 K and over the pressure range 7.4 – 471 Torr using the absolute method under the pseudo-first-order conditions ($[T2P]_0 \gg [OH]_0$). Experiments were carried out in the Cryocell system using the PLP-LIF detection of OH. A detailed description of the experimental set-up and the PLP-LIF instrument was displayed in section II.3.1.1.2. A summary of the photolysis and the detection laser characteristics is presented in Table VI.2.

Table VI.2: Summary of the laser characteristics used in the kinetic measurement of T2P and OH reaction.

Parameter	Photolysis laser	Probe laser
Wavelength	266 nm	282 nm
Beam diameter	8 mm	4 mm
Divergence	< 0.5 mrad	< 0.5 mrad
Fluence	5 – 40 mJ cm ⁻² pulse ⁻¹	1.5 – 2.5 mJ cm ⁻² pulse ⁻¹
Pulse duration (min)	10 ns	10 ns
Pulse repetition rate (max)	10 Hz	10 Hz

The hydroxyl radicals were produced by the 266 nm photolysis of hydrogen peroxide (H_2O_2) using the pulsed output of a Nd: YAG (continuum surelite) (R.1).



Vapors of T2P and H_2O_2 were introduced into the Cryocell in conjugation with the buffer gas (argon) by bubbling a small flow of argon through glass tubes containing T2P and H_2O_2 and controlled with pressure gauges (see section II.2.2.2.2). The injected flows are evacuated at the outlet of the Cryocell using a primary pump ($16 \text{ m}^3 \text{ h}^{-1}$). At the inlet of the latter, a control valve is fixed to regulate the total pressure. Because both reagents (T2P and H_2O_2) are liquid in the standard conditions, the knowledge of its saturated vapor pressure at the experiment's temperature is mandatory. The saturated vapor pressure of T2P at 298 K was calculated in section III.2.1 ($P_{\text{v,T2P}}^{\text{sat}} = 12.67 \text{ Torr}$). Table VI.3 displayed the Antoine coefficients used to calculate the saturated vapor pressure of H_2O_2 at 298 K.

Table VI.3: Antoine coefficients were used to calculate the saturated vapor pressure of H_2O_2 at 298 K (Yaws, 2015).

Compound	T / °C	$\log_{10} P(\text{Torr}) = A - B/[C+T(^{\circ}\text{C})]$			Range of T / °C	P / Torr
		A	B	C		
H_2O_2	25	8.07489	1958.1824	226.8	[-0.41 ; 457]	1.99

The concentrations of T2P and H_2O_2 were calculated as explained in section II.2.2.2.2 whereas, OH concentration (molecule cm^{-3}) was estimated using (Eq.1).

$$[\text{OH}] = \frac{[\text{H}_2\text{O}_2] \times \Phi \times \sigma \times F \times \lambda}{h \times C} \quad (\text{Eq.1})$$

where $[\text{H}_2\text{O}_2]$ is the concentration of H_2O_2 (molecule cm^{-3}), Φ is the quantum yield and equal to 2 in (R.1) (molecule), σ is the absorption cross-section of H_2O_2 at 265 nm ($4.2 \times 10^{-20} \text{ cm}^2 \text{ molecule}^{-1}$) (DeMore et al., 1985), F is the fluence of the photolysis laser (in J cm^{-2}), λ is the photolysis wavelength and equal to 266 nm ($2.66 \times 10^{-5} \text{ cm}^{-1}$), h is the Planck's constant ($6.62 \times 10^{-34} \text{ J s}$), C is the speed of light in vacuum and equal to 3×10^8

m s^{-1} ($3 \times 10^{10} \text{ cm s}^{-1}$). A summary of T2P, H_2O_2 , and OH's initial concentrations for kinetic measurements of T2P and OH radicals' reaction is presented in Table VI.4.

Table VI.4: Summary of the initial concentrations used for kinetic measurements of T2P and OH radical reaction at room temperature and (7 – 471 Torr) of pressure.

Reagent	Concentration / molecule cm^{-3}
T2P	$(0.6 - 4.1) \times 10^{15}$
H_2O_2	$(1.2 - 478) \times 10^{14}$
OH	$(5.3 - 21.1) \times 10^{11}$

The used carrier gas Argon (99.999%, Air Liquide) was used without further purification. The reagents employed in this work were obtained from the following sources: T2P ($\geq 95\%$, Sigma-Aldrich) and H_2O_2 (50% in water, Sigma-Aldrich). H_2O_2 was concentrated by bubbling argon through the solution to remove water for several days before use and constantly during experiments.

VI.2.1.2 Results

As already mentioned, kinetic decays were observed by recording the LIF signal variation as a function of the time delay between the pulses from the photolysis and probe lasers. Figure VI.1 shows the OH temporal profile measured at room temperature and under a total pressure of 7.4 Torr.

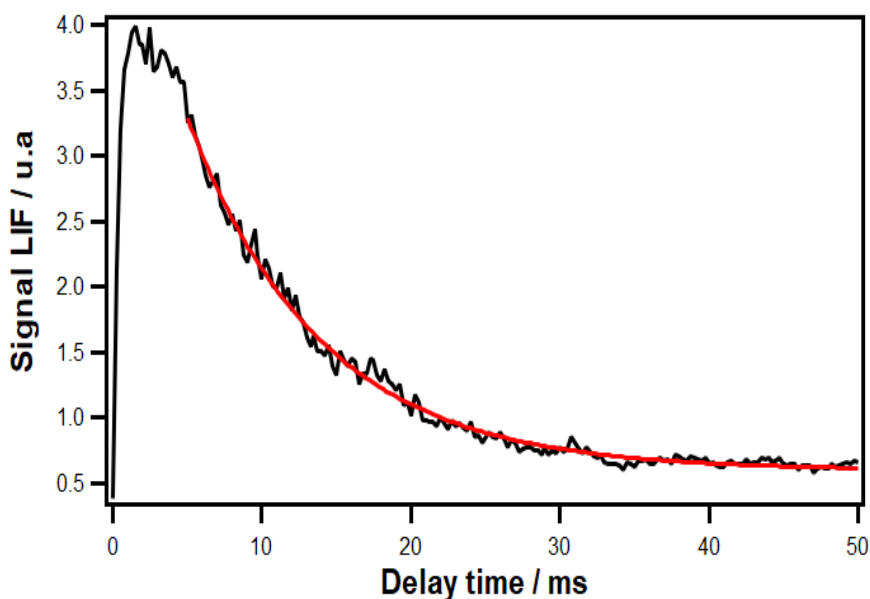


Figure VI.1: Example of OH's temporal LIF signal obtained at 298 K and 7.4 Torr, $[\text{OH}]_0 = 5.4 \times 10^{11} \text{ radical cm}^{-3}$, $[\text{T2P}]_0 = 6.5 \times 10^{14} \text{ molecule cm}^{-3}$, carrier gas: Ar. The red curve represents an exponential fit of the decaying LIF signal.

The good exponential fit suggests that OH secondary reactions were negligible. The profile was fitted to exponential function leading to the extraction of pseudo-first-order rate constant (k') as explained in section II.4.1.2.1. The bimolecular rate constant (k) was then obtained by plotting the pseudo-first-order decay constant (k') as a function of the aldehyde concentration, as shown in Figure VI.2.

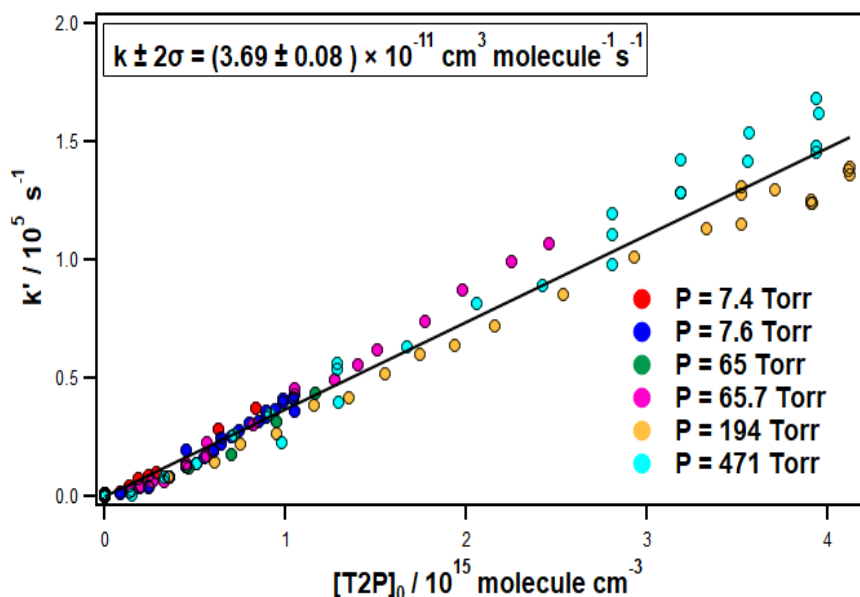


Figure VI.2: Pseudo-first-rate constant, k' , versus the initial concentration of the unsaturated aldehyde $[T2P]_0$ at 298 K and different pressures ranging from 7.4 to 471 Torr. Uncertainty is twice the statistical standard deviation ($\pm 2\sigma$).

As shown in Figure VI.2, a straight line was obtained with intercept close to the value of k' obtained in the absence of T2P ($k_0 = 300 - 600 \text{ s}^{-1}$). Statistical errors result from a least-squares analysis of the pseudo-first-order rate constant $\ln([OH]_0/[OH])$ vs. delay time ($\Delta(\text{stat}) = 2.2\%$). Systematic errors are mainly due to the difficulties in handling and measuring the concentrations of T2P with accuracy due to its vapor pressure and impurities ($\Delta(\text{syst}) = 10\%$). The overall error on the rate constant (Δk) was calculated as explained in section II.4.1.2.1, and found to be 10.2%. Therefore, the reaction T2P + OH's determined rate constant is $(3.69 \pm 0.38) \times 10^{-11} \text{ cm}^3 \text{ molecule}^{-1} \text{ s}^{-1}$. As can be seen, no pressure dependence of the measured rate constant was observed in the range of pressure (7.4 – 471 Torr).

The lack of pressure dependence may indicate that this OH radical reaction proceeds mainly by H-atom abstraction from the acetyl group ($-\text{CHO}$) since the OH addition reaction on the $\text{C}=\text{C}$ double bond is expected to be pressure-dependent. Consistently, (Atkinson, 1986) suggests that the carbonyl group ($-\text{CHO}$) can deactivate the double bond ($\text{C}=\text{C}$).

On the other hand, this result may also indicate that the high-pressure limit for the addition to the double bond is already reached at a pressure lower than 7 Torr of Argon.

VI.2.1.3 Discussion

a) Comparison with literature data

A comparison of the OH rate constant at 298 K obtained in this work with previous studies for C₃-C₇ unsaturated aldehydes is presented in Table VI.5. As it can be seen, the results obtained for T2P is in reasonable agreement (difference are lower than 21%) with those previously reported in literature experimentally by absolute method (Davis et al., 2007) and theoretically using structure-activity relationships (SAR) (Grosjean and Williams, 1992). However, the determined values in (Albaladejo et al., 2002) and (Upendra et al., 2012) were lower than the determined value in this work by 36% and 56%. A systematic error can be claimed here since Albaladejo et al.'s measurements of the rate constants of C₅-C₇ unsaturated aldehydes (T2P, T2H, and T2Hep) and OH radicals are lower than Davis et al.'s determination by 54%, 67%, and 56%, respectively. More specifically, four literature data of the rate constant of T2H and OH radical (Grosjean and Williams 1992, (Atkinson et al., 1995, Jiménez et al., 2007, Gao et al., 2009) are in good agreement with Davis et al.'s value. A factor of 2 was also observed for T2Hep and OH's rate constant between Davis et al., 2007 and Albaladejo et al., 2002 values.

Table VI.5: Summary of rate constants for the reaction of a series of C₃-C₇ unsaturated aldehydes with OH radicals at 298 K.

Compound Linear structure	$k \times 10^{11} /$ $\text{cm}^3 \text{ molecule}^{-1} \text{ s}^{-1}$	Reference
Acrolein (CH ₂ =CH-CHO)	2.66 ± 0.3	Maldotti et al., 1980
	1.9 ± 0.2	Kerr and Sheppard, 1981
	1.8 ± 1.3	Atkinson et al., 1983
	2.0 ± 0.1	Edney et al., 1986
	2.0 ± 0.1	Magneron et al., 2002
	5.0 ± 0.9	Aranda et al., 2003

Crotonaldehyde (CH ₃ -CH=CH-CHO)	3.3 ± 0.6	Kerr and Sheppard, 1981
	2.8	Grosjean and Williams, 1992
	3.5 ± 0.4	Atkinson et al., 1983
	3.5 ± 0.2	Magneron et al., 2002
	3.51 ± 0.71	Albaladejo et al., 2002
Trans-2-Pentenal (T2P) (CH ₃ -CH ₂ -CH=CH-CHO)	2.90	Grosjean and Williams, 1992
	2.35 ± 0.32	Albaladejo et al., 2002
	4.30 ± 0.6	Davis et al., 2007
	1.64	Upendra et al., 2012
	3.69 ± 0.38	This work
Trans-2-Hexenal (CH ₃ -CH ₂ -CH ₂ -CH=CH-CHO)	3.10	Grosjean and Williams, 1992
	4.41	Atkinson et al., 1995
	2.95 ± 0.45	Albaladejo et al., 2002
	4.68 ± 0.50	Jiménez et al. 2007
	4.40 ± 0.65	Davis et al., 2007
	3.93 ± 0.17	Gao et al., 2009
Trans-2-Hepenal (CH ₃ -CH ₂ -CH ₂ -CH ₂ -CH=CH-CHO)	2.45 ± 0.30	Albaladejo et al., 2002
	4.40 ± 0.70	Davis et al., 2007

b) Effect of the chain length

It is difficult to see a definite trend of rate constant values of C₃-C₇ unsaturated aldehydes with OH radicals at 298 K versus the chain length seen in the data's discrepancies (Table VI.5). Further experimental mechanistic studies on this reaction and other reactions for similar aldehydes (for example, T2H) are needed to evaluate the importance of these degradation reactions in the atmosphere. In the next part, we focused particularly on the gas-phase products of the reactions between C₅-C₆ unsaturated aldehydes and OH radicals and evaluated their contribution to the total budget of SOAs formation in the atmosphere.

VI.2.2 Determination of gas-phase products and particles formation

VI.2.2.1 Experimental conditions and protocols

This part aims to identify and quantify the gas-phase products, and SOAs formed through OH's reactions with T2P and T2H at 296 ± 2 K and atmospheric pressure. OH radicals were generated by the photolysis of methyl nitrite (CH_3ONO) in the actinic region (≥ 290 nm) in the QUAREC-ASC surrounded by 32 fluorescent lamps. This reaction mechanism is explained in reactions (R.2) – (R.4).



We also added a quantity of nitric oxide (NO) to improve hydroxyl radical formation in the reaction mixture. The experimental setup starts with the injection of the unsaturated aldehyde (T2P or T2H). The possible photodegradation of the compound was tested under 32 lights for one hour. Then, the methyl nitrite (CH_3ONO) and nitric oxide (NO) are injected. The stability of the reaction mixture (aldehyde + CH_3ONO + NO) in the dark was tested for 20 min. The reaction starts when we turn on the lights for 40 to 60 minutes. The initial concentration of T2P and T2H were obtained using a calibration method described previously (Etzkorn et al., 1999). The summary of the used experimental conditions is presented in Table VI.6.

Table VI.6: Summary of the experimental conditions used in product and SOA formations studies.

Reaction	Number of experiments	Number of lamps	[Ald] / $\times 10^{13}$ molecule cm^{-3}	[CH_3ONO] / $\times 10^{13}$ molecule cm^{-3}	[NO] / $\times 10^{13}$ molecule cm^{-3}
T2P + OH	3	16 – 32	2.2 – 4.4	12.3	12.3
T2H + OH	3	32	4.2 – 6.4	6.2 – 12.3	6.2 – 12.3

The products were identified and quantified by FTIR spectroscopy, where recorded spectra were compared with references available in IR databases at the Wuppertal laboratory. To quantify the mass of SOA formed, the number particle size distributions measured by the SMPS were converted to mass particle size distributions by the instrument. The assumptions were that particles were perfect spheres with a density of 1.4 g cm^{-3} (see section V.2.3.1). I mention that SOA losses were not accounted for in this section.

VI.2.2.2 Preliminary results and discussion

The IR spectra of the reacted sample were recorded as a function of reaction time. The analysis of these experiments is in progress. For that reason, we cannot show any products or to conclude the reaction mechanisms for the studied reactions at this point. The SOA formation was observed for both studied aldehydes. SOA growth is presented below in terms of particle number and total produced mass concentration.

a) Particle number concentrations

Examples of the measured particle size distributions are shown for several reaction times with the indicated initial conditions for the reaction T2P + OH (Figure VI.3) and the reaction T2H + OH (Figure VI.4).

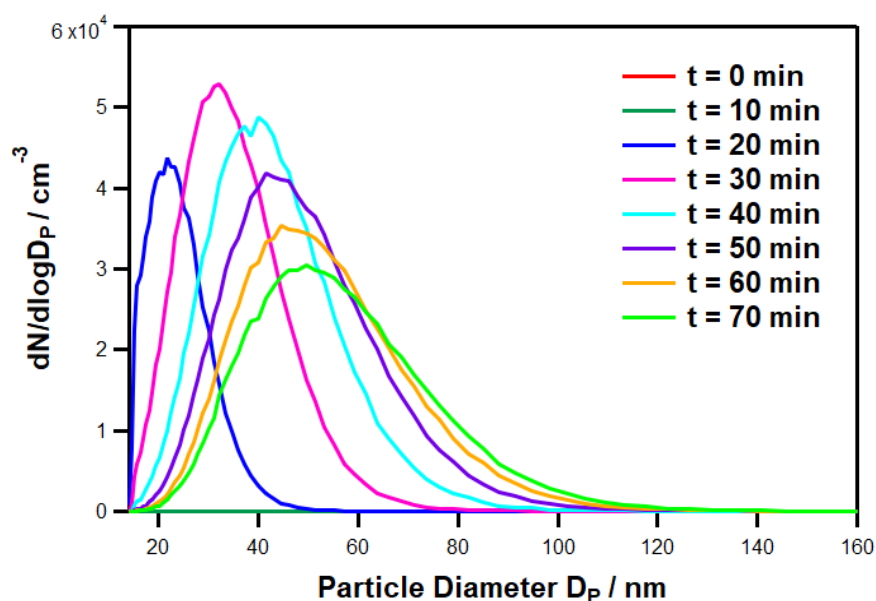


Figure VI.3: Evolution of the SOA number size distribution with reaction time (t) during the reaction between T2P and OH ($[T2P]_0 = 3.7 \times 10^{13}$ molecule cm^{-3} , $[CH_3ONO]_0 = 12.3 \times 10^{13}$ molecule cm^{-3} , $[NO]_0 = 12.3 \times 10^{13}$ molecule cm^{-3}) in QUAREC-ASC.

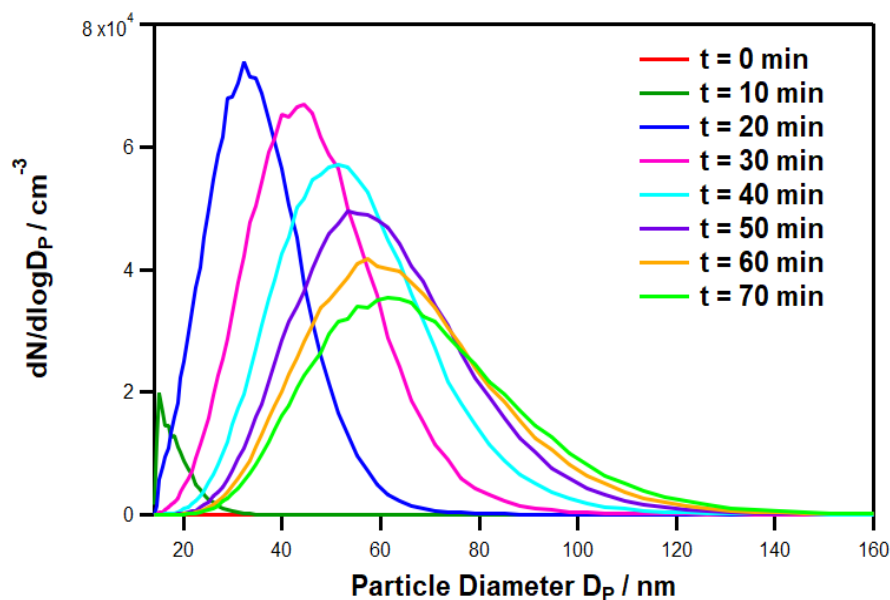


Figure VI.4: Evolution of the SOA number size distribution with reaction time (t) during the reaction between T2H and OH ($[T2H]_0 = 4.5 \times 10^{13}$ molecule cm^{-3} , $[CH_3ONO]_0 = 12.3 \times 10^{13}$ molecule cm^{-3} , $[NO]_0 = 12.3 \times 10^{13}$ molecule cm^{-3}) in QUAREC-ASC.

In Figure VI.3, after 30 min of irradiation of the mixture T2P + OH, a maximum number of particles (in terms of the normalized particle number, $dN/d\log D_p$) (5.3×10^4 particles cm^{-3}) was observed for particles with a mobility diameter centered at 31 nm. On the other hand, within 20 min of irradiation of the T2H + OH reaction mixture (Figure VI.4), the number of particles reaches a maximum (7.2×10^4 particles cm^{-3}) mobility diameter centered at 34 nm for similar experimental conditions. In both reaction systems, the number of particles decreased as their diameter slightly increased due to the condensation and the coagulation at the particles' surface.

b) Particle mass concentrations

In Figure VI.5 and Figure VI.6, I displayed the total SOA mass (M_{SOA}) versus the reaction times for the T2P + OH reaction and the T2H + OH reaction, respectively.

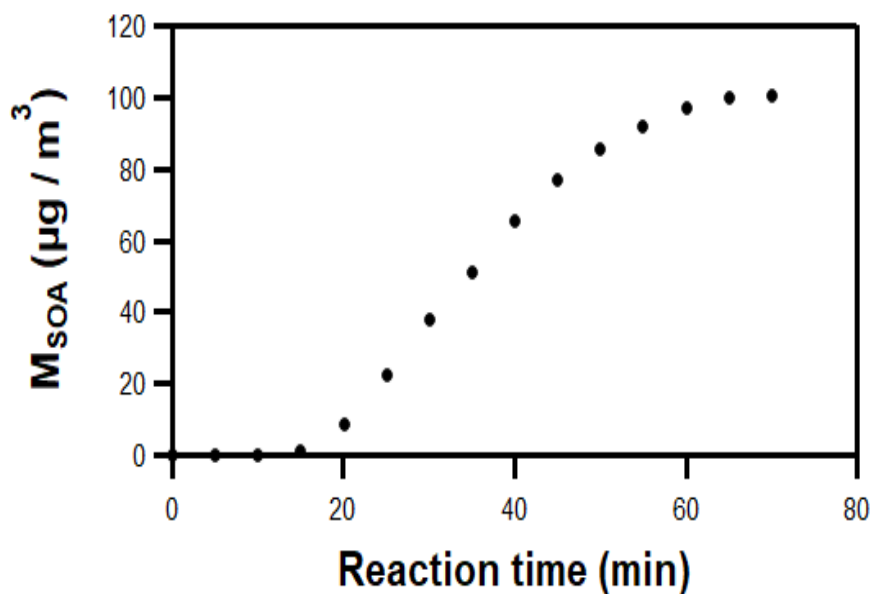


Figure VI.5: SOA formation as function of reaction time for T2P in QUAREC-ASC ($[\text{T2P}]_0 = 3.7 \times 10^{13} \text{ molecule cm}^{-3}$, $[\text{CH}_3\text{ONO}]_0 = 12.3 \times 10^{13} \text{ molecule cm}^{-3}$, $[\text{NO}]_0 = 12.3 \times 10^{13} \text{ molecule cm}^{-3}$).

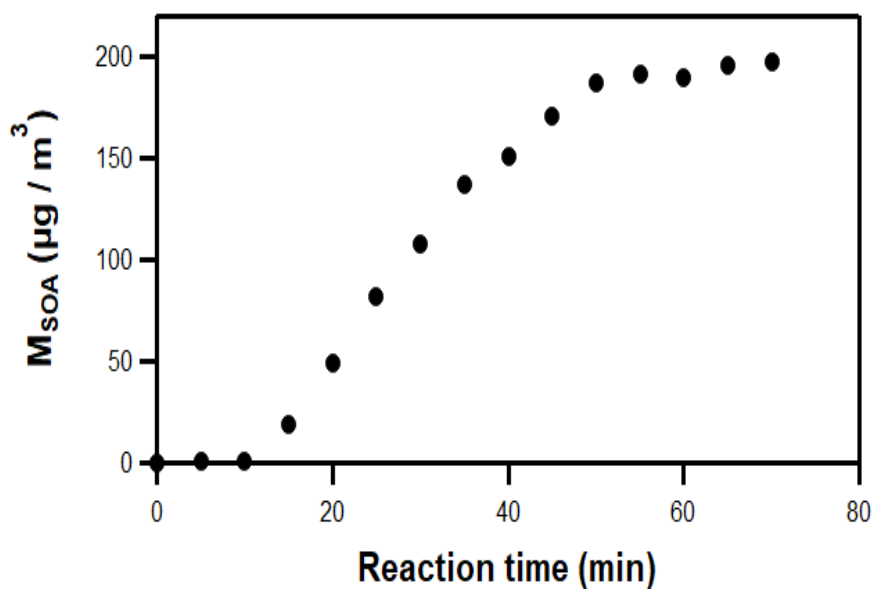


Figure VI.6: SOA formation as function of reaction time for T2H in QUAREC-ASC ($[\text{T2H}]_0 = 4.5 \times 10^{13} \text{ molecule cm}^{-3}$, $[\text{CH}_3\text{ONO}]_0 = 12.3 \times 10^{13} \text{ molecule cm}^{-3}$, $[\text{NO}]_0 = 12.3 \times 10^{13} \text{ molecule cm}^{-3}$).

As shown in Figure VI.5 and Figure VI.6, particles were formed after a certain induction time. This time is the period during which the parent VOC reacts away, but no aerosol is formed. In these experiments, the induction times were 15 min and 10 min for the T2P + OH reaction and the T2H + OH reaction, respectively. Kroll et al., 2007 explained that the parent VOC's oxidation produces semi-volatile species in the gas phase but cannot be identified. These species can undergo two processes: (i) reaction to form other gas-phase species or (ii) partitioning to the particle phase. The competition between these two processes leads to longer or shorter induction periods.

SOA mass concentrations reach a plateau after roughly one hour of reaction time. Comparing the amount of particle formation between both studied reactions suggests that at similar experimental conditions: the T2H + OH reaction generates 2 times higher total SOA masses than the T2P + OH reaction after 70 min of reaction time. As I mentioned above, we did only three experiments for each studied reaction. Therefore, up to now, we cannot determine the SOA yields as it was done for similar reactions with chlorine atoms (see chapter IV and chapter V).

VI.3 Conclusion

In this chapter, I presented the kinetic measurement of the rate constant of T2P and OH radical reaction using the absolute method via the PLP-LIF coupled to the Cryocell (IPR) at the pressure range between 7.4 and 471 Torr. Other experiments regarding the temperature dependence of rate constant for the same reaction are in progress. Besides, the investigation of the gas-phase products and SOA formation for T2P and T2H reaction with OH radicals were done at Wuppertal University. Complementary experiments and analyses are also in progress.

Summary and Future work

Thesis objectives

The current Ph.D. thesis falls within the general framework of understanding the atmospheric pollution produced by the oxygenated BVOC oxidations through laboratory experiments. This work investigates two aspects: the first concerns the study of gas-phase reactions of BVOCs through atmospheric oxidants (O_3 , Cl atoms and OH radicals), and the second concerns the study of the SOA formations from these reactions. This work aims to provide data that can enrich atmospheric models established to facilitate understanding of the physicochemical phenomena occurring in the atmosphere and assess their current and future impacts on air quality, human health and the climate system.

Thesis approach

This work concentrates practically on a series of unsaturated aldehydes and alcohols ($\geq C_5$). The following methodology was followed for each reaction system BVOC + Oxidant: (i) determination of IR and UV spectrum (only for aldehydes), (ii) determination of the rate constant at room temperature, (iii) identification and quantification of the gas-phase products, (iv) determination of the SOA yields.

To achieve these objectives, several experimental set-ups have been used. Six static (ASC) and two dynamic (flow) reactors, which were coupled to various analytical techniques either for the analysis of the gas-phase (FTIR, GC-FID/MS, SPME-GC/MS, Carbotrap-GC/MS, DNPH-HPLC/UV, PTR-ToF-MS, SIFT-MS, PLP-LIF) or the particle-phase (SMPS, FMPS). IR absorption cross-sections were determined using an FTIR spectrometer coupled to a 96-m Pyrex cell and an N_2 -cooled MCT detector. Besides, UV absorption cross-sections were investigated using a 107-cm absorption cell irradiated by a deuterium lamp.

Thesis contribution to the current state of knowledge and future work

➤ *IR and UV absorption cross-sections*

The first part deals with IR measurements ($650 - 4000 \text{ cm}^{-1}$) and UV measurements ($270 - 410 \text{ nm}$) of T2P, T2H and T2Hep absorption cross-sections (σ) as function of wavelengths.

The record of the three studied aldehydes IR spectra aims quantifying their concentrations accurately during their oxidation studies. As far as we know, the IR absorption cross-sections of these three aldehydes have never been determined before.

UV absorption cross-sections have provided insight into the photochemistry and allowed to estimate the photolysis atmospheric lifetimes. The UV spectra show a broad absorption band between 320 and 340 nm corresponding to the $n-\pi^*$ transition of the carbonyl group (C=O), linked to the possible photodissociation of 2-alkenals beyond 290 nm. The determined UV cross-sections for T2P and T2H are consistent with literature data. However, no previous determination of the T2Hep UV absorption cross-section was found in literature data. The influence of the double bond in conjugation for $\text{C}_3\text{-C}_7$ unsaturated aldehydes was studied through the comparison of their UV absorption cross-sections to their saturated homologous aldehydes. A bathochromic shift was observed between the two series of compounds. The C=C double bond conjugation can explain this shift with the C=O group leading to an easier excitation of the n and π electrons of the molecule.

Besides, photolysis rate constants $J(z, \theta)$ of the unsaturated aldehydes in the actinic region at a zenith angle ($\theta = 20^\circ$) and altitude ($z = 0 \text{ Km}$) were calculated at 298 K using quantum yields (Φ) of 100%. This yield gives the highest limit of their photolysis rates and then, the lowest limit for their photolysis lifetime ($\tau_{2\text{-alkenals}} < 1 \text{ hour}$). More investigations are required to assess more accurately the photolysis processes under atmospheric conditions. Moreover, as temperature decreases with altitude in the troposphere, the T -dependent contribution could modify the estimated photolysis rate constants at high latitudes, requiring additional investigations on Φ and σ .

➤ *Kinetic studies*

This work provides experimental measurements of the rate constants of three C₅-C₇ unsaturated aldehydes and six C₅-C₈ unsaturated alcohols with ozone, Cl atoms and OH radicals. The determined rate constants were consistent with literature data considering the reported uncertainties. They complete the kinetic databases and furnish accurate atmospheric lifetimes for the studied oxidation reactions. Kinetic rate constants were obtained using both the absolute method (for O₃- and OH-oxidation reactions) and the relative method (for Cl- oxidation reactions).

Those data allowed us to calculate the oxidation lifetimes. Indeed, the lifetimes of both alkenals and alkenols with OH and Cl (at high concentration = 10⁵ atom cm⁻³) and alkenols with O₃ and NO₃ were about a few hours. However, the lifetimes of both alkenals and alkenols with Cl atoms (at low concentration = 10³ atom cm⁻³) and alkenals with O₃ and NO₃ were about a few days.

The determination of rate constants for the oxidation reactions for oxygenated BVOCs also allowed their SAR assessment. The increases in the chain length of alkenals and alkenols show an activating effect on their oxidation reactions towards O₃ and Cl. Also, the substitution degree increases seem to have a positive effect on the reactivity of the studied BVOCs + Cl. I mention that the carbonyl group C=O and the hydroxyl group OH have a deactivating effect on the reactivity of both alkenals and alkenols with O₃ and Cl. Finally, the short distance between the double bond and the hydroxyl radical shows an activating effect on alkenols' reactivity with O₃ and Cl atoms.

➤ *Mechanistic studies*

This thesis displays an experimental study of the oxidation reaction of three C₅-C₇ unsaturated aldehydes with ozone and Cl atoms at atmospheric conditions (T = 298 K, P = 760 Torr). The proposed mechanisms have been designed based on the identified and/or quantified products and on similar degradation mechanisms taken from the literature. Oxidation of the studied BVOCs generates hydroxycarbonyl compounds and intermediate radicals called Criegee intermediate (for O₃-initiated reactions) and

chlorinated compounds (for Cl-initiated reactions). For the reaction mechanism of the ozonolysis of 2-alkenals, a slight preference was observed to the channel producing glyoxal. However, no preference was observed for the reaction mechanism between 2-alkenals and Cl atoms.

Studies on the fate of these products in the atmosphere are scarce or even nonexistent, hence the importance of investigating the kinetics and mechanism of their reactions with atmospheric photo-oxidants. This work calls for continuing mechanistic studies with more sensitive analytical techniques to improve the carbon balance and perform temperature studies to assess the T-dependence on the different reaction pathways. Besides, theoretical calculations at different temperatures are also required to better understand and interpret the different experimental findings and explore a generalized reaction mechanism of BVOCs.

➤ *SOA studies*

In the current work, we investigated the SOA formation from the oxidation reactions between three C₅-C₇ unsaturated aldehydes and atmospheric oxidants (ozone, Cl atoms and OH radicals). SOAs formation from the ozonolysis of 2-alkenals has a limited impact on the atmosphere due to the carbonyl group's presence. On the contrary, the formed SOAs from the reaction of 2-alkenals and Cl atoms have a potential impact on the atmosphere, especially if alkenal sources are close to continual areas.

The SOA yields were calculated based on the BVOC consumed masses and the SOA formed masses. The latter were calculated with the assumptions that particles were perfect spheres, and the density of the generated particles was 1.4 g cm⁻³ (recommended by Hallquist et al., 2009). In contrast with the gas-phase studies, to my knowledge, the formation of SOAs from the ozonolysis reactions was not studied before, neither was it for the oxidation of C₅-C₇ unsaturated aldehydes (\geq C₅).

This thesis studied oxygenated BVOC reactivities in "low-NO_x" environments. However, it would be interesting to carry out experiments in "high-NO_x" to better characterize their contribution to the formation of secondary pollutants (ozone, aerosols) during pollution

plumes episodes. Finally, the SOA formation through the degradation of C₅-C₇ unsaturated aldehydes can be extended to other molecules with atmospheric interest, such as C₅-C₇ unsaturated alcohols.

References

- Abeles, F. B., Morgan, P. W., & Saltveit Jr, M. E. (2012). Ethylene in plant biology. Academic press.
- ACOM: Quick TUV [WWW Document], n.d. URL http://cprm.acom.ucar.edu/Models/TUV/Interactive_TUV/ (accessed 11.30.20).
- Adams, N. G., & Smith, D. (1976). The selected ion flow tube (SIFT); a technique for studying ion-neutral reactions. *International Journal of Mass Spectrometry and Ion Physics*, 21(3-4), 349-359.
- Ahmad, W., Coeur, C., Cuisset, A., Coddeville, P., & Tomas, A. (2017). Effects of scavengers of Criegee intermediates and OH radicals on the formation of secondary organic aerosol in the ozonolysis of limonene. *Journal of Aerosol Science*, 110, 70-83.
- Akritidis, D., Katragkou, E., Zanis, P., Pytharoulis, I., Melas, D., Flemming, J., ... & Eskes, H. (2018). A deep stratosphere-to-troposphere ozone transport event over Europe simulated in CAMS global and regional forecast systems: analysis and evaluation. *Atmospheric Chemistry & Physics*, 18(20).
- Akritidis, D., Pozzer, A., Zanis, P., Tyrlis, E., Škerlak, B., Sprenger, M., & Lelieveld, J. (2016). On the role of tropopause folds in summertime tropospheric ozone over the eastern Mediterranean and the Middle East. *Atmospheric Chemistry and Physics*, 16(21), 14025-14039.
- Al Mulla, I., Viera, L., Morris, R., Sidebottom, H., Treacy, J., & Mellouki, A. (2010). Kinetics and mechanisms for the reactions of ozone with unsaturated oxygenated compounds. *ChemPhysChem*, 11(18), 4069-4078.
- Alam, M. S., Camredon, M., Rickard, A. R., Carr, T., Wyche, K. P., Hornsby, K. E., ... & Bloss, W. J. (2011). Total radical yields from tropospheric ethene ozonolysis. *Physical Chemistry Chemical Physics*, 13(23), 11002-11015.
- Albaladejo, J., Ballesteros, B., Jiménez, E., Martín, P., & Martínez, E. (2002). A PLP-LIF kinetic study of the atmospheric reactivity of a series of C4-C7 saturated and unsaturated aliphatic aldehydes with OH. *Atmospheric Environment*, 36(20), 3231-3239.
- Alicke, B., Platt, U., & Stutz, J. (2002). Impact of nitrous acid photolysis on the total hydroxyl radical budget during the Limitation of Oxidant Production/Pianura Padana Produzione di Ozono study in Milan. *Journal of Geophysical Research: Atmospheres*, 107(D22), LOP-9.
- Altshuller, A. P. (1983). Natural volatile organic substances and their effect on air quality in the United States. *Atmospheric Environment* (1967), 17(11), 2131-2165.
- Alwe, H. D., Walawalkar, M., Sharma, A., Pushpa, K. K., Dhanya, S., & Naik, P. D. (2013). Rate Coefficients for the Gas-Phase Reactions of Chlorine Atoms with Cyclic Ethers at 298 K. *International Journal of Chemical Kinetics*, 45(5), 295-305.
- Amann, A., Schwarz, K., Wimmer, G., & Witkovský, V. (2010). Model based determination of detection limits for proton transfer reaction mass spectrometer. *Measurement Science Review*, 10(6), 180-188.
- Andersen, C., Nielsen, O. J., Østerstrøm, F. F., Ausmeel, S., Nilsson, E. J., & Sulbaek Andersen, M. P. (2016). Atmospheric chemistry of tetrahydrofuran, 2-methyltetrahydrofuran, and 2, 5-dimethyltetrahydrofuran: kinetics of reactions with chlorine atoms, OD radicals, and ozone. *The Journal of Physical Chemistry A*, 120(37), 7320-7326.
- Anderson, R. S., Huang, L., Iannone, R., & Rudolph, J. (2007). Measurements of the ¹²C/¹³C kinetic isotope effects in the gas-phase reactions of light alkanes with chlorine atoms. *The Journal of Physical Chemistry A*, 111(3), 495-504.
- Andreae, M. O., Talbot, R. W., & Li, S. M. (1987). Atmospheric measurements of pyruvic and formic acid. *Journal of Geophysical Research: Atmospheres*, 92(D6), 6635-6641.
- Antiñolo, M., Asensio, M., Albaladejo, J., & Jiménez, E. (2020). Gas-Phase Reaction of trans-2-Methyl-2-butenal with Cl: Kinetics, Gaseous Products, and SOA Formation. *Atmosphere*, 11(7), 715.

- Antiñolo, M., del Olmo, R., Bravo, I., Albaladejo, J., & Jiménez, E. (2019). Tropospheric fate of allyl cyanide ($\text{CH}_2\text{CHCH}_2\text{CN}$): Kinetics, reaction products and secondary organic aerosol formation. *Atmospheric Environment*, 219, 117041.
- Aranda, A., Díaz de Mera, Y., Rodríguez, A., Rodríguez, D., & Martínez, E. (2003). A kinetic and mechanistic study of the reaction of Cl atoms with acrolein: temperature dependence for abstraction channel. *The Journal of Physical Chemistry A*, 107(30), 5717-5721.
- Arey, J., Crowley, D. E., Crowley, M., Resketo, M., & Lester, J. (1995). Hydrocarbon emissions from natural vegetation in California's South Coast Air Basin. *Atmospheric Environment*, 29(21), 2977-2988.
- Arey, J., Winer, A. M., Atkinson, R., Aschmann, S. M., Long, W. D., & Morrison, C. L. (1991). The emission of (Z)-3-hexen-1-ol, (Z)-3-hexenylacetate and other oxygenated hydrocarbons from agricultural plant species. *Atmospheric Environment. Part A. General Topics*, 25(5-6), 1063-1075.
- Arneth, A., Harrison, S. P., Zaehle, S., Tsigaridis, K., Menon, S., Bartlein, P. J., ... & Vesala, T. (2010). Terrestrial biogeochemical feedbacks in the climate system. *Nature Geoscience*, 3(8), 525-532.
- Aschmann, S. M., & Atkinson, R. (1995). Rate constants for the gas-phase reactions of alkanes with Cl atoms at 296 ± 2 K. *International Journal of Chemical Kinetics*, 27(6), 613-622.
- Aschmann, S. M., Chew, A. A., Arey, J., & Atkinson, R. (1997). Products of the gas-phase reaction of OH radicals with cyclohexane: reactions of the cyclohexoxy radical. *The Journal of Physical Chemistry A*, 101(43), 8042-8048.
- Ashmore, M. R. (2005). Assessing the future global impacts of ozone on vegetation. *Plant, Cell & Environment*, 28(8), 949-964.
- Aslan, L. (2017). Dégradation atmosphérique de composés organiques multifonctionnels: les hydroxycétones et les aldéhydes insaturés (Doctoral dissertation, Lille 1).
- Asmi, E., Sipilä, M., Vanhanen, J., Lehtipalo, K., Gagn'e, S., Neitola, K., ... & Kulmala, M. (2009). Results of the first air ion spectrometer calibration and intercomparison workshop. *Atmospheric Chemistry & Physics*, 9(1).
- Assaf, E., Sheps, L., Whalley, L., Heard, D., Tomas, A., Schoemaeker, C., & Fittschen, C. (2017). The reaction between CH_3O_2 and OH radicals: product yields and atmospheric implications. *Environmental Science & Technology*, 51(4), 2170-2177.
- Assaf, E., Song, B., Tomas, A., Schoemaeker, C., & Fittschen, C. (2016). Rate constant of the reaction between CH_3O_2 radicals and OH radicals revisited. *The Journal of Physical Chemistry A*, 120(45), 8923-8932.
- Athanasopoulou, E., Vogel, H., Vogel, B., Tsimpidi, A. P., Pandis, S. N., Knote, C., & Fountoukis, C. (2013). Modeling the meteorological and chemical effects of secondary organic aerosols during an EUCAARI campaign. *Atmospheric Chemistry and Physics*, 13(2), 625-645.
- Atkinson, R. (2007). Gas-phase tropospheric chemistry of organic compounds: a review. *Atmospheric Environment. Part A. General Topics*, 41(1), 200-240.
- Atkinson, R. (2000). Atmospheric chemistry of VOCs and NO_x . *Atmospheric environment*, 34(12-14), 2063-2101.
- Atkinson, R. (1990). Gas-phase tropospheric chemistry of organic compounds: a review. *Atmospheric Environment. Part A. General Topics*, 24(1), 1-41.
- Atkinson, R. (1986). Kinetics and mechanisms of the gas-phase reactions of the hydroxyl radical with organic compounds under atmospheric conditions. *Chemical Reviews*, 86(1), 69-201.
- Atkinson, R., & Arey, J. (2003). Atmospheric degradation of volatile organic compounds. *Chemical reviews*, 103(12), 4605-4638.
- Atkinson, R., & Arey, J. (1998). Atmospheric chemistry of biogenic organic compounds. *Accounts of Chemical Research*, 31(9), 574-583.
- Atkinson, R., Arey, J., Aschmann, S. M., Corchnoy, S. B., & Shu, Y. (1995). Rate constants for the gas-phase reactions of cis-3-Hexen-1-ol, cis-3-Hexenylacetate, trans-2-Hexenal, and Linalool

- with OH and NO₃ radicals and O₃ at 296±2 K, and OH radical formation yields from the O₃ reactions. *International Journal of Chemical Kinetics*, 27(10), 941-955.
- Atkinson, R., & Aschmann, S. M. (1985). Kinetics of the gas phase reaction of Cl atoms with a series of organics at 296±2 K and atmospheric pressure. *International journal of chemical kinetics*, 17(1), 33-41.
- Atkinson, R., Aschmann, S. M., & Pitts Jr, J. N. (1983). Kinetics of the gas-phase reactions of OH radicals with a series of α , β -unsaturated carbonyls at 299±2 K. *International Journal of Chemical Kinetics*, 15(1), 75-81.
- Atkinson, R., Aschmann, S. M., Winer, A. M., & Pitts Jr, J. N. (1981). Rate constants for the gas-phase reactions of O₃ with a series of carbonyls at 296 K. *International Journal of Chemical Kinetics*, 13(11), 1133-1142.
- Atkinson, R., Baulch, D. L., Cox, R. A., Crowley, J. N., Hampson Jr, R. F., Kerr, J. A., ... & Troe, J. (2001). Summary of evaluated kinetic and photochemical data for atmospheric chemistry. IUPAC Subcommittee on gas kinetic data evaluation for atmospheric chemistry, 20.
- Atkinson, R., Baulch, D. L., Cox, R. A., Crowley, J. N., Hampson, R. F., Hynes, R. G., ... & Troe, J. (2004). Evaluated kinetic and photochemical data for atmospheric chemistry: Volume I-gas phase reactions of O_x, HO_x, NO_x and SO_x species. *Atmospheric chemistry and physics*, 4(6), 1461-1738.
- Atkinson, R., Baulch, D. L., Cox, R. A., Crowley, J. N., Hampson, R. F., Hynes, R. G., ... & Subcommittee, I. U. P. A. C. (2006). Evaluated kinetic and photochemical data for atmospheric chemistry: Volume II-gas phase reactions of organic species. *Atmospheric chemistry and physics*, 6(11), 3625-4055.
- Atkinson, R., Tuazon, E. C., & Aschmann, S. M. (1995). Products of the gas-phase reactions of O₃ with alkenes. *Environmental science & technology*, 29(7), 1860-1866.
- Avzianova, E. V., & Ariya, P. A. (2002). Temperature-dependent kinetic study for ozonolysis of selected tropospheric alkenes. *International Journal of Chemical Kinetics*, 34(12), 678-684.
- Ballesteros, B., Ceacero-Vega, A. A., Garzon, A., Jimenez, E., & Albaladejo, J. (2009). Kinetics and mechanism of the tropospheric reaction of tetrahydropyran with Cl atoms. *Journal of Photochemistry and Photobiology A: Chemistry*, 208(2-3), 186-194.
- Barbosa, T. S., Barrera, J. A., Toro, R. J., Bauerfeldt, G. F., Arbilla, G., & Lane, S. I. (2017). Rate Coefficient for the Reaction of Cl Atoms with cis-3-Hexene at 296±2 K. *Journal of the Brazilian Chemical Society*, 28(11), 2267-2274.
- Barnes, I., Becker, K. H., & Zhu, T. (1993). Near UV absorption spectra and photolysis products of difunctional organic nitrates: Possible importance as NO_x reservoirs. *Journal of Atmospheric Chemistry*, 17(4), 353-373.
- Becker, K. H. (2006). Overview on the development of chambers for the study of atmospheric chemical processes. In *Environmental Simulation Chambers: Application to Atmospheric Chemical Processes* (pp. 1-26). Springer, Dordrecht.
- Bernard, F. (2009). Etude du devenir atmosphérique de composés organiques volatils biogéniques: Réactions avec OH, O₃ et NO₂ (Doctoral dissertation).
- Bernard, F., Fedioun, I., Peyroux, F., Quilgars, A., Daële, V., & Mellouki, A. (2012). Thresholds of secondary organic aerosol formation by ozonolysis of monoterpenes measured in a laminar flow aerosol reactor. *Journal of aerosol science*, 43(1), 14-30.
- Bertin, N., Staudt, M., Hansen, U., Seufert, G., Ciccioli, P., Foster, P., ... & Torres, L. (1997). Diurnal and seasonal course of monoterpene emissions from *Quercus ilex* (L.) under natural conditions application of light and temperature algorithms. *Atmospheric Environment*, 31, 135-144.
- Bilde, M., & Pandis, S. N. (2001). Evaporation rates and vapor pressures of individual aerosol species formed in the atmospheric oxidation of α -and β -pinene. *Environmental science & technology*, 35(16), 3344-3349.

- Blanco, M. B., Barnes, I., & Teruel, M. A. (2010). FTIR gas-phase kinetic study of the reactions of Cl atoms with (CH₃)₂C=CHCHO and CH₃CH=CHCHO. *Chemical Physics Letters*, 488(4-6), 135-139.
- Blitz, M. A., Heard, D. E., & Pilling, M. J. (2006). Study of acetone photodissociation over the wavelength range 248– 330 nm: Evidence of a mechanism involving both the singlet and triplet excited states. *The Journal of Physical Chemistry A*, 110(21), 6742-6756.
- Bonn, B., Schuster, G., & Moortgat, G. K. (2002). Influence of water vapor on the process of new particle formation during monoterpene ozonolysis. *The Journal of Physical Chemistry A*, 106(12), 2869-2881.
- Bonsang, B., Kanakidou, M., Lambert, G., & Monfray, P. (1988). The marine source of C₂-C₆ aliphatic hydrocarbons. *Journal of Atmospheric Chemistry*, 6(1-2), 3-20.
- Bouvier-Brown, N. C., Goldstein, A. H., Gilman, J. B., Kuster, W. C., & De Gouw, J. A. (2009). In-situ ambient quantification of monoterpenes, sesquiterpenes, and related oxygenated compounds during BEARPEX 2007: implications for gas-and particle-phase chemistry. *Atmospheric Chemistry & Physics*, 9(15).
- Bouzidi, H. (2014). Réactivité de composés organiques volatils oxygénés multifonctionnels: évaluation de l'importance de la voie de photolyse (Doctoral dissertation, Lille 1).
- Braure, T., Riffault, V., Tomas, A., Olariu, R. I., Arsene, C., Bedjanian, Y., & Coddeville, P. (2015). Ozonolysis of a Series of Methylated Alkenes: Reaction Rate Coefficients and Gas-Phase Products. *International Journal of Chemical Kinetics*, 47(9), 596-605.
- Le Breton, M., Hallquist, Å. M., Pathak, R. K., Simpson, D., Wang, Y., Johansson, J., ... & Hallquist, M. (2018). Chlorine oxidation of VOCs at a semi-rural site in Beijing: Significant chlorine liberation from ClNO₂ and subsequent gas- and particle-phase Cl-VOC production. *Atmospheric Chemistry and Physics*, 18(17), 13013-13030.
- Brown, S. S., & Stutz, J. (2012). Nighttime radical observations and chemistry. *Chemical Society Reviews*, 41(19), 6405-6447.
- Bucher, J. B. (1981). SO₂-induced ethylene evolution of forest tree foliage, and its potential use as stress-indicator. *European Journal of Forest Pathology*, 11(5-6), 369-373.
- Burkholder, J. B., Sander, S. P., Abbatt, J. P. D., Barker, J. R., Huie, R. E., Kolb, C. E., ... & Wine, P. H. (2015). Chemical kinetics and photochemical data for use in atmospheric studies: evaluation number 18. Pasadena, CA: Jet Propulsion Laboratory, National Aeronautics and Space Administration, 2015.
- Butter, R. G., Xu, C., & Ling, L. C. (1985). Volatile components of wheat leaves (and stems): possible insect attractants. *Journal of Agricultural and Food Chemistry*, 33(1), 115-117.
- Buttery, R. G., Ling, L. C., & Wellso, S. G. (1982). Oat leaf volatiles: possible insect attractants. *Journal of Agricultural and Food Chemistry*, 30(4), 791-792.
- Cabanas, B., Salgado, S., Martin, P., Baeza, M. T., & Martinez, E. (2001). Night-time atmospheric loss process for unsaturated aldehydes: Reaction with NO₃ radicals. *The Journal of Physical Chemistry A*, 105(18), 4440-4445.
- Calfapietra, C., Fares, S., & Loreto, F. (2009). Volatile organic compounds from Italian vegetation and their interaction with ozone. *Environmental Pollution*, 157(5), 1478-1486.
- Calvert, J., Mellouki, A., & Orlando, J. (2011). Mechanisms of atmospheric oxidation of the oxygenates. OUP USA.
- Canosa-Mas, C. E., Cotter, E. S., Duffy, J., Thompson, K. C., & Wayne, R. P. (2001). The reactions of atomic chlorine with acrolein, methacrolein and methyl vinyl ketone. *Physical Chemistry Chemical Physics*, 3(15), 3075-3084.
- Caravan, R. L., Khan, M. A. H., Zádor, J., Sheps, L., Antonov, I. O., Rotavera, B., ... & Taatjes, C. A. (2018). The reaction of hydroxyl and methylperoxy radicals is not a major source of atmospheric methanol. *Nature communications*, 9(1), 1-9.
- Carlier, P., Hannachi, H., & Mouvier, G. (1986). The chemistry of carbonyl compounds in the atmosphere-a review. *Atmospheric Environment* (1967), 20(11), 2079-2099.

- Carter, W. P., Cocker III, D. R., Fitz, D. R., Malkina, I. L., Bumiller, K., Sauer, C. G., ... & Song, C. (2005). A new environmental chamber for evaluation of gas-phase chemical mechanisms and secondary aerosol formation. *Atmospheric Environment*, 39(40), 7768-7788.
- Chameides, W. L., Lindsay, R. W., Richardson, J., & Kiang, C. S. (1988). The role of biogenic hydrocarbons in urban photochemical smog: Atlanta as a case study. *Science*, 241(4872), 1473-1475.
- Chan, A. W. H., Chan, M. N., Surratt, J. D., Chhabra, P. S., Loza, C. L., Crounse, J. D., ... & Seinfeld, J. H. (2010). Role of aldehyde chemistry and NO_x concentrations in secondary organic aerosol formation. *Atmospheric Chemistry and Physics*, 10(15), 7169-7188.
- Chang, S., & Allen, D. T. (2006). Atmospheric chlorine chemistry in southeast Texas: Impacts on ozone formation and control. *Environmental science & technology*, 40(1), 251-262.
- Chen, F., Tholl, D., D'Auria, J. C., Farooq, A., Pichersky, E., & Gershenzon, J. (2003). Biosynthesis and emission of terpenoid volatiles from *Arabidopsis* flowers. *The Plant Cell*, 15(2), 481-494.
- Chen, Y., Wang, J., Zhao, S., Tong, S., & Ge, M. (2016). An experimental kinetic study and products research of the reactions of O₃ with a series of unsaturated alcohols. *Atmospheric Environment*, 145, 455-467.
- Chen, Y. M., Tabner, B. J., & Wellburn, A. R. (1990). ACC-independent ethylene formation in brown Norway spruce needles involves organic peroxides rather than hydroperoxides as possible precursors. *Physiological and molecular plant pathology*, 37(5), 323-337.
- Ciccioli, P., Centritto, M., & Loreto, F. (2014). Biogenic volatile organic compound emissions from vegetation fires. *Plant, cell & environment*, 37(8), 1810-1825.
- Colmán, E. G., Blanco, M. B., Barnes, I., & Teruel, M. A. (2015a). Kinetics of the gas-phase reaction between ozone and three unsaturated oxygenated compounds: Ethyl 3, 3-dimethyl acrylate, 2-methyl-2-pentenal and 6-methyl-5-hepten-2-one at atmospheric pressure. *Atmospheric Environment*, 109, 272-278.
- Coquet, S., & Ariya, P. A. (2000). Kinetics of the gas-phase reactions of Cl atom with selected C₂-C₅ unsaturated hydrocarbons at 283< T< 323 K. *International Journal of Chemical Kinetics*, 32(8), 478-484.
- Costa, A., Pinheiro, M., Magalhães, J., Ribeiro, R., Seabra, V., Reis, S., & Sarmento, B. (2016). The formulation of nanomedicines for treating tuberculosis. *Advanced drug delivery reviews*, 102, 102-115.
- Criegee, R. (1975). Mechanism of ozonolysis. *Angewandte Chemie International Edition in English*, 14(11), 745-752.
- Crunaire, S., Tarmoul, J., Fittschen, C., Tomas, A., Lemoine, B., & Coddeville, P. (2006). Use of cw-CRDS for studying the atmospheric oxidation of acetic acid in a simulation chamber. *Applied Physics B*, 85(2-3), 467-476.
- Czoschke, N. M., Jang, M., & Kamens, R. M. (2003). Effect of acidic seed on biogenic secondary organic aerosol growth. *Atmospheric Environment*, 37(30), 4287-4299.
- Davis, D. D., Braun, W., & Bass, A. M. (1970). Reactions of Cl₂P₃/2: Absolute rate constants for reaction with H₂, CH₄, C₂H₆, CH₂Cl₂, C₂Cl₄, and c-C₆H₁₂. *International Journal of Chemical Kinetics*, 2(2), 101-114.
- Davis, M. E., & Burkholder, J. B. (2011). Rate coefficients for the gas-phase reaction of OH with (Z)-3-hexen-1-ol, 1-penten-3-ol, (E)-2-penten-1-ol, and (E)-2-hexen-1-ol between 243 and 404 K. *Atmospheric Chemistry and Physics*, 11(7), 3347.
- Davis, M. E., Gilles, M. K., Ravishankara, A. R., & Burkholder, J. B. (2007). Rate coefficients for the reaction of OH with (E)-2-pentenal, (E)-2-hexenal, and (E)-2-heptenal. *Physical Chemistry Chemical Physics*, 9(18), 2240-2248.
- Delmas, R., & Mégie, G. (2015). *Physique et chimie de l'atmosphère: 2e édition*. Belin.
- Dement, W. A., Tyson, B. J., & Mooney, H. A. (1975). Mechanism of monoterpene volatilization in *Salvia mellifera*. *Phytochemistry*, 14(12), 2555-2557.
- DeMore, W. B., Margitan, J. J., Molina, M. J., Watson, R. T., Golden, D. M., Hampson, R. F., ... & Ravishankara, A. R. (1985). Tables of rate constants extracted from chemical kinetics and

- photochemical data for use in stratospheric modeling. Evaluation number 7. International journal of chemical kinetics, 17(10), 1135-1151.
- Diskin, A. M., Wang, T., Smith, D., & Španěl, P. (2002). A selected ion flow tube (SIFT), study of the reactions of H_3O^+ , NO^+ and O_2^+ ions with a series of alkenes; in support of SIFT-MS. International Journal of Mass Spectrometry, 218(1), 87-101.
- Dodge, M. C. (2000). Chemical oxidant mechanisms for air quality modeling: critical review. Atmospheric Environment, 34(12-14), 2103-2130.
- Dornelles, K., Roriz, M., Roriz, V., & Caram, R. (2011). Thermal Performance of White Solar-Reflective Paints for Cool Roofs and the Influence on the Thermal Comfort and Building Energy. Use in Hot Climates. In Solar World Congress. ISES. International Solar Energy Society.
- Duhl, T. R., Helmig, D., & Guenther, A. (2008). Sesquiterpene emissions from vegetation: a review.
- Duncanu, M. (2012). Réacteur à écoulement pour l'étude de la formation des aérosols organiques secondaires par ozonolyse de composés organiques volatils: développement analytique, validation cinétique et ozonolyse d'un composé biogénique (Doctoral dissertation, Lille 1).
- Duncanu, M., Olariu, R. I., Riffault, V., Visez, N., Tomas, A., & Coddeville, P. (2012). Development of a new flow reactor for kinetic studies. Application to the ozonolysis of a series of alkenes. The Journal of Physical Chemistry A, 116(24), 6169-6179.
- Edney, E. O., Kleindienst, T. E., & Corse, E. W. (1986). Room temperature rate constants for the reaction of OH with selected chlorinated and oxygenated hydrocarbons. International journal of chemical kinetics, 18(12), 1355-1371.
- El Dib, G., Sleiman, C., Canosa, A., Travers, D., Courbe, J., Sawaya, T., ... & Chakir, A. (2013). First experimental determination of the absolute gas-phase rate coefficient for the reaction of OH with 4-hydroxy-2-butanone (4H2B) at 294 K by vapor pressure measurements of 4H2B. The Journal of Physical Chemistry A, 117(1), 117-125.
- Emmerson, K. M., & Carslaw, N. (2009). Night-time radical chemistry during the TORCH campaign. Atmospheric Environment, 43(20), 3220-3226.
- Engelberth, J., Alborn, H. T., Schmelz, E. A., & Tumlinson, J. H. (2004). Airborne signals prime plants against insect herbivore attack. Proceedings of the National Academy of Sciences, 101(6), 1781-1785.
- Etzkorn, T., Klotz, B., Sørensen, S., Patroescu, I. V., Barnes, I., Becker, K. H., & Platt, U. (1999). Gas-phase absorption cross sections of 24 monocyclic aromatic hydrocarbons in the UV and IR spectral ranges. Atmospheric Environment, 33(4), 525-540.
- Ezell, M. J., Johnson, S. N., Yu, Y., Perraud, V., Bruns, E. A., Alexander, M. L., ... & Finlayson-Pitts, B. J. (2010). A new aerosol flow system for photochemical and thermal studies of tropospheric aerosols. Aerosol Science and Technology, 44(5), 329-338.
- Ezell, M. J., Wang, W., Ezell, A. A., Soskin, G., & Finlayson-Pitts, B. J. (2002). Kinetics of reactions of chlorine atoms with a series of alkenes at 1 atm and 298 K: structure and reactivity. Physical Chemistry Chemical Physics, 4(23), 5813-5820.
- Fall, R. (2003). Abundant oxygenates in the atmosphere: a biochemical perspective. Chemical reviews, 103(12), 4941-4952.
- Fantechi, G., Jensen, N. R., Hjorth, J., & Peeters, J. (1998a). Determination of the rate constants for the gas-phase reactions of methyl butenol with OH radicals, ozone, NO_3 radicals, and Cl atoms. International journal of chemical kinetics, 30(8), 589-594.
- Fantechi, G., Jensen, N. R., Saastad, O., Hjorth, J., & Peeters, J. (1998b). Reactions of Cl atoms with selected VOCs: Kinetics, products and mechanisms. Journal of atmospheric chemistry, 31(3), 247-267.
- Faxon, C. B., & Allen, D. T. (2013). Chlorine chemistry in urban atmospheres: A review, Environ. Chem, 10, 221.
- Fayad, L., Coeur, C., Fagniez, T., Secordel, X., & Mouret, G. (2019, January). Ozonolysis of γ -terpinene in the new indoor atmospheric chamber CHARME: analysis of gas-phase and particulate reaction products. In Geophysical Research Abstracts (Vol. 21).

- Felzer, B. S., Cronin, T., Reilly, J. M., Melillo, J. M., & Wang, X. (2007). Impacts of ozone on trees and crops. *Comptes Rendus Geoscience*, 339(11-12), 784-798.
- Fenske, J. D., & Paulson, S. E. (1999). Human breath emissions of VOCs. *Journal of the Air & Waste Management Association*, 49(5), 594-598.
- Ferracci, V., Heimann, I., Abraham, N. L., Pyle, J. A., & Archibald, A. T. (2018). Global modelling of the total OH reactivity: investigations on the “missing” OH sink and its atmospheric implications.
- Filella, I., & Penuelas, J. (2006). Daily, weekly and seasonal relationships among VOCs, NO_x and O₃ in a semi-urban area near Barcelona. *Journal of Atmospheric Chemistry*, 54(2), 189-201.
- Fineschi, S., & Loreto, F. (2012). Leaf volatile isoprenoids: an important defensive armament in forest tree species. *Forest-Biogeosciences and Forestry*, 5(1), 13.
- Finlayson-Pitts, B. J., Ezell, M. J., & Pitts, J. N. (1989). Formation of chemically active chlorine compounds by reactions of atmospheric NaCl particles with gaseous N₂O₅ and ClONO₂. *Nature*, 337(6204), 241-244.
- Finlayson-Pitts, B. J., & Hemminger, J. C. (2000). Physical chemistry of airborne sea salt particles and their components. *The Journal of Physical Chemistry A*, 104(49), 11463-11477.
- Finlayson-Pitts, B. J., & Pitts Jr, J. N. (1999). *Chemistry of the upper and lower atmosphere: theory, experiments, and applications*. Elsevier.
- Finlayson-Pitts, B. J., & Pitts Jr, J. N. (1986). *Atmospheric chemistry. Fundamentals and experimental techniques*.
- Fischbach, R. J., Staudt, M., Zimmer, I., Rambal, S., & Schnitzler, J. P. (2002). Seasonal pattern of monoterpene synthase activities in leaves of the evergreen tree *Quercus ilex*. *Physiologia Plantarum*, 114(3), 354-360.
- Fitzky, A. C., Sandén, H., Karl, T., Fares, S., Calfapietra, C., Grote, R., ... & Rewald, B. (2019). The interplay between ozone and urban vegetation-BVOC emissions, ozone deposition and tree ecophysiology. *Frontiers in Forests and Global Change*, 2, 50.
- Fleming, E. L., Chandra, S., Barnett, J. J., & Corney, M. (1990). Zonal mean temperature, pressure, zonal wind and geopotential height as functions of latitude. *Advances in Space Research*, 10(12), 11-59.
- Fruekilde, P., Hjorth, J., Jensen, N. R., Kotzias, D., & Larsen, B. (1998). Ozonolysis at vegetation surfaces: a source of acetone, 4-oxopentanal, 6-methyl-5-hepten-2-one, and geranyl acetone in the troposphere. *Atmospheric Environment*, 32(11), 1893-1902.
- Fuchs, H., Hofzumahaus, A., Rohrer, F., Bohn, B., Brauers, T., Dorn, H. P., ... & Wahner, A. (2013). Experimental evidence for efficient hydroxyl radical regeneration in isoprene oxidation. *Nature Geoscience*, 6(12), 1023-1026.
- Fuentes, J. D., Lerdau, M., Atkinson, R., Baldocchi, D., Bottenheim, J. W., Ciccioli, P., ... & Stockwell, W. (2000). Biogenic hydrocarbons in the atmospheric boundary layer: a review. *Bulletin of the American Meteorological Society*, 81(7), 1537-1575.
- Fukui, Y., & Doskey, P. V. (1998). Air-surface exchange of nonmethane organic compounds at a grassland site: Seasonal variations and stressed emissions. *Journal of Geophysical Research: Atmospheres*, 103(D11), 13153-13168.
- Gai, Y., Ge, M., & Wang, W. (2011). Kinetics of the gas-phase reactions of some unsaturated alcohols with Cl atoms and O₃. *Atmospheric environment*, 45(1), 53-59.
- Gantt, B., Meskhidze, N., Zhang, Y., & Xu, J. (2010). The effect of marine isoprene emissions on secondary organic aerosol and ozone formation in the coastal United States. *Atmospheric Environment*, 44(1), 115-121.
- Gao, T., Andino, J. M., Rivera, C. C., & Márquez, M. F. (2009). Rate constants of the gas-phase reactions of OH radicals with trans-2-hexenal, trans-2-octenal, and trans-2-nonenal. *International Journal of Chemical Kinetics*, 41(7), 483-489.
- Gao, Y., Jin, Y. J., Li, H. D., & Chen, H. J. (2005). Volatile organic compounds and their roles in bacteriostasis in five conifer species. *Journal of Integrative Plant Biology*, 47(4), 499-507.

- Gaona Colmán, E., Blanco, M. B., Barnes, I., Wiesen, P., & Teruel, M. A. (2017). Mechanism and Product Distribution of the O₃-Initiated Degradation of (E)-2-Heptenal, (E)-2-Octenal, and (E)-2-Nonenal. *The Journal of Physical Chemistry A*, 121(27), 5147-5155.
- Gibilisco, R. G., Bejan, I., Barnes, I., Wiesen, P., & Teruel, M. A. (2015). FTIR gas kinetic study of the reactions of ozone with a series of hexenols at atmospheric pressure and 298 K. *Chemical Physics Letters*, 618, 114-118.
- Gibilisco, R. G., Bejan, I., Barnes, I., Wiesen, P., & Teruel, M. A. (2014). Rate coefficients at 298 K and 1 atm for the tropospheric degradation of a series of C₆, C₇ and C₈ biogenic unsaturated alcohols initiated by Cl atoms. *Atmospheric Environment*, 94, 564-572.
- Gibilisco, R. G., Blanco, M. B., Bejan, I., Barnes, I., Wiesen, P., & Teruel, M. A. (2015). Atmospheric sink of (E)-3-hexen-1-ol, (Z)-3-hepten-1-ol, and (Z)-3-octen-1-ol: Rate coefficients and mechanisms of the OH-radical initiated degradation. *Environmental science & technology*, 49(13), 7717-7725.
- Gibilisco, R. G., Santiago, A. N., & Teruel, M. A. (2013). OH-initiated degradation of a series of hexenols in the troposphere. Rate coefficients at 298 K and 1 atm. *Atmospheric Environment*, 77, 358-364.
- Giri, B. R., & Roscoe, J. M. (2010). Kinetics of the reactions of Cl atoms with several ethers. *The Journal of Physical Chemistry A*, 114(32), 8369-8375.
- Goldan, P. D., Kuster, W. C., Fehsenfeld, F. C., & Montzka, S. A. (1993). The observation of a C₅ alcohol emission in a North American pine forest. *Geophysical Research Letters*, 20(11), 1039-1042.
- Graedel, T. E. (1979). Terpenoids in the atmosphere. *Reviews of Geophysics*, 17(5), 937-947.
- Graedel, T. E., Hawkins, D. T., & Claxton, L. D. (2012). *Atmospheric chemical compounds: sources, occurrence and bioassay*. Elsevier.
- Graedel, T. E., & Keene, W. C. (1996). The budget and cycle of Earth's natural chlorine. *Pure and Applied Chemistry*, 68(9), 1689-1697.
- Green, C. R., & Atkinson, R. (1992). Rate constants for the gas-phase reactions of I₃ with a series of alkenes at 296 K.
- Griffin, R. J., Cocker III, D. R., Flagan, R. C., & Seinfeld, J. H. (1999). Organic aerosol formation from the oxidation of biogenic hydrocarbons. *Journal of Geophysical Research: Atmospheres*, 104(D3), 3555-3567.
- Grimm, A., Amarandei, C., Romanias, M. N., El Dib, G., Canosa, A., Arsene, C., ... & Tomas, A. (2020). Kinetic Measurements of Cl Atom Reactions with C₅-C₈ Unsaturated Alcohols. *Atmosphere*, 11(3), 256.
- Grosjean, D., Grosjean, E., & Williams, E. L. (1993). Rate constants for the gas-phase reactions of ozone with unsaturated alcohols, esters, and carbonyls. *International Journal of Chemical Kinetics*, 25(9), 783-794.
- Grosjean, D., & Williams II, E. L. (1992). Environmental persistence of organic compounds estimated from structure-reactivity and linear free-energy relationships. *Unsaturated aliphatics. Atmospheric Environment. Part A. General Topics*, 26(8), 1395-1405.
- Grosjean, D., Williams, E. L., & Grosjean, E. (1993). Atmospheric chemistry of isoprene and of its carbonyl products. *Environmental science & technology*, 27(5), 830-840.
- Grosjean, E., Grosjean, D., & Seinfeld, J. H. (1996). Gas-phase reaction of ozone with trans-2-hexenal, trans-2-hexenyl acetate, ethylvinyl ketone, and 6-methyl-5-hepten-2-one. *International Journal of Chemical Kinetics*, 28(5), 373-382.
- Grosjean, E., & Grosjean, D. (1999). The reaction of unsaturated aliphatic oxygenates with ozone. *Journal of Atmospheric Chemistry*, 32(2), 205-232.
- Grosjean, E., & Grosjean, D. (1998). Rate constants for the gas-phase reaction of ozone with unsaturated oxygenates. *International Journal of Chemical Kinetics*, 30(1), 21-29.
- Grosjean, E., & Grosjean, D. (1997). The gas phase reaction of unsaturated oxygenates with ozone: Carbonyl products and comparison with the alkene-ozone reaction. *Journal of atmospheric chemistry*, 27(3), 271-289.

- Grosjean, E., & Grosjean, D. (1996). Rate constants for the gas-phase reaction of ozone with 1, 1-disubstituted alkenes. *International Journal of Chemical Kinetics*, 28(12), 911-918.
- Grosjean, E., & Grosjean, D. (1994). Rate constants for the gas-phase reactions of Ozone with unsaturated Aliphatic Alcohols. *International Journal of Chemical Kinetics*, 26(12), 1185-1191.
- Grosjean, E., Williams II, E. L., & Grosjean, D. (1994). Atmospheric chemistry of acrolein. *Science of the total environment*, 153(3), 195-202.
- Guenther, A. (2013). Biological and chemical diversity of biogenic volatile organic emissions into the atmosphere. *ISRN Atmospheric Sciences*, 2013.
- Guenther, A. (2002). The contribution of reactive carbon emissions from vegetation to the carbon balance of terrestrial ecosystems. *Chemosphere*, 49(8), 837-844.
- Guenther, A., Hewitt, C. N., Erickson, D., Fall, R., Geron, C., Graedel, T., ... & Zimmerman, P. (1995). A global model of natural volatile organic compound emissions. *Journal of Geophysical Research: Atmospheres*, 100(D5), 8873-8892.
- Guenther, A., Karl, T., Harley, P., Wiedinmyer, C., Palmer, P. I., & Geron, C. (2006). Estimates of global terrestrial isoprene emissions using MEGAN (Model of Emissions of Gases and Aerosols from Nature).
- Guenther, A., Zimmerman, P., & Wildermuth, M. (1994). Natural volatile organic compound emission rate estimates for US woodland landscapes. *Atmospheric Environment*, 28(6), 1197-1210.
- Guenther, A. B., Jiang, X., Heald, C. L., Sakulyanontvittaya, T., Duhl, T., Emmons, L. K., & Wang, X. (2012). The Model of Emissions of Gases and Aerosols from Nature version 2.1 (MEGAN2.1): an extended and updated framework for modeling biogenic emissions.
- Guenther, A. B., Monson, R. K., & Fall, R. (1991). Isoprene and monoterpene emission rate variability: observations with eucalyptus and emission rate algorithm development. *Journal of Geophysical Research: Atmospheres*, 96(D6), 10799-10808.
- Guicherit, R., & Roemer, M. (2000). Tropospheric ozone trends. *Chemosphere-Global Change Science*, 2(2), 167-183.
- Hallquist, M., Wenger, J. C., Baltensperger, U., Rudich, Y., Simpson, D., Claeys, M., ... & Wildt, J. (2009). The formation, properties and impact of secondary organic aerosol: current and emerging issues. *Atmospheric chemistry and physics*, 9(14), 5155-5236.
- Harley, P. C. (2013). The roles of stomatal conductance and compound volatility in controlling the emission of volatile organic compounds from leaves. In *Biology, controls and models of tree volatile organic compound emissions* (pp. 181-208). Springer, Dordrecht.
- Hatakeyama, S., & Akimoto, H. (1994). Reactions of Criegee intermediates in the gas phase. *Research on chemical intermediates*, 20(3-5), 503-524.
- Hatanaka, A. (1996). The fresh green odor emitted by plants. *Food Reviews International*, 12(3), 303-350.
- Hatanaka, A. (1993). The biogenesis of green odour by green leaves. *Phytochemistry*, 34(5), 1201-1218.
- Hatanaka, A., & Harada, T. (1973). Formation of cis-3-hexenal, trans-2-hexenal and cis-3-hexenol in macerated *Thea sinensis* leaves. *Phytochemistry*, 12(10), 2341-2346.
- Hatanaka, A., Kajiwar, T., & Sekiya, J. (1987). Biosynthetic pathway for C6-aldehydes formation from linolenic acid in green leaves. *Chemistry and Physics of Lipids*, 44(2-4), 341-361.
- Hearn, J. D., & Smith, G. D. (2004). Kinetics and product studies for ozonolysis reactions of organic particles using aerosol CIMS. *The Journal of Physical Chemistry A*, 108(45), 10019-10029.
- Heiden, A. C., Hoffmann, T., Kahl, J., Kley, D., Klockow, D., Langebartels, C., ... & Wildt, J. (1999). Emission of volatile organic compounds from ozone-exposed plants. *Ecological Applications*, 9(4), 1160-1167.
- Heil, M., & Bueno, J. C. S. (2007). Within-plant signaling by volatiles leads to induction and priming of an indirect plant defense in nature. *Proceedings of the National Academy of Sciences*, 104(13), 5467-5472.

- Helmig, D., Ortega, J., Duhl, T., Tanner, D., Guenther, A., Harley, P., ... & Sakulyanontvittaya, T. (2007). Sesquiterpene emissions from pine trees– identifications, emission rates and flux estimates for the contiguous United States. *Environmental science & technology*, 41(5), 1545-1553.
- Himanen, S. J., Blande, J. D., Klemola, T., Pulkkinen, J., Heijari, J., & Holopainen, J. K. (2010). Birch (*Betula* spp.) leaves adsorb and re-release volatiles specific to neighbouring plants–a mechanism for associational herbivore resistance?. *New Phytologist*, 186(3), 722-732.
- Hoffmann, T., Odum, J. R., Bowman, F., Collins, D., Klockow, D., Flagan, R. C., & Seinfeld, J. H. (1997). Formation of organic aerosols from the oxidation of biogenic hydrocarbons. *Journal of Atmospheric Chemistry*, 26(2), 189-222.
- Hofmann, U., Weller, D., Ammann, C., Jork, E., & Kesselmeier, J. (1997). Cryogenic trapping of atmospheric organic acids under laboratory and field conditions. *Atmospheric Environment*, 31(9), 1275-1284.
- Hofzumahaus, A., Rohrer, F., Lu, K., Bohn, B., Brauers, T., Chang, C. C., ... & Zhang, Y. (2009). Amplified trace gas removal in the troposphere. *science*, 324(5935), 1702-1704.
- Holloway, A. M., & Wayne, R. P. (2015). *Atmospheric chemistry*. Royal Society of Chemistry.
- Holopainen, J. K. (2011). Can forest trees compensate for stress-generated growth losses by induced production of volatile compounds?. *Tree physiology*, 31(12), 1356-1377.
- Hooshiyar, P. A., & Niki, H. (1995). Rate constants for the gas-phase reactions of Cl-atoms with C2-C8 alkanes at $T = 296 \pm 2$ K. *International journal of chemical kinetics*, 27(12), 1197-1206.
- Horie, O., & Moortgat, G. K. (1998). Gas-phase ozonolysis of alkenes. Recent advances in mechanistic investigations. *Accounts of chemical research*, 31(7), 387-396.
- Horie, O., & Moortgat, G. K. (1991). Decomposition pathways of the excited Criegee intermediates in the ozonolysis of simple alkenes. *Atmospheric Environment. Part A. General Topics*, 25(9), 1881-1896.
- Hynes, R. G., Angove, D. E., Saunders, S. M., Haverd, V., & Azzi, M. (2005). Evaluation of two MCM v3. 1 alkene mechanisms using indoor environmental chamber data. *Atmospheric Environment*, 39(38), 7251-7262.
- Hyšpler, R., Crhová, Š., Gasparič, J., Zadák, Z., Čížková, M., & Balasová, V. (2000). Determination of isoprene in human expired breath using solid-phase microextraction and gas chromatography–mass spectrometry. *Journal of Chromatography B: Biomedical Sciences and Applications*, 739(1), 183-190.
- Iannone, R., Anderson, R. S., Vogel, A., Eby, P. S., Whiticar, M. J., & Rudolph, J. (2005). The hydrogen kinetic isotope effects of the reactions of n-alkanes with chlorine atoms in the gas phase. *Journal of atmospheric chemistry*, 50(2), 121-138.
- Isidorov, V. A., Zenkevich, I. G., & Ioffe, B. V. (1985). Volatile organic compounds in the atmosphere of forests. *Atmospheric Environment* (1967), 19(1), 1-8.
- IUPAC 2006 - URL: <http://publications.iupac.org/pac/reports/year/2006/index.html>
- Jacob, D. J., Field, B. D., Li, Q., Blake, D. R., De Gouw, J., Warneke, C., ... & Guenther, A. (2005). Global budget of methanol: Constraints from atmospheric observations. *Journal of Geophysical Research: Atmospheres*, 110(D8).
- Jacob, D. J., Field, B. D., Jin, E. M., Bey, I., Li, Q., Logan, J. A., ... & Singh, H. B. (2002). Atmospheric budget of acetone. *Journal of Geophysical Research: Atmospheres*, 107(D10), ACH-5.
- Jaeglé, L., Quinn, P. K., Bates, T. S., Alexander, B., & Lin, J. T. (2011). Global distribution of sea salt aerosols: new constraints from in situ and remote sensing observations. *Atmospheric Chemistry and Physics*, 11(7), 3137.
- Jang, M., Czoschke, N. M., Lee, S., & Kamens, R. M. (2002). Heterogeneous atmospheric aerosol production by acid-catalyzed particle-phase reactions. *Science*, 298(5594), 814-817.
- Jang, M., Lee, S., & Kamens, R. M. (2003). Organic aerosol growth by acid-catalyzed heterogeneous reactions of octanal in a flow reactor. *Atmospheric Environment*, 37(15), 2125-2138.
- Janson, R., & de Serves, C. (2001). Acetone and monoterpene emissions from the boreal forest in northern Europe. *Atmospheric Environment*, 35(27), 4629-4637.

- Janson, R. W. (1993). Monoterpene emissions from Scots pine and Norwegian spruce. *Journal of geophysical research: atmospheres*, 98(D2), 2839-2850.
- Jardine, K., Harley, P., Karl, T., Guenther, A., Lerdau, M., & Mak, J. E. (2008). Plant physiological and environmental controls over the exchange of acetaldehyde between forest canopies and the atmosphere. *Biogeosciences*, 5(6), 1559-1572.
- Jardine, K., Karl, T., Lerdau, M., Harley, P., Guenther, A., & Mak, J. E. (2009). Carbon isotope analysis of acetaldehyde emitted from leaves following mechanical stress and anoxia. *Plant Biology*, 11(4), 591-597.
- Jenkin, M. E., & Clemitshaw, K. C. (2000). Ozone and other secondary photochemical pollutants: chemical processes governing their formation in the planetary boundary layer. *Atmospheric Environment*, 34(16), 2499-2527.
- Jimenez, E., Lanza, B., Antinolo, M., & Albaladejo, J. (2009). Photooxidation of leaf-wound oxygenated compounds, 1-penten-3-ol, (Z)-3-hexen-1-ol, and 1-penten-3-one, initiated by OH radicals and sunlight. *Environmental science & technology*, 43(6), 1831-1837.
- Jiménez, E., Lanza, B., Garzón, A., Ballesteros, B., & Albaladejo, J. (2005). Atmospheric degradation of 2-butanol, 2-methyl-2-butanol, and 2, 3-dimethyl-2-butanol: OH kinetics and UV absorption cross sections. *The Journal of Physical Chemistry A*, 109(48), 10903-10909.
- Jiménez, E., Lanza, B., Martínez, E., & Albaladejo, J. (2007). Daytime tropospheric loss of hexanal and trans-2-hexenal: OH kinetics and UV photolysis.
- Johnson, D., & Marston, G. (2008). The gas-phase ozonolysis of unsaturated volatile organic compounds in the troposphere. *Chemical Society Reviews*, 37(4), 699-716.
- Kai, M., Effmert, U., & Piechulla, B. (2016). Bacterial-plant-interactions: approaches to unravel the biological function of bacterial volatiles in the rhizosphere. *Frontiers in microbiology*, 7, 108.
- Kaiser, E. W., Donahue, C. J., Pala, I. R., Wallington, T. J., & Hurley, M. D. (2007). Kinetics, Products, and Stereochemistry of the Reaction of Chlorine Atoms with *cis*- and *trans*-2-Butene in 10– 700 Torr of N₂ or N₂/O₂ Diluent at 297 K. *The Journal of Physical Chemistry A*, 111(7), 1286-1299.
- Kaiser, E. W., & Wallington, T. J. (1996). Pressure dependence of the reaction Cl+ C₃H₆. *The Journal of Physical Chemistry*, 100(23), 9788-9793.
- Kalalian, C. (2018). Réactivité atmosphérique des composés organiques volatils oxygénés biogéniques (aldéhydes et alcools insaturés). Etudes cinétiques de la réaction entre les radicaux peroxy et le radical nitrate (Doctoral dissertation, Reims).
- Kalalian, C., El Dib, G., Singh, H. J., Rao, P. K., Roth, E., & Chakir, A. (2020). Temperature dependent kinetic study of the gas phase reaction of ozone with 1-penten-3-ol, *cis*-2-penten-1-ol and *trans*-3-hexen-1-ol: Experimental and theoretical data. *Atmospheric Environment*, 223, 117306.
- Kalalian, C., Roth, E., & Chakir, A. (2017). Rate Coefficients for the Gas-Phase Reaction of Ozone with C₅ and C₆ Unsaturated Aldehydes. *International Journal of Chemical Kinetics*, 50(1), 47-56.
- Kalalian, C., Samir, B., Roth, E., & Chakir, A. (2019). UV absorption spectra of *trans*-2-pentenal, *trans*-2-hexenal and 2-methyl-2-pentenal. *Chemical Physics Letters*, 718, 22-26.
- Kanakidou, M., Seinfeld, J. H., Pandis, S. N., Barnes, I., Dentener, F. J., Facchini, M. C., ... & Wilson, J. (2005). Organic aerosol and global climate modelling: a review. *Atmospheric Chemistry and Physics*, 5(4), 1053-1123.
- Karl, T., Guenther, A., Lindinger, C., Jordan, A., Fall, R., & Lindinger, W. (2001). Eddy covariance measurements of oxygenated volatile organic compound fluxes from crop harvesting using a redesigned proton-transfer-reaction mass spectrometer. *Journal of Geophysical Research: Atmospheres*, 106(D20), 24157-24167.
- Keene, W. C., Stutz, J., Pszenny, A. A., Maben, J. R., Fischer, E. V., Smith, A. M., ... & Varner, R. K. (2007). Inorganic chlorine and bromine in coastal New England air during summer. *Journal of Geophysical Research: Atmospheres*, 112(D10).

- Kerdouci, J., Picquet-Varrault, B., Durand-Jolibois, R., Gaimoz, C., & Doussin, J. F. (2012). An experimental study of the gas-phase reactions of NO₃ radicals with a series of unsaturated aldehydes: trans-2-hexenal, trans-2-heptenal, and trans-2-octenal. *The Journal of Physical Chemistry A*, 116(41), 10135-10142.
- Kerr, J. A., & Sheppard, D. W. (1981). Kinetics of the reactions of hydroxyl radicals with aldehydes studied under atmospheric conditions. *Environmental science & technology*, 15(8), 960-963.
- Kesselmeier, J., Ciccioli, P., Kuhn, U., Stefani, P., Biesenthal, T., Rottenberger, S., ... & Andreae, M. O. (2002). Volatile organic compound emissions in relation to plant carbon fixation and the terrestrial carbon budget. *Global Biogeochemical Cycles*, 16(4), 73-1.
- Kesselmeier, J., Bode, K., Hofmann, U., Müller, H., Schäfer, L., Wolf, A., ... & Torres, L. (1997). Emission of short chained organic acids, aldehydes and monoterpenes from *Quercus ilex* L. and *Pinus pinea* L. in relation to physiological activities, carbon budget and emission algorithms. *Atmospheric Environment*, 31, 119-133.
- Kesselmeier, J., & Staudt, M. (1999). Biogenic volatile organic compounds (VOC): an overview on emission, physiology and ecology. *Journal of atmospheric chemistry*, 33(1), 23-88.
- Khalil, M. A. K., & Rasmussen, R. A. (1992). Forest hydrocarbon emissions: relationships between fluxes and ambient concentrations. *Journal of the Air & Waste Management Association*, 42(6), 810-813.
- Kimmerer, T. W., & Kozlowski, T. T. (1982). Ethylene, ethane, acetaldehyde, and ethanol production by plants under stress. *Plant Physiology*, 69(4), 840-847.
- Kirstine, W., Galbally, I., Ye, Y., & Hooper, M. (1998). Emissions of volatile organic compounds (primarily oxygenated species) from pasture. *Journal of Geophysical Research: Atmospheres*, 103(D9), 10605-10619.
- Kleist, E., Mentel, T. F., Andres, S., Bohne, A., Folkers, A., Kiendler-Scharr, A., ... & Wildt, J. (2012). Irreversible impacts of heat on the emissions of monoterpenes, sesquiterpenes, phenolic BVOC and green leaf volatiles from several tree species. *Biogeosciences*, 9(12), 5111.
- Klinger, L. F., Zimmerman, P. R., Greenberg, J. P., Heidt, L. E., & Guenther, A. B. (1994). Carbon trace gas fluxes along a successional gradient in the Hudson Bay lowland. *Journal of Geophysical Research: Atmospheres*, 99(D1), 1469-1494.
- Knipping, E. M., & Dabdub, D. (2003). Impact of chlorine emissions from sea-salt aerosol on coastal urban ozone. *Environmental science & technology*, 37(2), 275-284.
- Knote, C., Hodzic, A., Jimenez, J. L., Volkamer, R., Orlando, J. J., Baidar, S., ... & Zhang, Q. (2014). Simulation of semi-explicit mechanisms of SOA formation from glyoxal in aerosol in a 3-D model. *Atmospheric Chemistry & Physics*, 14(12).
- König, G., Brunda, M., Puxbaum, H., Hewitt, C. N., Duckham, S. C., & Rudolph, J. (1995). Relative contribution of oxygenated hydrocarbons to the total biogenic VOC emissions of selected mid-European agricultural and natural plant species. *Atmospheric Environment*, 29(8), 861-874.
- Koppmann, R. (Ed.). (2008). *Volatile organic compounds in the atmosphere*. John Wiley & Sons.
- Krol, M., van Leeuwen, P. J., & Lelieveld, J. (1998). Global OH trend inferred from methylchloroform measurements. *Journal of Geophysical Research: Atmospheres*, 103(D9), 10697-10711.
- Kroll, J. H., Chan, A. W., Ng, N. L., Flagan, R. C., & Seinfeld, J. H. (2007). Reactions of semivolatile organics and their effects on secondary organic aerosol formation. *Environmental science & technology*, 41(10), 3545-3550.
- Kroll, J. H., & Seinfeld, J. H. (2008). Chemistry of secondary organic aerosol: Formation and evolution of low-volatility organics in the atmosphere. *Atmospheric Environment*, 42(16), 3593-3624.
- Kulmala, M., Suni, T., Lehtinen, K. E. J., Dal Maso, M., Boy, M., Reissell, A., ... & Hari, P. (2004). A new feedback mechanism linking forests, aerosols, and climate.
- Kuzma, J., & Fall, R. (1993). Leaf isoprene emission rate is dependent on leaf development and the level of isoprene synthase. *Plant physiology*, 101(2), 435-440.

- Lamb, B., Westberg, H., Allwine, G., & Quarles, T. (1985). Biogenic hydrocarbon emissions from deciduous and coniferous trees in the United States. *Journal of Geophysical Research: Atmospheres*, 90(D1), 2380-2390.
- Laothawornkitkul, J., Taylor, J. E., Paul, N. D., & Hewitt, C. N. (2009). Biogenic volatile organic compounds in the Earth system. *New Phytologist*, 183(1), 27-51.
- Lärstad, M. A. E., Torén, K., Bake, B., & Olin, A. C. (2007). Determination of ethane, pentane and isoprene in exhaled air-effects of breath-holding, flow rate and purified air. *Acta Physiologica*, 189(1), 87-98.
- Lathiere, J., Hauglustaine, D. A., Friend, A. D., De Noblet-Ducoudré, N., Viovy, N., & Folberth, G. A. (2006). Impact of climate variability and land use changes on global biogenic volatile organic compound emissions.
- Le Crâne, J. P., Villenave, E., Hurley, M. D., Wallington, T. J., Nishida, S., Takahashi, K., & Matsumi, Y. (2004). Atmospheric chemistry of pivalaldehyde and isobutyraldehyde: Kinetics and mechanisms of reactions with Cl atoms, fate of (CH₃)₃CC(O) and (CH₃)₂CHC(O) radicals, and self-reaction kinetics of (CH₃)₃CC(O)O₂ and (CH₃)₂CHC(O)O₂ radicals. *The Journal of Physical Chemistry A*, 108(5), 795-805.
- Le Person, A., Solignac, G., Oussar, F., Daele, V., Mellouki, A., Winterhalter, R., & Moortgat, G. K. (2009). Gas phase reaction of allyl alcohol (2-propen-1-ol) with OH radicals and ozone. *Physical Chemistry Chemical Physics*, 11(35), 7619-7628.
- Leather, K. E., McGillen, M. R., & Percival, C. J. (2010). Temperature-dependent ozonolysis kinetics of selected alkenes in the gas phase: an experimental and structure-activity relationship (SAR) study. *Physical Chemistry Chemical Physics*, 12(12), 2935-2943.
- Lee, A., Goldstein, A. H., Kroll, J. H., Ng, N. L., Varutbangkul, V., Flagan, R. C., & Seinfeld, J. H. (2006). Gas-phase products and secondary aerosol yields from the photooxidation of 16 different terpenes. *Journal of Geophysical Research: Atmospheres*, 111(D17).
- Lee, B. H., Lopez-Hilfiker, F. D., Schroder, J. C., Campuzano-Jost, P., Jimenez, J. L., McDuffie, E. E., ... & Thornton, J. A. (2018). Airborne observations of reactive inorganic chlorine and bromine species in the exhaust of coal-fired power plants. *Journal of Geophysical Research: Atmospheres*, 123(19), 11-225.
- Lee, S., & Kamens, R. M. (2005). Particle nucleation from the reaction of α -pinene and O₃. *Atmospheric Environment*, 39(36), 6822-6832.
- Lelieveld, J., Butler, T. M., Crowley, J. N., Dillon, T. J., Fischer, H., Ganzeveld, L., ... & Williams, J. (2008). Atmospheric oxidation capacity sustained by a tropical forest. *Nature*, 452(7188), 737-740.
- Li, W., Chen, Y., Tong, S., Guo, Y., Zhang, Y., & Ge, M. (2018). Kinetic study of the gas-phase reaction of O₃ with three unsaturated alcohols. *Journal of Environmental Sciences*, 71, 292-299.
- Li, Z., & Pirasteh, A. (2006). Kinetic study of the reactions of atomic chlorine with several volatile organic compounds at 240–340 K. *International journal of chemical kinetics*, 38(6), 386-398.
- Liang, P., Mu, Y. J., Daële, V., & Mellouki, A. (2011). Kinetic studies of Cl reactions with 3-buten-1-ol and 2-buten-1-ol over the temperature range 298–363 K. *Chemical Physics Letters*, 502(4-6), 154-158.
- Likens, G. E., Edgerton, E. S., & Galloway, J. N. (1983). The composition and deposition of organic carbon in precipitation 1. *Tellus B*, 35(1), 16-24.
- Lin, X., Ma, Q., Yang, C., Tang, X., Zhao, W., Hu, C., ... & Zhang, W. (2016). Kinetics and mechanisms of gas phase reactions of hexenols with ozone. *RSC advances*, 6(87), 83573-83580.
- Lindinger, W., Hansel, A., & Jordan, A. (1998). On-line monitoring of volatile organic compounds at pptv levels by means of proton-transfer-reaction mass spectrometry (PTR-MS) medical applications, food control and environmental research. *International Journal of Mass Spectrometry and Ion Processes*, 173(3), 191-241.
- Lindskog, A. (1997). The influence of the biosphere on the budgets of VOC: Ethane, propane, n-butane and i-butane. *Biogenic Volatile Organic Compounds in the Atmosphere-Summary of Present Knowledge*, SPB Academic Publishers, Amsterdam, The Netherlands, 45-52.

- Lorenzo, R. (2007). Sources and characteristics of fine and ultrafine particles in ambient air (Doctoral dissertation, Université de Fribourg).
- Loreto, F., Ciccioli, P., Cecinato, A., Brancaleoni, E., Frattoni, M., & Tricoli, D. (1996). Influence of environmental factors and air composition on the emission of [alpha]-pinene from *Quercus ilex* leaves. *Plant Physiology*, 110(1), 267-275.
- Loreto, F., Fischbach, R. J., Schnitzler, J. P., Ciccioli, P., Brancaleoni, E. N. Z. O., Calfapietra, C., & Seufert, G. (2001). Monoterpene emission and monoterpene synthase activities in the Mediterranean evergreen oak *Quercus ilex* L. grown at elevated CO₂ concentrations. *Global Change Biology*, 7(6), 709-717.
- Loreto, F., & Schnitzler, J. P. (2010). Abiotic stresses and induced BVOCs. *Trends in plant science*, 15(3), 154-166.
- Lunde, G., Gether, J., Gjøns, N., & Lande, M. B. S. (1977). Organic micropollutants in precipitation in Norway. *Atmospheric Environment* (1967), 11(11), 1007-1014.
- MacDonald, R. C., & Fall, R. (1993). Detection of substantial emissions of methanol from plants to the atmosphere. *Atmospheric Environment. Part A. General Topics*, 27(11), 1709-1713.
- Macdonald, R. C., & Fall, R. (1993). Acetone emission from conifer buds. *Phytochemistry*, 34(4), 991-994.
- Madronich, S., & Flocke, S. (1999). The role of solar radiation in atmospheric chemistry. In *Environmental photochemistry* (pp. 1-26). Springer, Berlin, Heidelberg.
- Magneron, I., Thevenet, R., Mellouki, A., Le Bras, G., Moortgat, G. K., & Wirtz, K. (2002). A study of the photolysis and OH-initiated oxidation of acrolein and trans-crotonaldehyde. *The Journal of Physical Chemistry A*, 106(11), 2526-2537.
- Maiman, T. H. (1960). Stimulated optical radiation in ruby. *nature*, 187(4736), 493-494.
- Maldotti, A., Chiorboli, C., Bignozzi, C. A., Bartocci, C., & Carassiti, V. (1980). Photooxidation of 1, 3-butadiene containing systems: Rate constant determination for the reaction of acrolein with OH radicals. *International journal of chemical kinetics*, 12(12), 905-913.
- Massoli, P., Lambe, A. T., Ahern, A. T., Williams, L. R., Ehn, M., Mikkilä, J., ... & Worsnop, D. R. (2010). Relationship between aerosol oxidation level and hygroscopic properties of laboratory generated secondary organic aerosol (SOA) particles. *Geophysical Research Letters*, 37(24).
- Matsunaga, S. N., Guenther, A. B., Izawa, Y., Wiedinmyer, C., Greenberg, J. P., & Kawamura, K. (2007). Importance of wet precipitation as a removal and transport process for atmospheric water soluble carbonyls. *Atmospheric Environment*, 41(4), 790-796.
- McCall, P. J., Turlings, T. C., Loughrin, J., Proveaux, A. T., & Tumlinson, J. H. (1994). Herbivore-induced volatile emissions from cotton (*Gossypium hirsutum* L.) seedlings. *Journal of chemical ecology*, 20(12), 3039-3050.
- McGillen, M. R., Archibald, A. T., Carey, T., Leather, K. E., Shallcross, D. E., Wenger, J. C., & Percival, C. J. (2011). Structure-activity relationship (SAR) for the prediction of gas-phase ozonolysis rate coefficients: an extension towards heteroatomic unsaturated species. *Physical Chemistry Chemical Physics*, 13(7), 2842-2849.
- McGillen, M. R., Carey, T. J., Archibald, A. T., Wenger, J. C., Shallcross, D. E., & Percival, C. J. (2008). Structure-activity relationship (SAR) for the gas-phase ozonolysis of aliphatic alkenes and dialkenes. *Physical Chemistry Chemical Physics*, 10(13), 1757-1768.
- Mellouki, A., Le Bras, G., & Sidebottom, H. (2003). Kinetics and mechanisms of the oxidation of oxygenated organic compounds in the gas phase. *Chemical Reviews*, 103(12), 5077-5096.
- Mellouki, A., Wallington, T. J., & Chen, J. (2015). Atmospheric chemistry of oxygenated volatile organic compounds: impacts on air quality and climate. *Chemical reviews*, 115(10), 3984-4014.
- Mentel, T. F., Wildt, J., Kiendler-Scharr, A., Kleist, E., Tillmann, R., Maso, M. D., ... & Wahner, A. (2009). Photochemical production of aerosols from real plant emissions. *Atmospheric Chemistry & Physics Discussions*, 9(1).
- Mielke, L. H., Furgeson, A., & Osthoff, H. D. (2011). Observation of ClNO₂ in a mid-continental urban environment. *Environmental science & technology*, 45(20), 8889-8896.

- Millet, D. B., Jacob, D. J., Custer, T. G., De Gouw, J. A., Goldstein, A. H., Karl, T., ... & Williams, J. (2008). New constraints on terrestrial and oceanic sources of atmospheric methanol.
- Monks, P. S., Granier, C., Fuzzi, S., Stohl, A., Williams, M. L., Akimoto, H., ... & von Glasow, R. (2009). Atmospheric composition change—global and regional air quality. *Atmospheric environment*, 43(33), 5268-5350.
- Monson, R. K., & Fall, R. (1989). Isoprene emission from aspen leaves: influence of environment and relation to photosynthesis and photorespiration. *Plant Physiology*, 90(1), 267-274.
- Monson, R. K., Harley, P. C., Litvak, M. E., Wildermuth, M., Guenther, A. B., Zimmerman, P. R., & Fall, R. (1994). Environmental and developmental controls over the seasonal pattern of isoprene emission from aspen leaves. *Oecologia*, 99(3-4), 260-270.
- Monson, R. K., Lerdau, M. T., Sharkey, T. D., Schimel, D. S., & Fall, R. (1995). Biological aspects of constructing volatile organic compound emission inventories. *Atmospheric Environment*, 29(21), 2989-3002.
- Moortgat, G. K., Meyrahn, H., & Warneck, P. (2010). Photolysis of acetaldehyde in air: CH₄, CO and CO₂ quantum yields. *ChemPhysChem*, 11(18), 3896-3908.
- Morgan, E. D., & Tyler, R. C. (1977). Microchemical methods for the identification of volatile pheromones. *Journal of Chromatography A*, 134(1), 174-177.
- Morris, J. W., Davidovits, P., Jayne, J. T., Jimenez, J. L., Shi, Q., Kolb, C. E., ... & Cass, G. (2002). Kinetics of submicron oleic acid aerosols with ozone: A novel aerosol mass spectrometric technique. *Geophysical Research Letters*, 29(9), 71-1.
- Müller, J. F., Liu, Z., Nguyen, V. S., Stavrou, T., Harvey, J. N., & Peeters, J. (2016). The reaction of methyl peroxy and hydroxyl radicals as a major source of atmospheric methanol. *Nature communications*, 7(1), 1-11.
- Muñoz, A., Le Person, A., Le Calvé, S., Mellouki, A., Borrás, E., Daële, V., & Vera, T. (2011). Studies on atmospheric degradation of diazinon in the EUPHORE simulation chamber. *Chemosphere*, 85(5), 724-730.
- Nádasdi, R., Kovács, G., Szilágyi, I., Demeter, A., Dóbbé, S., Bérces, T., & Márta, F. (2007). Exciplex laser photolysis study of acetone with relevance to tropospheric chemistry. *Chemical physics letters*, 440(1-3), 31-35.
- Nakamura, S., & Hatanaka, A. (2002). Green-leaf-derived C₆-aroma compounds with potent antibacterial action that act on both gram-negative and gram-positive bacteria. *Journal of Agricultural and Food Chemistry*, 50(26), 7639-7644.
- Nelson, L., Rattigan, O., Neavyn, R., Sidebottom, H., Treacy, J., & Nielsen, O. J. (1990). Absolute and relative rate constants for the reactions of hydroxyl radicals and chlorine atoms with a series of aliphatic alcohols and ethers at 298 K. *International journal of chemical kinetics*, 22(11), 1111-1126.
- Nemecek-Marshall, M., MacDonald, R. C., Franzen, J. J., Wojciechowski, C. L., & Fall, R. (1995). Methanol emission from leaves (enzymatic detection of gas-phase methanol and relation of methanol fluxes to stomatal conductance and leaf development). *Plant Physiology*, 108(4), 1359-1368.
- Ng, N. L., Brown, S. S., Archibald, A. T., Atlas, E., Cohen, R. C., Crowley, J. N., ... & Zaveri, R. A. (2017). Nitrate radicals and biogenic volatile organic compounds: oxidation, mechanisms, and organic aerosol. *Atmospheric chemistry and physics*, 17(3), 2103.
- Ng, N. L., Chhabra, P. S., Chan, A. W. H., Surratt, J. D., Kroll, J. H., Kwan, A. J., ... & Seinfeld, J. H. (2007). Effect of NO_x level on secondary organic aerosol (SOA) formation from the photooxidation of terpenes.
- Nishino, N., Arey, J., & Atkinson, R. (2009). Rate constants for the gas-phase reactions of OH radicals with a series of C₆–C₁₄ alkenes at 299 ± 2 K. *The Journal of Physical Chemistry A*, 113(5), 852-857.
- O'Connor, M. P., Wenger, J. C., Mellouki, A., Wirtz, K., & Muñoz, A. (2006). The atmospheric photolysis of E-2-hexenal, Z-3-hexenal and E, E-2, 4-hexadienal. *Physical Chemistry Chemical Physics*, 8(44), 5236-5246.

- O'Dwyer, M. A., Carey, T. J., Healy, R. M., Wenger, J. C., Picquet-Varrault, B., & Doussin, J. F. (2010). The gas-phase ozonolysis of 1-penten-3-ol, (Z)-2-penten-1-ol and 1-penten-3-one: Kinetics, products and secondary organic aerosol formation. *Zeitschrift für Physikalische Chemie*, 224(7), 1059.
- Odum, J. R., Hoffmann, T., Bowman, F., Collins, D., Flagan, R. C., & Seinfeld, J. H. (1996). Gas/particle partitioning and secondary organic aerosol yields. *Environmental Science & Technology*, 30(8), 2580-2585.
- Olariu, R. I., Barnes, I., Bejan, I., Arsene, C., Vione, D., Klotz, B., & Becker, K. H. (2013). FT-IR Product Study of the Reactions of NO₃ Radicals With ortho-, meta-, and para-Cresol. *Environmental science & technology*, 47(14), 7729-7738.
- Orlando, J. J., & Tyndall, G. S. (2002). Mechanisms for the reactions of OH with two unsaturated aldehydes: crotonaldehyde and acrolein. *The Journal of Physical Chemistry A*, 106(51), 12252-12259.
- Orlando, J. J., Tyndall, G. S., Apel, E. C., Riemer, D. D., & Paulson, S. E. (2003). Rate coefficients and mechanisms of the reaction of Cl-atoms with a series of unsaturated hydrocarbons under atmospheric conditions. *International Journal of Chemical Kinetics*, 35(8), 334-353.
- Osseiran, N., Romanias, M. N., Gaudion, V., Angelaki, M. E., Papadimitriou, V. C., Tomas, A., ... & Thevenet, F. (2020). Development and validation of a thermally regulated atmospheric simulation chamber (THALAMOS): A versatile tool to simulate atmospheric processes. *Journal of Environmental Sciences*.
- Owen, S. M., Boissard, C., & Hewitt, C. N. (2001). Volatile organic compounds (VOCs) emitted from 40 Mediterranean plant species: VOC speciation and extrapolation to habitat scale. *Atmospheric Environment*, 35(32), 5393-5409.
- Pankow, J. F. (1994). An absorption model of gas/particle partitioning of organic compounds in the atmosphere. *Atmospheric Environment*, 28(2), 185-188.
- Papagni, C., Arey, J., & Atkinson, R. (2001). Rate constants for the gas-phase reactions of OH radicals with a series of unsaturated alcohols. *International Journal of Chemical Kinetics*, 33(2), 142-147.
- Parker, J. K., & Espada-Jallad, C. (2009). Kinetics of the gas-phase reactions of OH and NO₃ radicals and O₃ with allyl alcohol and allyl isocyanate. *The Journal of Physical Chemistry A*, 113(36), 9814-9824.
- Paulson, S. E., Chung, M. Y., & Hasson, A. S. (1999). OH radical formation from the gas-phase reaction of ozone with terminal alkenes and the relationship between structure and mechanism. *The Journal of Physical Chemistry A*, 103(41), 8125-8138.
- Peirone, S. A., Barrera, J. A., Taccone, R. A., Cometto, P. M., & Lane, S. I. (2014). Relative rate coefficient measurements of OH radical reactions with (Z)-2-hexen-1-ol and (E)-3-hexen-1-ol under simulated atmospheric conditions. *Atmospheric Environment*, 85, 92-98.
- Peiser, G. D., & Yang, S. F. (1979). Ethylene and ethane production from sulfur dioxide-injured plants. *Plant physiology*, 63(1), 142-145.
- Peñuelas, J., Asensio, D., Tholl, D., Wenke, K., Rosenkranz, M., Piechulla, B., & Schnitzler, J. P. (2014). Biogenic volatile emissions from the soil. *Plant, cell & environment*, 37(8), 1866-1891.
- Peñuelas, J., & Llusià, J. (2003). BVOCs: plant defense against climate warming?. *Trends in plant science*, 8(3), 105-109.
- Peñuelas, J., & Llusià, J. (2001). The complexity of factors driving volatile organic compound emissions by plants. *Biologia Plantarum*, 44(4), 481-487.
- Peñuelas, J., & Staudt, M. (2010). BVOCs and global change. *Trends in plant science*, 15(3), 133-144.
- Pfrang, C., Martin, R. S., Canosa-Mas, C. E., & Wayne, R. P. (2006). Gas-phase reactions of NO₃ and N₂O₅ with (Z)-hex-4-en-1-ol, (Z)-hex-3-en-1-ol ('leaf alcohol'), (E)-hex-3-en-1-ol, (Z)-hex-2-en-1-ol and (E)-hex-2-en-1-ol. *Physical Chemistry Chemical Physics*, 8(3), 354-363.
- Pichersky, E., Raguso, R. A., Lewinsohn, E., & Croteau, R. (1994). Floral scent production in *Clarkia* (Onagraceae) (I. Localization and developmental modulation of monoterpene emission and linalool synthase activity). *Plant Physiology*, 106(4), 1533-1540.

- Plass-Dülmer, C., Koppmann, R., Ratte, M., & Rudolph, J. (1995). Light nonmethane hydrocarbons in seawater. *Global Biogeochemical Cycles*, 9(1), 79-100.
- Priya, A. M., El Dib, G., Senthilkumar, L., Sleiman, C., Tomas, A., Canosa, A., & Chakir, A. (2015). An experimental and theoretical study of the kinetics of the reaction between 3-hydroxy-3-methyl-2-butanone and OH radicals. *Rsc Advances*, 5(34), 26559-26568.
- Ragains, M. L., & Finlayson-Pitts, B. J. (1997). Kinetics and mechanism of the reaction of Cl atoms with 2-methyl-1, 3-butadiene (isoprene) at 298 K. *The Journal of Physical Chemistry A*, 101(8), 1509-1517.
- Rasmussen, R. A., & Went, F. W. (1965). Volatile organic material of plant origin in the atmosphere. *Proceedings of the National Academy of Sciences of the United States of America*, 53(1), 215.
- Rayez, M. T., Rayez, J. C., Kerdouci, J., & Picquet-Varrault, B. (2014). Theoretical study of the gas-phase reactions of NO₃ radical with a series of trans-2-unsaturated aldehydes: From acrolein to trans-2-octenal. *The Journal of Physical Chemistry A*, 118(28), 5149-5155.
- Ren, X., Brune, W. H., Oliger, A., Metcalf, A. R., Simpas, J. B., Shirley, T., ... & Hou, J. (2006). OH, HO₂, and OH reactivity during the PMTACS-NY Whiteface Mountain 2002 campaign: Observations and model comparison. *Journal of Geophysical Research: Atmospheres*, 111(D10).
- Ren, Y., Grosselin, B., Daële, V., & Mellouki, A. (2017). Investigation of the reaction of ozone with isoprene, methacrolein and methyl vinyl ketone using the HELIOS chamber. *Faraday Discussions*, 200, 289-311.
- Roberts, G. C., Day, D. A., Russell, L. M., Dunlea, E. J., Jimenez, J. L., Tomlinson, J. M., ... & Clarke, A. D. (2010). Characterization of particle cloud droplet activity and composition in the free troposphere and the boundary layer during INTEX-B. 1foldr Import 2019-10-08 Batch 14.
- Rodríguez, D., Rodríguez, A., Notario, A., Aranda, A., Diaz-de-Mera, Y., & Marínez, E. (2005). Kinetic study of the gas-phase reaction of atomic chlorine with a series of aldehydes.
- Rodríguez, A., Rodríguez, D., Garzón, A., Soto, A., Aranda, A., & Notario, A. (2010). Kinetics and mechanism of the atmospheric reactions of atomic chlorine with 1-penten-3-ol and (Z)-2-penten-1-ol: an experimental and theoretical study. *Physical Chemistry Chemical Physics*, 12(38), 12245-12258.
- Rodriguez, D., Rodriguez, A., Soto, A., Aranda, A., Diaz-de-Mera, Y., & Notario, A. (2008). Kinetics of the reactions of Cl atoms with 2-buten-1-ol, 2-methyl-2-propen-1-ol, and 3-methyl-2-buten-1-ol as a function of temperature. *Journal of atmospheric chemistry*, 59(3), 187-197.
- Rodríguez, A., Rodríguez, D., Soto, A., Notario, A., Aranda, A., Díaz-de-Mera, Y., & Bravo, I. (2007). Relative rate measurements of reactions of unsaturated alcohols with atomic chlorine as a function of temperature. *Atmospheric Environment*, 41(22), 4693-4702.
- Rosenthal, G. A., & Berenbaum, M. R. (2012). *Herbivores: their interactions with secondary plant metabolites: ecological and evolutionary processes* (Vol. 2). Academic Press.
- Rowley, D. M., Lesclaux, R., Lightfoot, P. D., Noziere, B., Wallington, T. J., & Hurley, M. D. (1992). Kinetic and mechanistic studies of the reactions of cyclopentylperoxy and cyclohexylperoxy radicals with hydroperoxy radical. *The Journal of Physical Chemistry*, 96(12), 4889-4894.
- Rudolph, J. (1995). The tropospheric distribution and budget of ethane. *Journal of Geophysical Research: Atmospheres*, 100(D6), 11369-11381.
- Rudolph, J., Koppmann, R., & Plass-Dülmer, C. (1996). The budgets of ethane and tetrachloroethene: Is there evidence for an impact of reactions with chlorine atoms in the troposphere?. *Atmospheric Environment*, 30(10-11), 1887-1894.
- Rudolph, J., Ramacher, B., Plass-Dülmer, C., Müller, K. P., & Koppmann, R. (1997). The indirect determination of chlorine atom concentration in the troposphere from changes in the patterns of non-methane hydrocarbons. *Tellus B: Chemical and Physical Meteorology*, 49(5), 592-601.

- Sakulyanontvittaya, T., Duhl, T., Wiedinmyer, C., Helmig, D., Matsunaga, S., Potosnak, M., ... & Guenther, A. (2008). Monoterpene and sesquiterpene emission estimates for the United States. *Environmental science & technology*, 42(5), 1623-1629.
- Sanadze, G. A. (2004). Biogenic isoprene (a review). *Russian Journal of Plant Physiology*, 51(6), 729-741.
- Sanhueza, E., & Andreae, M. O. (1991). Emission of formic and acetic acids from tropical savanna soils. *Geophysical Research Letters*, 18(9), 1707-1710.
- Santoemma, G. (2018). Recent methodologies for studying the soil organic matter. *Applied Soil Ecology*, 123, 546-550.
- Sato, K., Klotz, B., Taketsugu, T., & Takayanagi, T. (2004). Kinetic measurements for the reactions of ozone with crotonaldehyde and its methyl derivatives and calculations of transition-state theory. *Physical Chemistry Chemical Physics*, 6(15), 3969-3976.
- Schlitt, H., Knoepfel, H., Versino, B., Peil, A., Schauenburg, H., & Vissers, H. (1980). Organics in air: Sampling and identification. In *Sampling and Analysis of Toxic Organics in the Atmosphere*. ASTM International.
- Schoon, N., Amelynck, C., Debie, E., Bultinck, P., & Arijs, E. (2007). A selected ion flow tube study of the reactions of H₃O⁺, NO⁺ and O₂⁺ with a series of C₅, C₆ and C₈ unsaturated biogenic alcohols. *International Journal of Mass Spectrometry*, 263(2-3), 127-136.
- Schuman, M. C., Valim, H. A., & Joo, Y. (2016). Temporal dynamics of plant volatiles: Mechanistic bases and functional consequences. In *Deciphering Chemical Language of Plant Communication* (pp. 3-34). Springer, Cham.
- Seakins, P. W. (2010). A brief review of the use of environmental chambers for gas phase studies of kinetics, chemical mechanisms and characterisation of field instruments. In *EPJ Web of Conferences* (Vol. 9, pp. 143-163). EDP Sciences.
- Seco, R., Penuelas, J., & Filella, I. (2007). Short-chain oxygenated VOCs: Emission and uptake by plants and atmospheric sources, sinks, and concentrations. *Atmospheric Environment*, 41(12), 2477-2499.
- Seinfeld, J. H., & Pandis, S. N. (2016). *Atmospheric chemistry and physics: from air pollution to climate change*. John Wiley & Sons.
- Sharkey, T. D. (1996). Isoprene synthesis by plants and animals. *Endeavour*, 20(2), 74-78.
- Sharkey, T. D., Chen, X., & Yeh, S. (2001). Isoprene increases thermotolerance of fosmidomycin-fed leaves. *Plant Physiology*, 125(4).
- Sharkey, T. D., Wiberley, A. E., & Donohue, A. R. (2008). Isoprene emission from plants: why and how. *Annals of botany*, 101(1), 5-18.
- Shen, H., Chen, Z., Li, H., Qian, X., Qin, X., & Shi, W. (2018). Gas-particle partitioning of carbonyl compounds in the ambient atmosphere. *Environmental science & technology*, 52(19), 10997-11006.
- Shulaev, V., Silverman, P., & Raskin, I. (1997). Airborne signalling by methyl salicylate in plant pathogen resistance. *Nature*, 385(6618), 718-721.
- Simon, H., Kimura, Y., McGaughey, G., Allen, D. T., Brown, S. S., Osthoff, H. D., ... & Lee, D. (2009). Modeling the impact of ClNO₂ on ozone formation in the Houston area. *Journal of Geophysical Research: Atmospheres*, 114(D7).
- Simpson, D., Winiwarter, W., Börjesson, G., Cinderby, S., Ferreiro, A., Guenther, A., ... & Öquist, M. G. (1999). Inventorying emissions from nature in Europe. *Journal of Geophysical Research: Atmospheres*, 104(D7), 8113-8152.
- Sindelarova, K., Granier, C., Bouarar, I., Guenther, A., Tilmes, S., Stavrakou, T., ... & Knorr, W. (2014). Global data set of biogenic VOC emissions calculated by the MEGAN model over the last 30 years.
- Singh, H. B., O'hara, D., Herlth, D., Sachse, W., Blake, D. R., Bradshaw, J. D., ... & Crutzen, P. J. (1994). Acetone in the atmosphere: Distribution, sources, and sinks. *Journal of Geophysical Research: Atmospheres*, 99(D1), 1805-1819.

- Singh, H. B., O'hara, D., Herlth, D., Sachse, W., Blake, D. R., Bradshaw, J. D., ... & Crutzen, P. J. (1994). Acetone in the atmosphere: Distribution, sources, and sinks. *Journal of Geophysical Research: Atmospheres*, 99(D1), 1805-1819.
- Singh, H. B., Thakur, A. N., Chen, Y. E., & Kanakidou, M. (1996). Tetrachloroethylene as an indicator of low Cl atom concentrations in the troposphere. *Geophysical Research Letters*, 23(12), 1529-1532.
- Singsaas, E. L., Lerdau, M., Winter, K., & Sharkey, T. D. (1997). Isoprene increases thermotolerance of isoprene-emitting species. *Plant physiology*, 115(4), 1413-1420.
- Sleiman, C., González, S., Klippenstein, S. J., Talbi, D., El Dib, G., & Canosa, A. (2016). Pressure dependent low temperature kinetics for $\text{CN} + \text{CH}_3\text{CN}$: competition between chemical reaction and van der Waals complex formation. *Physical Chemistry Chemical Physics*, 18(22), 15118-15132.
- Smith, D., Španěl, P., & Dryahina, K. (2019). H_3O^+ , NO^+ and O_2^+ reactions with saturated and unsaturated monoketones and diones; focus on hydration of product ions. *International Journal of Mass Spectrometry*, 435, 173-180.
- Solomon, S., Manning, M., Marquis, M., & Qin, D. (2007). *Climate change 2007-the physical science basis: Working group I contribution to the fourth assessment report of the IPCC (Vol. 4)*. Cambridge university press.
- Španěl, P., & Smith, D. (1999). Selected ion flow tube studies of the reactions of H_3O^+ , NO^+ , and O_2^+ with several aromatic and aliphatic monosubstituted halocarbons. *International journal of mass spectrometry*, 189(2-3), 213-223.
- Spicer, C. W., Chapman, E. G., Finlayson-Pitts, B. J., Plastringe, R. A., Hubbe, J. M., Fast, J. D., & Berkowitz, C. M. (1998). Unexpectedly high concentrations of molecular chlorine in coastal air. *Nature*, 394(6691), 353-356.
- Spielmann, F. M., Langebner, S., Ghirardo, A., Hansel, A., Schnitzler, J. P., & Wohlfahrt, G. (2017). Isoprene and α -pinene deposition to grassland mesocosms. *Plant and Soil*, 410(1-2), 313-322.
- Staudt, M., Wolf, A., & Kesselmeier, J. (2000). Influence of environmental factors on the emissions of gaseous formic and acetic acids from orange (*Citrus sinensis* L.) foliage. *Biogeochemistry*, 48(2), 199-216.
- Stavrakou, T., Guenther, A., Razavi, A., Clarisse, L., Clerbaux, C., Coheur, P. F., ... & Müller, J. F. (2011). First space-based derivation of the global atmospheric methanol emission fluxes.
- Steinbrecher, R., Rappenglück, B., Hansel, A., Graus, M., Klemm, O., Held, A., ... & Nowak, A. (2004). The emissions of biogenic volatile organic compounds (BVOC) and their relevance to atmospheric particle dynamics. In *Biogeochemistry of Forested Catchments in a Changing Environment* (pp. 215-232). Springer, Berlin, Heidelberg.
- Szabó, E., Tarmoul, J., Tomas, A., Fittschen, C., Dóbbé, S., & Coddeville, P. (2009). Kinetics of the $\bullet\text{OH}$ -radical initiated reactions of acetic acid and its deuterated isomers. *Reaction Kinetics and Catalysis Letters*, 96(2), 299-309.
- Tadić, J., Juranić, I., & Moortgat, G. K. (2001). Pressure dependence of the photooxidation of selected carbonyl compounds in air: n-butanal and n-pentanal. *Journal of Photochemistry and Photobiology A: Chemistry*, 143(2-3), 169-179.
- Talbot, R. W., Beecher, K. M., Harriss, R. C., & Cofer III, W. R. (1988). Atmospheric geochemistry of formic and acetic acids at a mid-latitude temperate site. *Journal of Geophysical Research: Atmospheres*, 93(D2), 1638-1652.
- Tang, Y., & Zhu, L. (2004). Wavelength-Dependent Photolysis of n-Hexanal and n-Heptanal in the 280–330-nm Region. *The Journal of Physical Chemistry A*, 108(40), 8307-8316.
- Tanner, R. L., & Zielinska, B. (1994). Determination of the biogenic emission rates of species contributing to VOC in the San Joaquin Valley of California. *Atmospheric Environment*, 28(6), 1113-1120.
- Teruel, M. A., Achad, M., & Blanco, M. B. (2009). Kinetic study of the reactions of Cl atoms with α , β -unsaturated carbonyl compounds at atmospheric pressure and structure activity relations (SARs). *Chemical Physics Letters*, 479(1-3), 25-29.

- Thévenet, R., Mellouki, A., & Le Bras, G. (2000). Kinetics of OH and Cl reactions with a series of aldehydes. *International Journal of Chemical Kinetics*, 32(11), 676-685.
- Thompson, A. M. (1992). The oxidizing capacity of the Earth's atmosphere: Probable past and future changes. *Science*, 256(5060), 1157-1165.
- Thornton, J. A., Kercher, J. P., Riedel, T. P., Wagner, N. L., Cozic, J., Holloway, J. S., ... & Brown, S. S. (2010). A large atomic chlorine source inferred from mid-continental reactive nitrogen chemistry. *Nature*, 464(7286), 271-274.
- Tingey, D. T., Evans, R., & Gumpertz, M. (1981). Effects of environmental conditions on isoprene emission from live oak. *Planta*, 152(6), 565-570.
- Toome, M., Randjärv, P., Copolovici, L., Niinemets, Ü., Heinsoo, K., Luik, A., & Noe, S. M. (2010). Leaf rust induced volatile organic compounds signalling in willow during the infection. *Planta*, 232(1), 235-243.
- Treacy, J., Hag, M. E., O'Farrell, D., & Sidebottom, H. (1992). Reactions of ozone with unsaturated organic compounds. *Berichte der Bunsengesellschaft für physikalische Chemie*, 96(3), 422-427.
- Tuazon, E. C., Aschmann, S. M., Arey, J., & Atkinson, R. (1997). Products of the gas-phase reactions of O₃ with a series of methyl-substituted ethenes. *Environmental science & technology*, 31(10), 3004-3009.
- Turnipseed, A. A., Andersen, P. C., Williford, C. J., Ennis, C. A., & Birks, J. W. (2017). Use of a heated graphite scrubber as a means of reducing interferences in UV-absorbance measurements of atmospheric ozone. *Atmospheric Measurement Techniques*, 10(6).
- Turpin, E. (2004). Cinétique et mécanisme de dégradation atmosphérique de trois composés organiques volatils: l'acétone, le phénol et le catéchol (Doctoral dissertation, Université des Sciences et Technologie de Lille-Lille I).
- Turpin, E., Tomas, A., Fittschen, C., Devolder, P., & Galloo, J. C. (2006). Acetone-h₆ or-d₆+ OH reaction products: Evidence for heterogeneous formation of acetic acid in a simulation chamber. *Environmental science & technology*, 40(19), 5956-5961.
- Uchida, R., Sato, K., & Imamura, T. (2015). Gas-phase Ozone Reactions with Z-3-Hexenal and Z-3-Hexen-1-ol: Formation Yields of OH Radical, Propanal, and Ethane. *Chemistry Letters*, 44(4), 457-458.
- Ullerstam, M., Ljungström, E., & Langer, S. (2001). Reactions of acrolein, crotonaldehyde and pivalaldehyde with Cl atoms: structure-activity relationship and comparison with OH and NO₃ reactions. *Physical Chemistry Chemical Physics*, 3(6), 986-992.
- Uppendra, B., Prasanna, D. L., & Rajakumar, B. (2012). Kinetic parameters for the reaction of OH radical initiated atmospheric oxidation of (E)-2-pentenal: ab initio and transition state theory calculations. *Current Science*, 460-469.
- US EPA, O., 2014. Particle Pollution and Cardiovascular Effects. URL <https://www.epa.gov/pmcourse/particle-pollution-and-cardiovascular-effects>.
- Van Dam, N. M., & Bouwmeester, H. J. (2016). Metabolomics in the rhizosphere: tapping into belowground chemical communication. *Trends in plant science*, 21(3), 256-265.
- Volkamer, R., Spietz, P., Burrows, J., & Platt, U. (2005). High-resolution absorption cross-section of glyoxal in the UV-vis and IR spectral ranges. *Journal of Photochemistry and Photobiology A: Chemistry*, 172(1), 35-46.
- Vuorinen, T., Reddy, G. V. P., Nerg, A. M., & Holopainen, J. K. (2004). Monoterpene and herbivore-induced emissions from cabbage plants grown at elevated atmospheric CO₂ concentration. *Atmospheric Environment*, 38(5), 675-682.
- Walavalkar, M., Sharma, A., Alwe, H. D., Pushpa, K. K., Dhanya, S., Naik, P. D., & Bajaj, P. N. (2013). Cl atom initiated oxidation of 1-alkenes under atmospheric conditions. *Atmospheric Environment*, 67, 93-100.
- Wallace, J. M., & Hobbs, P. V. (2006). *Atmospheric science: an introductory survey* (Vol. 92). Elsevier.

- Wallington, T. J., Skewes, L. M., Siegl, W. O., Wu, C. H., & Japar, S. M. (1988). Gas phase reaction of Cl atoms with a series of oxygenated organic species at 295 K. *International journal of chemical kinetics*, 20(11), 867-875.
- Wang, T., Španěl, P., & Smith, D. (2003). Selected ion flow tube, SIFT, studies of the reactions of H₃O⁺, NO⁺ and O₂⁺ with eleven C₁₀H₁₆ monoterpenes. *International Journal of Mass Spectrometry*, 228(1), 117-126.
- Wang, J., Doussin, J. F., Perrier, S., Perraudin, E., Katrib, Y., Pangui, E., & Picquet-Varrault, B. (2011). Design of a new multi-phase experimental simulation chamber for atmospheric photo-smog, aerosol and cloud chemistry research. *Atmospheric Measurement Techniques*, 4(11), 2465.
- Wang, N., Jorga, S. D., Pierce, J. R., Donahue, N. M., & Pandis, S. N. (2018). Particle wall-loss correction methods in smog chamber experiments. *Atmospheric Measurement Techniques*, 11(12), 6577-6588.
- Wang, W., Ezell, M. J., Ezell, A. A., Soskin, G., & Finlayson-Pitts, B. J. (2002). Rate constants for the reactions of chlorine atoms with a series of unsaturated aldehydes and ketones at 298 K: structure and reactivity. *Physical Chemistry Chemical Physics*, 4(10), 1824-1831.
- Wayne, R. P., & Gemeinschaften, G. W. E. (1990). The nitrate radical: physics, chemistry, and the atmosphere. na.
- Wegener, R., Brauers, T., Koppmann, R., Rodríguez Bares, S., Rohrer, F., Tillmann, R., ... & Wisthaler, A. (2007). Simulation chamber investigation of the reactions of ozone with short-chained alkenes. *Journal of Geophysical Research: Atmospheres*, 112(D13).
- Went, F. W. (1960). Blue hazes in the atmosphere. *Nature*, 187(4738), 641-643.
- Wildermuth, M. C., & Fall, R. (1996). Light-dependent isoprene emission (characterization of a thylakoid-bound isoprene synthase in *Salix discolor* chloroplasts). *Plant Physiology*, 112(1), 171-182.
- Wildt, J., Kobel, K., Schuh-Thomas, G., & Heiden, A. C. (2003). Emissions of oxygenated volatile organic compounds from plants Part II: emissions of saturated aldehydes. *Journal of Atmospheric Chemistry*, 45(2), 173-196.
- Williams, J. (2004). Organic trace gases in the atmosphere: an overview. *Environmental Chemistry*, 1(3), 125-136.
- Winer, A. M., Arey, J., Atkinson, R., Aschmann, S. M., Long, W. D., Morrison, C. L., & Olszyk, D. M. (1992). Emission rates of organics from vegetation in California's Central Valley. *Atmospheric Environment. Part A. General Topics*, 26(14), 2647-2659.
- Wingenter, O. W., Blake, D. R., Blake, N. J., Sive, B. C., Rowland, F. S., Atlas, E., & Flocke, F. (1999). Tropospheric hydroxyl and atomic chlorine concentrations, and mixing timescales determined from hydrocarbon and halocarbon measurements made over the Southern Ocean. *Journal of Geophysical Research: Atmospheres*, 104(D17), 21819-21828.
- Winiwarter, W., Puxbaum, H., Fuzzi, S., Facchini, M. C., Orsi, G., Beltz, N., ... & Jaeschke, W. (1988). Organic acid gas and liquid-phase measurements in Po Valley fall-winter conditions in the presence of fog. *Tellus B*, 40(5), 348-357.
- Winterhalter, R., Neeb, P., Grossmann, D., Kolloff, A., Horie, O., & Moortgat, G. (2000). Products and mechanism of the gas phase reaction of ozone with β -pinene. *Journal of Atmospheric Chemistry*, 35(2), 165-197.
- Witter, M., Berndt, T., Böge, O., Stratmann, F., & Heintzenberg, J. (2002). Gas-phase ozonolysis: Rate coefficients for a series of terpenes and rate coefficients and OH yields for 2-methyl-2-butene and 2, 3-dimethyl-2-butene. *International journal of chemical kinetics*, 34(6), 394-403.
- Xing, J. H., Ono, M., Kuroda, A., Obi, K., Sato, K., & Imamura, T. (2012). Kinetic study of the daytime atmospheric fate of (Z)-3-hexenal. *The Journal of Physical Chemistry A*, 116(33), 8523-8529.
- Yakir, E., Hilman, D., Harir, Y., & Green, R. M. (2007). Regulation of output from the plant circadian clock. *The FEBS journal*, 274(2), 335-345.

- Yan, C., Kocevskaja, S., & Krasnoperov, L. N. (2016). Kinetics of the reaction of CH₃O₂ radicals with OH studied over the 292–526 K temperature range. *The Journal of Physical Chemistry A*, 120(31), 6111-6121.
- Yang, S. F., & Hoffman, N. E. (1984). Ethylene biosynthesis and its regulation in higher plants. *Annual review of plant physiology*, 35(1), 155-189.
- Yaws, C. L. (2015). *The Yaws handbook of vapor pressure: Antoine coefficients*. Gulf Professional Publishing.
- Yokouchi, Y., & Ambe, Y. (1984). Factors affecting the emission of monoterpenes from red pine (*Pinus densiflora*). *Plant Physiology*, 75(4), 1009-1012.
- Young, C. J., Washenfelder, R. A., Edwards, P. M., Parrish, D. D., Gilman, J. B., Kuster, W. C., ... & Brown, S. S. (2014). Chlorine as a primary radical: evaluation of methods to understand its role in initiation of oxidative cycles. *Atmospheric Chemistry and Physics*, 14(7), 3427-3440.
- Zagrobelny, M., & Møller, B. L. (2011). Cyanogenic glucosides in the biological warfare between plants and insects: the burnet moth-birdsfoot trefoil model system. *Phytochemistry*, 72(13), 1585-1592.
- Zhang, Y., Gong, Z., de Sa, S., Bateman, A. P., Liu, Y., Li, Y., ... & Martin, S. T. (2018). Production and measurement of organic particulate matter in the harvard environmental chamber. *JoVE (Journal of Visualized Experiments)*, (141), e55685.
- Zhao, Z., Husainy, S., & Smith, G. D. (2011). Kinetics studies of the gas-phase reactions of NO₃ radicals with series of 1-alkenes, dienes, cycloalkenes, alkenols, and alkenals. *The Journal of Physical Chemistry A*, 115(44), 12161-12172.

List of Publications

1. The reaction of hydroxyl and methylperoxy radicals is not a major source of atmospheric methanol. *Natures communications*, 2018. (Published)
2. Article in the book. *Voir l'invisible-Puits Fleuri*, 2019. (Published)
3. Kinetic Measurements of Cl Atom Reactions with C₅–C₈ Unsaturated Alcohols. *Atmosphere*, 2020. (Published)
4. Gas-phase ozonolysis of trans-2-hexenal: Kinetics, products, mechanism and SOA formation. *Atmospheric Environment*, 2020. (Published)
5. An experimental study of the gas-phase reaction between Cl atoms and trans-2-pentenal: kinetics, products and SOA formation. *Atmospheric Environment*, 2020. (Published)
6. Ozone reaction kinetics of C₅–C₈ unsaturated alcohols of biogenic interest. (In preparation)
7. Gas-phase ozonolysis of trans-2-pentenal: Kinetics, products, mechanism and SOA formation. (In preparation)
8. IR and UV absorption of C₅–C₇ unsaturated aldehydes: Contribution to the atmospheric transmission and tropospheric lifetimes. (In preparation)
9. An experimental study of the gas-phase reaction between Cl atoms and trans-2-hexenal: kinetics, products and SOA formation. (In preparation)
10. An experimental study of the gas-phase reaction between Cl atoms and trans-2-heptenal: kinetics, products and SOA formation. (In preparation)
11. Kinetic Measurements of hydroxyl radicals Reactions with of C₅–C₆ unsaturated aldehydes of biogenic interest. (In preparation)

Résumé de la thèse en français

Ce manuscrit présente les travaux que j'ai réalisés au cours de ma thèse de doctorat dans le cadre d'une collaboration entre l'IMT Lille Douai et l'Institut de Physique de Rennes (IPR). Les résultats présentés sont issus d'expériences de laboratoire réalisées en collaboration avec quatre laboratoires : "Le Centre d'Enseignement, de Recherche et d'Innovation (CERI)-Energie et Environnement de l'IMT Lille Douai, le département "Physique Moléculaire" de l'Institut de Physique de Rennes, le laboratoire de l'Université de Wuppertal (Allemagne) et le laboratoire de l'Université UCLM (Espagne).

Ce travail s'inscrit dans le cadre du programme national LEFE "Les Enveloppes Fluides et l'Environnement" coordonné par l'INSU-CNRS, visant à mieux comprendre le fonctionnement de l'atmosphère et de l'océan et leurs interactions avec les autres composantes du système climatique. Notre travail représente une partie de l'axe "CHAT-CHimie Atmosphérique" qui vise à mieux comprendre et prédire les émissions de polluants, leurs transformations, leurs dispersions dans l'atmosphère, leurs dépôts et à estimer leurs impacts sur l'environnement et la qualité de l'air.

Ce travail de thèse se concentre sur une meilleure compréhension de la dégradation des composés organiques volatils (COVO) dans l'atmosphère. Ces composés sont principalement émis par des sources biogéniques, jouent un rôle majeur dans la chimie de l'atmosphère, le changement climatique, l'environnement et la santé publique. Il a été récemment démontré que ces émissions augmentent en cas de stress biotique et/ou abiotique. Les COVO biogéniques peuvent subir une variété de réactions, tant chimiques que photolytiques, et ils sont impliqués dans la formation d'Aérosols Organiques Secondaires (AOS).

Ces composés ont été détectés dans diverses régions, mais il y a très peu d'informations sur leurs processus de dégradation sous conditions troposphériques. La compréhension des mécanismes d'oxydation de ces espèces est d'un intérêt fondamental et fournit des données cruciales pour les modèles atmosphériques qui sont utilisés par les responsables politiques pour formuler et décider des stratégies d'amélioration de la qualité de l'air.

Cette thèse vise à améliorer les connaissances actuelles sur le comportement de ces COVO, pour une meilleure compréhension de leur impact sur la chimie atmosphérique. Dans ce travail, nous nous sommes particulièrement intéressés à une série d'aldéhydes et d'alcools insaturés ($\geq C_5$) : Trans-2-Pentenal (T2P), Trans-2-Hexenal (T2H), Trans-2-Heptenal (T2Hep), Cis-2-Penten-1-ol (C2P-OL), Trans-2-Hexen-1-ol (T2H-OL), Trans-3-Hexen-1-OL (T3H-OL), Cis-3-Hexen-1-OL (C3H-OL), 1-Octen-3-ol (1O-3-OL) et Trans-2-Octen-2-OL (T2O-OL).

Ces composés peuvent être soit émis directement par la végétation, en particulier en présence de conditions de stress (Konig, 1995), soit formés in situ dans l'atmosphère à partir d'hydrocarbures par des réactions chimiques et photochimiques. La sélection des COVO biogéniques étudiés et de leurs réactions d'oxydation a été basée sur leur intérêt dans la chimie de l'atmosphère.

Cette thèse a pour but d'étudier la réactivité des COV biogéniques sélectionnés avec les principaux oxydants atmosphériques (O_3 , atomes de Cl et radicaux OH). Les réactions étudiées ont été générées dans des réacteurs de laboratoire simulant les conditions physiques et chimiques de la troposphère. Les principaux objectifs étaient de mieux comprendre le mécanisme de réaction et de mettre en évidence leur potentiel à former des AOS. Pour atteindre ces objectifs, nous nous sommes concentrés sur quatre volets :

- Détermination du spectre IR et UV des aldéhydes insaturés en C_5 - C_7 .
- Détermination de la constante de vitesse pour les systèmes COVO + Oxydant étudiés à température ambiante.
- Identification et quantification des produits en phase gazeuse.
- Détermination des rendements en AOS.

Les constantes de vitesse des réactions chimiques ont été mesurées à la température atmosphérique, les mécanismes de réaction ont été déterminés et leurs contributions au budget total des SOA formés ont été quantifiées.

Ce manuscrit se compose de six chapitres :

- Le chapitre I est un aperçu général de la composition de l'atmosphère, des couches atmosphériques, du rayonnement solaire, des sources de COV biogéniques, et les

divers processus physiques et photochimiques influençant leurs émissions et leurs concentrations atmosphériques ont été présentés. Outre leur grande diversité chimique, les COV biogéniques présentent une large gamme de réactivité vis-à-vis du radical hydroxyle (OH), de l'ozone troposphérique et de l'atome chlore (Cl) pendant la journée et du radical nitrate (NO₃) pendant la nuit. L'impact de ces réactions d'oxydation sur la santé, l'environnement et la qualité de l'air a également été exposé.

- Le chapitre II présente les principaux systèmes et méthodes utilisés au cours de mon doctorat pour étudier la réaction d'oxydation des COV biogéniques sélectionnés avec l'ozone, l'atome Cl et le radical OH. Nombreux systèmes ont été utilisés : huit réacteurs statiques (chambres) ou dynamiques (flux), et diverses techniques analytiques ont été utilisées pour étudier la phase gazeuse de réaction (FTIR, GC-FID/MS, SPME-GC/MS, Carbotrap 202-GC/MS, DNPH-HPLC, PTR-ToF-MS, SIFT-MS, PLP-LIF) et la phase particulaire (SMPS, FMPS). Les sections efficaces d'absorption IR ont été déterminées à l'aide d'un spectromètre FTIR couplé à une cellule Pyrex de 96 m et à un détecteur MCT refroidi à l'azote liquide. En outre, les sections efficaces d'absorption UV ont été étudiées à l'aide d'une cellule d'absorption de 107 cm irradiée par une lampe à deutérium.
- Le chapitre III présente les sections efficaces d'absorption IR et UV des aldéhydes insaturés C₅-C₇. Les sections efficaces d'absorption IR à température ambiante de T2P, T2H et T2Hep ont été rapportées entre 650 et 4000 cm⁻¹. L'étude des spectres IR des trois composés étudiés vise à quantifier avec précision leurs concentrations lors de leurs études d'oxydation à l'Université UCLM. Les spectres d'absorption UV de T2P, T2H et T2Hep ont été déterminés à température ambiante sur la plage spectrale 270 – 410 nm. Ce travail fournit le premier spectre UV pour T2Hep et le second pour T2P. Dans le cas de T2H, il permet d'élucider la divergence existante entre les études expérimentales précédentes (O'Connor et al., 2006, Jiménez et al., 2007, Kalalian et al., 2019). Les sections efficaces d'absorption UV obtenues montrent que la photolyse peut être un processus de perte important pour les aldéhydes C₅-C₇ insaturés. Les taux de photolyse des aldéhydes insaturés étudiés

ont été calculés en utilisant un rendement quantique de photolyse $\Phi(\lambda)$ égal à 100%.

- Le chapitre IV montre la réactivité des aldéhydes insaturés en C₅-C₆ et des alcools insaturés en C₅-C₈ avec l'ozone. La première partie a été consacrée aux mesures cinétiques dans un réacteur batch (D-ASC) et un réacteur continu (LFR), à l'étude des produits (QUAREC-ASC) et à la formation de SOA (D-ASC) pour l'ozonolyse des aldéhydes insaturés sans ajout d'un piègeur des radicaux OH. Cependant, la deuxième partie traite des mesures cinétiques de l'ozonolyse des alcools insaturés C₅-C₈ dans la chambre D-ASC.
- Le chapitre V présente la réactivité des aldéhydes insaturés en C₅-C₇ et des alcools insaturés en C₅-C₈ avec les atomes Cl. Dans la première partie, j'ai étudié les cinétiques, les produits de réaction et la formation de SOA pour la réaction des aldéhydes insaturés en C₅-C₇ avec le chlore dans deux chambres de l'UCLM (16L-ASC et CR-ASC). Ensuite, j'ai présenté les constantes de vitesse de la réaction entre les alcools insaturés C₅-C₈ avec le Cl mesurées dans la chambre THALAMOS-ASC de laboratoire de l'IMT Lille Douai couplée à la technique SIFT-MS.
- Dans le chapitre VI, j'ai étudiée la cinétique des aldéhydes insaturés en C₅-C₆ avec les radicaux OH dans la cellule cryogénique Cryocell de l'IPR en utilisant la technique PLP-LIF dans la gamme de pression 7.4 – 471 Torr. D'autres expériences concernant la dépendance de la température de la constante de vitesse pour la même réaction sont en cours. En outre, l'étude des produits en phase gazeuse et de la formation de AOS pour la réaction de T2P et T2H avec des radicaux OH a été réalisée à l'Université de Wuppertal. Des expériences et des analyses complémentaires vont être réalisées dans la prochaine étape.

Ce manuscrit se termine par une conclusion de ce travail de doctorat, y compris des suggestions pour des recherches futures pour chaque partie des travaux.

Titre : Dégradation atmosphérique des Composés Organiques Volatils Oxygénés

Mots clés : COVOs, Réactivité atmosphérique, Spectre IR et UV, Cinétique, Mécanisme, AOS

Résumé : Les composés organiques volatils oxygénés (COVOs), principalement émis par des sources biogéniques, jouent un rôle majeur dans la chimie de l'atmosphère, le changement climatique, l'environnement et la santé. Il a été récemment démontré que ces émissions augmentent en cas de stress biotique et/ou abiotique. Les COVOs biogéniques peuvent subir une variété de réactions, tant chimiques que photolytiques, et ils sont impliqués dans la formation d'Aérosols Organiques Secondaires (AOS). Ces composés ont été détectés dans diverses régions, mais il y a très peu d'informations sur leurs processus de dégradation sous conditions troposphériques. La compréhension des mécanismes d'oxydation de ces espèces est d'un intérêt fondamental et fournit des données cruciales pour les modèles atmosphériques qui sont utilisés par les responsables politiques pour formuler et décider des stratégies d'amélioration de la qualité de l'air. Cette thèse vise à améliorer les connaissances actuelles sur le comportement de ces COVO, pour une meilleure compréhension de leur impact sur la chimie atmosphérique.

Dans ce travail, nous avons présenté une étude détaillée de la dégradation atmosphérique des aldéhydes insaturés en C₅-C₇ et des alcools insaturés en C₅-C₈ par ozone, l'atome Cl et le radical OH. Les principaux objectifs étaient de mieux comprendre le mécanisme de réaction et de mettre en évidence leur potentiel à former des AOS. Pour atteindre ces objectifs, nous nous sommes concentrés sur quatre volets : (i) détermination du spectre IR et UV des aldéhydes insaturés en C₅-C₇, (ii) détermination de la constante de vitesse pour les systèmes COVO + Oxydant étudiés à température ambiante, (iii) identification et quantification des produits en phase gazeuse, (iv) détermination des rendements en AOS. Les études sur les produits ont été menées avec et sans ajout d'un piègeur des radicaux OH. Les expériences ont été réalisées dans huit réacteurs, statiques (chambres) ou dynamiques (flux), et diverses techniques analytiques ont été utilisées pour étudier les produits de réaction (FTIR, GC-FID/MS, SPME-GC/MS, HPLC, PTR-ToF-MS, SIFT-MS, PLP-LIF) et la formation de AOS (SMPS, FMPS).

Title : Atmospheric degradation of Oxygenated Volatile Organic Compounds

Keywords : OVOCs, Atmospheric reactivity, IR and UV spectrum, Kinetic, Mechanism, SOA

Abstract : Oxygenated Volatile Organic Compounds (OVOCs), mainly released from biogenic sources, play a major role in atmospheric chemistry, climate change, environment, and health. These emissions have been recently shown to increase in the case of biotic and/or abiotic stresses. Biogenic OVOCs may undergo a wide variety of reactions, both chemical and photolytic, and they contribute in the formation of Secondary Organic Aerosols (SOAs). These compounds have been detected in various areas, but little is known about their degradation processes under tropospheric conditions. Understanding the oxidation mechanisms of these species is of fundamental interest and yields crucial data for atmospheric models used by policymakers in formulating and deciding strategies for improving air quality. This dissertation aims to improve the current knowledge of those OVOCs behaviors to better understand their impact on atmospheric chemistry.

This work reports a detailed study of the atmospheric degradation of C₅-C₇ unsaturated aldehydes and C₅-C₈ unsaturated alcohols by ozone, Cl atom, and OH radical. The main objectives were to better understand the reaction mechanism and to feature the SOA formation potential. To achieve these objectives, we focused on four topics: (i) determination of IR and UV spectrum of C₅-C₇ unsaturated aldehydes, (ii) determination of the rate constant for the studied OVOCs + Oxidant at room temperature, (iii) identification and quantification of the gas-phase products, (iv) determination of the SOA yields. The product studies were investigated both with and without adding an OH radical scavenger. Experiments were performed in eight different static (chambers) or dynamic (flow) reactors, and various analytical techniques were used to investigate the reaction products (FTIR, GC-FID/MS, SPME-GC/MS, HPLC, PTR-ToF-MS, SIFT-MS, PLP-LIF) and SOA formation (SMPS, FMPS).